INFORMATION TO USERS

This manuscript has been reproduced from the microfilm master. UMI films the text directly from the original or copy submitted. Thus, some thesis and dissertation copies are in typewriter face, while others may be from any type of computer printer.

The quality of this reproduction is dependent upon the quality of the copy submitted. Broken or indistinct print, colored or poor quality illustrations and photographs, print bleedthrough, substandard margins, and improper alignment can adversely affect reproduction.

In the unlikely event that the author did not send UMI a complete manuscript and there are missing pages, these will be noted. Also, if unauthorized copyright material had to be removed, a note will indicate the deletion.

Oversize materials (e.g., maps, drawings, charts) are reproduced by sectioning the original, beginning at the upper left-hand corner and continuing from left to right in equal sections with small overlaps.

Photographs included in the original manuscript have been reproduced xerographically in this copy. Higher quality 6" x 9" black and white photographic prints are available for any photographs or illustrations appearing in this copy for an additional charge. Contact UMI directly to order.

Bell & Howell Information and Learning
300 North Zeeb Road, Ann Arbor, MI 48106-1346 USA
800-521-0600

UMI®

SEPARATION OF COMPONENTS IN WASTE OXIDES BY EVAPORATION AND CONDENSATION UNDER REDUCED PRESSURE

BY

AHAD ZABETT, B.Sc., M.A.Sc.

DECEMBER 1998

A Thesis
Submitted to the School of Graduate Studies
in Partial Fulfillment of the Requirements
for the Degree
Doctor of Philosophy

SEPARATION OF COMPONENTS IN WASTE OXIDES BY EVAPORATION AND CONDENSATION UNDER REDUCED PRESSURE

Doctor of Philosophy (1999)
(Department of Materials Science and Engineering)

McMaster University
Hamilton, Ontario

TITLE:	Separation of Components in Waste Oxides by Evaporation and Condensation under Reduced Pressure
AUTHOR:	Ahad Zabett, B.Sc. (Tehran University, Tehran, Iran) M.A.Sc. (University of Waterloo, Waterloo, Canada)
SUPERVISOR:	Professor W-K. Lu
NUMBER OF PAGES:	xxi, 204

ABSTRACT

Steelmaking dust is generated in high temperature refining step at a rate of about 2% of the steel produced. Electric Arc Furnace (EAF) dust is classified as a hazardous material due to its content of leachable heavy metals, i.e., Pb, Cd, and Cr. Therefore, it must be treated before disposal to meet certain environmental regulations.

Most processes for the treatment of EAF dust involve recovery of valuable metals, such as zinc. In most cases alkali halides and lead in the dust are problematic in both processing and product quality. In the present work a pre-treatment is proposed to separate "more volatile species" which include the alkali halides, lead compounds and cadmium oxide, from "less volatile species" which include iron, zinc and calcium oxides. Evaporation of volatile species in this process takes place at about 900°C in a virtually closed system under reduced pressure, and condensation of the vapors occurs at a lower temperature.

The thermodynamic aspects of the process are considered. With the use of three different experimental apparatuses the kinetics of the system are studied. The rate of individual kinetic steps; evaporation, condensation, heat and mass transfer, are calculated and compared with the observed overall rate of reaction. A numerical model for the heat transfer inside the dust bed is developed. Applying the principles of mass and heat transfer to the system under investigation, and using the results of the experiments and the numerical model of heat transfer, it is shown that heat transfer across the porous dust bed is most likely the rate controlling step.

A rotary reaction chamber is designed to facilitate the heat transfer to dust particles and eliminate the slow kinetic step of heat transfer across the stationary dust bed. With the use of the rotary reaction chamber the duration of treatment is significantly reduced under otherwise identical conditions.

The benefit of the rotational movement may be appreciated by direct comparison of the treatment of twenty five grams EAF dust. At a furnace temperature of $1100^{\circ}C$ for 95% removal of the volatile species the time required (from the introduction of the apparatus at $25^{\circ}C$ to its withdrawal from the furnace) is 12 minutes for the stationary and 8 minutes for the rotational chamber. At a lower furnace temperature of $950^{\circ}C$, the degrees of removal of lead and potassium are about 51% and 27% for 12 minutes in the stationary reaction chamber and about 83% and 78% for 10 minutes in the rotary reaction chamber.

A secondary incinerator dust is also investigated in the present work. In 6 minutes at a furnace temperature of $950^{\circ}C$ about 99% of the volatile species including $NaCl$, KCl, and lead compounds are removed from twenty five grams dust. The residue has an enrichment of zinc from $27\%wt$ to $78\%wt$.

This environmentally friendly and energy efficient process may be applicable for the separation of “more volatile species” in dust generated from most high temperature processes such as steelmaking, incineration, nonferrous processes and cement manufacturing.

ACKNOWLEDGMENT

بِسْمِ اللَّهِ الرَّحْمَٰنِ الرَّحِيمِ

In the Name of God, the most Gracious, the most Merciful.

مَنْ لَمْ يَشْكُرِ الْمَخْلُوقَ، لَمْ يَشْكُرِ الْخَالِقَ

One who does not thank creatures (humans), does not thank creator (God).

The author wishes to express his sincere gratitude to his supervisor Dr. Wei-Kao Lu for his continuous guidance and encouragement throughout the course of this work. The author would like to thank the other members of his supervisory committee, Dr. G.A. Irons and Dr. D.R. Woods, for their constructive criticism, helpful suggestions and words of advice. The author would also like to thank his fellow graduate students for many fruitful discussions.

Special thanks go to the technical staff of the department of materials science and engineering and in particular Mr. Martin Van Oosten for all the help around the laboratories and chemical analyses. The author wishes to extend his thanks to Mrs. Veronika Szerneda and Betty Petro for their administrative helps.

Financial support from the Natural Science and Research Council of Canada in the form of a research grant to Dr. Lu is highly appreciated. The author would also like to thank the Ministry of Culture and Higher Education of Iran for a scholarship and McMaster university for other financial supports through departmental scholarship and teaching assistantship

Last but not the least, the author feels obliged to thank his wife and two daughters who suffered the most yet offered their moral support continuously throughout the course of this study.

Contents

1 INTRODUCTION 1

2 LITERATURE REVIEW 4

2.1 Formation and Characterization of EAF Dust 4

2.1.1 Chemical composition of EAF dust 6

2.1.2 Mineralogical phases in EAF dust 7

2.1.3 Morphology of EAF dust particles 8

2.2 Treatment of EAF Dust in Industry 9

2.3 Secondary Incinerator Dust 12

2.4 Current Challenges 14

3 THERMODYNAMIC COMPUTATIONS 16

3.1 Computations of Chemical Equilibrium 17

3.1.1 Procedure of computations 19

3.1.2 Computations with the use of a carrier gas 21

3.1.3 Computations with the use of additives 23

3.2 Equilibrium Vapor Pressure 23

3.3 Enthalpy Changes in the System 24
3.4 Results and Discussion 24

4 EXPERIMENTAL DESIGNS AND PROCEDURES 53

4.1 Outline of the Strategy for Experiments 53
4.2 Preliminary Experiments 54
4.3 Stationary Cylindrical Reaction Chamber 55
    4.3.1 Apparatus 55
    4.3.2 Experimental procedure 55
    4.3.3 Temperature profile 58
    4.3.4 Experiments with the use of a nickel boat 58
4.4 Rectangular Reaction Chamber 59
    4.4.1 Apparatus 59
    4.4.2 Experimental procedure 61
    4.4.3 Sampling procedure for chemical analysis 63
4.5 Rotary Reaction Chamber 65
    4.5.1 Apparatus 65
    4.5.2 Experimental procedure 65
4.6 Chemical Analysis 67
    4.6.1 Solution preparation 67
    4.6.2 Chemical analysis 67

5 EXPERIMENTAL RESULTS 68

5.1 Results of Temperature and Pressure Measurements 69
    5.1.1 Temperature profile inside the reaction chamber 74

5.1.2 Temperature vs. time inside the chamber and dust bed 74

5.1.3 Temperature vs. height in the dust bed 75

5.2 X-Ray Diffraction 75

5.3 Chemical Composition and Degree of Removal 75

5.3.1 Plots of chemical composition 76

5.3.2 Degree of removal vs. time and temperature 79

5.4 Error Analysis 79

5.4.1 Temperature measurement 79

5.4.2 Pressure measurement 80

5.4.3 Dust weight 80

5.4.4 Chemical analysis 81

5.4.5 Statistical analysis of final results (Reproducibility of results) . 81

6 Mass and Heat Transfer **129**

6.1 Mass Transfer 129

6.1.1 Vapor phase properties 130

6.1.2 Evaporation and condensation 134

6.1.3 Mass transfer within the dust bed 138

6.2 Heat Transfer 147

6.2.1 Heat radiation inside the hot zone 148

6.2.2 Numerical analysis of heat transfer inside the bed 154

6.2.3 Results of computations 163

6.2.4 Temperature profile inside the dust bed in cylindrical reaction chamber 165

7 DISCUSSION 174

7.1 Significance of Thermodynamic Computations 174

7.1.1 Chemical equilibrium 174

7.1.2 Vapor pressure and enthalpy changes 175

7.2 Discussion of the Experimental Results 176

7.2.1 Consistency of experimental observations 176

7.3 Review of Mass and Heat Transfer 187

7.4 Rate Controlling Step 188

7.4.1 Effect of apparent density of the dust bed 188

7.4.2 Effect of rotating the reaction chamber 191

7.5 Potential Industrial Applications 193

7.6 Summary 195

8 CONCLUSIONS 196

8.1 Thermodynamic and Kinetic Considerations 196

8.2 Experimental Observations 197

8.3 Mass and Heat Transfer Studies 198

Bibliography 199

List of Tables

3.1 Chemical composition of EAF dust type-A and -B used in thermodynamic computations, in %*wt*. 25

3.2 Main constituents of liquid phase for EAF dust type-A with 20 moles of carrier gas at 1000°*C*. 27

3.3 Total equilibrium vapor pressure of EAF dust type-A and -B. 28

3.4 Partial pressure of volatile species in vapor at equilibrium with EAF dust type-A and -B at different temperatures, in Pa. 28

3.5 Total and partial pressure of volatile species at equilibrium with a typical condensate at the cold compartment, in Pa. 29

5.1 Type and number of experiments. 69

5.2 Experiments with stationary cylindrical reaction chamber. 70

5.3 Experiments with rectangular reaction chamber. 71

5.4 Experiments with rotary cylindrical reaction chamber. 72

5.5 Experiment with rotary cylindrical reaction chamber (continued). . . 73

5.6 Chemical composition of EAF and secondary Incinerator dust in %*wt*. 76

5.7 Chemical composition of the dust residues after treatment in rotary reaction chamber.%wt. 76

5.8 Chemical composition of residues after treatment of EAF dust type-B in rotary reaction chamber.%wt. 77
5.9 Chemical composition of the secondary incinerator dust residues after treatment in rotary reaction chamber.%wt. 77
5.10 Degrees of removal of volatile species from EAF dust type-A, with different carrier gases. 78
5.11 Degrees of removal of volatile species from secondary incinerator dust. 78
5.12 Maximum error associated with each element. 81
5.13 Chemical composition of the residue of EAF dust type-B treated at 1100°C for 6 minutes, in %wt. 82
5.14 Chemical composition of the residue of EAF dust type-B treated at 950°C for 8 minutes, in %wt. 82

6.1 Diameters of species in the gas phase 131
6.2 Critical properties of vapor species 133
6.3 Viscosity of the vapor species at 900°C. 133
6.4 Rate and time required for evaporation and condensation of each species from 25 grams EAF dust type-A under experimental conditions. . . . 137
6.5 Calculated net power delivered at the surface of dust bed in cylindrical reaction chamber. 154

7.1 Degree of removal of volatile species from EAF dust type-A treated for 10 minutes in stationary cylindrical reaction chamber. 178
7.2 Degree of removal of volatile species from EAF dust type-A treated for 8 minutes in stationary cylindrical reaction chamber at 1100°C. . . . 178

7.3 Degree of removal of volatile species for EAF dust type-B treated in rotary reaction chamber at 900°C. 186

7.4 Degree of removal of volatile species for two different types of EAF dust treated in stationary reaction chamber at 1100°C. 189

7.5 Estimated effective thermal conductivity of the dust bed for EAF dust type-A. 190

7.6 Degree of removal of volatile species for two different types of EAF dust treated in rotary reaction chamber at 1100°C. 190

7.7 Degree of removal of volatile species for EAF dust type-B treated in stationary and rotary reaction chambers at 950°C. 191

7.8 Degree of removal of volatile species for EAF dust type-B treated in stationary and rotary reaction chambers at 1100°C. 191

List of Figures

2.1 Zinc splash condenser [7]. 13

3.1 A simple representative of separation process with a carrier gas in a continuous operation. 22

3.2 Calculated changes of phases and enthalpy during heating of EAF dust type-A under reduced pressure. 30

3.3 Calculated changes of phases and enthalpy during heating of EAF dust type-B under reduced pressure. 31

3.4 Calculated amount of liquid phase in 100 grams EAF dust type-A in equilibrium with air. 32

3.5 Calculated amount of liquid phase in 100 grams EAF dust type-A in equilibrium with air and nitrogen at different temperatures. 33

3.6 Calculated amount of liquid phase in 100 grams EAF dust type-A at 900°C in equilibrium with different carrier gases. 34

3.7 Calculated amount of liquid phase in 100 grams EAF dust type-A at 1000°C in equilibrium with different carrier gases. 35

3.8 Calculated amount of liquid phase in 100 grams EAF dust type-A with some additives at 900°C in equilibrium with nitrogen. 36

3.9 Calculated amount of liquid phase in 100 grams EAF dust type-A with some additives at 1000°C in equilibrium with nitrogen. 37
3.10 Calculated amount of lead in condense phases of 100 grams EAF dust type-A in eauilibrium with a carrier gas at 900°C. 38
3.11 Calculated amount of sodium in condense phases of 100 grams EAF dust type-A in eauilibrium with a carrier gas at 900°C. 39
3.12 Calculated amount of potassium in condense phases of 100 grams EAF dust type-A in eauilibrium with a carrier gas at 900°C. 40
3.13 Calculated amount of lead in condense phases of 100 grams EAF dust type-A in eauilibrium with a carrier gas at 1000°C. 41
3.14 Calculated amount of sodium in condense phases of 100 grams EAF dust type-A in eauilibrium with a carrier gas at 1000°C. 42
3.15 Calculated amount of potassium in condense phases of 100 grams EAF dust type-A in eauilibrium with a carrier gas at 1000°C. 43
3.16 Calculated amount of lead in condense phases of 100 grams EAF dust type-A with additives in eauilibrium with nitrogen at 900°C. 44
3.17 Calculated amount of lead in condense phases of 100 grams EAF dust type-A with additives in eauilibrium with nitrogen at 1000°C. 45
3.18 Calculated percentage of removal of volatile species from EAF dust type-A by air at 900°C. 46
3.19 Calculated percentage of removal of volatile species from EAF dust type-A by air at 1000°C. 47
3.20 Calculated percentage of removal of volatile species from EAF dust type-A by nitrogen at 1000°C. 48

3.21 Calculated zinc content of the vapor phase in equilibrium with a carrier gas. 49
3.22 Calculated zinc content of the vapor phase in equilibrium with nitrogen when some additives added to EAF dust. 50
3.23 Equilibrium vapor pressure of some pure compounds. 51
3.24 Calculated total vapor pressure in the hot zone and cold zone for the condition of cylindrical reaction chamber. 52

4.1 First experimental setup with cylinderical reaction chamber. 56
4.2 Design of cylinderical reaction chamber. 57
4.3 Experiment setup with rectangular reaction chamber. 60
4.4 Nickel boat used for treatment of EAF dust in rectangular reaction chamber. 61
4.5 Schematic representation of the plastic tube used for sampling. 64
4.6 Experimental setup with rotary reaction chamber. 66

5.1 Temperature profile inside the cylindrical reaction chamber. 83
5.2 Temperature at the hot end of the cylindrical reaction chamber the time chamber is inserted inside the furnace. 84
5.3 Temperature and pressure variation inside the rotary reaction chamber during treatment of EAF dust type-B. 85
5.4 Temperature and pressure variation inside the rotary reaction chamber during treatment of EAF dust type-B. 86
5.5 Temperature and pressure variation inside the rotary reaction chamber during treatment of secondary incinerator dust. 87
5.6 Temperature variation inside the dust bed during heating of alumina. 88

5.7 Temperature and pressure variation during heating of a mixture of alumina and KCl. 89

5.8 Temperature and pressure variation during treatment of EAF dust type-C. 90

5.9 Temperature and pressure variation during treatment of EAF dust type-A. 91

5.10 Temperature and pressure variation during treatment of EAF dust type-A. 92

5.11 Temperature and pressure variation during treatment of EAF dust type-B. 93

5.12 Temperature profile inside dust bed at different time during treatment of EAF dust type-A. 94

5.13 Temperature profile inside dust bed at different time during heating of alumina powder. 95

5.14 Temperature profile inside dust bed at different time during treatment of EAF dust type-B. 96

5.15 Temperature profile inside dust bed at different time during treatment of EAF dust type-B. 97

5.16 A comparison of temperature profile inside dust bed after 18 minutes heating in different experiments. 98

5.17 A comparison of temperature profile inside dust bed after 28 minutes heating in different experiments. 99

5.18 X-ray diffraction patterns of EAF dust type-A a) before and b) after 7 minutes treatment at 1100$^\circ C$ in rotary reaction chamber. 100

5.19 Effect of temperature on removal of volatile species. (Note: Pb and K data at 1100°C are shown at slightly different temperature for clarity) 101
5.20 Effect of time on removal of volatile species at 900°C. 102
5.21 Effect of time on removal of volatile species at 950°C. (Note: Pb and K data at 8 minute are shown at slightly different time for clarity) . . 103
5.22 Effect of time on removal of volatile species at 1100°C. (Note: Pb and K data at 6 minute are shown at slightly different time for clarity) . . 104
5.23 Comparison of the results of treatment at 950°C in stationary reaction chamber with those of rotary reaction chamber. 105
5.24 Comparison of the results of treatment at 1100°C in stationary reaction chamber with those of rotary reaction chamber. 106
5.25 Lead content in residues after treatment of EAF dust type-B in rotary reaction chamber. 107
5.26 Sodium content in residues after treatment of EAF dust type-B in rotary reaction chamber. 108
5.27 Potassium content in residues after treatment of EAF dust type-B in rotary reaction chamber. 109
5.28 Surface diagrams representing the effect of time and temperature on composition of residues after treatment of EAF dust type-B in rotary reaction chamber. 110
5.29 Constant content contour diagram representing the lead content in residues after treatment of EAF dust type-B in rotary reaction chamber. 111
5.30 Constant content contour diagram representing the sodium content in residues after treatment of EAF dust type-B in rotary reaction chamber. 112

5.31 Constant content contour diagram representing the potassium content in residues after treatment of EAF dust type-B in rotary reaction chamber. 113
5.32 Effect of temperature on removal of volatile species from secondary incinerator dust. 114
5.33 Effect of time on removal of volatile species from secondary incinerator dust. 115
5.34 Lead content in residues taken from different heights of the dust bed, EAF dust type-A. 116
5.35 Sodium content in residues taken from different heights of the dust bed, EAF dust type-A. 117
5.36 Potassium content in residues taken from different heights of the dust bed, EAF dust type-A. 118
5.37 Lead content in residues taken from different heights of the dust bed, EAF dust type-A. 119
5.38 Sodium content in residues taken from different heights of the dust bed, EAF dust type-A. 120
5.39 Potassium content in residues taken from different heights of the dust bed, EAF dust type-A. 121
5.40 Lead content in residues taken from different heights of the dust bed, EAF dust type-B. 122
5.41 Sodium content in residues taken from different heights of the dust bed, EAF dust type-B. 123

5.42 Potassium content in residues taken from different heights of the dust bed, EAF dust type-B. 124

5.43 Degree of removal of volatile species from EAF dust type-B treated in rotary reaction chamber at 950°C. 125

5.44 Degree of removal of volatile species from EAF dust type-B treated in rotary reaction chamber at 1100°C. 126

5.45 Degree of removal of volatile species from EAF dust type-B after 6 minutes of treatment in rotary reaction chamber at different temperatures. 127

5.46 Degree of removal of volatile species from EAF dust type-B after 8 minutes of treatment in rotary reaction chamber at different temperatures. 128

6.1 View of two cross sections for dust bed inside cylindrical reaction chamber. 141

6.2 Calculated time required for removal of volatile species from dust bed based on molecular flow. 143

6.3 A schematic representation of the hot zone for cylindrical reaction chamber. 149

6.4 Analog electric circuit of the hot zone for the cylindrical reaction chamber. 150

6.5 Temperature variation of EAF dust type-A at different heights inside the bed, Experiment #49, furnace temperature 1100°C. 167

6.6 Temperature variation of EAF dust type-A at different heights inside the bed, Experiment #50, furnace temperature 1100°C. 168

6.7 Temperature variation of EAF dust type-A at different heights inside the bed, Experiment #54, furnace temperature 1100°C. 169

6.8 Temperature variation of alumina at different heights inside the bed, Experiment #61, furnace temperature 1100°C. 170

6.9 Temperature variation of EAF dust type-C at different heights inside the bed, Experiment #62, furnace temperature 1100°C. 171

6.10 Calculated temperature of EAF dust type-A at different heights inside the bed for cylindrical reaction chamber, furnace temperature 1100°C. 172

6.11 Calculated temperature of EAF dust type-B at different heights inside the bed for cylindrical reaction chamber, furnace temperature 1100°C. 173

7.1 Apparent thermal conductivity of powders. I. quartz sand, grains 0.26 mm; II. zinc dust, grains 0.028 mm; III. zinc dust, grains 0.0062 mm; IV. spongy diatomaceous earth; V. spongy lamp soot; VI. air [48]. . . 184

Chapter 1

INTRODUCTION

It is the nature of high temperature processes that dust is always generated as a result of metal vaporization and subsequent oxidation, and/or vaporization of volatile species such as alkali halides and oxides of heavy metals as well as carry over fines. Examples of such high temperature processes in industry are steelmaking, smelting of non-ferrous metals, municipal waste incineration and cement manufacturing. In steelmaking shops the amount of dust generated is $1.5 - 2\%$ of the steel produced. In excess of $650,000$ tons of dust is annually generated in carbon steel electric arc furnace (EAF) shops in the United States alone and this is expected to increase to $900,000$ tons in year 2000 as the EAF steel production continues to rise[1].

Implementation of the Clean Air Act requires dust to be captured. The U.S. Environment Protection Agency (EPA) designates dusts containing lead ($> 5\,ppm$), cadmium ($> 1\,ppm$), and chromium ($> 5\,ppm$) as hazardous materials[2]. The regulation put into effect in 1988 does not allow landfill of such dusts unless the hazardous compounds are stabilized or removed.

EAF dust as a particular example of hazardous dust being regulated by EPA, has been the focus of attention in a number of studies [1, 3-12] The most important practices for treatment of EAF dust are those of high temperature recovery of valuable metals such as zinc in the form of either metal or oxide. Other solutions to the problems of EAF dust are minimization, recycling, and fixation processes such as low temperature stabilization and high temperature vitrification.

Pyrometallurgical recovery processes of metallic zinc are the most economically viable technologies for on-site treatment of EAF dust. These involve high temperature reduction, volatilization and condensation. After reduction the gas which contains zinc vapor is led from a hot cyclone to a splash condenser. The rotating splasher mechanically makes metal droplets and disperses them in the condenser in order to provide a larger surface area for condensation. The splash condenser encounters an operational problem arising from the formation of dross. Dross which is made of condensed alkali halides and re-oxidized metal oxides and carried over dust, forms a viscous layer on the top of zinc bath and covers the surface of droplets generated by the splasher. This prevents contact between zinc vapor and droplets and the bath of liquid metal and hinders condensation.

In order to avoid the problem of alkali halides in the splash condenser, dust may be washed to remove the alkali halides. The potential water contamination from wet processes are more serious for inland plants. Therefore, it is important to find a suitable solution with the least risk of further environmental problems.

In the present work which consists of both theoretical analysis and laboratory experimentation, the fundamentals of a separation process is studied. This process involves evaporation of volatile species at about $900°C$ in a virtually closed system under reduced pressure and condensation of the vapors at a lower temperature. It is based on the fact that zinc and iron oxides have lower equilibrium vapor pressures in comparison to alkali halides, cadmium oxide and lead compounds.

This dissertation will be presented in eight chapters. Chapter two reviews the literature on formation, characterization and treatment of EAF dust. A thermodynamic study of the system under investigation will be presented in chapter three. Experimental procedures and results are given in chapters four and five. Chapter six deals with the mass and heat transfer in the system. The flux for each kinetic step is calculated and compared with the overall rate of reaction in the system. Chapter seven will discuss the experimental results and the reaction mechanisms. The separation process to remove alkali halides and lead compounds before reduction of dust is proposed in this work to improve the efficiency of the splash condenser and produce a higher grade of zinc. The potential industrial application of this process will be presented in chapter seven.

Chapter 2

LITERATURE REVIEW

2.1 Formation and Characterization of EAF Dust

The mechanisms of EAF dust formation reported in the literature are summarized by Cowx[11] as follows:

1. vaporization of metals, i.e. Fe, Zn, Pb, Cd, Mn,
2. ejection of metal and slag droplets by bubble bursting,
3. entrainment of large slag droplets,
4. evaporation of volatile species, and
5. physical entrainment of solids.

The main mechanism of iron oxide fume formation is thought to be the bursting CO bubbles ejecting iron droplets into the gas stream where they are explosively oxidized to form a very fine iron oxide fume[13, 14, 15]. Metal vaporization occurs as a result of high temperatures and oxygen jet-metal interaction. Iron vaporization is only significant under non-boiling conditions or where a hot spot exists at the oxygen jet or the arc impact zone. Evaporation is followed by oxidation of metal vapor with the oxygen within the furnace.

In well stirred oxygen steelmaking processes such as AOD or Q-BOP, vaporization contributes to about 3% of the dust formation but in top blown BOF with a more pronounced hot spot beneath the oxygen jet, vaporization contributes to about 15% of the dust formation[11]. The proportion of dust formed by iron vaporization in the EAF may be higher than that found in the BOF because there are likely to be significant hot spots at the arc, oxy-fuel and oxygen jet impingement zones. Furthermore, the surface area/volume ratio of an EAF is higher than a BOF and the EAF bath is not well stirred.

One of the most comprehensive studies on formation and characterization of EAF dust has been published by Lehigh University[3]. In that report, the predominant mechanism of EAF dust formation is assumed to be vapor deposition and oxidation on the surface of solids such as fugitive dust.

In another comprehensive study on mineralogical characterization of EAF dust, Hagni [4] reported Pb, Na, K, Cl, and F to be some of the elements on the surface of dust particles detected by means of electron spectroscopy. In the Lehigh study[3] lead compounds were also found on the surface of iron rich particles. This is in agreement with the proposed mechanism of deposition of vapor on condensed surfaces, since the alkali halides and lead compounds are most likely to condense at later stages of dust formation due to their lower boiling temperature.

Law [16] reported that zinc and lead had the tendency to concentrate in the smallest size fraction of dust particles, whereas iron and chromium concentrated in the coarse fraction. The Lehigh study [3], Hagni [4] and Li [17] also found the ratio of zinc oxide to zinc ferrite spinel to increase with decreasing particle size.

2.1.1 Chemical composition of EAF dust

The composition of EAF dust depends on the type of steel produced and is directly influenced by the type of scrap and alloy addition. Major elements present in an EAF dust are iron, zinc, calcium, lead, manganese, magnesium, sodium, potassium, chlorine and oxygen. Aluminum, silicon, cadmium, sulfur, carbon, fluorine, chromium, nickel, molybdenum, and other components of scrap may also be present in EAF dust. Alloying elements such as chromium, nickel and molybdenum are found more in stainless steel EAF dust.

Zinc enters the furnace as coated scrap, residual die castings in auto-scrap, etc. Lead and cadmium are found in coatings, paints, and in association with zinc. Other sources of lead are solders, brasses and wheel weights in automotive scrap. Sodium, potassium and chlorine are mainly associated with auto scrap exposed to road de-icing chemicals. Chlorine can also enter the furnace by oils, organics and plastics. Fluorine is found in EAF dust when fluorspar, CaF_2, is used as flux. The calcium content of EAF dust varies greatly and depends on the type of lime charged in the furnace.

Based on a number of studies[3, 4, 12, 17] carried out on more than 60 EAF dust samples from different carbon steel shops, the following range of chemical compositions is found.

%wt.	Fe	Zn	Ca	Pb	Na	K	Cl	Cd	Cr
Low	18	10	4	0.5	0.5	0.4	1.0	0.05	0.05
High	37	31	12	3.2	5.6	1.7	7.0	0.95	0.65

2.1.2 Mineralogical phases in EAF dust

The Lehigh study[3] suggested that the dominant phase in EAF dust particles is a spinel with lattice parameters indicating compositions close to that of magnetite (Fe_3O_4) or zinc ferrite ($ZnO.Fe_2O_3$). Most of their samples contained zinc oxide (ZnO) and minor amounts of hematite (Fe_2O_3). Calcite ($CaCO_3$) and/or lime (CaO) were present in the samples with higher calcium content. Other minor constituents identified include graphite, sodium chloride, potassium chloride, calcium difluoride, wustite, magnesium oxide and cadmium oxide. The presence of lead compounds was observed on the surface of iron rich particles by transmission electron microscopy.

Hagni [4, 18] and Badger et al. [12] reported the main phase to be the spinel solid solutions in the form of $(Zn, Fe, Mn, Ca, Mg)(Fe, Cr, Mn, Al)_2O_4$ crystals within $Ca - Fe - Si$ glass matrix spheres. Zinc also is found in the form of zinc oxide (ZnO). Other major mineralogical phases referred to in these studies are graphite (C), sylvite(KCl), halite($NaCl$), fluorite (CaF_2), hematite (Fe_2O_3), periclase (MgO), calcite ($CaCO_3$) and hatrurite (Ca_3SiO_5). Hagni [4] did not exactly determine the lead compounds, but assumed them to be in the form of Pb-O, Pb-F, Pb-Cl, and Pb-O-Cl. Lead was also found in association with phosphorus in clusters of 200 – 500Å spheres. Badger et al. [12] mentioned that halite ($NaCl$) and sulvite (KCl) accounted for less than 5% of the dusts examined, but the major source of chlorine in their samples. Sodium and potassium chlorides and lead compounds were detected as surface coatings for the top few atomic layers of the dust particles. These volatile species and zinc oxide are also found to form the finest fraction of the dust.

Li et al. [17, 19] claimed the mineral composition of EAF dust samples from some Taiwanese steel shops to be mainly $(Mn, Zn) Fe_2O_4$, ZnO, and $ZnCl_2.4Zn(OH)_2.H_2O$. They suggested that the latter phase existed as an extremely thin coating on the dust particle surface acting as a bonding material, agglomerating dust particles. It should be noted that the amount of chlorine reported in some of their samples is up to $7\%wt$. The higher amount of chlorine may be the main reason zinc chloride was present in their samples while no other researcher reported a mineralogical phase containing zinc chloride.

2.1.3 Morphology of EAF dust particles

For the 33 EAF dust samples considered in the Lehigh study[3], the particles were found to be generally spherical with sizes ranging from 0.1 μm to 10 μm, the majority of which were less than 1 μm, while the greatest mass of the dust is contained in the larger size particles. This report describes EAF dust as being composed primarily of a self-agglomerated collection of microfine and chemically complex particles. Typical agglomerates are made up of submicron particles, which are spherical, while some faceted particles were also observed. In the smaller agglomerates, particles were often linearly aligned. This alignment was interpreted as being magnetic in nature.

Hagni reported [4, 18] that for the 14 EAF dust samples investigated, particle sizes ranged from less than 1 μm to more than 300 μm, with the majority of particles in the range of $1 - 6$ μm. Most particles were found to be spherical together with some angular fragments of broken spheres. Many particles where found to be hollow.

Li et al. [17, 19] found EAF dust particles to be between 3 μm to 20 μm, being irregular agglomerates of much smaller particles ($0.3 - 1\ \mu m$ in size). They showed spherical particles were bound together with a substance they assumed to be zinc hydroxide chloride, while other researchers [3, 4] have pointed to surface charge and magnetic properties as the cause of agglomeration.

2.2 Treatment of EAF Dust in Industry

EAF dust is designated as a hazardous waste due to its content of lead, cadmium and chromium. Therefore, it must be treated before being placed in a landfill. One approach to the problem of dust is through minimization of its generation. In a CMP report [1] a number of recommendations have been given for this purpose with the most important one being recycling or partial recycling of the dust. While minimization of dust is an important task, it can not be a complete solution because further treatment is always required. Different techniques for treatment of EAF dust have been pursued by different researchers. These can be categorized as follows:

1. stabilization or vitrification of the dust to allow disposal
    a) low temperature chemical stabilization
    b) high temperature vitrification or glass formation
2. zinc recovery and removal of heavy metals
    a) hydrometallurgical recovery of metals
    b) fuming and zinc metal recovery
    c) fuming and zinc oxide recovery.

An EAF dust with relatively low zinc content may be treated chemically to stabilize the heavy metals, thereby reducing their leach rates to acceptable levels. The process involves mixing the dust with water and a soluble silicate or aluminosilicate. A bonding agent such as portland cement and some other additives may be added and the slurry is cast into forms for solidification, precipitating, and curing. The resulting structure is covalently bonded, with complex silicates and aluminosilicate chains that immobilize the basic oxides, including the heavy metal [1, 10].

Vitrification or glassification is a high temperature stabilization process. In this process EAF dust is mixed with a silica source and heated to form a molten glass. EAF dust in the molten state behaves like an ionic solution. When the silica source is added, the ionic species bind together to form long complex polymers of silicates and aluminosilicates. This glass network incorporates the heavy metals, providing them with a higher degree of covalent bonding, thereby reducing their leachability[1, 10].

Hydrometallurgical treatment of EAF dust for zinc recovery is not yet commercially attractive. The methods explored include sulfate, chloride, and caustic leaching. The presence of zinc ferrite and halide compounds in EAF dust seem to be problematic in hydrometallurgical techniques. Zinc ferrite is insoluble in the leachant, hence, is collected with iron oxides and recycled to the EAF[1]. In order to take full advantage of the leaching stage, a combined pyrometallurgical/hydrometallurgical process has been developed and recently commercialized[1]. This process uses a high temperature pre-treatment, involving reduction, volatilization, and re-oxidation to decompose the zinc ferrite. Collected dust from this pre-treatment, containing zinc, lead and cadmium oxides plus other volatile species such as alkali halides, is treated in a hydrometallurgical process to recover zinc oxide and metallic lead.

High temperature zinc recovery processes involve zinc fuming. The dust is mixed with a reductant and fluxes, and is heated in a fuming reactor. Several processes with different reactors have been used, including rotary kiln roaster[20, 21], electric resistance furnace[22], flame reactor[23], plasma arc furnace[7, 24, 25], rotary hearth[26], flash reactor[27], and dust injection into a molten iron bath[28]. In all cases, the objective is to reduce and fume zinc, lead and cadmium, leaving a metallic and/or oxide residue substantially free of these heavy metals. The heavy metals are then collected from the off-gas stream as condensed metal or metal oxide. In high temperature zinc recovery processes, zinc may be collected as metal or oxide.

In zinc oxide recovery processes zinc and other metal vapors are re-oxidized after fuming. This crude zinc oxide may be further refined in a second furnace at temperatures between $1100 - 1300°C$ to remove lead and cadmium compounds, and alkali halides. Zinc oxide recovery processes are economically attractive at larger capacities and play a major role in treatment of EAF dust. Examples of this process are Waelz Kiln, Flame Reactor and Sirosmelt[1].

In a metal recovery process, after reduction and fuming, the gas is led from hot cyclone to a splash condenser, Figure 2.1. The splasher mechanically makes droplets and disperses them in the condenser. The droplets provide larger total surface area for condensation of zinc vapor. However, the presence of alkali halides in the system causes the formation of dross which is a mixture of alkali halides, re-oxidized metal oxides and carried over dust. Dross forms a viscous layer on the top surface of the zinc bath. It also covers the surface of droplets generated by the splasher. This adversely affects the performance of the splash condenser and decreases its efficiency.

Metal zinc recovery processes do not depend on an intermediate zinc oxide market and fit in well with existing operations in the steel industry, hence, they are suitable for on site treatment of EAF dust. Examples of these processes are Swedish ScanArc Plasma Technology[25, 29], Japanese blast furnace[30], Laclede Steel's sealed electric furnace (modified Elkem process)[1, 22], AllMet rotary hearth-plasma process[1, 26], IMS Tetronics Plasma[31] and Hi Plas[24, 32].

The main problems referred to in all pyrometallurgical metal zinc recovery processes are dross formation and iron carry over to the condenser which degrades the zinc product. Swedish ScanArc Plasma, which has been working since1984, has replaced the original splash condenser with a lead spray condenser to resolve the problem associated with dross formation. IMS Tetronics Plasma and Hi Plas are shut down due to low grade zinc and dross formation. AllMet uses a rotary hearth to reduce pellets made up of mill scale, sludges, EAF dust and other iron oxide wastes. Reduced zinc and lead are vaporized along with other volatile species such as salts and led to the splash condenser. In this way the problem of iron carry over to the splash condenser is resolved. Yet, in the AllMet process and other processes using a splash condenser, dross formed in the condenser has to be dealt with and removed from the system.

2.3 Secondary Incinerator Dust

In addition to EAF dust, a secondary incinerator dust is included in this study. Bottom ash and collected dust from municipal solid waste incinerators contain heavy metals and need further treatment[33, 34]. Bottom ash and off-gas dust are melted

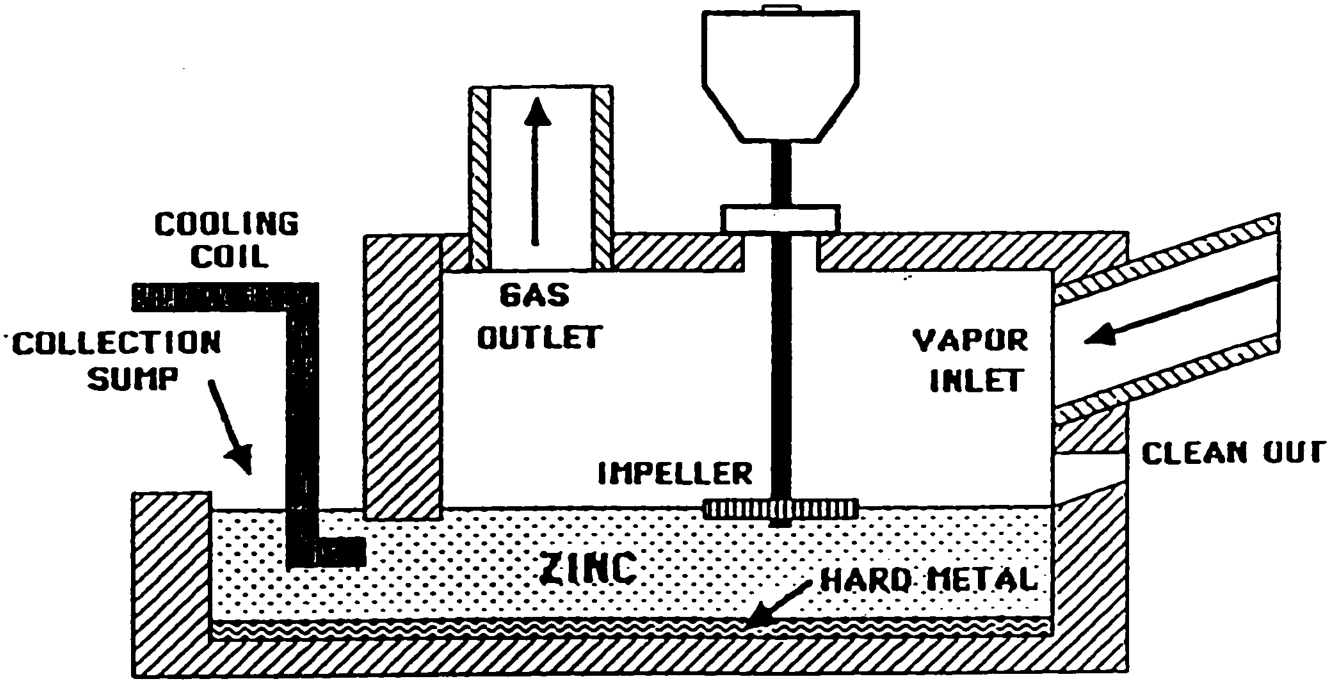

Figure 2.1: Zinc splash condenser [7].

in an electric resistance furnace to produce a chemically stable slag suitable for disposal. Secondary dust is generated in this process that contains up to $10\%wt.$ Pb and $30\%wt.$ Zn. $NaCl$ and KCl are major constituents of this type of dust and could form $50\%wt.$ of the dust. Lime, silica, alumina and iron oxides are the other compounds found in the secondary incinerator dust[33, 34].

2.4 Current Challenges

Most metal zinc recovery processes use a splash condenser to condense and collect zinc. Dross formation is a major problem in these processes and often impairs the condenser operation. A number of plants have been shut down [1, 24, 31] due to this problem and iron carry over and some have been modified to avoid this problem[22, 25].

Alkali halides not only affect the metal zinc recovery processes but also are problematic in most other processes and therefore have to be dealt with one way or another. In hydrometallurgical processes, salt is carried over to the electrowinning bath and accumulated in the electrolyte. The amounts of impurities are controlled by purging the electrolyte through an evaporator that separates salts by concentration and crystallization. In zinc oxide recovery processes such as the rotary kiln process, which is the world's largest recycler of EAF dust, the crude zinc oxide is further refined in a second rotary kiln under oxidizing conditions at temperatures of $1100 - 1300°C$ to remove lead and cadmium compounds, and alkali halides.

Considering the current regulatory issues related to hazardous dusts and the rising generation of dust, it is well understood that the concerned industries must seek new technologies for treatment of hazardous dust as well as improving the status of those currently in operation. Dust generated in many high temperature industrial processes contains alkali halides and other compounds of heavy metals. Most processes of treating hazardous dusts are adversely affected by these volatile species. Therefore, the objective of this thesis is to investigate the possibility of a new treatment to separate "more volatile species" from "less volatile species" in hazardous dusts containing heavy metals and alkali halides by a dry separation process in a virtually closed system. This treatment can effectively resolve the problem of dross formation in zinc metal recovery processes by removing alkali halides from the dust and eliminate extra steps in refining zinc alloy to produce Prime Western grade zinc by removing lead compounds from the dust.

Chapter 3

THERMODYNAMIC COMPUTATIONS

In this chapter the thermodynamic aspects of the separation process of "more volatile species" from "less volatile species" in EAF dust will be considered. For this purpose extensive computations of the reactions following an equilibrium path have been carried out. Computations have been performed for different atmospheric conditions and with consideration of different additives to EAF dust. Here the fundamentals of thermodynamic calculations and the procedure of the computations will be explained and the results will be presented and discussed.

3.1 Computations of Chemical Equilibrium

For all thermodynamic computations "FACT" program version 2.1 (Facility for Analysis of Chemical Thermodynamics) [35, 36] is used. For computations of the chemical equilibrium "FACT" program uses "ChemSage" module developed by Eriksson [36, 37] under the name "EQUILIB". This program takes advantage of the database available in "FACT".

In general, for a closed system containing a known amount of matter at specified temperature and pressure "EQUILIB" finds the combination of species in different phases which possesses the lowest Gibbs free energy and therefore, is at the most stable condition. The input data may be chosen in the form of compounds or elements. When the input data is introduced to "EQUILIB", all possible compounds containing the elements in the input data are looked up from the "FACT" database. These include all species in gas, liquid or solid phases. Gibbs free energy of each species is calculated based on available thermodynamic database. A total Gibbs free energy, G, for a possible product group can be determined by summing the product of the molar Gibbs free energy of each species, g_i, and the corresponding mole numbers, n_i, and then adding appropriate Gibbs free energy of mixing terms.

$$G = \sum_{i=1}^{m} n_i g_i + RT \sum_{j=1}^{a} n_j \ln(X_j P) + RT \sum_{k=a+1}^{b} n_k \ln(X_k)$$

where R is the gas constant, T is the absolute temperature, P is the total pressure of the gaseous phase and X is the mole fraction. The second term on the right hand side is the Gibbs free energy of mixing for gas phase, and the last term is the Gibbs free energy of mixing for liquid phase. In the present study both gas and liquid phases are assumed to be ideal solutions.

In order to find the most stable set of chemical species, "EQUILIB" systematically varies the moles of each species in a way that makes "G" of minimum value at a particular combination of temperature and pressure. If the existence of a particular solution phase does not assist in minimizing G, it will be dropped in the course of successive iterations. The maximum number of equilibrium phases can not exceed the number of different elements in the reactants in order to respect the Gibbs Phase Rule.

Certain assumptions are implied in the computations that should be taken into account for the interpretation of the output results. The reactions take place in a closed system and all compounds are at a uniform temperature specified in the computations. The volume of condense phases is assumed to be zero and therefore, at any given pressure and temperature the volume of the system will be calculated based on the number of moles of the gas phase in equilibrium with the condense phases. If the volume is specified then the program will calculate the total pressure of the system based on the summation of the partial pressure of the gaseous species in the system at the equilibrium state.

It should be noted that carbon ($< 0.5\%wt.$ in EAF dusts investigated in the present work) is not considered in the computation in order to avoid permanent gas[1] in the system. This is important for the calculations under the reduced pressure and when the total pressure or the partial pressure of volatile species are to be calculated. Based on the measurements of the pressure at the cold end in the present work, it is most likely that carbon is removed from the system in the form of carbon monoxide in the early stages of the separation process by means of the vacuum pump.

---

[1] Here permanent gas is referred to a gas phase stable at room temperature.

3.1.1 Procedure of computations

Since the final chemical equilibrium condition does not depend on the initial form of the reactants, a simple elemental form of chemical composition of 100 grams EAF dust is used in each calculation. Following is a typical input data for computations of the chemical equilibrium with "EQUILIB" program.

(gram)	32.60 Fe +	21.60 Zn +	3.10 Pb +	4.50 Ca +
	(25C, 1ATM, S1)	(25C, 1ATM, S1)	(25C, 1ATM, S1)	(25C, 1ATM, S1)
(gram)	2.60 Mn +	2.10 Mg +	1.40 Na +	1.00 K +
	(25C, 1ATM, S1)	(25C, 1ATM, S1)	(25C, 1ATM, S1)	(25C, 1ATM, S1)
(gram)	0.40 Al +	0.30 Si +	0.10 Cd +	2.80 Cl_2 +
	(25C, 1ATM, S1)	(25C, 1ATM, S1)	(25C, 1ATM, S1)	(25C, 1ATM, G)
(gram)	0.05 F_2 +	27.45 O_2 +	28.00 N_2 =	
	(25C, 1ATM, G)	(25C, 1ATM, G)	(25C, 1ATM, G)	

For this calculation possible phases from FACT database are listed in appendix-A. A typical output result from "EQUILIB" after calculation of the chemical equilibrium at 1000°C and one atmosphere is given in the following three text-boxes for gaseous phase, ideal liquid solution and solid phases. For the solid phases, S1 and S2 stand for different crystalline structures of the same compound.

Composition of gas phase,
from "EQUILIB" output.

```
     104.95          litre
(    78.600          vol%      N2
+    20.574          vol%      O2
+    0.39231         vol%      NaCl
+    0.24512         vol%      KCl
+    0.60808E-01     vol%      (NaCl)2
+    0.35949E-01     vol%      NO
+    0.26242E-01     vol%      PbO
+    0.18151E-01     vol%      PbCl4
+    0.17228E-01     vol%      (KCl)2
+    0.13457E-01     vol%      PbCl2
+    0.75806E-02     vol%      Cd
+    0.56829E-02     vol%      CdO
+    0.77737E-03     vol%      PbCl
+    0.67196E-03     vol%      ZnCl2
+    0.64374E-03     vol%      NaF
+    0.41804E-03     vol%      NO2
+    0.37259E-03     vol%      KF
+    0.16397E-03     vol%      Cl
+    0.15462E-03     vol%      OAlF2
+    0.56559E-05     vol%      Pb
+    0.55437E-05     vol%      (NaF)2
+    0.51837E-05     vol%      MnCl2
+    0.48629E-05     vol%      O
+    0.28799E-05     vol%      Cl2
+    0.25764E-05     vol%      ClO
+    0.20961E-05     vol%      N2O
+    0.11661E-05     vol%      PbF2
+    0.53948E-06     vol%      Zn
+    0.35873E-06     vol%      PbF
+    0.26788E-06     vol%      Na
+    0.21799E-06     vol%      CaCl2
+    0.16431E-06     vol%      ONCl
+    0.13138E-06     vol%      (KF)2
+    0.75087E-07     vol%      FeCl2
+    0.63701E-07     vol%      MgCl2
+    0.44441E-07     vol%      NaO
+    0.37860E-07     vol%      PbF4
+    0.29013E-07     vol%      K
+    0.18005E-07     vol%      MgClF
+    0.60845E-08     vol%      MgF2
+    0.48118E-08     vol%      CaF2
+    ...             )
(    1000.00 C,      1.0000    atm , gas)
```

Composition of liquid phase,
from "EQUILIB" output.

```
+    11.200          gram
(    27.474          wt.%      NaCl
+    27.284          wt.%      PbO
+    13.362          wt.%      KCl
+    11.104          wt.%      Ca2SiO4
+    9.3439          wt.%      ZnO
+    2.1456          wt.%      CaSiO3
+    1.5801          wt.%      CaAl2O4
+    1.3794          wt.%      MnO
+    0.79911         wt.%      Ca2ZnSi2O7
+    0.76985         wt.%      MgO
+    0.76328         wt.%      Mg2SiO4
+    0.65116         wt.%      NaF
+    0.64188         wt.%      MnAl2O4
+    0.46679         wt.%      (Na2O)(SiO2)
+    0.36976         wt.%      Ca2Al2SiO7
+    0.35005         wt.%      NaAlO2
+    0.26997         wt.%      PbSiO3
+    0.26734         wt.%      CaF2
+    0.19718         wt.%      Fe3O4
+    0.17816         wt.%      Pb2SiO4
+    0.11526         wt.%      FeO
+    0.93519E-01     wt.%      Zn2SiO4
+    0.49797E-01     wt.%      MgAl2O4
+    0.47827E-01     wt.%      KF
+    0.47778E-01     wt.%      MgOCaOSi2O4
+    0.40081E-01     wt.%      CaO
+    0.38888E-01     wt.%      CdCl2
+    0.30992E-01     wt.%      KAlO2
+    0.27882E-01     wt.%      Mn2SiO4
+    0.24954E-01     wt.%      SiO2
+    0.24824E-01     wt.%      PbCl2
+    0.16527E-01     wt.%      Al2O3
+    0.11234E-01     wt.%      CaAl4O7
+    0.76728E-02     wt.%      CaCl2
+    0.67983E-02     wt.%      Pb
+    0.61576E-02     wt.%      MgF2
+    0.49303E-02     wt.%      (Na2O)(SiO2)2
+    0.43016E-02     wt.%      K2SiO3
+    0.11782E-02     wt.%      Cd
+    0.35981E-03     wt.%      (Na2O)2(SiO2)
+    0.23403E-03     wt.%      PbF2
+    ...             )
(    1000.00 C,      1.0000    atm, liquid)
```

```
Solid phases, from "EQUILIB" output.

+  53.896        gram      (ZnO)(Fe2O3)
   ( 1000.00 C,  1.0000    atm,                S1,   a= 1.0000 )
+  16.426        gram      CaFe2O4
   ( 1000.00 C,  1.0000    atm,                S1,   a= 1.0000 )
+  9.6056        gram      ZnO
   ( 1000.00 C,  1.0000    atm,                S1,   a= 1.0000 )
+  2.9949        gram      Mn3O4
   ( 1000.00 C,  1.0000    atm,                S1,   a= 1.0000 )
+  2.8827        gram      MgO
   ( 1000.00 C,  1.0000    atm,                S1,   a= 1.0000 )
+  1.2543        gram      MnAl2O4
   ( 10C0.00 C,  1.0000    atm,                S1,   a= 1.0000 )
+  1.0588        gram      MgOCa3O3Si2O4
   ( 1000.00 C,  1.0000    atm,                S1,   a= 1.0000 )
+  0.93928E      -01 gram  CdO
   ( 1000.00 C,  1.0000    atm,                S1,   a= 1.0000 )
+  0.00000       gram      Fe2O3
   ( 1000.00 C,  1.0000    atm,                S2,   a=0.85774 )
+  0.00000       gram      Mn3O4
   ( 1000.00 C,  1.0000    atm,                S2,   a=0.79279 )
+  0.00000       gram      Mn2O3
   ( 1000.00 C,  1.0000    atm,                S1,   a=0.73711 )
+  0.00000       gram      ZnAl2O4
   ( 1000.00 C,  1.0000    atm,                S1,   a=0.61948 )
+  0.00000       gram      (MgO)(Fe2O3)
   ( 1000.00 C,  1.0000    atm,                S1,   a=0.61225 )
+  0.00000       gram      CaOMgOSiO2
   ( 1000.00 C,  1.0000    atm,                S1,   a=0.59968 )
+  0.00000       gram      Ca2Fe2O5
   ( 1000.00 C,  1.0000    atm,                S1,   a=0.58122 )
+  0.00000       gram      (MnO)(Fe2O3)
   ( 1000.00 C,  1.0000    atm,                S1,   a=0.55259 )
+  ...
```

3.1.2 Computations with the use of a carrier gas

Figure 3.1 shows a simple case of the separation process with the use of a carrier gas. This process basically consists of volatilization and removal of the vapor phase by the carrier gas. For the computation of chemical equilibrium states, a batch operation or a continuous operation can be assumed. For a batch operation, the total volume (number of moles) of the carrier gas is specified in the input data. The volume of carrier gas is increased gradually until more than 99.98% of the volatile species are removed to the gas phase.

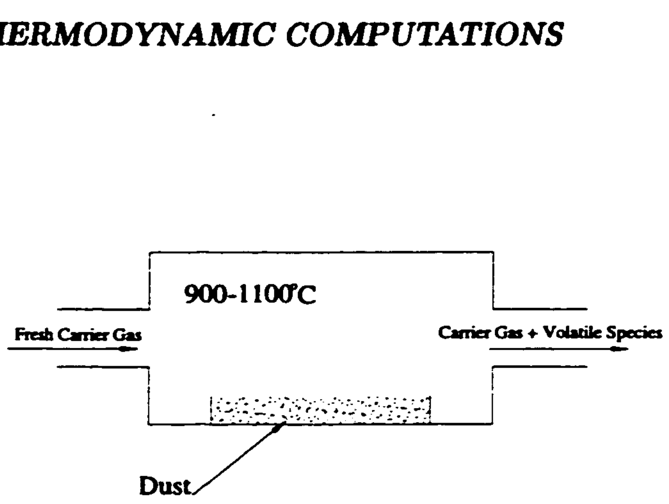

Figure 3.1: A simple representative of separation process with a carrier gas in a continuous operation.

For the purpose of calculation, a continuous operation is assumed to consist of many individual batch operations. After calculating the equilibrium state, gas phase is removed from the system and the next calculation is performed using the remaining condense phases plus the same amount of fresh carrier gas. This computation is repeated until 99.98% of the volatile species is separated from the condense phases. For the purpose of these iterations a program is written which reads the "EQUILIB" output data, calculates the amount of each element in the condense phases and then creates a new input data file for the "EQUILIB"[2].

If the amount of the carrier gas used in each iteration is reduced to a very small value, the calculation implies the simulation of a continuous operation. Since a very small volume of gas requires a large number of iterations, the volume of carrier gas used in each iteration is decreased until the total amount of carrier gas required for the separation converges to a certain value and does not change significantly with further decrease of the carrier gas used in each iteration.

---

[2] New release of "FACT" program has an "open" option which performs similar itteration.

Computations of the chemical equilibrium for both batch and continuous operation have been carried out with the use of air, nitrogen and a mixture of $CO/CO_2(1:9)$ as carrier gases. Air is used as an oxidizing gas and mixture of CO/CO_2 is chosen as a reducing gas. Nitrogen is used for the purpose of comparison.

3.1.3 Computations with the use of additives

In order to examine the effects of different additives on the volatilization of alkali halides and lead oxide, some chemicals are added to the input material for the computation of the chemical equilibrium. For this purpose, Fe is used as a reducing agent, Fe_2O_3 is used as an oxidizing agent and $CaCl_2$ is added to elevate the partial pressure of the chlorides by increasing the chlorine in the system. The chemical equilibrium is calculated for different amounts of these additives at different temperatures. Nitrogen is used as the carrier gas for these calculations.

3.2 Equilibrium Vapor Pressure

The equilibrium vapor pressure of the volatile species and the total pressure of the system at different temperatures are calculated with the aid of the "FACT" program. For the calculation of total pressure, the volume of the system is specified along with the temperature in the "EQUILIB" program. For this purpose the volume of reaction chamber is used as the volume of the closed system. It should be noted that due to the presence of the condense phases, the total pressure is not sensitive to small changes of the volume. The partial pressure of each species is calculated based on the volume fraction of that species in the gas phase, see "EQUILIB" output on page 20.

3.3 Enthalpy Changes in the System

In the computations of heat transfer inside the dust bed, the changes of enthalpy in the system have been used instead of the heat capacity. The enthalpy changes of EAF dust between the initial state and the equilibrium state are calculated by the "EQUILIB" program, from 0 to 1200°C with intervals of 25 degrees. Since the input data are introduced in elemental form, the calculated enthalpy changes for any temperature include the enthalpy of formation of the compounds. However, the enthalpy of formation is canceled out when the enthalpy changes from 25°C to any specified temperature (ΔH_{298}^{T}) are calculated. Therefore, the enthalpy changes used in heat transfer computations include only the enthalpy changes of sensible heat, latent heat of melting and evaporation, and the enthalpy changes due to any reaction or phase transformation.

3.4 Results and Discussion

In the thermodynamic calculations the chemical compositions of two different EAF dusts, namely type-A and type-B are used, see Table 3.1. The calculated mass changes of solid, liquid and gas phases during the heating of EAF dusts type-A and -B under reduced pressure are plotted against the temperature in Figures 3.2 and 3.3. Each set of data points represent the co-existing phases generated in one calculation. The lines connecting points are drawn only for visual presentation. Partial melting starts at about 450°C and the amount of liquid phase increases with temperature. Above 800°C due to the evaporation of volatile species, the amount of liquid phase decreases. Volatile species form a major part of the liquid phase and their removal significantly

Table 3.1: Chemical composition of EAF dust type-A and -B used in thermodynamic computations, in %*wt*.

Dust	Fe	Zn	Pb	Na	K	Cd	Ca	Mn	Mg	Al	Si	Cl
EAF Type-A	32.6	21.6	3.03	1.40	1.01	0.09	4.45	2.62	2.06	0.36	0.27	2.81
EAF Type-B	30.5	18.6	1.97	1.23	0.66	0.07	12.3	2.33	1.38	0.55	0.41	2.68

changes the composition of the remaining liquid. This elevates the melting temperature of the liquid phase and eventually the remaining liquid solidifies. An increase in the weight of solid phase on the graphs indicates this solidification. The enthalpy changes of 100 grams EAF dust are shown in the same figures. The beginning of the partial melting corresponds to a small positive change of slope on these curves while a clear acceleration of enthalpy changes exists at the onset of evaporation.

In almost all cases studied, the end of evaporation corresponds to the disappearance of the liquid phase. No significant change of phase occurs afterwards. Therefore, for the overall process under the conditions investigated, the changes of liquid phase may be used to signal the completion of the separation process. Figure 3.4 shows the amount of liquid phase vs. the number of moles of air at different temperatures for a batch operation. The number of moles of air needed to treat 100 grams of EAF dust type-A in a batch operation is approximately 18 at 1100°C, 36 at 1000°C and 141 at 900°C. For a continuous operation with iteration of the equilibrium computations, the number of moles of air required for the same treatment is approximately 11 at 1100°C, 30 at 1000°C and 128 at 900°C.

The effect of different carrier gases and additives can be seen in Figures 3.5 to 3.9 where the amount of liquid phase is calculated and plotted against the number of moles of the carrier gas. Comparing the results of using different carrier gases in Figures 3.6 and 3.7, the mixture of CO/CO_2 (1 : 9) shows a negative effect on the separation process, i.e. requiring much more carrier gas for the completion of the process. Air has a slight advantage over nitrogen in this regard. Comparison of the results in Figures 3.8 and 3.9 indicates that Fe has a retarding effect similar to that of CO/CO_2. On the other hand the completion of the separation process requires less carrier gas with the addition of Fe_2O_3.

In order to see the effect of different carrier gases or additives on the removal of each volatile species individually, the amounts of lead, sodium and potassium remaining in the condense phases in equilibrium with a certain amount of carrier gas are illustrated in Figures 3.10 to 3.17. These figures exhibit similar trends to those of variations in liquid phase.

These observations may be attributed to the changes of oxygen potential. The same effect of the oxygen potential is observed with different carrier gases as with the use of additives. At lower oxygen potential the liquid phase has a larger mass with noticeable increase in the content of iron and zinc. Table 3.2 contains calculated weight and weight percentage of the main constituents in the liquid phase for EAF dust type-A with 20 moles of nitrogen or $CO/CO_2(1:9)$ at $1000°C$. This change of composition results in smaller mole fractions of $NaCl$, KCl and PbO in the liquid phase, causing lower activities and thus, lower equilibrium vapor pressures of these volatile species.

The addition of $CaCl_2$ promotes the evaporation of volatile species by increasing the chlorine content in the system which results in a higher vapor pressure of chlorides, see Figures 3.8, 3.9, 3.16 and 3.17. At the same time, this enhances the gasification of zinc in the form of $ZnCl_2$. The reducing condition also leads to the increase of zinc loss in the form of zinc vapor. The results of zinc loss in the vapor phase are given in Figures 3.21 and 3.22.

Table 3.2: Main constituents of liquid phase for EAF dust type-A with 20 moles of carrier gas at 1000°C.

Carrier Gas	$CO/CO_2(9:1)$		Nitrogen	
	$\%wt.$	wt(gram)	$\%wt.$	wt(gram)
Total Liquid	100	16.47	100	3.53
FeO	26.3	4.33	3.20	0.11
PbO	0.11	0.02	25.2	0.89
ZnO	9.68	1.59	7.75	0.27
Pb	15.4	2.54	12.1	0.43
Ca_2SiO_4	13.7	2.26	12.1	0.43
MnO	10.1	1.66	3.56	0.13
NaCl	9.11	1.50	11.6	0.41
KCl	4.29	0.71	4.86	0.17

Figure 3.23 illustrate the variation of equilibrium pressure of some volatile species over their pure compounds with temperature. $ZnCl_2$ has the highest vapor pressure, then Zn followed by $PbCl_2$. It is obvious that at temperatures suitable for a separation process, zinc gasification would significantly increase with increased chlorine content in the system.

Figures 3.18 to 3.20 show the percentage of lead, sodium and potassium removed from the EAF dust type-A in equilibrium with a certain amount of carrier gas in the system. These figures illustrate that at earlier stages of the separation process $NaCl$ and KCl are removed faster than lead compounds. The rate of removal of $NaCl$ and KCl decreases significantly towards the end of the process while the rate of removal of lead compounds shows less changes over the course of the separation process.

The total pressure of the system at different temperatures for EAF dusts type-A and -B is given in Table 3.3 and Table 3.4 contains the values of partial pressure of the volatile species for these two types of EAF dust.

Table 3.3: Total equilibrium vapor pressure of EAF dust type-A and -B.

Temperature	**EAF Dust Type-A**			**EAF Dust Type-B**		
	Pa	**atm**	**torr**	**Pa**	**atm**	**torr**
650 °C	1.53	1.51×10^{-5}	0.011	1.53	1.53×10^{-5}	0.011
700 °C	5.19	5.12×10^{-5}	0.039	5.17	5.10×10^{-5}	0.039
750 °C	15.1	1.49×10^{-4}	0.113	15.2	1.50×10^{-4}	0.114
800 °C	39.7	3.92×10^{-4}	0.298	39.7	3.92×10^{-4}	0.298
850 °C	94.2	9.30×10^{-4}	0.707	93.0	9.18×10^{-4}	0.698
900 °C	206	2.03×10^{-3}	1.55	198	1.95×10^{-3}	1.49
950 °C	413	4.08×10^{-3}	3.10	384	3.79×10^{-3}	2.88
1000 °C	747	7.37×10^{-3}	5.60	688	6.79×10^{-3}	5.16

Table 3.4: Partial pressure of volatile species in vapor at equilibrium with EAF dust type-A and -B at different temperatures, in Pa.

Temperature	**Dust Type-A**			**Dust Type-B**		
	NaCl	**KCl**	**Pb – comp.**	**NaCl**	**KCl**	**Pb – comp.**
800 °C	19.3	17.3	0.94	24.7	14.1	0.77
850 °C	50.5	40.4	2.46	58.3	32.5	1.98
900 °C	95.4	79.2	7.51	125	67.3	4.75
950 °C	243	171	13.7	243	130	10.5
1000 °C	425	312	29.2	435	229	21.7

After removal of the volatile species from EAF dust, the vapor phase is condensed somewhere else in the system. Based on the experimental observations, most of the condensation takes place in a region where temperature is approximately $550 - 650°C$. The total equilibrium vapor pressure and the equilibrium partial pressure of the volatile species over a typical condensate at some relevant temperatures are given in Table 3.5.

Figure 3.24 shows the total vapor pressure of the system computed at different temperatures for EAF dust type-A and a typical condensate.

Table 3.5: Total and partial pressure of volatile species at equilibrium with a typical condensate at the cold compartment, in Pa.

Temperature	Total Pressure	Partial Pressure		
		NaCl	KCl	Pb – comp.
550 °C	0.09	0.027	0.058	4.3×10^{-4}
600 °C	0.41	0.17	0.23	2.5×10^{-3}
650 °C	1.65	0.78	0.87	1.2×10^{-2}
700 °C	5.70	2.69	2.95	6.0×10^{-2}

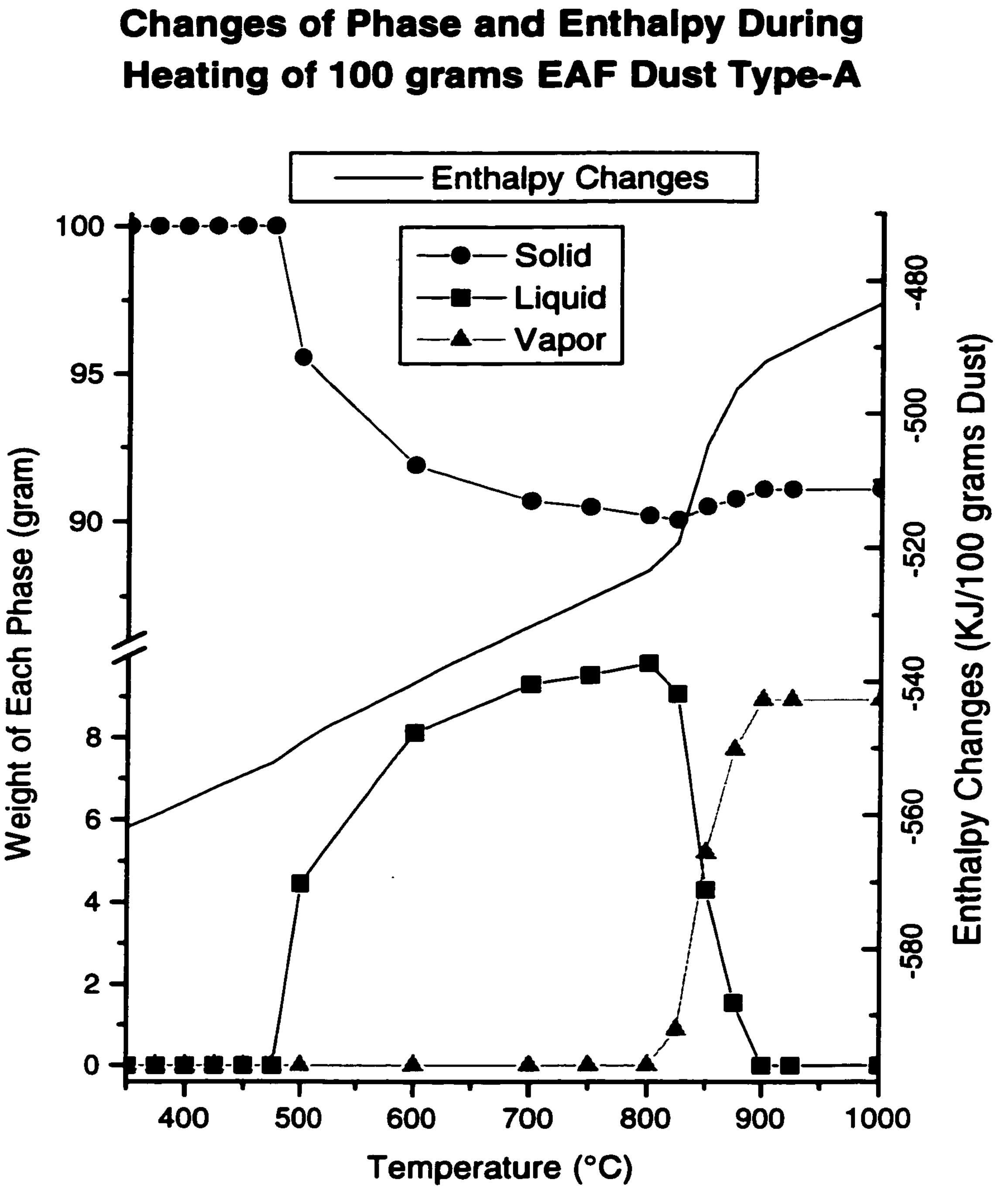

Figure 3.2: Calculated changes of phases and enthalpy during heating of EAF dust type-A under reduced pressure.

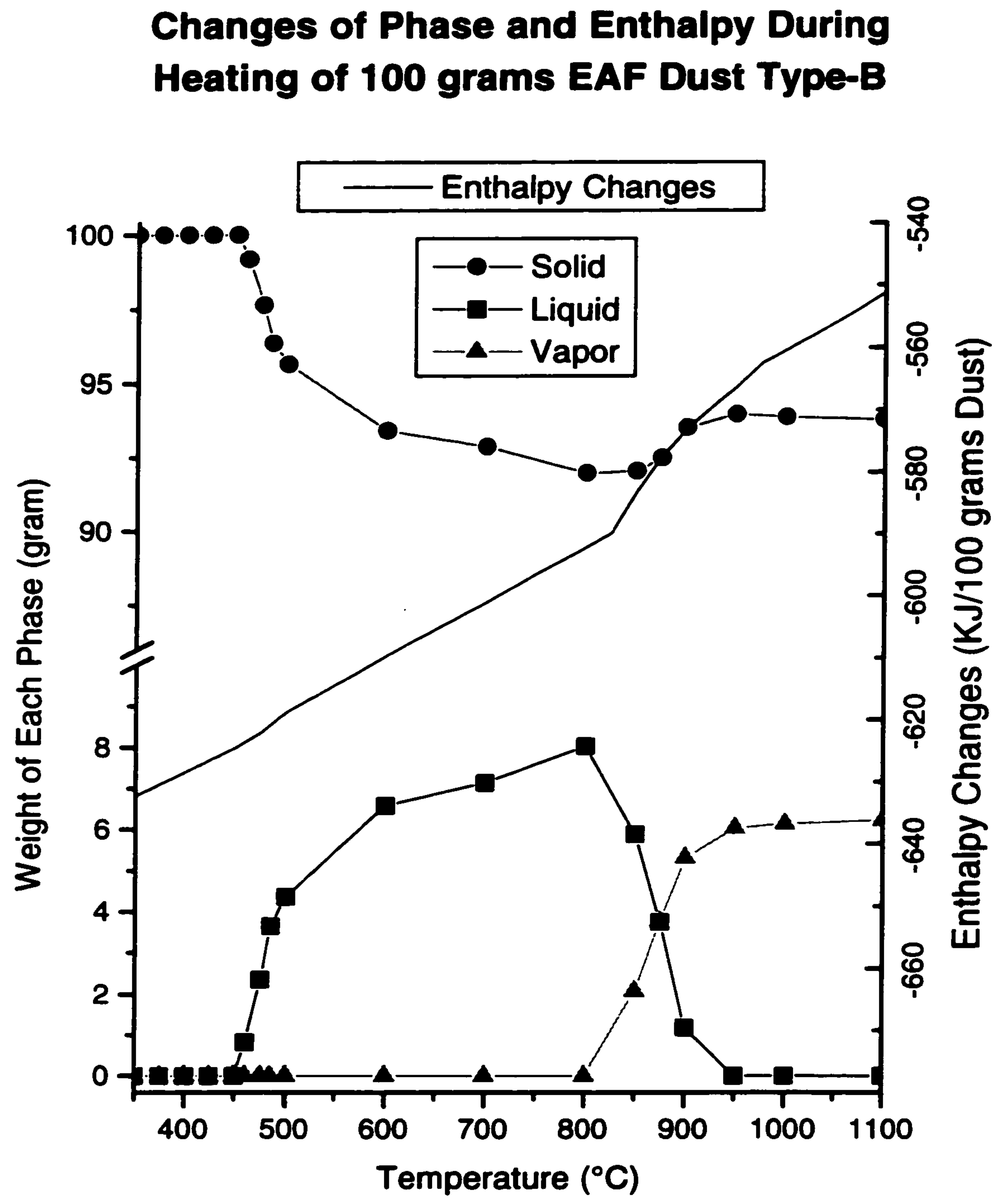

Figure 3.3: Calculated changes of phases and enthalpy during heating of EAF dust type-B under reduced pressure.

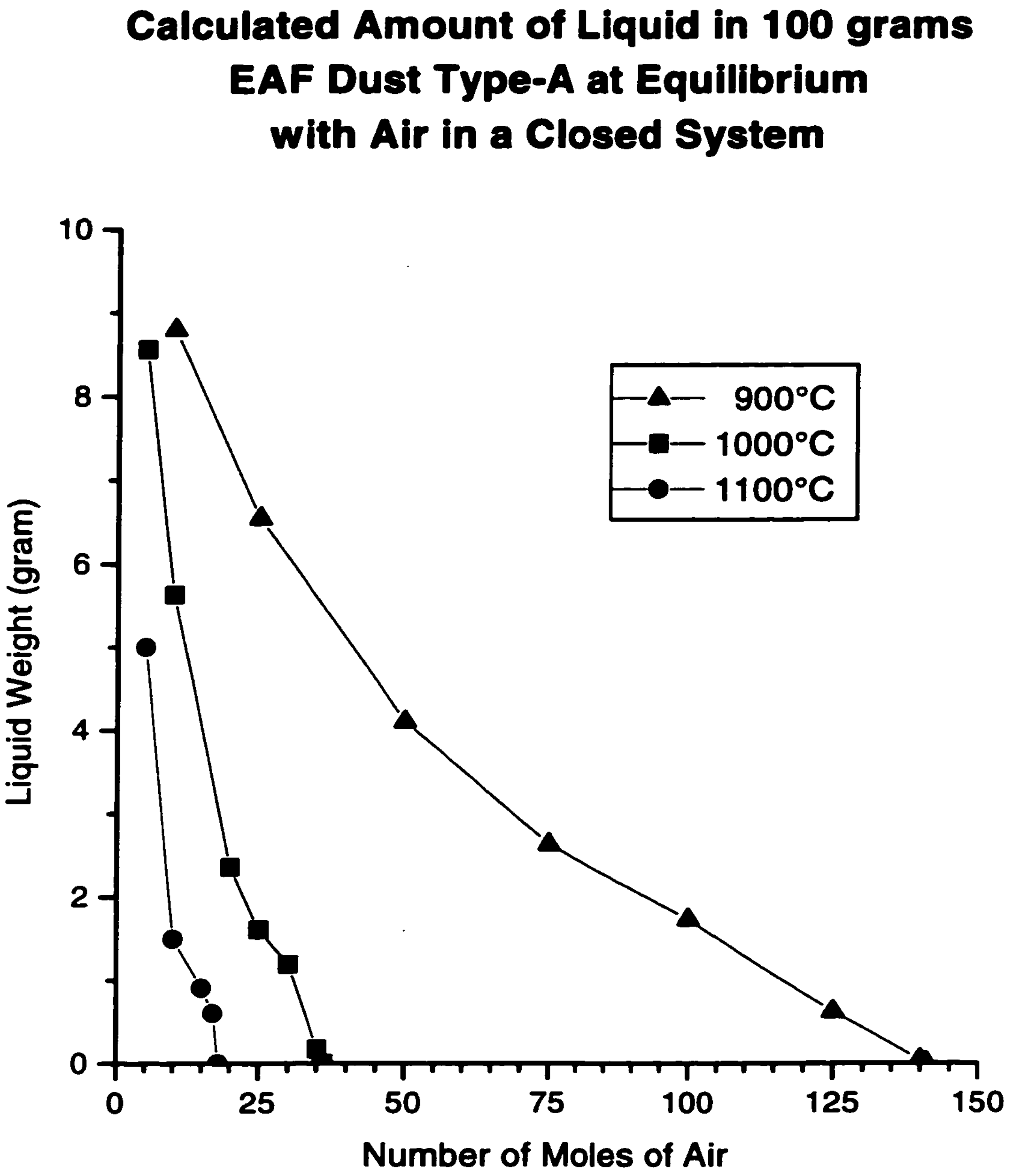

Figure 3.4: Calculated amount of liquid phase in 100 grams EAF dust type-A in equilibrium with air.

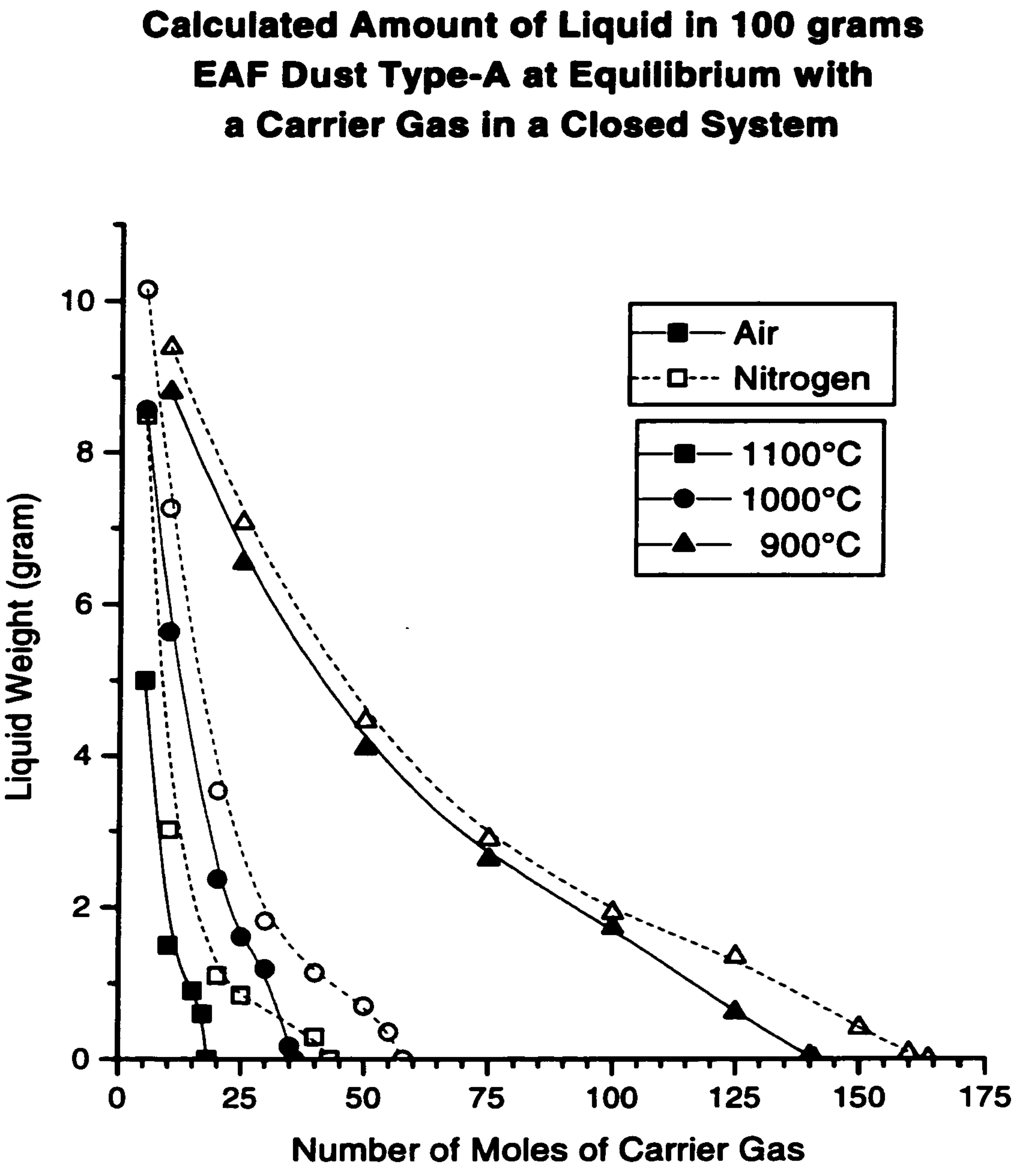

Figure 3.5: Calculated amount of liquid phase in 100 grams EAF dust type-A in equilibrium with air and nitrogen at different temperatures.

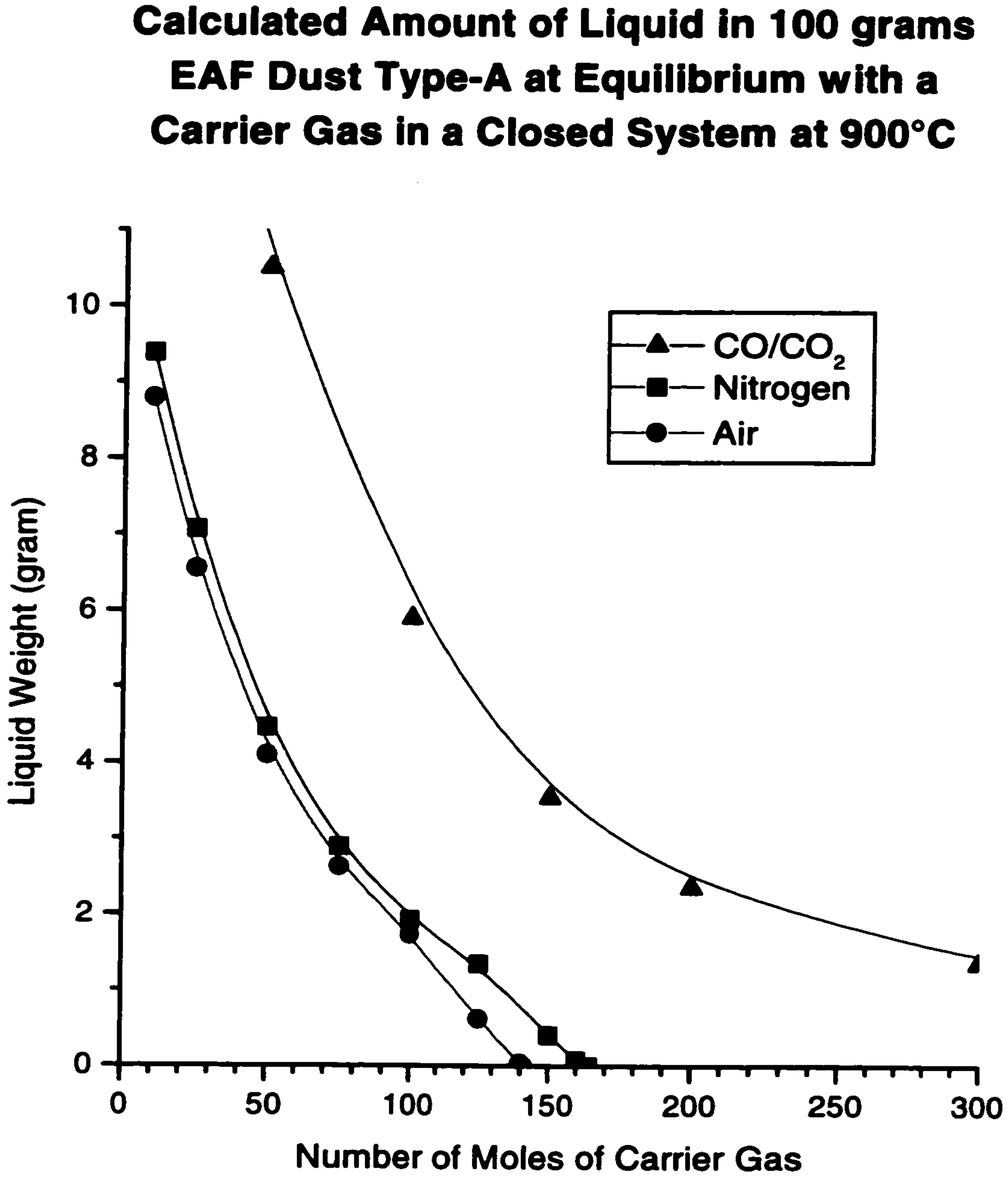

Figure 3.6: Calculated amount of liquid phase in 100 grams EAF dust type-A at 900°C in equilibrium with different carrier gases.

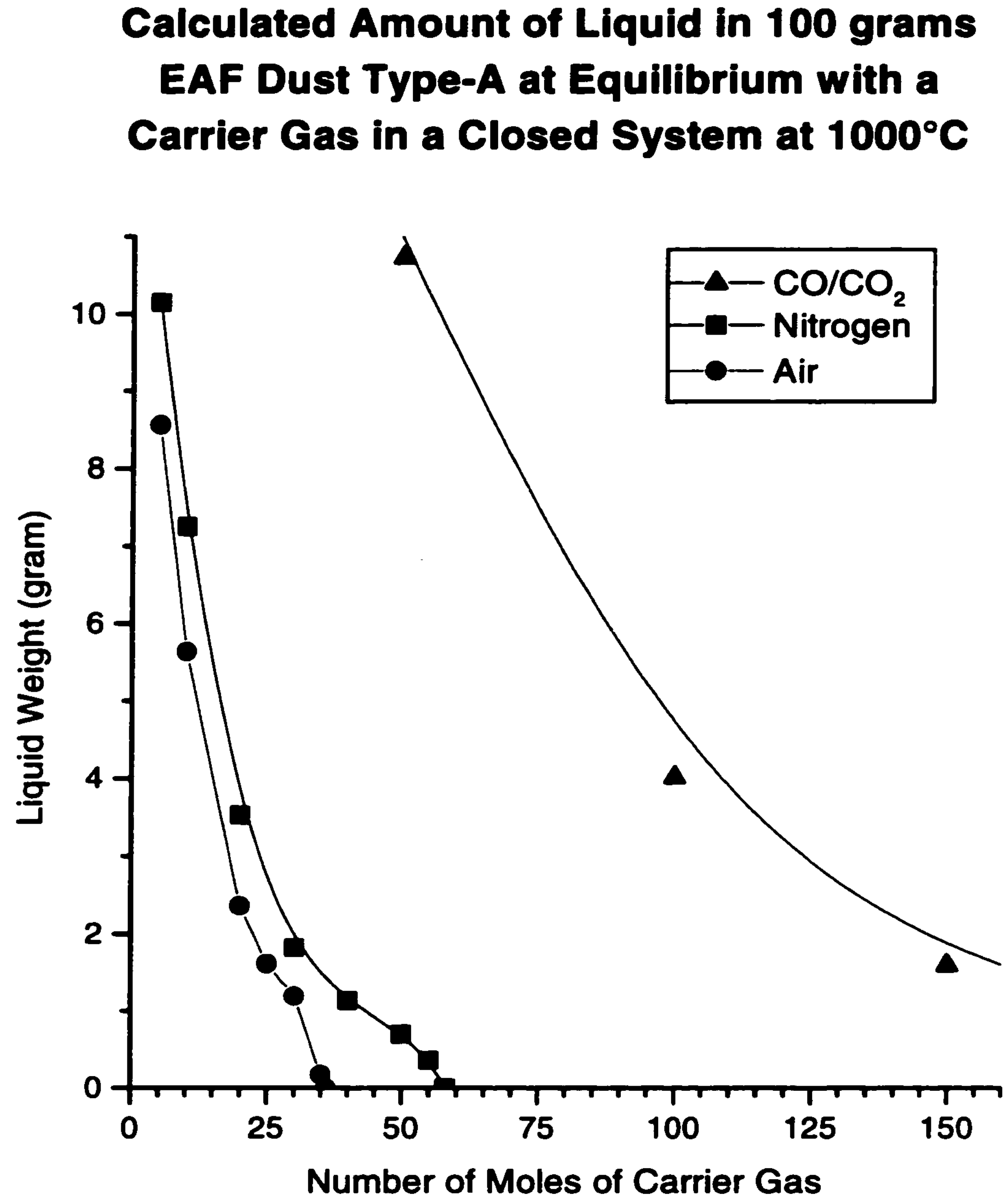

Figure 3.7: Calculated amount of liquid phase in 100 grams EAF dust type-A at 1000°C in equilibrium with different carrier gases.

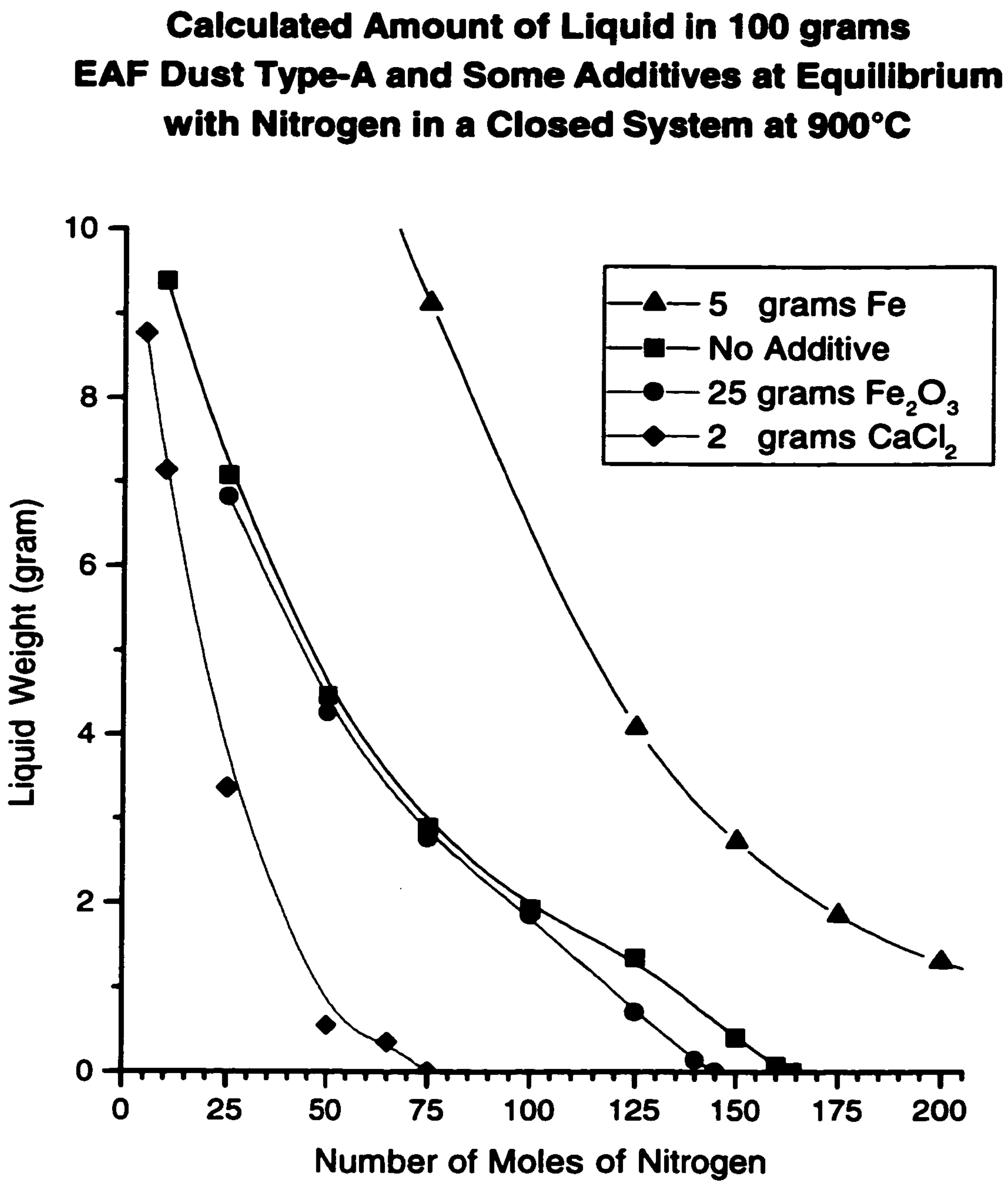

Figure 3.8: Calculated amount of liquid phase in 100 grams EAF dust type-A with some additives at 900°C in equilibrium with nitrogen.

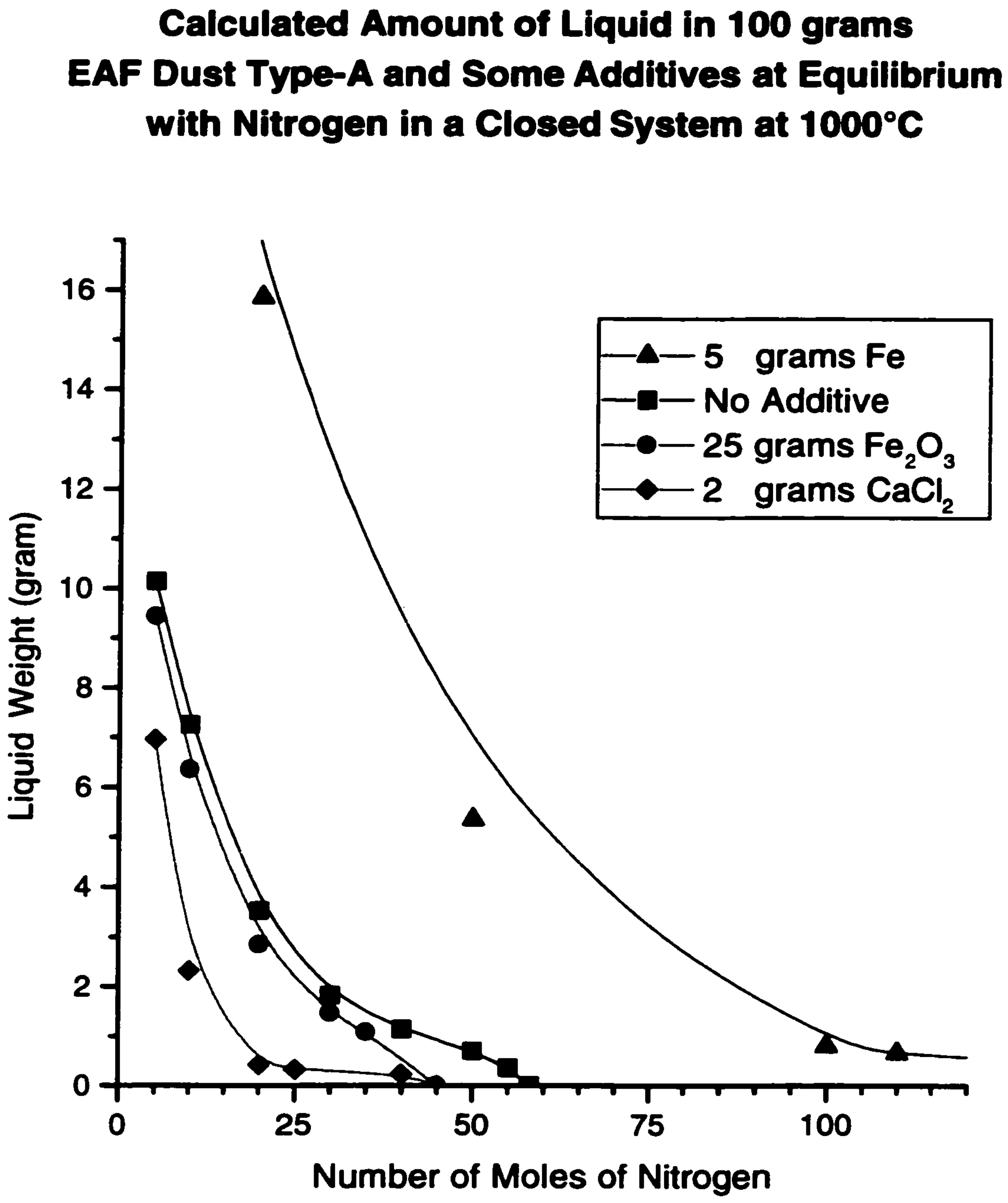

Figure 3.9: Calculated amount of liquid phase in 100 grams EAF dust type-A with some additives at 1000°*C* in equilibrium with nitrogen.

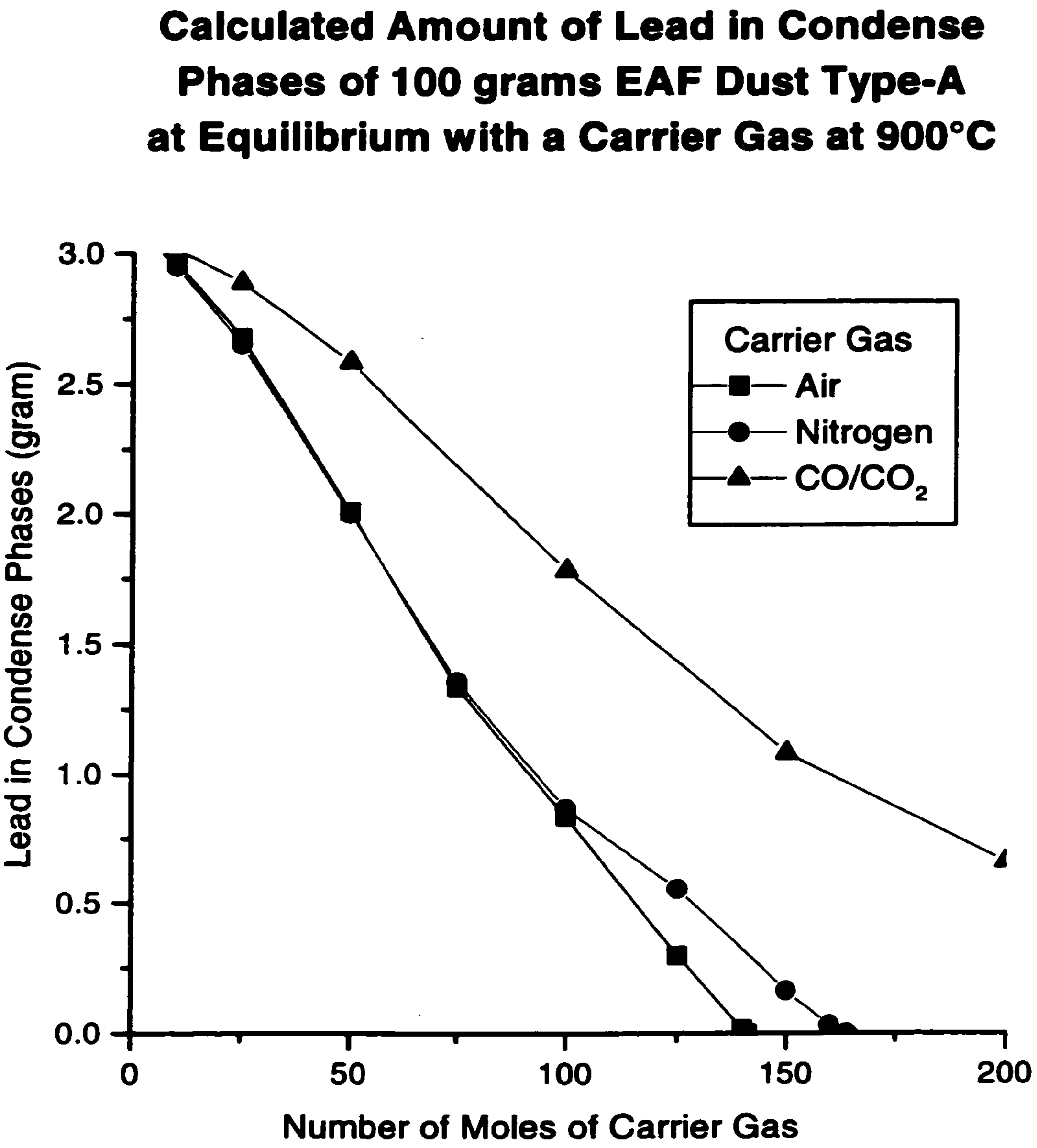

Figure 3.10: Calculated amount of lead in condense phases of 100 grams EAF dust type-A in eauilibrium with a carrier gas at 900°*C*.

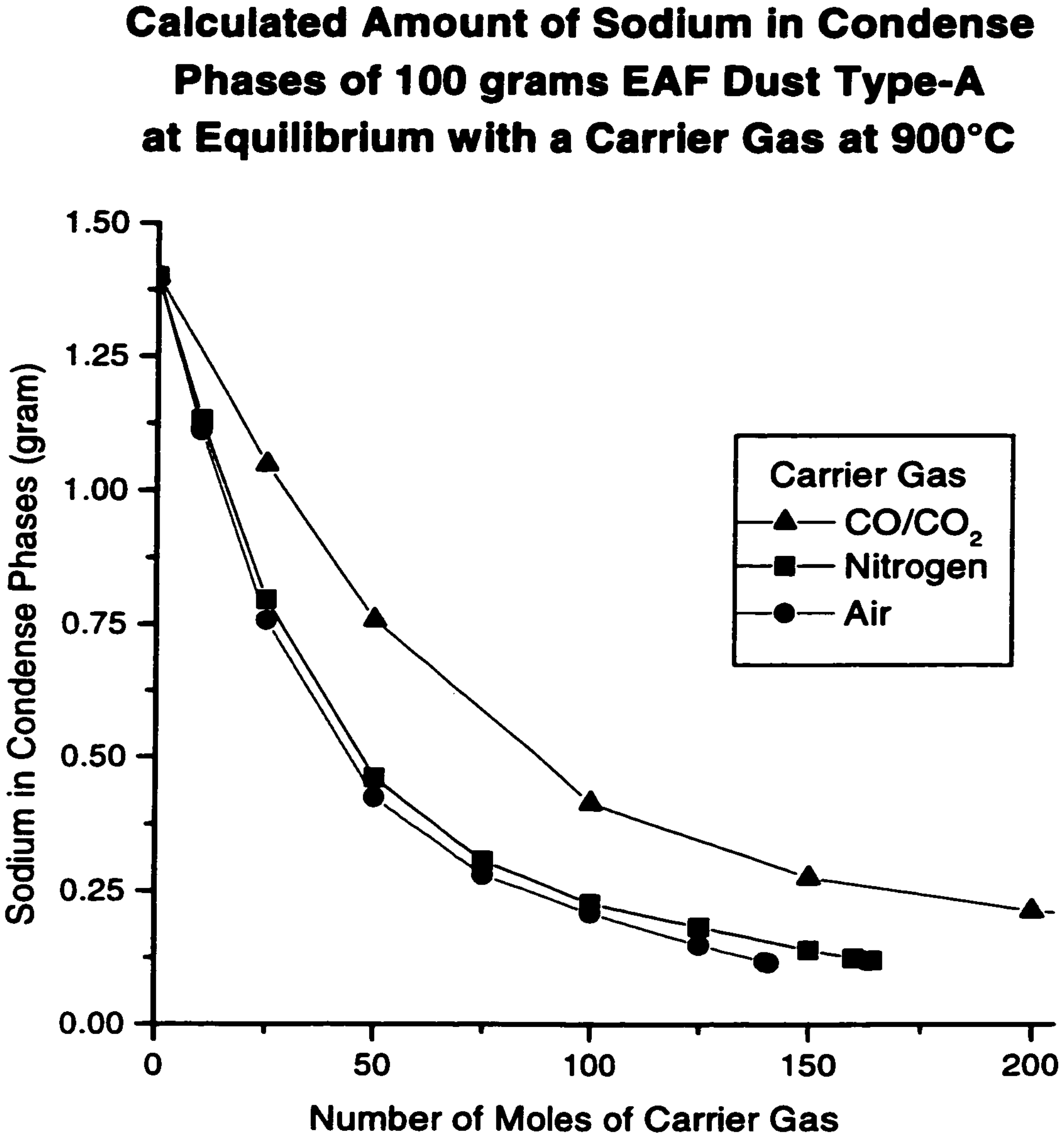

Figure 3.11: Calculated amount of sodium in condense phases of 100 grams EAF dust type-A in eauilibrium with a carrier gas at 900°*C*.

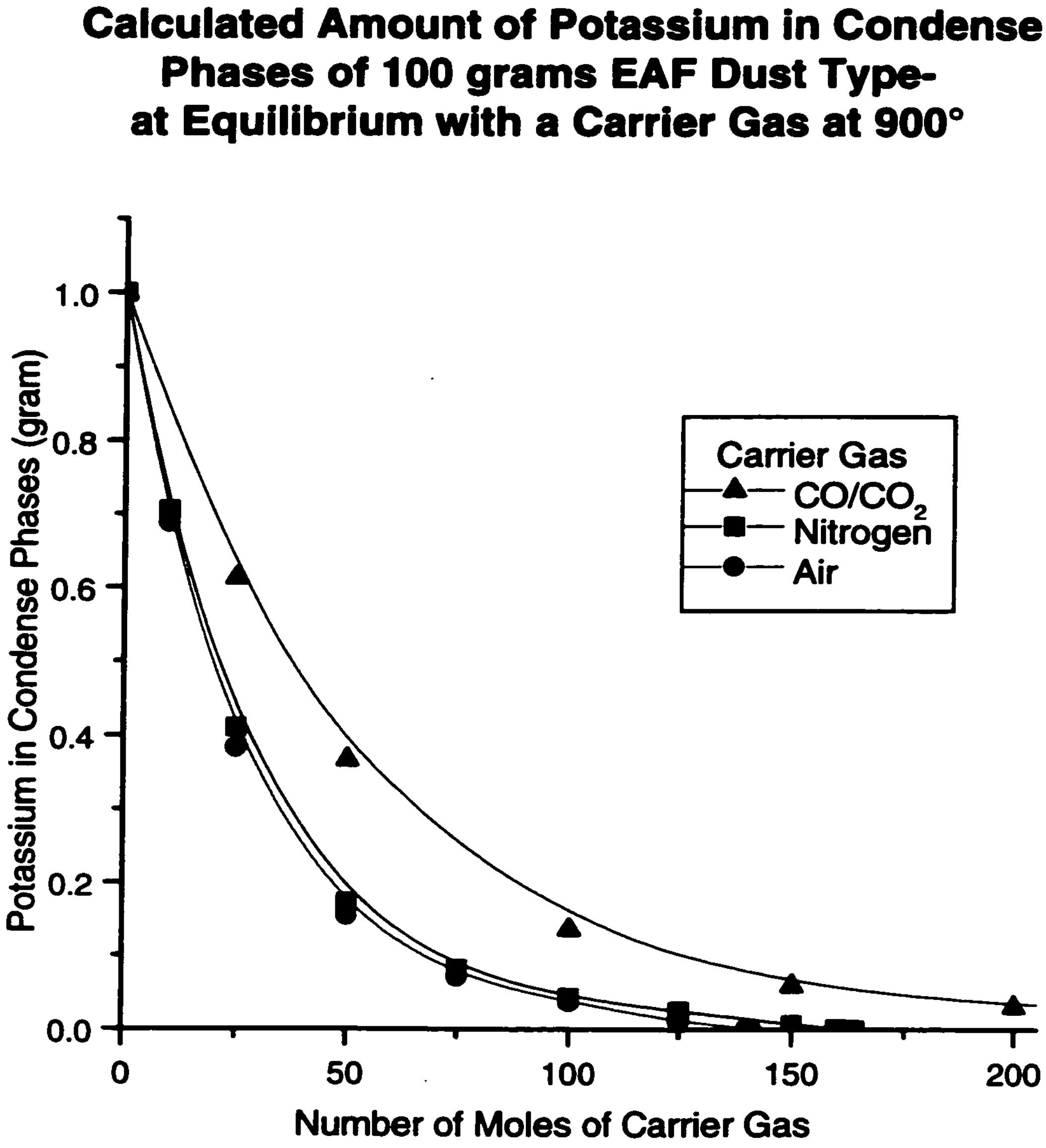

Figure 3.12: Calculated amount of potassium in condense phases of 100 grams EAF dust type-A in eauilibrium with a carrier gas at 900°*C*.

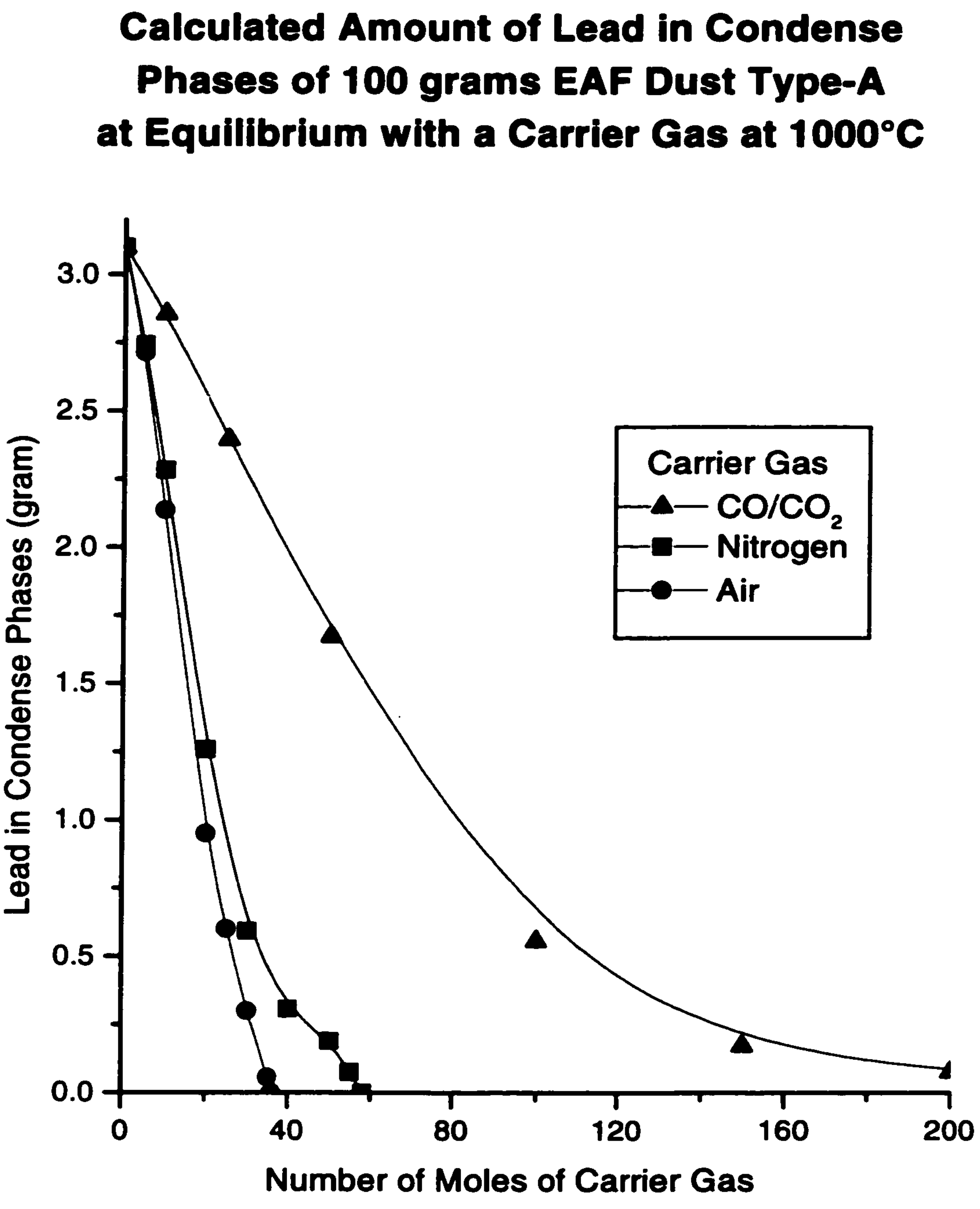

Figure 3.13: Calculated amount of lead in condense phases of 100 grams EAF dust type-A in eauilibrium with a carrier gas at 1000°C.

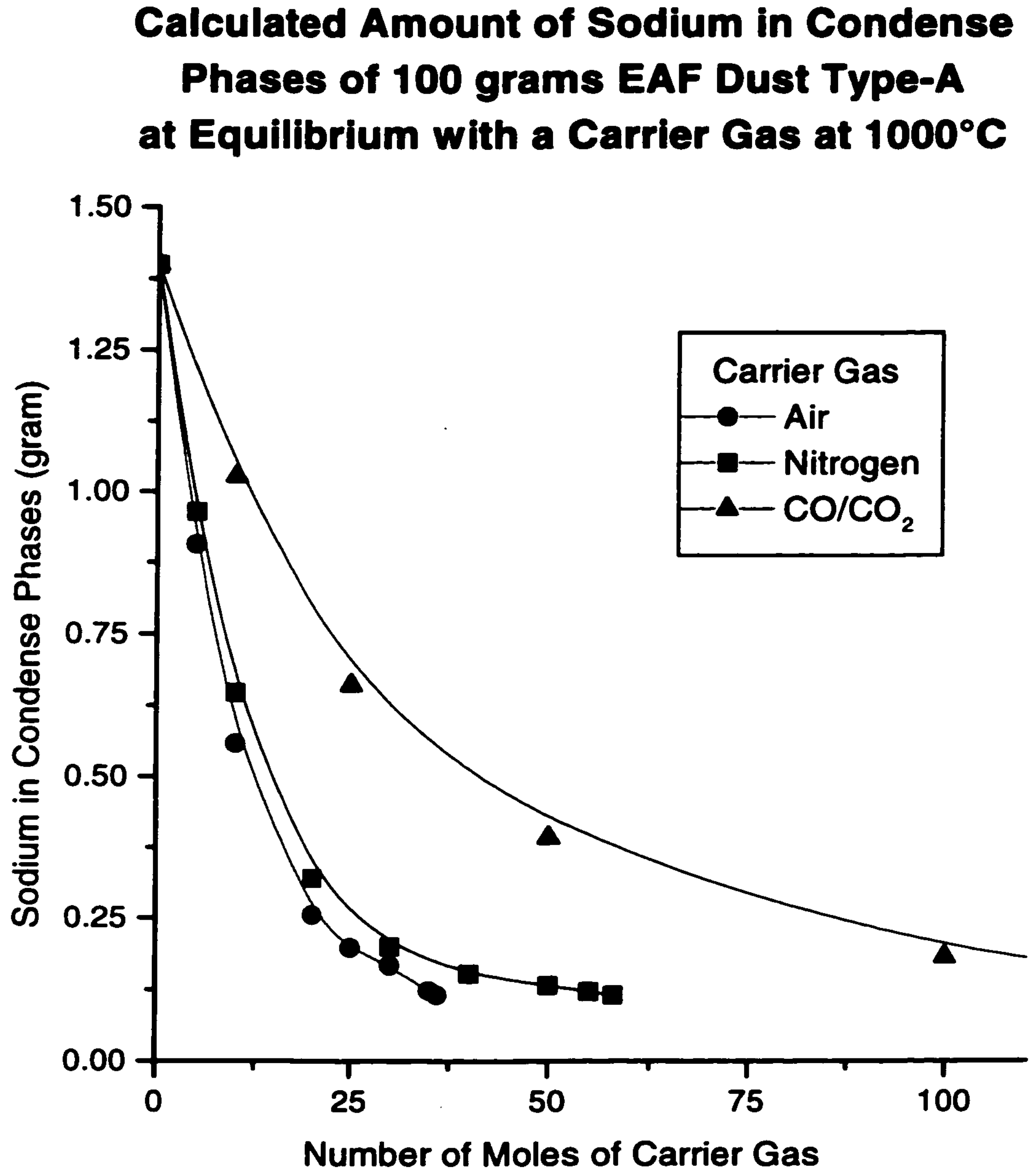

Figure 3.14: Calculated amount of sodium in condense phases of 100 grams EAF dust type-A in eauilibrium with a carrier gas at 1000°*C*.

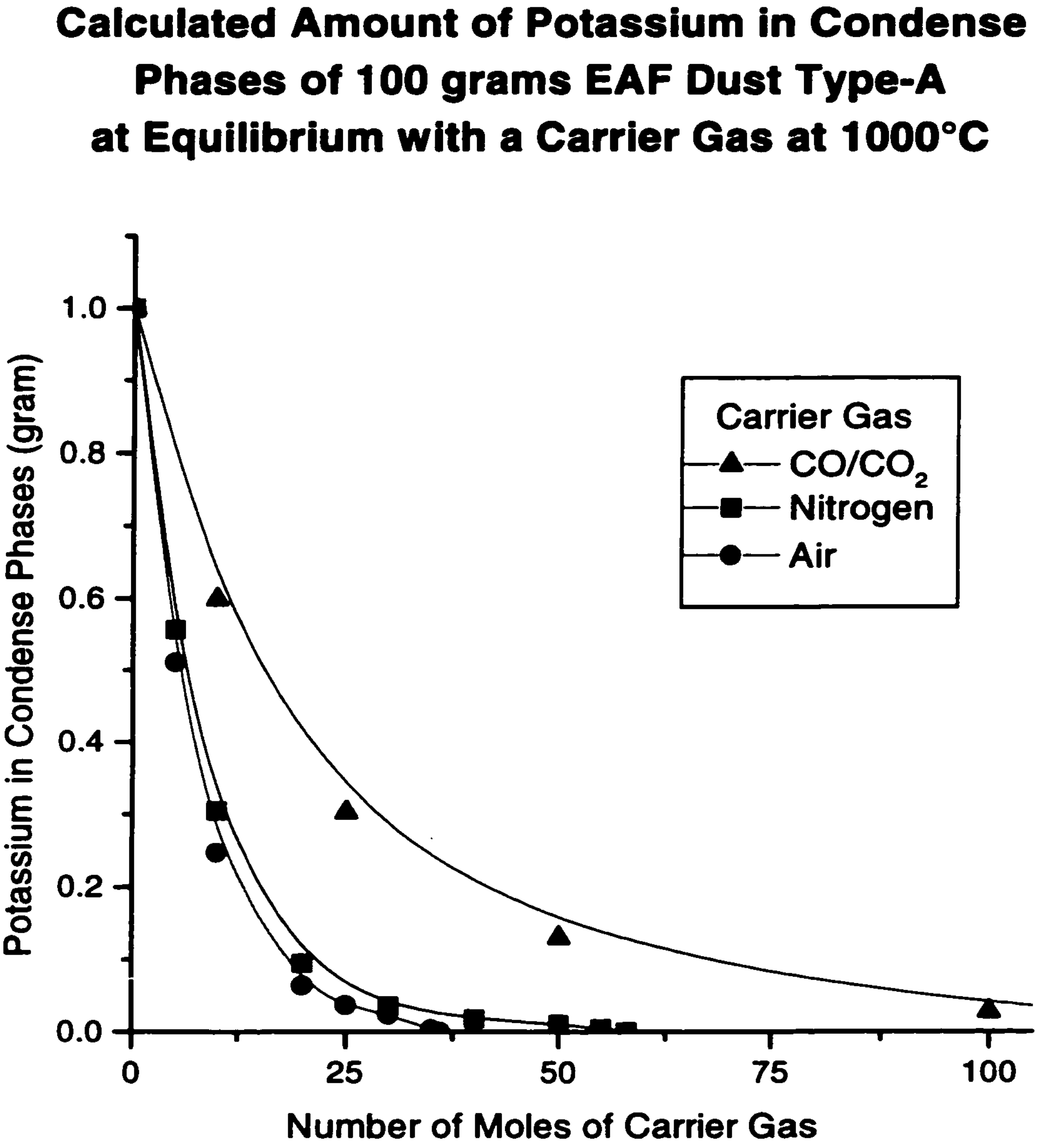

Figure 3.15: Calculated amount of potassium in condense phases of 100 grams EAF dust type-A in eauilibrium with a carrier gas at 1000°C.

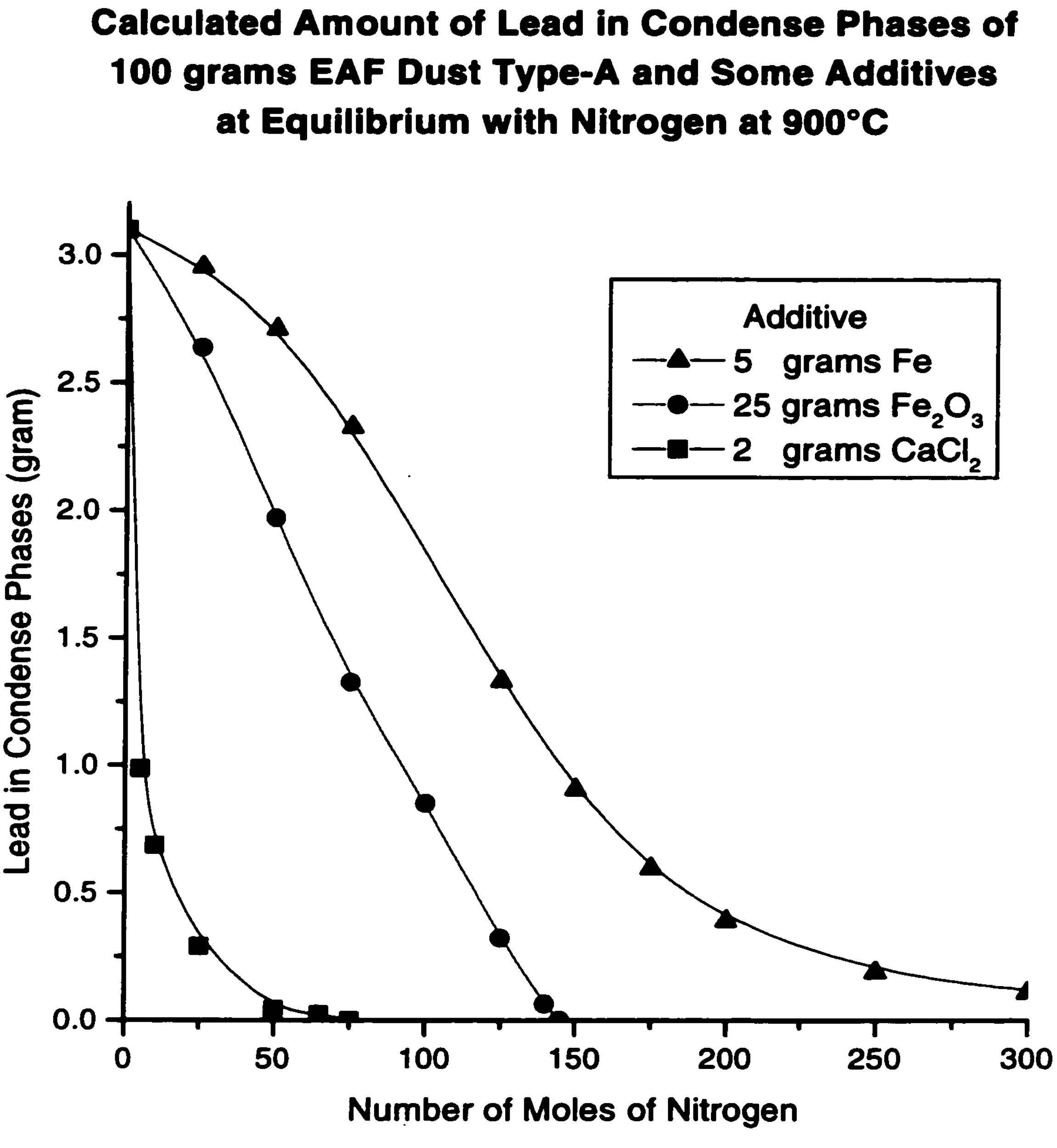

Figure 3.16: Calculated amount of lead in condense phases of 100 grams EAF dust type-A with additives in eauilibrium with nitrogen at 900°C.

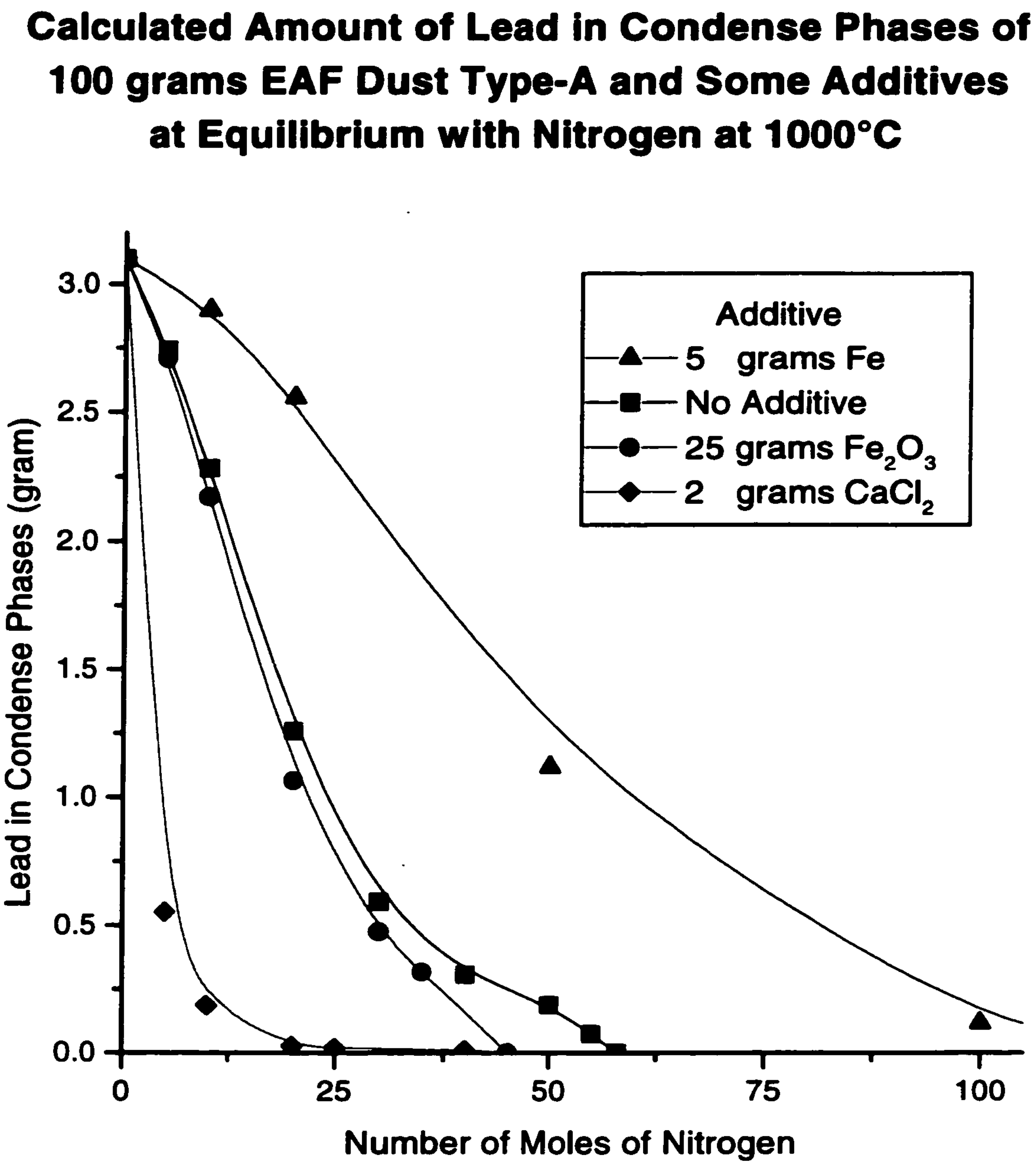

Figure 3.17: Calculated amount of lead in condense phases of 100 grams EAF dust type-A with additives in eauilibrium with nitrogen at 1000°*C*.

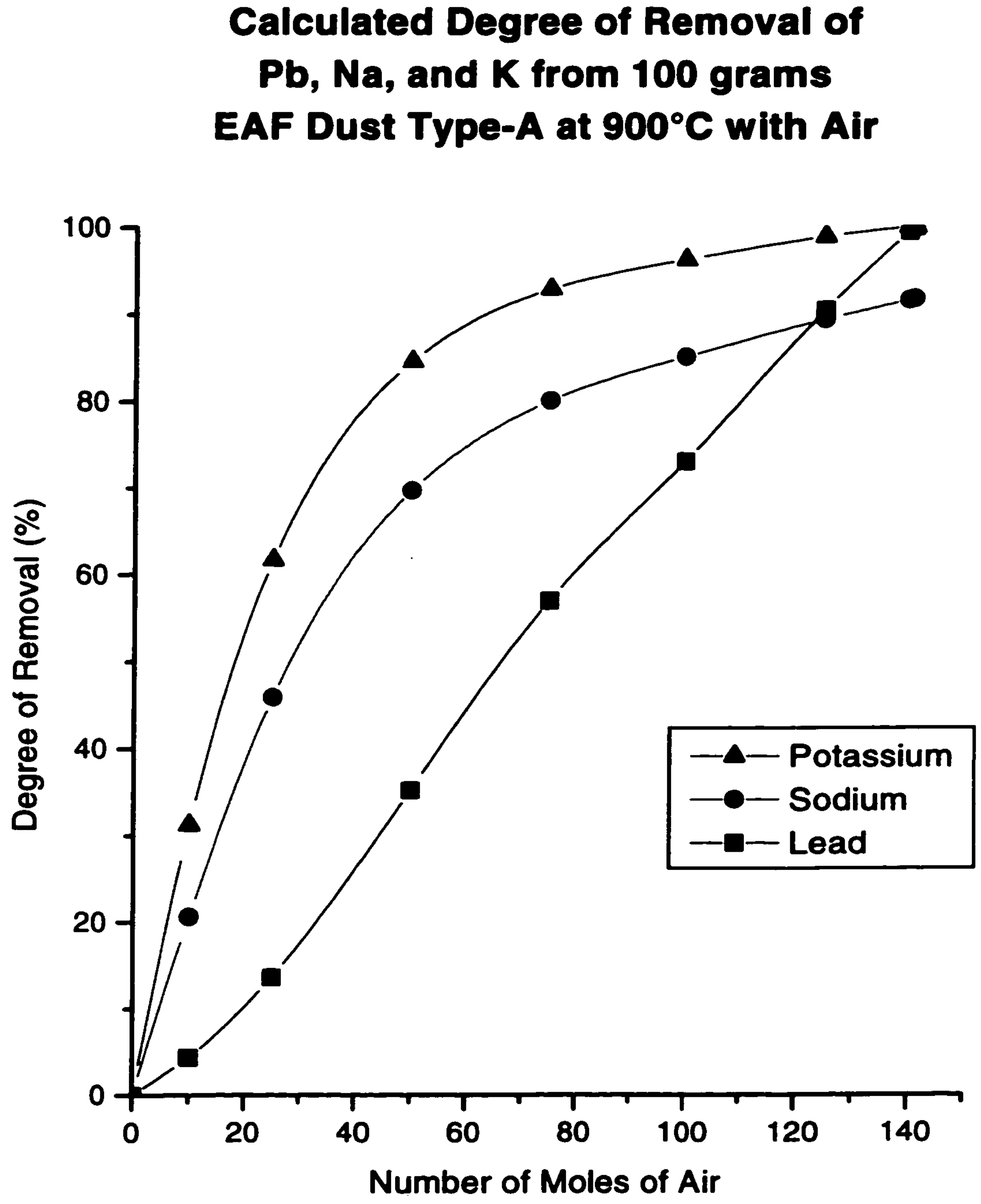

Figure 3.18: Calculated percentage of removal of volatile species from EAF dust type-A by air at 900°*C*.

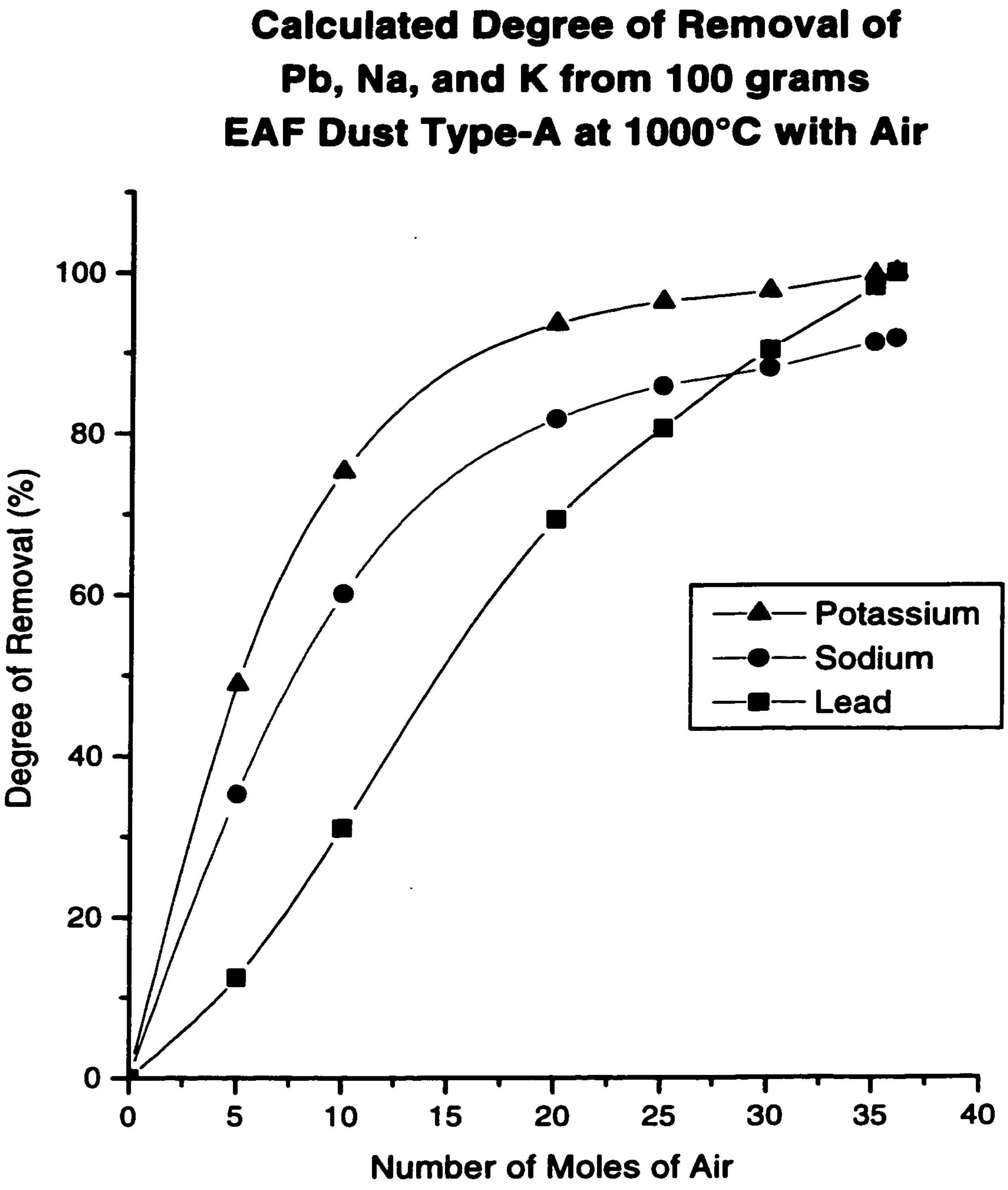

Figure 3.19: Calculated percentage of removal of volatile species from EAF dust type-A by air at 1000°C.

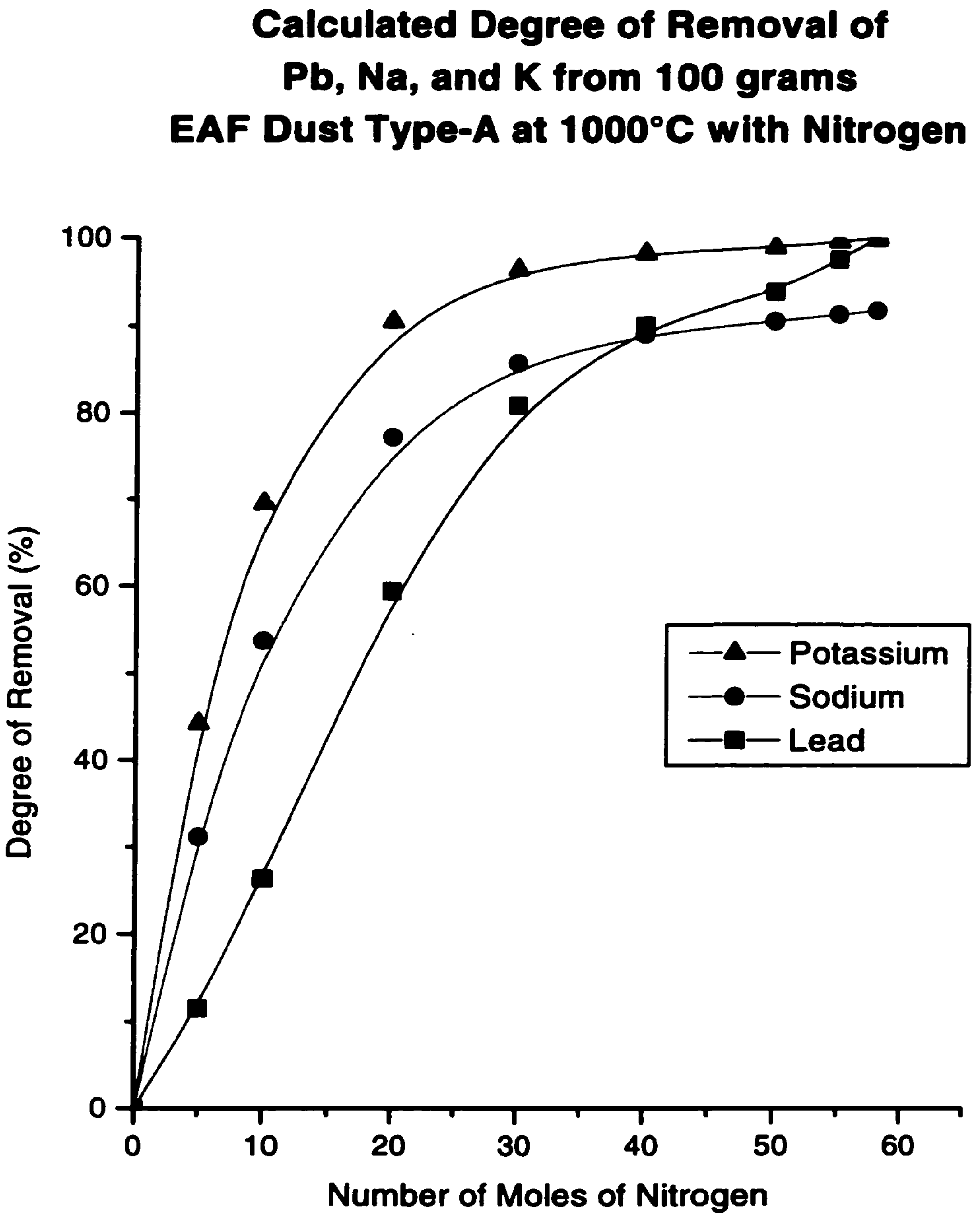

Figure 3.20: Calculated percentage of removal of volatile species from EAF dust type-A by nitrogen at 1000°C.

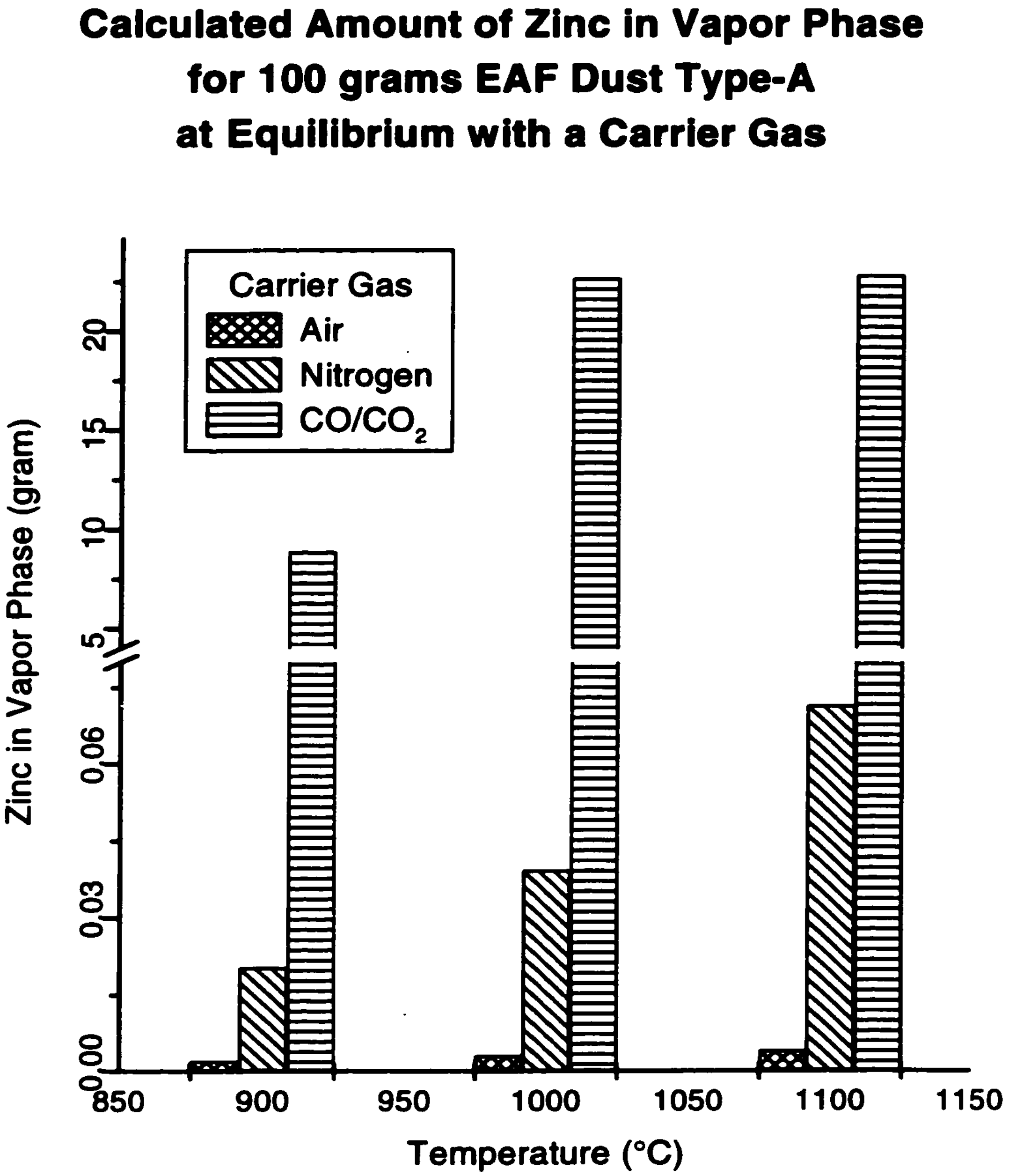

Figure 3.21: Calculated zinc content of the vapor phase in equilibrium with a carrier gas.

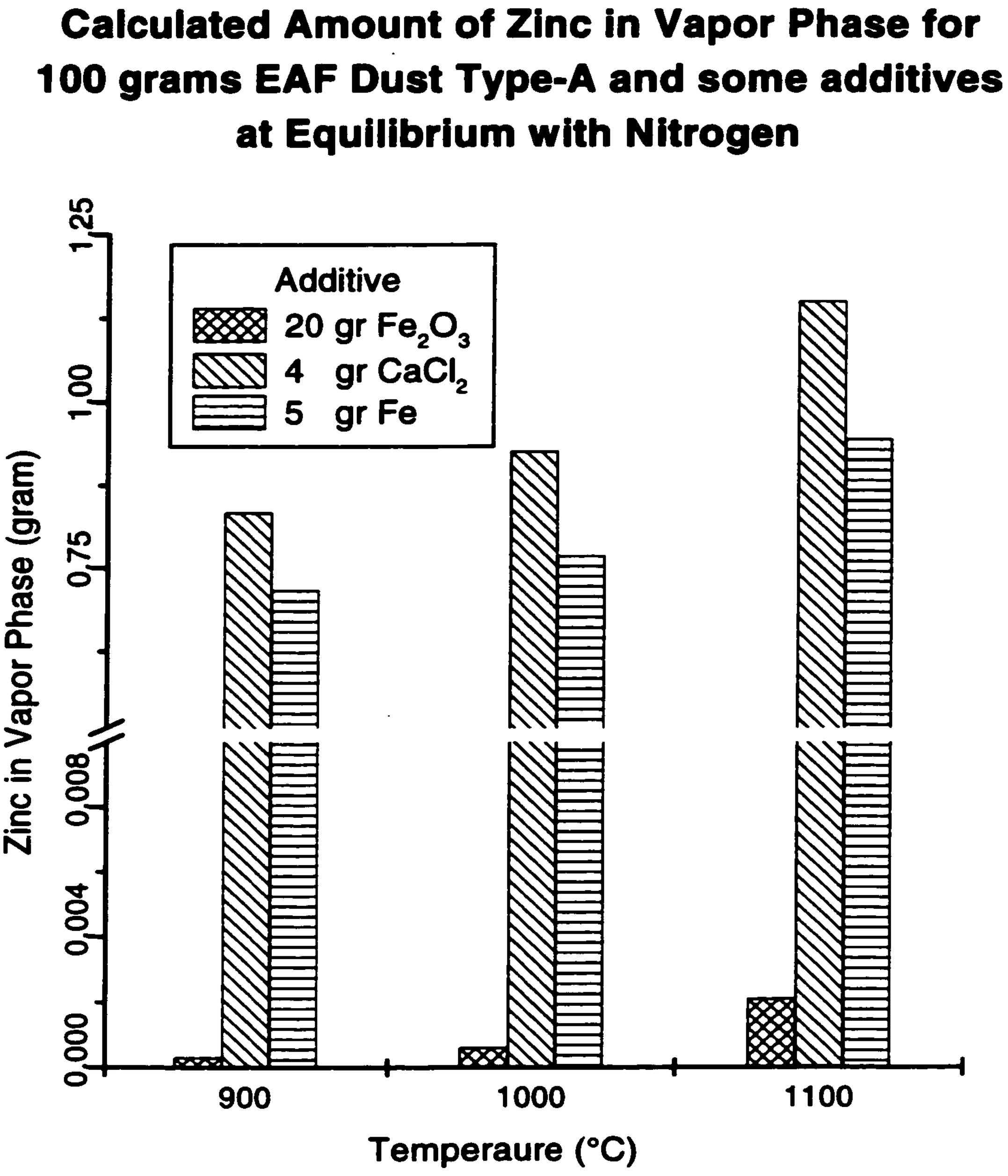

Figure 3.22: Calculated zinc content of the vapor phase in equilibrium with nitrogen when some additives added to EAF dust.

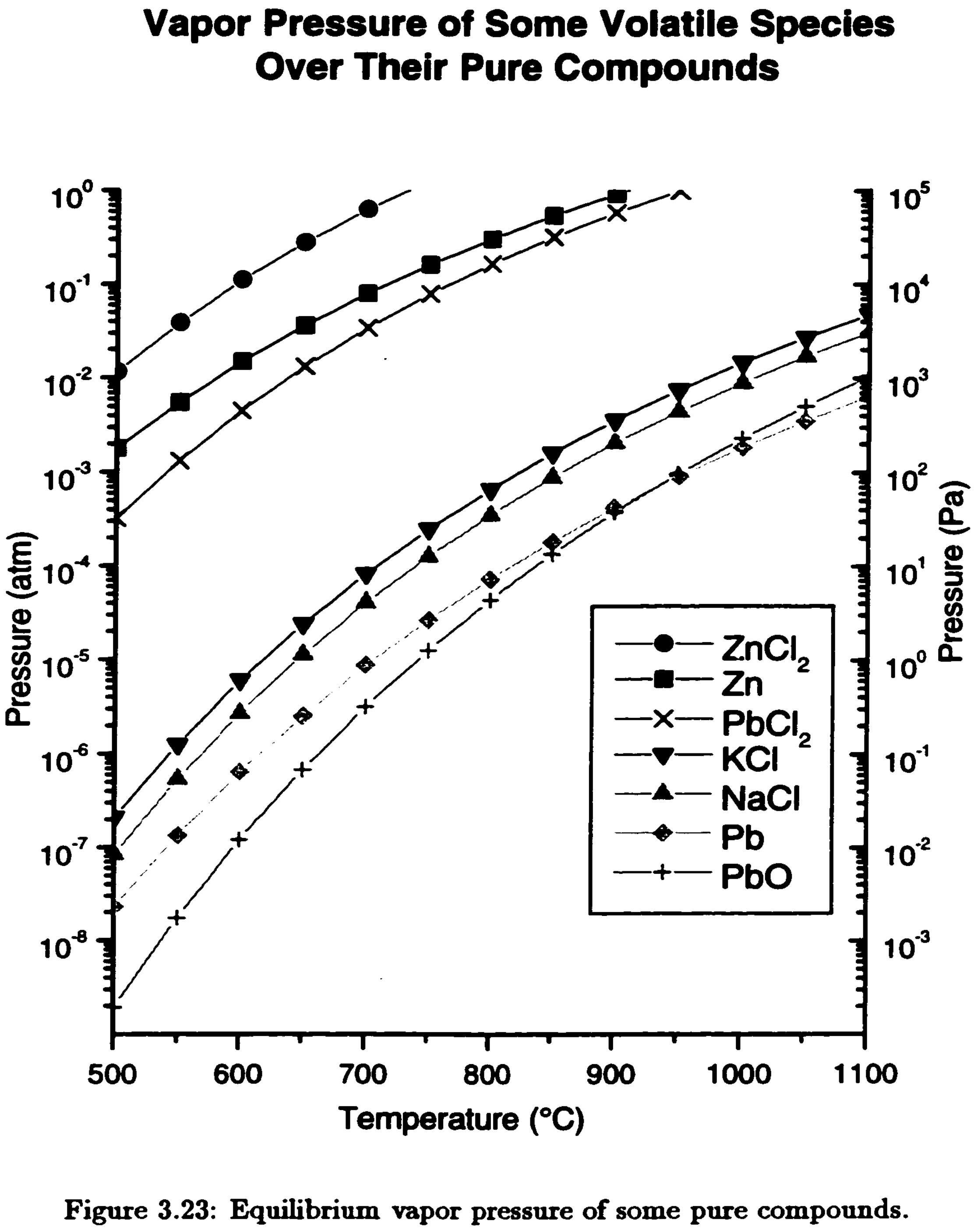

Figure 3.23: Equilibrium vapor pressure of some pure compounds.

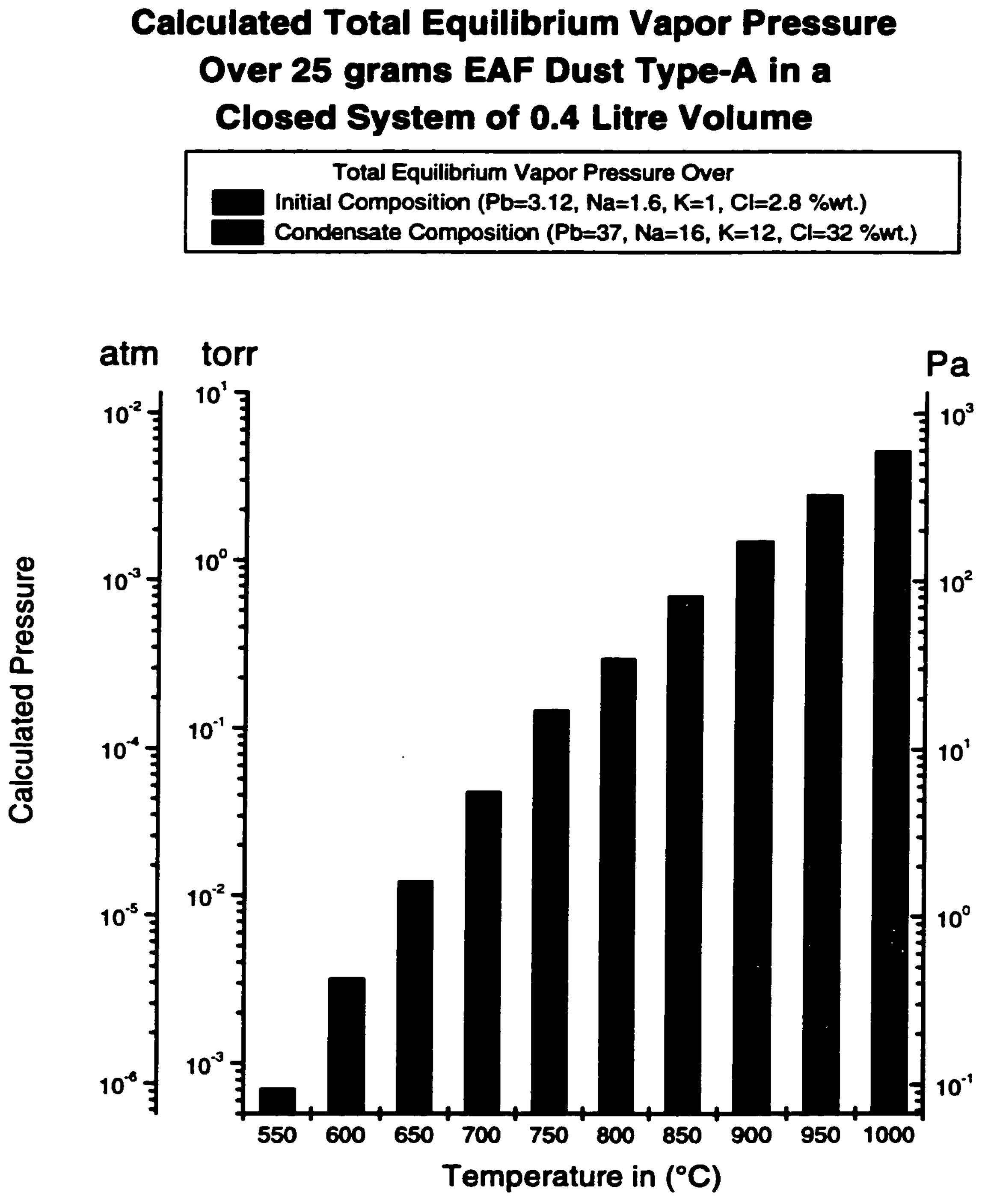

Figure 3.24: Calculated total vapor pressure in the hot zone and cold zone for the condition of cylindrical reaction chamber.

Chapter 4

EXPERIMENTAL DESIGNS AND PROCEDURES

Since major contributions of this work are based on the experimental study, a good understanding of the experimental design for each apparatus and the procedure of experiments is required. In this chapter, the strategy for experimentation will be outlined. Each experimental apparatus will be described and its experimental procedure will be explained. Sampling procedure and the means of chemical analysis will be presented.

4.1 Outline of the Strategy for Experiments

The following explains the sequence of different experiments used to study the separation process.

- A set of preliminary experiments with different carrier gases was carried out in a horizontal furnace to investigate the feasibility of separation of more volatile species from less volatile compounds.
- A cylindrical reaction chamber consisting of two separate compartments for evaporation and condensation was designed to study the separation process in a virtually closed system under reduced pressure.
- A rectangular reaction chamber was designed to investigate the heat transfer across a stationary dust bed with the aid of temperature measurement at different locations inside the bed.
- A rotary cylindrical reaction chamber was designed to examine the enhancement of heat transfer to dust particles.

4.2 Preliminary Experiments

Preliminary experiments were carried out in a tubular resistance furnace at different temperatures (1000, 1100, 1200, and 1300°C) and for different duration of time (40, 50, and 60 minutes). In these experiments 5 grams of dry EAF dust type-A were treated in a 80 × 18 × 12 mm nickel boat. Different carrier gases (air, nitrogen and a mixture of $CO/CO_2 = 1:9$) were used with a flow rate of 1 litre per minute.

4.3 Stationary Cylindrical Reaction Chamber

4.3.1 Apparatus

The first experimental apparatus was designed to be a closed system with two separate sections for evaporating the volatile species and condensing the vapor phases. Figure 4.1 shows the first experimental apparatus. The reaction chamber is made of stainless steel. Details of the reaction chamber can be seen in figure 4.2. A stopper was used between the hot section of the chamber and the condensation compartment. The role of this stopper was to keep the dust in place in the hot section of the reaction chamber and to shield the colder sections of the apparatus from heat radiation.

The condensation compartment is a water cooled copper cylinder which can be attached to the stainless steel chamber with proper sealing. A vacuum pump was connected to the condensation compartment for evacuating the system from permanent gases. Three vacuum tight fittings were attached to the end of the connection tube of condensation compartment so that thermocouples could be inserted into the apparatus and positioned for monitoring temperature inside the apparatus. A pressure transducer was connected to the apparatus at a position between the condensation compartment and the vacuum pump to measure the pressure.

4.3.2 Experimental procedure

In each experiment 25 grams of dry dust were placed in the reaction chamber and the stopper was inserted in its position. The condensation compartment was then connected to the stainless steel chamber and the permanent gases evacuated. The pressure was stabilized between $133 - 666\ Pa$ ($0.1 - 0.5\ torr$). Circulating water was

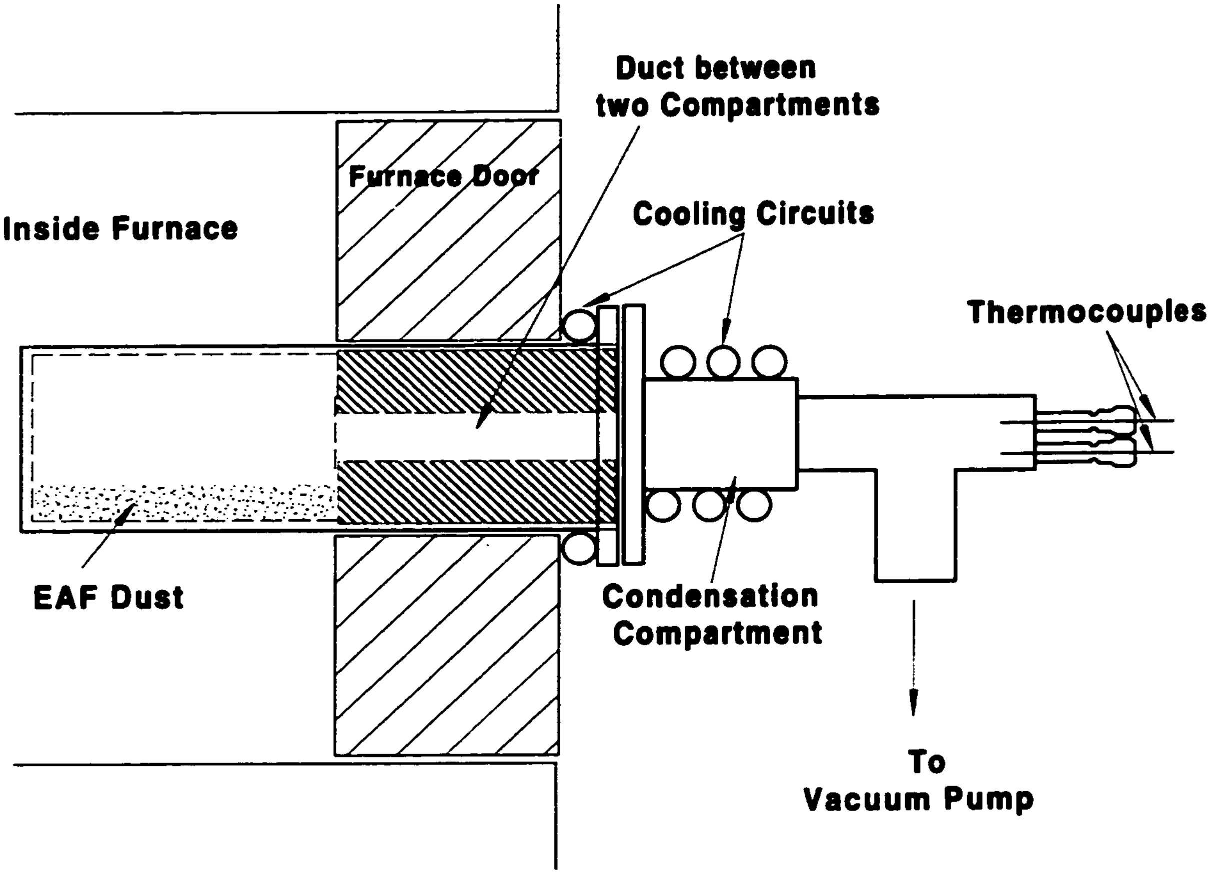

Figure 4.1: First experimental setup with cylinderical reaction chamber.

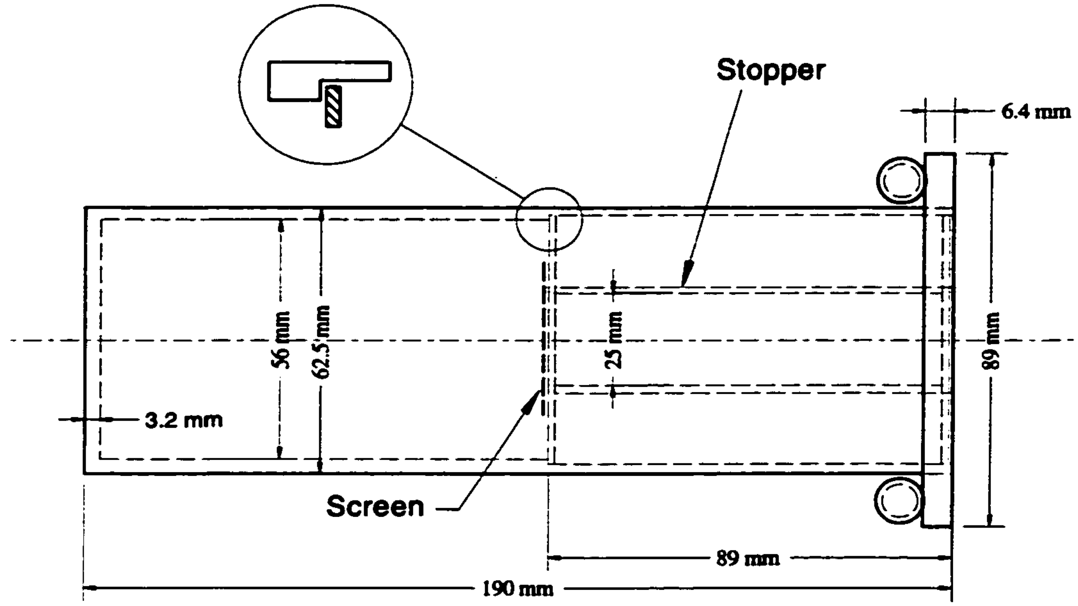

Figure 4.2: Design of cylinderical reaction chamber.

set at approximately 3 liters per minute.

A silicon carbide muffle furnace of 10 *kW* heating capacity with a cavity volume of $320 \times 225 \times 205$ *mm* was used for all experiments except for the preliminary trials. The furnace was preheated well before each experiment started. The stainless steel reaction chamber was inserted into the furnace from an opening hole on the furnace door, so that the evaporation compartment was inside the furnace. This is considered time zero for the experiments. The stopper which forms the vapor passage between the two compartments was located within the furnace door and the condensation compartment stayed outside the furnace.

After a certain period of time the apparatus was withdrawn from the furnace and cooled down in air. The experiments duration is considered the time during which the reaction chamber is inside the hot furnace.

When the reaction chamber was cooled down to room temperature, the residue, i.e. treated dust, could be removed and weighed. Samples for chemical analysis were taken after mixing the residue for homogeneity in composition.

During the experiment, temperature and pressure were measured and recorded by a personal computer through a data acquisition interface. The rate of sampling was 400 readings per second. An average value over a period of 5 seconds was recorded in the data log. For these experiments thermocouples could not be positioned precisely, therefore dust temperature for these experiments are not reported.

4.3.3 Temperature profile

In order to establish the temperature profile of the reaction chamber, the temperature of the inside wall of the reaction chamber was measured and plotted vs. time. When the temperature of the inner wall of the reaction chamber was stabilized, the thermocouple was withdrawn gradually and the temperature was measured along the centre line at different distances from the end of the reaction chamber.

4.3.4 Experiments with the use of a nickel boat

A nickel boat ($85 \times 40 \times 20\ mm$) was used in some of the experiments with the first apparatus. This nickel boat was built to facilitate positioning of two or three thermocouples inside the dust bed. With the use of the nickel boat dust temperature at different heights inside the dust bed could be measured. Nickel which is more inert than iron also prevents the reactions between the steel chamber and some oxide contents of the dust. In these experiments, $18 - 20$ grams of EAF dust were treated each time.

4.4 Rectangular Reaction Chamber

4.4.1 Apparatus

The rectangular reaction chamber, which was larger than the cylindrical chamber, was built to obtain more accurate data of the temperature variations inside the dust bed and to avoid possible side effects of the small nickel boat used in the first design. With the use of appropriate fixtures in this apparatus, possible errors involved in positioning of the thermocouples inside the dust bed were minimized. Figure 4.3 shows the rectangular stainless steel chamber ($230 \times 138 \times 138\ mm$). This stainless steel chamber was reinforced with high temperature resistant nickel alloy (INCOLLOY 80HT[1]).

For this apparatus, a tray was designed (see Figure 4.3) which can hold a boat containing dust. This tray also shields the cold section of the apparatus against heat radiation. The tray could be assembled together with the boat and the condensation compartment before each experiment and slid into the reaction chamber, hence, avoiding any disturbance of the thermocouples inside the dust bed.

A nickel boat, Figure 4.4, was designed to hold four thermocouples inside the dust bed. Two alumina thermocouple shields were used to cover the thermocouples inside the dust bed. Two other thermocouples were also used to measure temperature of the nickel boat and the tray shield.

A cold trap was positioned between the condensation compartment and the vacuum pump. Upstream and downstream pressures on both sides of this cold trap

---

[1] A registered trade name of INCO Limited, a corporation of Canada.

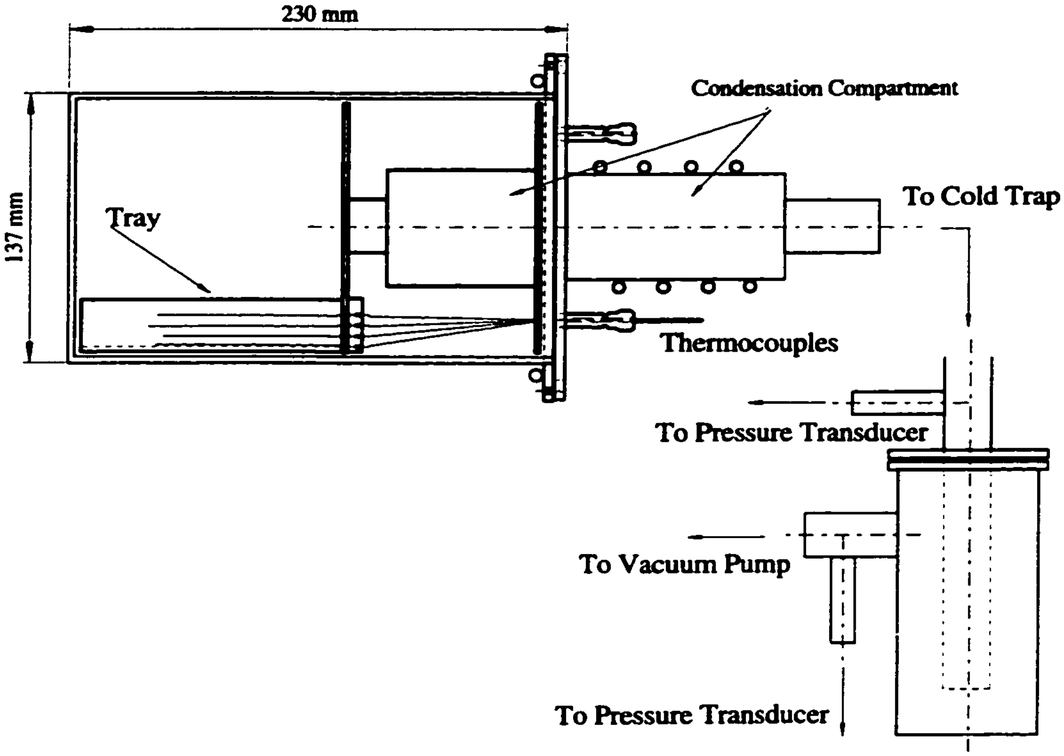

Figure 4.3: Experiment setup with rectangular reaction chamber.

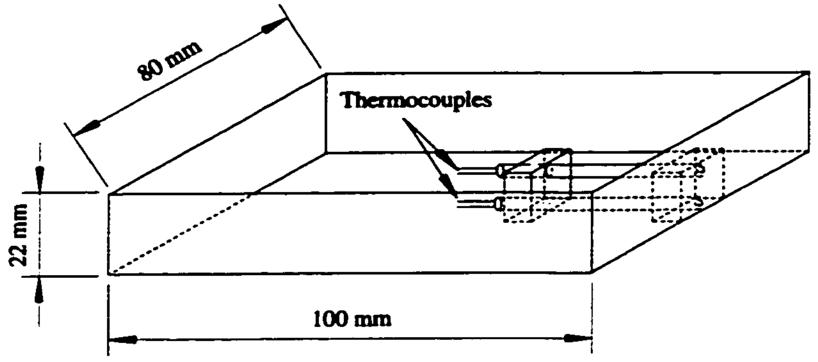

Figure 4.4: Nickel boat used for treatment of EAF dust in rectangular reaction chamber.

were monitored with two pressure transducers.

4.4.2 Experimental procedure

In each experiment with the rectangular apparatus, 100 grams of EAF dust were heated at a furnace temperature of 1100°C. Some of these experiments were conducted without pre-heating the furnace and were cooled down inside the furnace. For other experiments, the furnace was preheated to 1100°C and the experiments were finished by removing the reaction chamber from the furnace and cooling it in air. The steps taken in these experiments are summarized as follows.

1. Thermocouples were set to specific positions and their heights from the bottom of the nickel boat were recorded.

2. 100 grams of dry EAF dust were weighed and placed inside the nickel boat.

3. A vibrator was used for approximately 30 seconds to settle the dust inside the boat.
4. The height of the dust bed was measured.
5. The tray and the condensation compartment were assembled together and slid into the reaction chamber.
6. Vacuum hoses, pressure transducers and other attachments were connected.

A) For experiments without pre-heating the furnace

7a. The reaction chamber was placed inside the cold furnace

8a. The permanent gases were evacuated from the system and the furnace was turned on.

9a. The furnace was turned off after a certain period of time.

10a. The chamber was cooled down inside the furnace.

B) For experiments with pre-heating the furnace

7b. The furnace was pre-heated to experiment temperature (1100°C) well before experiment began.

8b. The permanent gases were evacuated from the system.

9b. The reaction chamber was placed inside the hot furnace.

10b. The reaction chamber was withdrawn from the furnace and cooled in air.

11. After removing the tray from the reaction chamber, the height of the dust bed was measured.

12. Samples were taken from different depths with the procedure that will be described later.
13. The positions of the thermocouples were measured again to ensure that the thermocouples had not moved during the experiment.

The condensation compartment and the cold trap were filled with steel wool to increase the surface area for a better condensation condition. Steel wool from the condensation compartment was disposed of after each experiment and new material was used every time.

4.4.3 Sampling procedure for chemical analysis

In order to investigate the variation of chemical composition across the dust bed, samples were taken from different heights. To accomplish this, a plastic tube (straw, see Figure 4.5) with an I.D. of approximately 5.5 mm was used. The following describes the procedure step by step.

1. The straw was inserted vertically into the dust bed.
2. A core of dust remained inside the straw after its careful withdrawal.
3. With the use of a glass rod, dust was pushed out little by little, collecting the dust in five portions.
4. Each portion was weighed separately.
5. Steps 1 to 4 were repeated several times until enough dust was collected for the chemical analysis of each portion.

6. The depth each sample was taken from, was determined by its weight in proportion to the total weight of all samples and by relating it to the height of the dust bed.

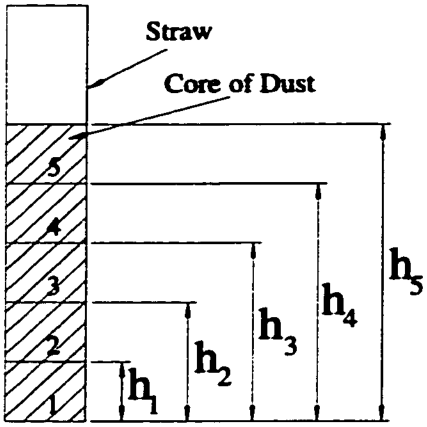

Figure 4.5: Schematic representation of the plastic tube used for sampling.

$h_i \quad = h \times \frac{\sum_{j=1}^{i} w_i}{W}$

h = height of the dust bed

h_i = upper height related to part i in the dust core

W_j = weight of part j of the dust core

W = total weight of the samples

Part i is from h_{i-1} to h_i in the dust core

4.5 Rotary Reaction Chamber

4.5.1 Apparatus

The objective of the design for this apparatus was to enhance the heat transfer to dust particles by taking advantage of mixing of the dust and direct heat radiation to dust particles. The apparatus resembles a rotary kiln working under reduced pressure. The reaction chamber was built identically to that of the stationary cylindrical chamber so that their results could be compared. To prevent reaction of oxides with the stainless steel chamber, the interior surface of the chamber was nickel plated.

A simplified sketch of the apparatus is given in Figure 4.6. An UltraTorr vacuum fitting was used for the sealing between the rotating and the stationary parts. Two ball bearings held the rotary chamber and kept it aligned along the axis of the rotation. A variable speed DC motor rotated the reaction chamber through a drive chain at a speed of one rpm.

In this apparatus only one thermocouple could be used to measure the temperature of the chamber inner wall at the evaporation compartment. A cold trap was installed between the condensation compartment and the vacuum pump and the pressure was measured downstream after the cold trap. The whole assembly was mounted on a wheeled rig which could be moved to insert the reaction chamber into the furnace and to withdraw it at the end of experiment.

4.5.2 Experimental procedure

The experimental procedure of the rotary reaction chamber was similar to that of the stationary cylindrical chamber except for few differences. For the rotary reaction

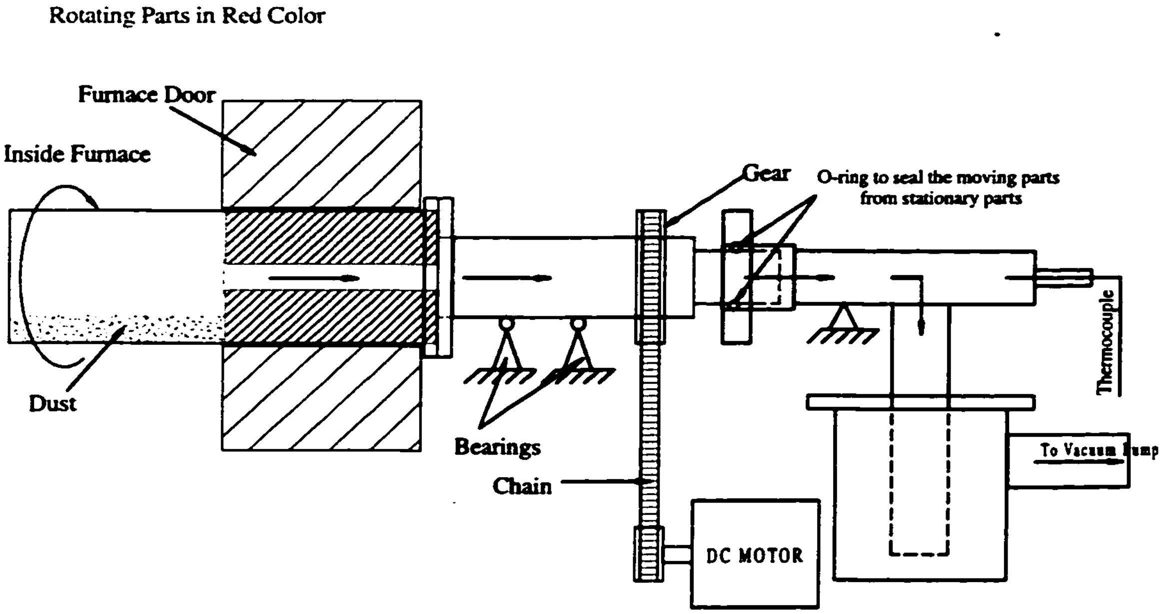

Figure 4.6: Experimental setup with rotary reaction chamber.

chamber the condensation compartment had to be air cooled and the position of the sealing was cooled with air jet for protection of the vitan o-ring against overheating. The evaporation compartment was also cooled down with air jet after withdrawal of the reaction chamber from the furnace. The speed of rotation was approximately one rpm for all these experiments.

4.6 Chemical Analysis

4.6.1 Solution preparation

After mixing the collected residue, a sample of 0.1 gram was weighed and dissolved in a solution of 5 $ml.$ HNO_3, 5 $ml.$ HCl and 10 $ml.$ distilled water on a hot plate. The solution is filtered and diluted to volume in a 100 $ml.$ volumetric flask. The same procedure was used to prepare the solution for the as received dust.

4.6.2 Chemical analysis

The chemical compositions were determined by a JARREL ASH Induction Coupled Argon Plasma spectrometer ($ICAP$ 9000). Some variations of the intensity signals for sodium and potassium could be detected which caused some uncertainty on the extent of errors. Therefore, these two elements were analyzed by a double channel atomic absorption spectrometer. In order to reduce the effect of background on the sodium analysis, relevant amounts of other components present in residue were added to the standard solutions. Standard addition technique was also used for some of these samples to verify the accuracy of the results from the atomic absorption spectrometer.

The chemical composition of chlorine and fluorine were determined by a Dionex 4500 Ion Chromatograph. For aluminum and silicon, the undissolved portion of the residue remained on the filter paper was burned in a furnace at $1000°C$ and weighed to determine the amount of silica and alumina. This residue was dissolved in a solution of 50% HF and filtered. The filter paper was burned in a furnace at $1000°C$ and the remaining residue, was weighed to determine the content of aluminum. The silicon content was determined from the weight change of the residue after dissolution in HF.

Chapter 5

EXPERIMENTAL RESULTS

In this chapter the results of experiments are presented. These include:

1. the results of temperature and pressure measurements for monitoring the experimental conditions;
2. the results of temperature measurements inside the dust bed for the investigation of heat transfer within the dust bed;
3. x-ray diffraction of the EAF dust before and after treatment for the identification of the mineralogical phases in the dust; and,
4. the chemical compositions of the dust before and after treatment with emphasis on the contents of volatile species.

A matrix of the experiments carried out in the present work is given in Table 5.1. Tables 5.2 to 5.4 include the list of experiments run using each apparatus. The important parameters and conditions of the experiments are stated in these tables.

Table 5.1: Type and number of experiments.

Apparatus	**Total**	**EAF Dust** A	**B**	**C**	**Secondary Dust**	**Alumina**
Preliminary experiments with carrier gas *	12	12	0	0	0	0
Preliminary experiments under reduced pressure	5	5	0	0	0	0
Cylindrical reaction chamber	30	25	5	0	0	0
Rotary reaction chamber	46	2	31	0	13	0
Rectangular reaction chamber	18	9	4	2	0	3

* Experiments carried out by a research associate.

This chapter is concluded with an error analysis to demonstrate the degree of confidence in the experimental results.

5.1 Results of Temperature and Pressure Measurements

Due to the fact that volatile species in the system are not stable at low temperature, measurement of the pressure at the hot zone was not possible in the laboratory. Pressure transducers used for pressure measurement work at about $50°C$. The volatile species condense at higher temperature inside the connecting tubes. Therefore, the pressure was only measured at the cold sections of the apparatus. This was done usually upstream and downstream the cold trap as shown in Figure 4.3. The results are shown on the plots of the temperature profiles.

The temperatures of dust and the reaction chamber were measured at different locations depending on the type of apparatus. Except for a few experiments with the rectangular reaction chamber, all experiments were carried out in a pre-heated

Table 5.2: Experiments with stationary cylindrical reaction chamber.

Exp. No.	Dust		Additive		Furnace Temp.	time
	type	wt. g	type	wt. g	°C	min.
6	EAF-A	25.0	N/A		1150	12
7	EAF-A	25.0	N/A		1100	12
8	EAF-A	25.0	N/A		1050	12
9	EAF-A	25.0	N/A		1100	10
10	EAF-A	25.0	N/A		1100	8
11	EAF-A	25.0	Fe_2O_3	5.00	1100	10
12	EAF-A	25.00	N/A		1100	10 : 10
13	EAF-A	25.01	Fe_2O_3	5.03	1100	10
14	EAF-A	25.01	Fe_2O_3	5.00	1100	8
15	EAF-A	25.00	N/A		1100	7
17	EAF-A	25.02	Fe_2O_3	5.00	1100	10
18	EAF-A	25.00	Fe_2O_3	5.02	1100	8
19	EAF-A	25.00	Fe_2O_3	5.01	1100	6
20	EAF-A	25.08	Fe_2O_3	5.06	1100	10
21	EAF-A	25.03	Fe_2O_3	5.07	1100	8
22	EAF-A	25.00	Fe_2O_3+ $CaCl_2$	5.50	1100	8
23	EAF-A	25.00	Fe_2O_3	5.10	1100	6
112	EAF-B	25.01	N/A		950	8
113	EAF-B	25.03	N/A		950	12
114	EAF-B	25.01	N/A		1100	12
115	EAF-B	25.01	N/A		1100	8
116	EAF-B	25.01	N/A		1100	8

Table 5.3: Experiments with rectangular reaction chamber.

Exp. No.	**Dust**			**Furnace Temp. °C**	**time min.**	**Furnace preheat**
	type	**weight**	**bed height**			
48	EAF-A	99.9 *g*	16.1 *mm*	1100	40	No
49	EAF-A	100 *g*	16.5 *mm*	1100	50	No
50	EAF-A	100 *g*	13.5 *mm*	1100	40	Yes
54	EAF-A	100 *g*	15 *mm*	1100	28	Yes
55	EAF-A	100 *g*	14 *mm*	1100	30	Yes
56	EAF-A	100 *g*	14 *mm*	1100	30	Yes
57	EAF-A	100 *g*	15 *mm*	1100	35	Yes
58	EAF-A	100 *g*	15 *mm*	1100	30	Yes
59	EAF-A	100 *g*	16.5 *mm*	1100	25	Yes
60	EAF-C	100 *g*	18 *mm*	1100	38	Yes
61	Alumina	100 *g*	15 *mm*	1100	40	Yes
62	EAF-C	100 *g*	17 *mm*	1100	38	Yes
63	EAF-B	100 *g*	17 *mm*	1100	38	Yes
64	EAF-B	100 *g*	18.5 *mm*	1100	28	Yes
85	Alumina	100 *g*	15.5 *mm*	1100	60	No
86	Alumina	100 *g*	15.5 *mm*	1100	45	No
87	EAF-B	100 *g*	18.2 *mm*	1100	28	Yes
88	EAF-B	100 *g*	17.5 *mm*	1100	32	Yes

Table 5.4: Experiments with rotary cylindrical reaction chamber.

Exp. No.	**Dust** **type**	 **wt. g**	**Speed** **rpm**	**Furnace Temp.** **°C**	**time** **min.**
45	EAF-A	25.4	7	1100	5
46	EAF-A	25.8	1	1100	7
51	Secondary	25.1	1	1100	6
52	Secondary	25.0	1	1100	4
65	EAF-B	25.01	1	1100	4
66	EAF-B	25.01	1	1100	6
67	EAF-B	25.00	1	1100	8
68	EAF-B	25.00	1	1100	6
69	EAF-B	25.00	1	1050	6
70	EAF-B	25.00	1	1000	6
71	EAF-B	25.00	1	950	6
72	EAF-B	25.02	1	950	10
73	EAF-B	25.00	1	950	8
74	Secondary	25.00	1	1100	2
75	Secondary	25.00	1	1050	2
76	Secondary	25.00	1	900	6
77	Secondary	24.99	1	950	4
78	Secondary	25.00	1	1000	4
79	Secondary	25.00	1	1050	4
80	Secondary	25.00	1	1000	2
81	Secondary	25.00	1	1000	6
82	Secondary	25.00	1	1050	6
83	Secondary	25.00	1	950	6
84	Secondary	50.00	1	1000	8

Table 5.5: Experiment with rotary cylindrical reaction chamber (continued).

Exp. No.	**Dust**		**Speed**	**Furnace Temp.**	**time**
	type	**wt. g**	**rpm**	**°C**	**min.**
89	EAF-B	25.02	1	950	10
90	EAF-B	25.02	1	950	14
91	EAF-B	25.01	1	950	8
92	EAF-B	25.01	1	900	18
93	EAF-B	25.01	1	1000	6
94	EAF-B	25.01	1	1000	8
95	EAF-B	25.00	1	1000	10
96	EAF-B	25.02	1	1050	5
97	EAF-B	25.03	1	1050	6
98	EAF-B	25.01	1	1050	8
99	EAF-B	25.00	1	900	6
100	EAF-B	25.00	1	900	8
101	EAF-B	25.00	1	900	10
102	EAF-B	25.00	1	900	6
103	EAF-B	25.00	1	900	15
105	EAF-B	24.99	1	1100	5
106	EAF-B	25.02	1	1100	8
107	EAF-B	25.01	1	1100	6
108	EAF-B	25.02	1	1100	6
109	EAF-B	25.00	1	950	8
110	EAF-B	25.02	1	950	8
111	EAF-B	25.00	1	950	12

furnace. Since only the "furnace temperature" can be controlled as an experimental parameter, it would be referred to as the temperature of experiment. It should be noted that furnace temperature is not the only parameter affecting the rate of heat transfer to the reaction chamber and from the reaction chamber to the dust bed. Other parameters, such as the heat capacity of the apparatus, the furnace wall temperature and the temperature of the silicon carbide elements, are also important. The temperature of dust was measured at different locations inside the dust bed in experiments with the rectangular reaction chamber. In experiments with the rotary and the stationary cylindrical chambers, due to the restrictions imposed by the experimental apparatus, only the temperature of the inner wall of the reaction chamber was recorded.

5.1.1 Temperature profile inside the reaction chamber

The temperature inside an empty cylindrical chamber was measured at different positions along its axis. These values are plotted against the distance from the end wall of the reaction chamber in Figure 5.1. The plateau of temperature indicates that a relatively large dust bed ($\backsim 95\,mm$) may be used in a hot zone of uniform temperature.

5.1.2 Temperature vs. time inside the chamber and dust bed

The temperature of the inner wall for an empty cylindrical reaction chamber was measured and the results are plotted in Figure 5.2. The temperature of the inner wall was also recorded during the experiments with the rotary reaction chamber and the results are given in Figures 5.3 to 5.5. The rotation of the reaction chamber could result in movement of the thermocouple and cause some irregularity of the readings. The reproducibility of the results in these experiments indicates that only little movement of the thermocouple tip has occurred during these experiments and the real minor discrepancies can be distinguished on these curves.

In experiments with the rectangular reaction chamber the temperature of dust was measured at different heights inside the dust bed, see Figure 4.4. Some of these measurements are shown as plots of temperature vs. time in Figures 5.6 to 5.11.

5.1.3 Temperature vs. height in the dust bed

The temperature profile inside the dust bed at some given time intervals is better illustrated by a plot of temperature vs. the height of the dust inside the dust bed. Figures 5.12 to 5.17 show some of these plots.

5.2 X-Ray Diffraction

Figures 5.18 shows the results of x-ray diffraction on EAF dust type-A and those of its residue after treatment. Main mineralogical phases found in the EAF dust type-A were $ZnFe_2O_4$ and ZnO. $NaCl$, KCl, and PbO were also detected in "as is" samples. The corresponding peaks are marked in Figure 5.18.

5.3 Chemical Composition and Degree of Removal

EAF dust from three different origins and one secondary incinerator dust were used in this study. Table 5.6 contains the chemical composition of these dusts. Typical chemical compositions of the residue after treatment in rotary reaction chamber at

Table 5.6: Chemical composition of EAF and secondary Incinerator dust in %*wt*.

Dust	No. of Samples	Fe	Zn	Pb	Na	K	Cd	Ca	Mn	Mg	Al	Si	Cl
EAF Type-A	6	32.6	21.6	3.03	1.40	1.01	0.09	4.45	2.62	2.06	0.36	0.27	2.81
EAF Type-B	3	30.5	18.6	1.97	1.23	0.66	0.07	12.3	2.33	1.38	0.55	0.41	2.68
EAF Type-C	1	36.6	18.1	0.45	0.28	0.37	0.05	9.51	3.61	1.44	N/A	N/A	N/A
Secondary	1	1.13	27.1	9.32	14.4	16.1	0.10	N/A	N/A	N/A	N/A	N/A	34

Table 5.7: Chemical composition of the dust residues after treatment in rotary reaction chamber.%wt.

Dust	Temp. °*C*	Duration *min.*	Fe	Zn	Pb	Na	K	Cd	Ca	Mn	Mg	Cl
EAF type-A	1100	7	32.0	22.5	0.20	0.40	0.05	0.04	4.95	2.90	2.40	0.13
EAF type-B	1100	8	33.0	20.0	0.20	0.25	0.05	0.04	13.6	2.50	1.80	0.18
Secondary	1100	6	2.33	75.1	0.16	2.91	0.48	N/A	N/A	N/A	N/A	0.87

1100°*C* for EAF dust type-A and -B and for the secondary incinerator dust are given in Table 5.7. The chemical compositions of the residues after treatment of EAF dust type-B and the secondary incinerator dust in the rotary reaction chamber for different times and temperatures are given in Tables 5.8 and 5.9, respectively. Table 5.10 includes the degrees of removal of volatile species from EAF dust type-A treated with different carrier gases and degrees of removal of the volatile species from the incinerator dust for different experiments are reported in Table 5.11.

5.3.1 Plots of chemical composition

The content of *Pb*, *Na*, and *K* in residues of EAF dust type-B after treatment at different temperatures are plotted vs. duration of the experiment in Figures 5.19 to 5.22. A comparison of the results of treatment in the cylindrical reaction chamber can be made with those of the rotary reaction chamber in Figures 5.23 to 5.24. The combined effects of time and temperature on the treatment of EAF dust type-B are shown in 3-D graphs, Figures 5.25 to 5.27. Surface plots and contour curves of these results are illustrated in Figures 5.28 to 5.31. Figures 5.32 and 5.33 show the results

Table 5.8: Chemical composition of residues after treatment of EAF dust type-B in rotary reaction chamber.%wt.

Exp. No.	Temp. °*C*	Duration *min.*	Fe	Zn	Pb	Na	K	Cd	Ca	Mn	Mg
65	1100	4	29.1	17.0	0.44	0.57	0.26	0.044	14.4	2.77	1.4
68	1100	6	32.3	17.4	0.18	0.07	0.01	0.035	13.3	2.64	1.63
69	1050	6	34.4	19.9	0.22	0.14	0.04	0.040	13.1	2.54	1.56
70	1000	6	32.0	18.4	0.37	0.56	0.21	0.42	13.6	2.52	1.63
71	950	6	30.9	17.8	0.86	0.80	0.39	0.044	13.5	2.45	1.55
73	950	8	32.4	19.4	0.45	0.58	0.25	0.052	12.7	2.56	1.52
72	950	10	32.8	19.5	0.41	0.40	0.17	0.057	12.6	2.57	1.52
99	900	6	30.6	18.2	1.65	1.12	0.64	0.066	12.8	2.48	1.53
100	900	8	31.9	22.0	0.89	0.89	0.48	0.056	13.0	2.55	1.48
101	900	10	31.2	18.4	0.42	0.74	0.38	0.058	13.8	2.73	1.64
92	900	18	31.1	18.6	0.31	0.38	0.13	0.048	13.7	2.68	1.71

Table 5.9: Chemical composition of the secondary incinerator dust residues after treatment in rotary reaction chamber.%wt.

Exp. No.	Temp. °*C*	Duration *min.*	Dust Wt. *g*	Zn	Pb	Na	K	Cd	Fe	Sn
83	950	6	25	78.9	0.28	2.82	0.16	0.05	2.91	0.68
81	1000	6	25	76.5	0.18	2.87	0.51	0.05	2.84	0.62
82	1050	6	25	78.8	0.07	2.84	< 0.1	0.05	2.99	0.66
84	1000	8	50	78.2	0.08	2.61	< 0.1	0.06	3.01	0.66

Table 5.10: Degrees of removal of volatile species from EAF dust type-A, with different carrier gases.

Carrier Gas	Temp. °C	Dust weight g	Duration $min.$	Zn %	Pb %	Na %	K %	Cl %
Air	1000	5	80	3.1	90.8	64.1	88.2	97
Air	1100	5	40	3.0	93.0	54.0	80.8	99
Air	1200	5.	60	3.8	96.3	57.6	83.4	99
Air	1300	5	80	17.9	92.7	80.0	97.5	99
N_2	1000	5	40	2.9	86.7	48.1	79.2	87
N_2	1100	5	60	6.5	97.8	82.4	99.2	99
N_2	1200	5	80	6.6	98.5	78.6	98.2	99
N_2	1300	5	40	11.6	97.4	76.2	98.2	99
CO/CO_2	1000	5	60	6.8	95.1	76.9	97.1	95
CO/CO_2	1100	5	80	36.5	98.8	84.6	99.0	99
CO/CO_2	1200	5	40	27.2	99.3	76.2	98.8	99
CO/CO_2	1300	5	60	51.7	97.5	80.2	98.2	99

Experiments are carried out by a research associate.

Table 5.11: Degrees of removal of volatile species from secondary incinerator dust.

Expeiment No.	Temperature °C	Duration $min.$	Dust Wt. g	Zn %	Pb %	Na %	K %
83	950	6	25	12.5	99.1	94.4	99.7
81	1000	6	25	17.7	99.4	94.5	99.1
82	1050	6	25	15.7	99.8	94.6	99.8
84	1000	8	50	13.6	99.8	94.9	99.8

of chemical analyses of the residues after treatment of the secondary incinerator dust in the rotary reaction chamber.

The chemical composition of the samples taken from different heights of the dust bed for some experiments carried out with the rectangular reaction chamber are illustrated in Figures 5.34 to 5.42.

5.3.2 Degree of removal vs. time and temperature

For the experiments with the rotary reaction chamber, bar charts of the degree of removal that have been calculated based on the changes of weight and chemical composition of the residue, are given in Figures 5.43 to 5.46 for different temperatures and times.

5.4 Error Analysis

5.4.1 Temperature measurement

The furnace temperature was measured with a R-type thermocouple. The tip of the thermocouple was shielded inside an alumina tube and was positioned about 50 mm away from the rear wall of the furnace. The standard error associated with this type of thermocouple is about ±0.25% of the reading. In most experiments the temperature of the furnace was measured and checked with another K-type thermocouple to avoid possible malfunctioning of the main thermocouple connected to the furnace controller.

Other temperature measurements including temperature of the dust, inner wall of the reaction chamber and some other check points inside the rectangular reaction chamber were made by K-type thermocouples. The standard error for the K-type thermocouple is $\pm 2°C$ at low temperatures and $\pm 0.75\%$ at high temperature. This is equal to $\pm 8.3°C$ at $1100°C$. Since the cold junction of the thermocouple was at room temperature, the reference temperature was compensated for by $20°C$ in the data acquisition program. The associated error may be up to $-3°C$ as the room temperature could vary between $20 - 23°C$.

5.4.2 Pressure measurement

Pressure was measured with two MKS Baratron type $122A$ Absolute Pressure Gauge transducers with a range of $13.3 - 13300\,Pa$ $(0.1 - 100\,torr)$. These pressure transducers provide a $0 - 10\,volt\,DC$ full scale output. The accuracy is 0.5% of the reading and the lowest recommended reading is $4\,Pa$ $(0.03\,torr)$. Zero adjustments for both transducers were performed periodically to assure the accuracy of the readings.

5.4.3 Dust weight

Dry dust was used in all experiments, however, it might absorb moisture during weighing and assembling of the apparatus, which could be accounted for up to $0.05\%wt$. The dust was weighed with a high accuracy $(0.1\,mg)$ Mettler $AE\,160$ scale for the experiment with the cylindrical reaction chamber. For the experiments with the rectangular reaction chamber a Mettler $PM\,6000$ scale with an accuracy of $0.1\,gr$ was used to weigh the dust. The residues after the experiment could not be collected completely and the amount remaining inside the chamber could be up to $0.25\,gr$ (1.25%) for the cylindrical reaction chamber and up to $0.5\ gr$ (0.65%) for the rectangular reaction chamber.

Samples for the chemical analysis were taken with extra care using the high

Table 5.12: Maximum error associated with each element.

	Fe	*Zn*	*Pb*	*Na**	*K**	*Cd*	*Ca*	*Mn*	*Mg*
Max. STD	0.33	0.21	0.045	0.01	0.006	0.03	0.17	0.06	0.03
Max. Error	7%	7%	2%	5%	5%	10%	7%	10%	10%

* At values under 0.1%*wt* the error could be up to ±0.02%*wt*.

accuracy scale. The moisture might have been absorbed during the sampling which could account for up to 0.05%*wt* error.

5.4.4 Chemical analysis

Each chemical analysis taken by ICAP was the average of four readings and each reading was taken over a 15 second exposure. The maximum standard deviation for each set of readings was reasonably low; however, some drifts in the intensities of the wave signals could be detected over a period of time. In order to establish a measure of the error involved in the chemical analysis of the samples, some known standard solutions were checked periodically among the sample solutions and the deviation of the resulting signals from the known values for the standard solutions were reported as the percentage of the error for each element. The maximum standard deviation for each set of readings and the maximum error of the chemical composition for each element are tabulated in Table 5.12.

5.4.5 Statistical analysis of final results (Reproducibility of results)

Since the experiments were time consuming and the repetition for each data point was not possible, the experiments for two different temperatures and times were repeated four times and the results were analyzed. Tables 5.13 and 5.14 contain the chemical

Table 5.13: Chemical composition of the residue of EAF dust type-B treated at 1100°C for 6 minutes, in %wt.

Experiment No.	Fe	Zn	Pb	Na	K	Cd	Ca	Mn	Mg
66	30.8	18.7	0.22	0.23	0.04	0.042	13.8	2.61	1.34
68	32.3	17.4	0.18	0.07	0.02	0.038	13.3	2.64	1.63
107	32.7	19.9	0.23	0.25	0.06	0.051	15.3	2.52	1.78
108	33.3	20.0	0.21	0.20	0.03	0.050	13.6	2.50	1.73
Average	32.3	19.0	0.208	0.188	0.037	0.045	14.0	2.57	1.62
Standard Deviation	1.08	1.21	0.023	0.080	0.016	0.006	0.91	0.066	0.198

Table 5.14: Chemical composition of the residue of EAF dust type-B treated at 950°C for 8 minutes, in %wt.

Experiment No.	Fe	Zn	Pb	Na	K	Cd	Ca	Mn	Mg
73	32.4	19.4	0.45	0.58	0.04	0.052	12.7	2.56	1.52
91	31.0	19.0	0.50	0.61	0.02	0.060	14.0	2.65	1.66
109	31.3	17.9	0.47	0.68	0.06	0.052	13.7	2.52	1.73
110	30.6	20.0	0.51	0.63	0.03	0.065	14.5	2.45	1.57
Average	31.4	19.1	0.482	0.625	0.037	0.057	13.7	2.55	1.62
Standard Deviation	0.78	0.89	0.027	0.042	0.016	0.006	0.75	0.082	0.096

compositions of the residues from these experiments. These tables include the average and the standard deviation values associated with each element. Figures 5.19, 5.21 and 5.22 include the standard deviation error bars for the repeated data points.

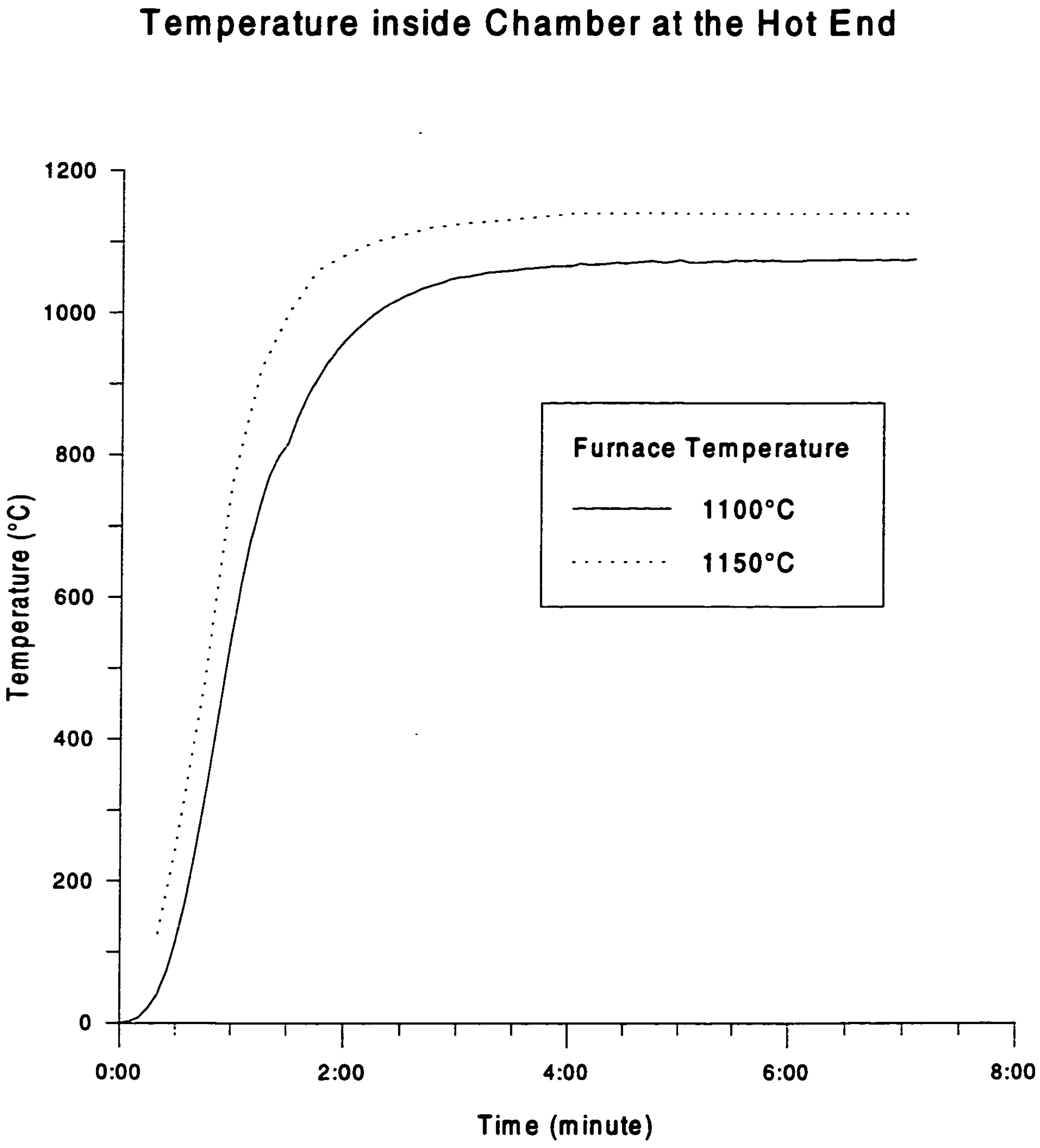

Figure 5.1: Temperature profile inside the cylindrical reaction chamber.

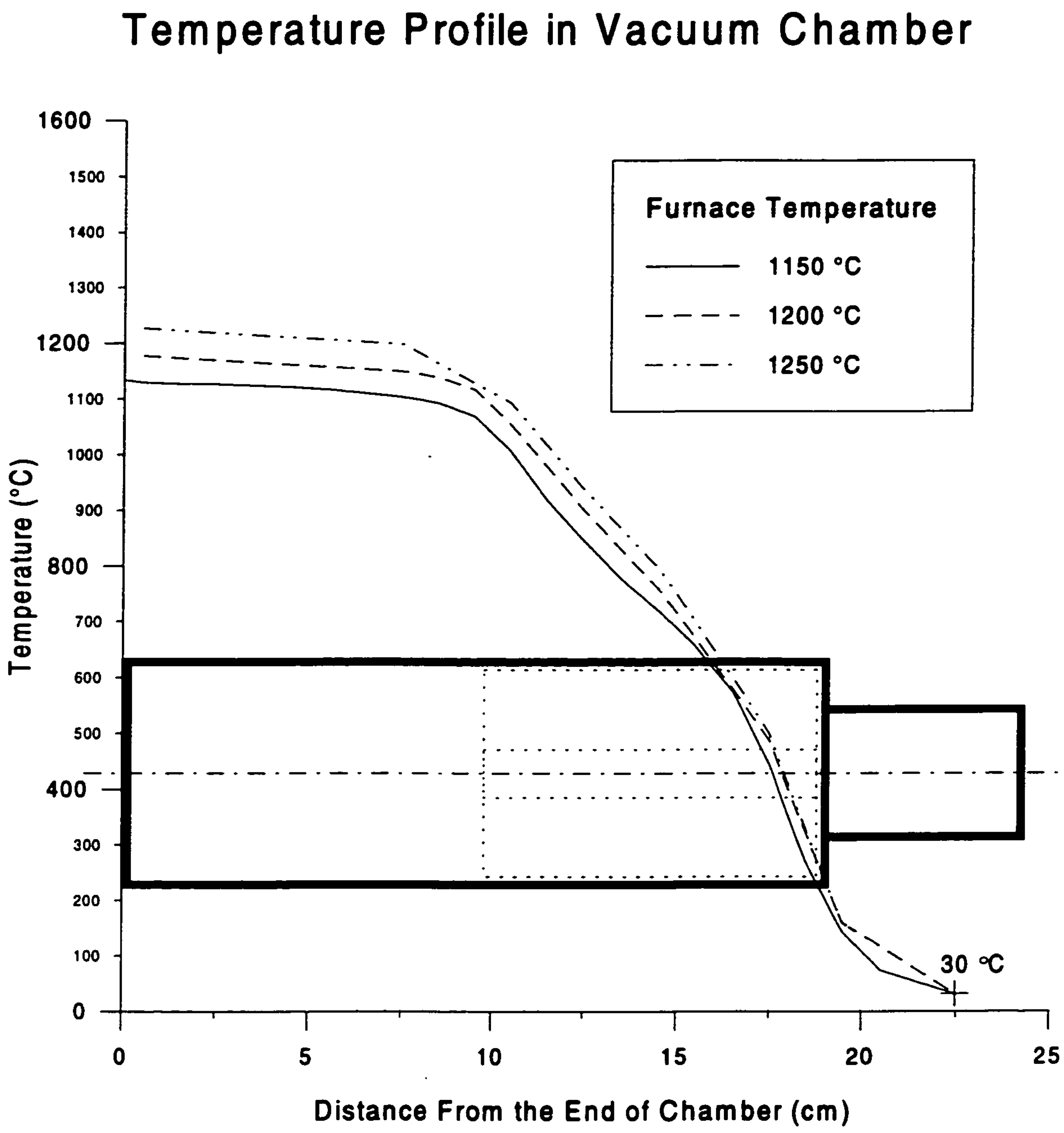

Figure 5.2: Temperature at the hot end of the cylindrical reaction chamber the time chamber is inserted inside the furnace.

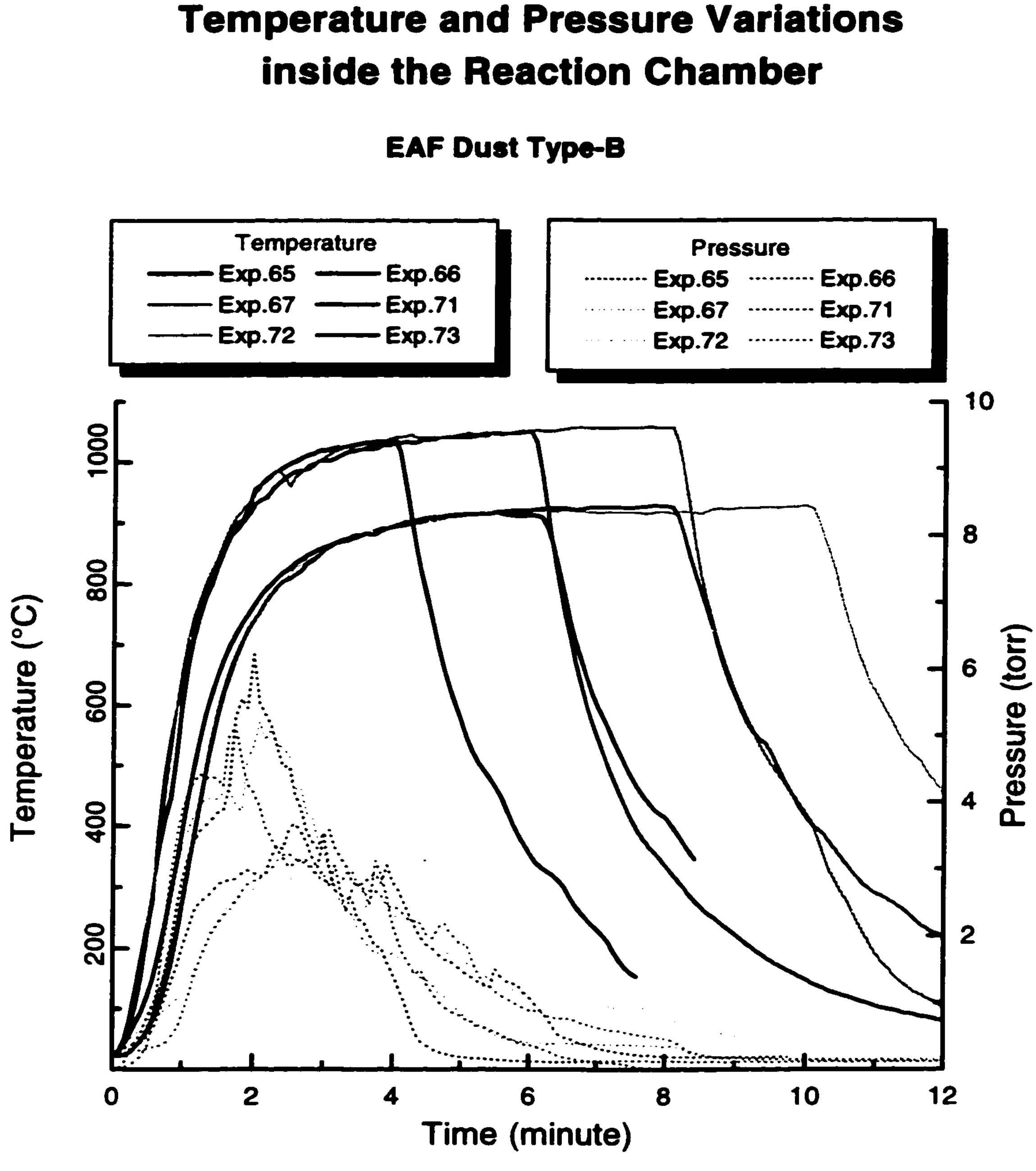

Figure 5.3: Temperature and pressure variation inside the rotary reaction chamber during treatment of EAF dust type-B.

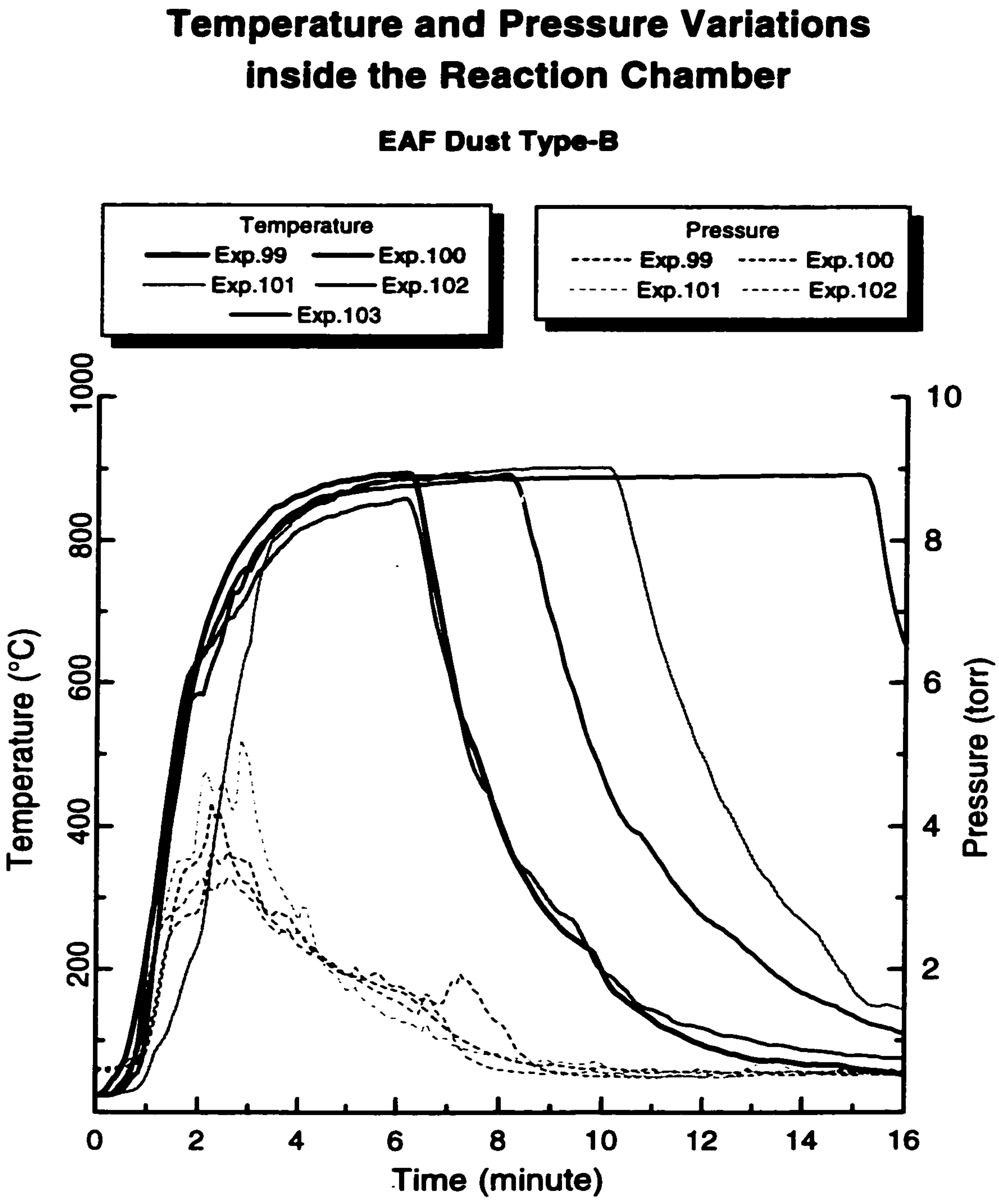

Figure 5.4: Temperature and pressure variation inside the rotary reaction chamber during treatment of EAF dust type-B.

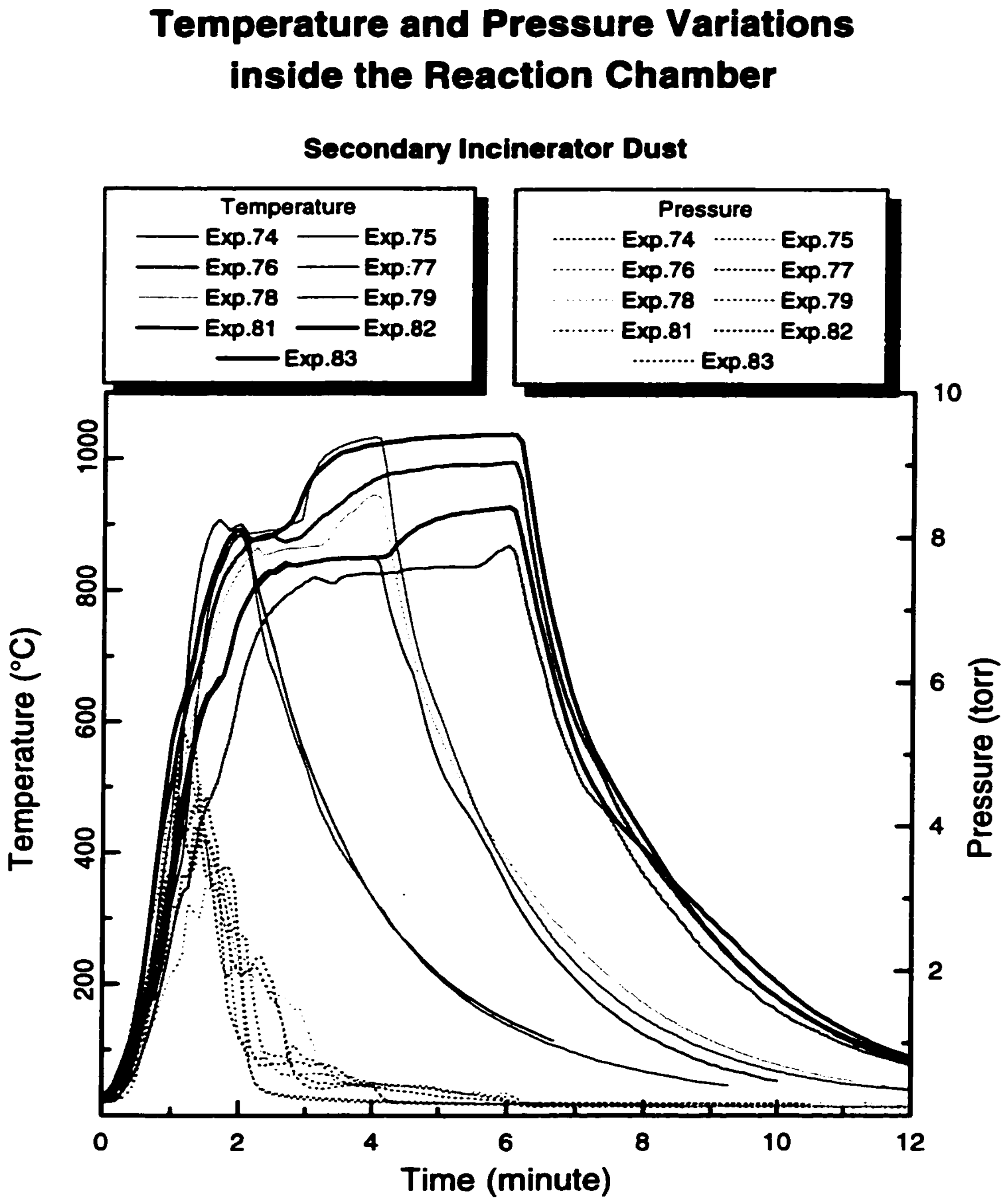

Figure 5.5: Temperature and pressure variation inside the rotary reaction chamber during treatment of secondary incinerator dust.

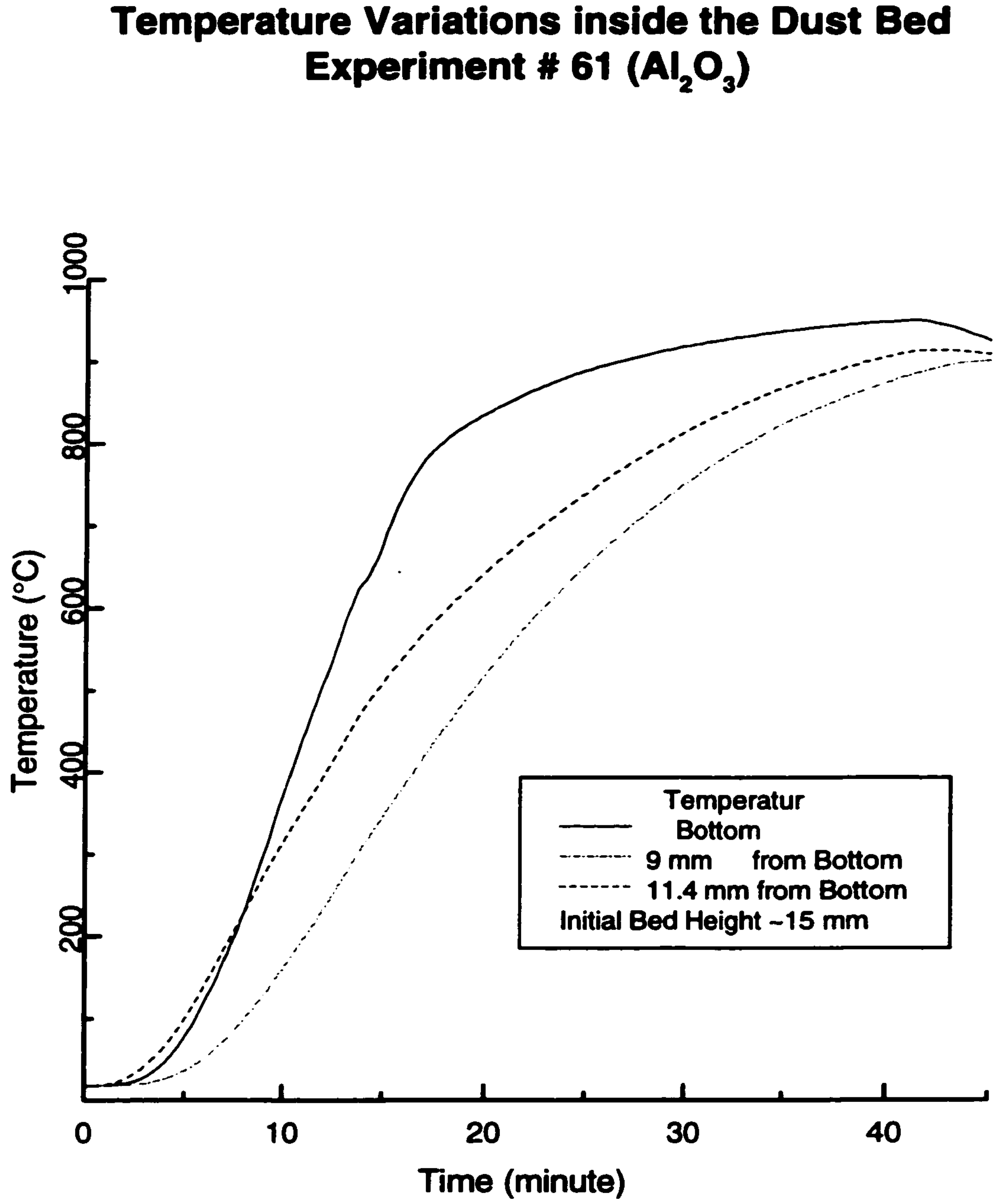

Figure 5.6: Temperature variation inside the dust bed during heating of alumina.

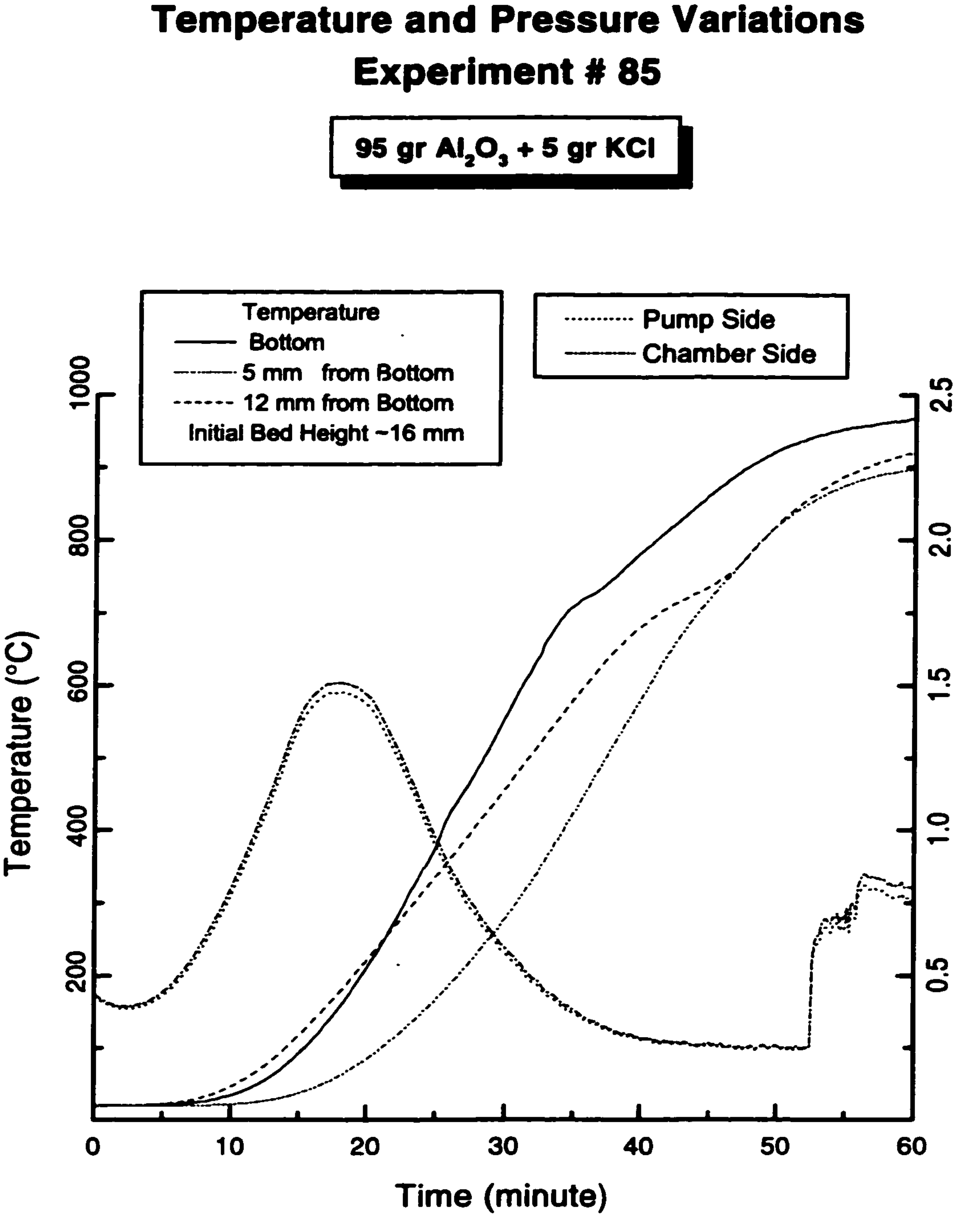

Figure 5.7: Temperature and pressure variation during heating of a mixture of alumina and KCl.

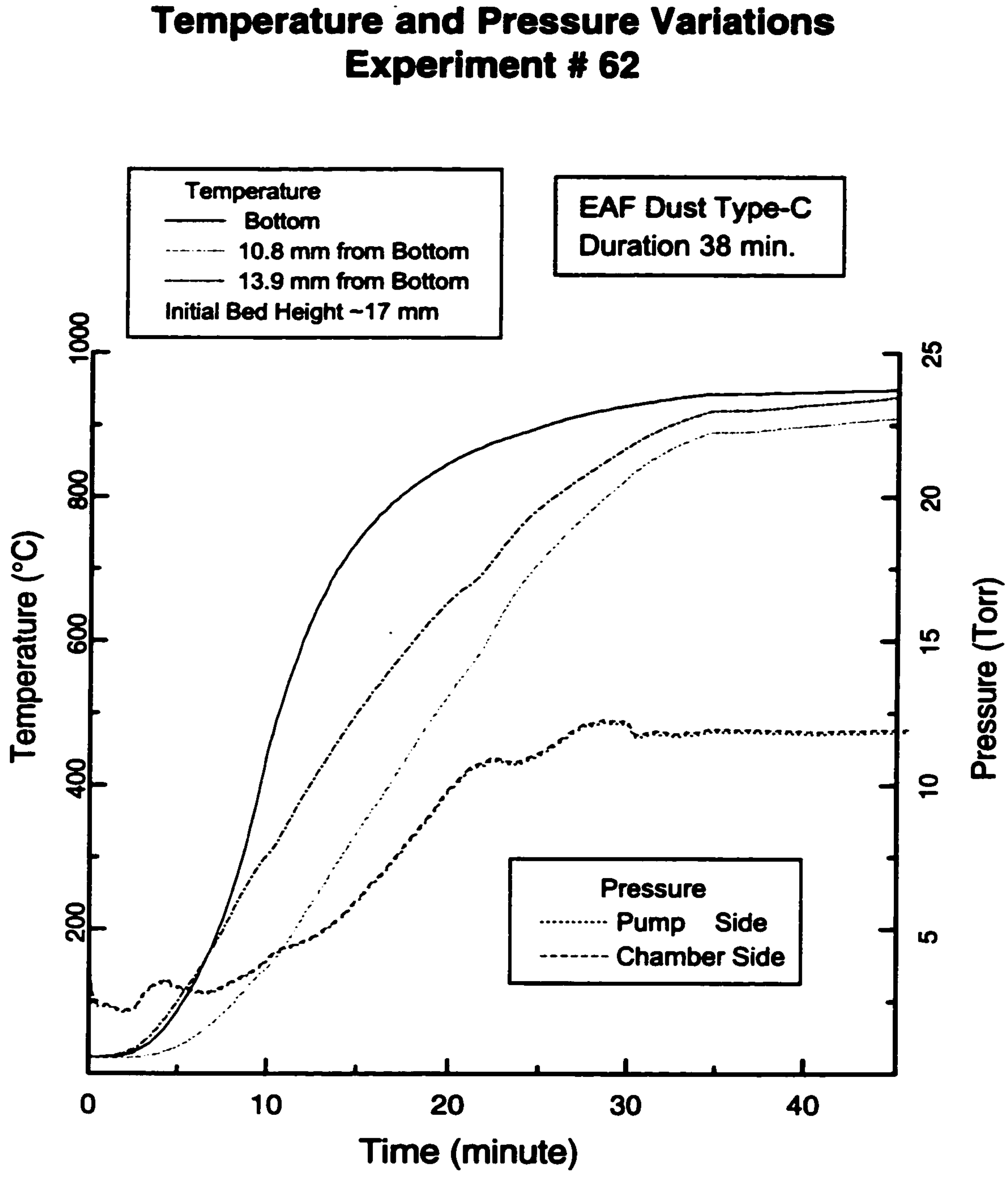

Figure 5.8: Temperature and pressure variation during treatment of EAF dust type-C.

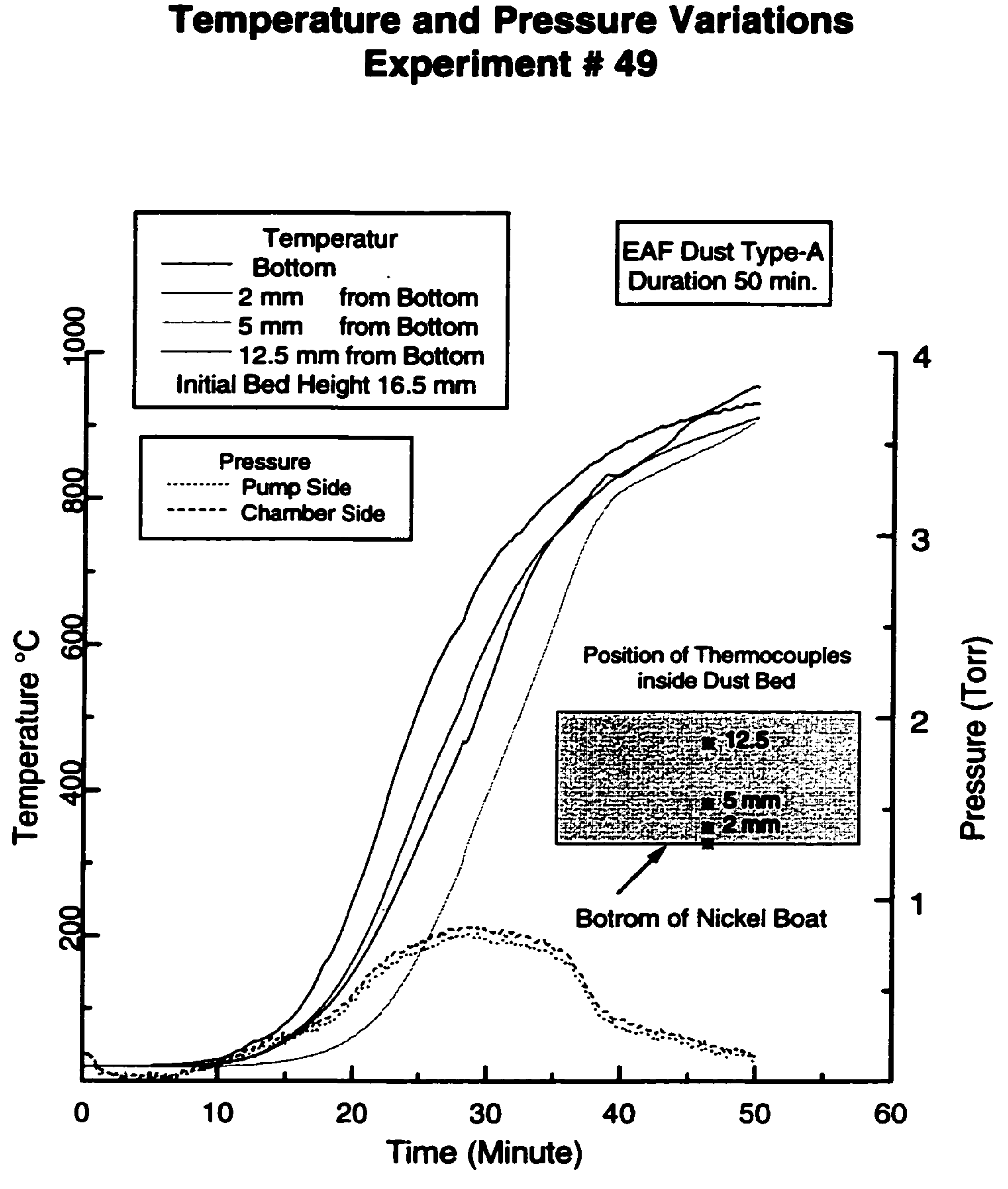

Figure 5.9: Temperature and pressure variation during treatment of EAF dust type-A.

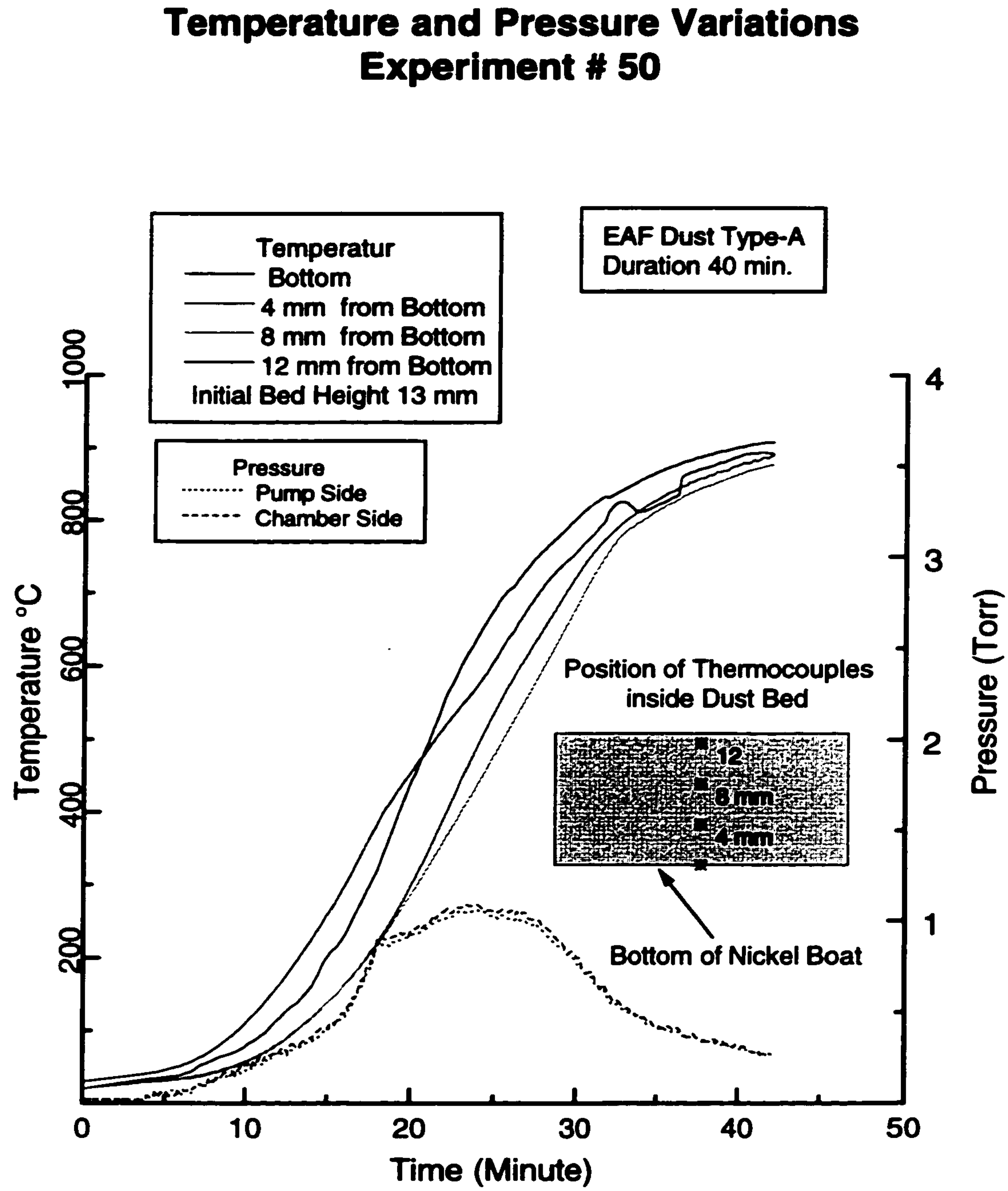

Figure 5.10: Temperature and pressure variation during treatment of EAF dust type-A.

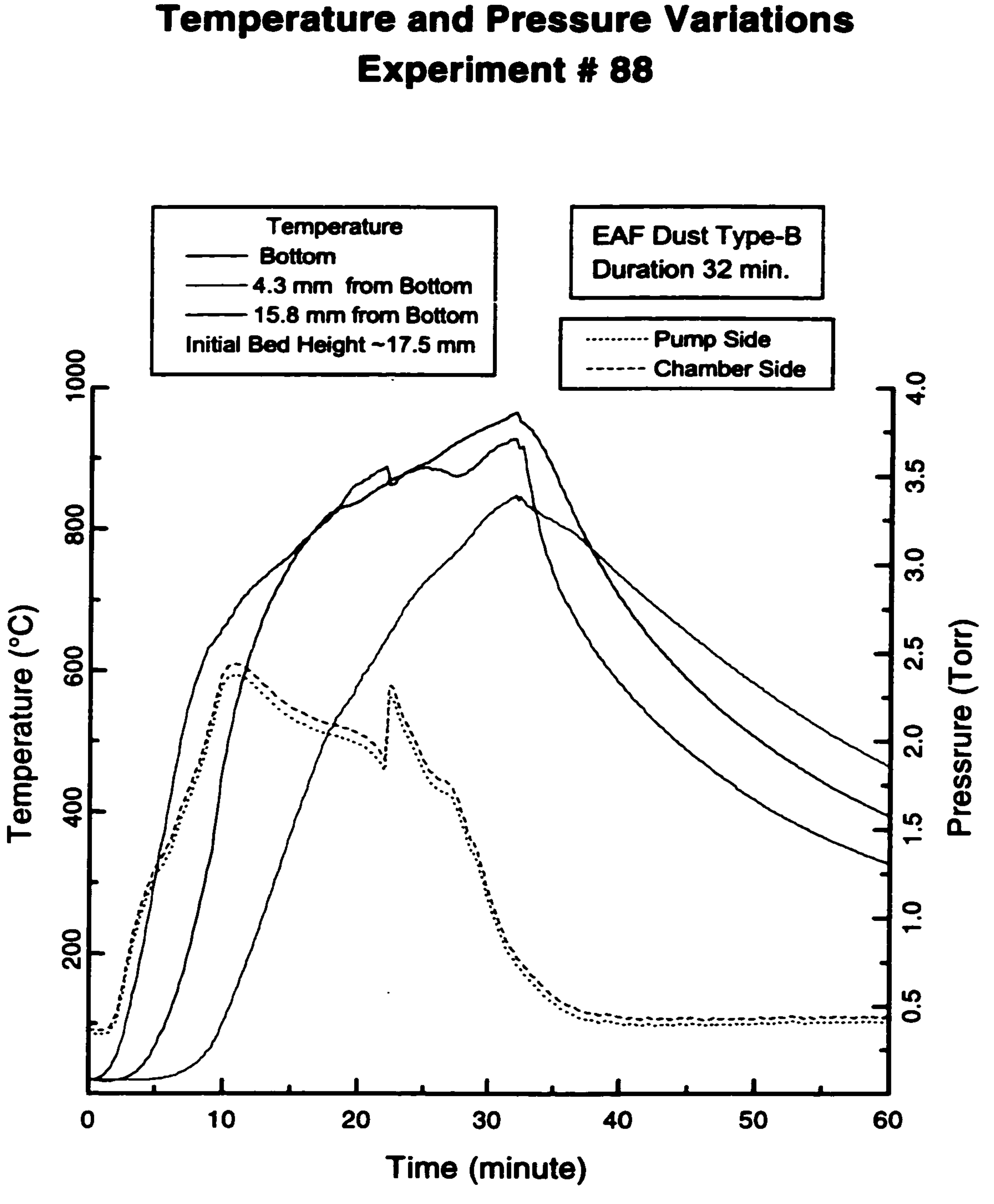

Figure 5.11: Temperature and pressure variation during treatment of EAF dust type-B.

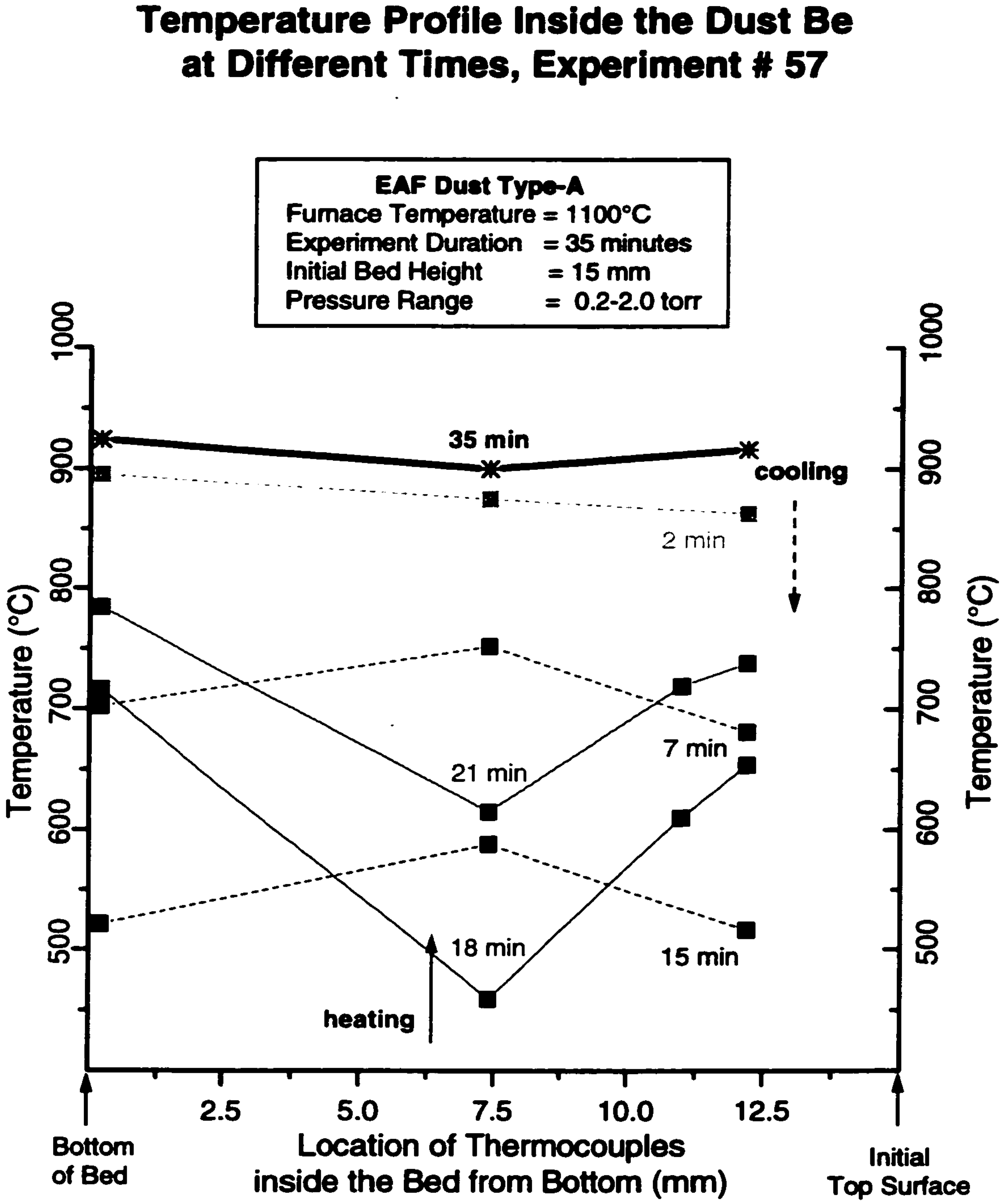

Figure 5.12: Temperature profile inside dust bed at different time during treatment of EAF dust type-A.

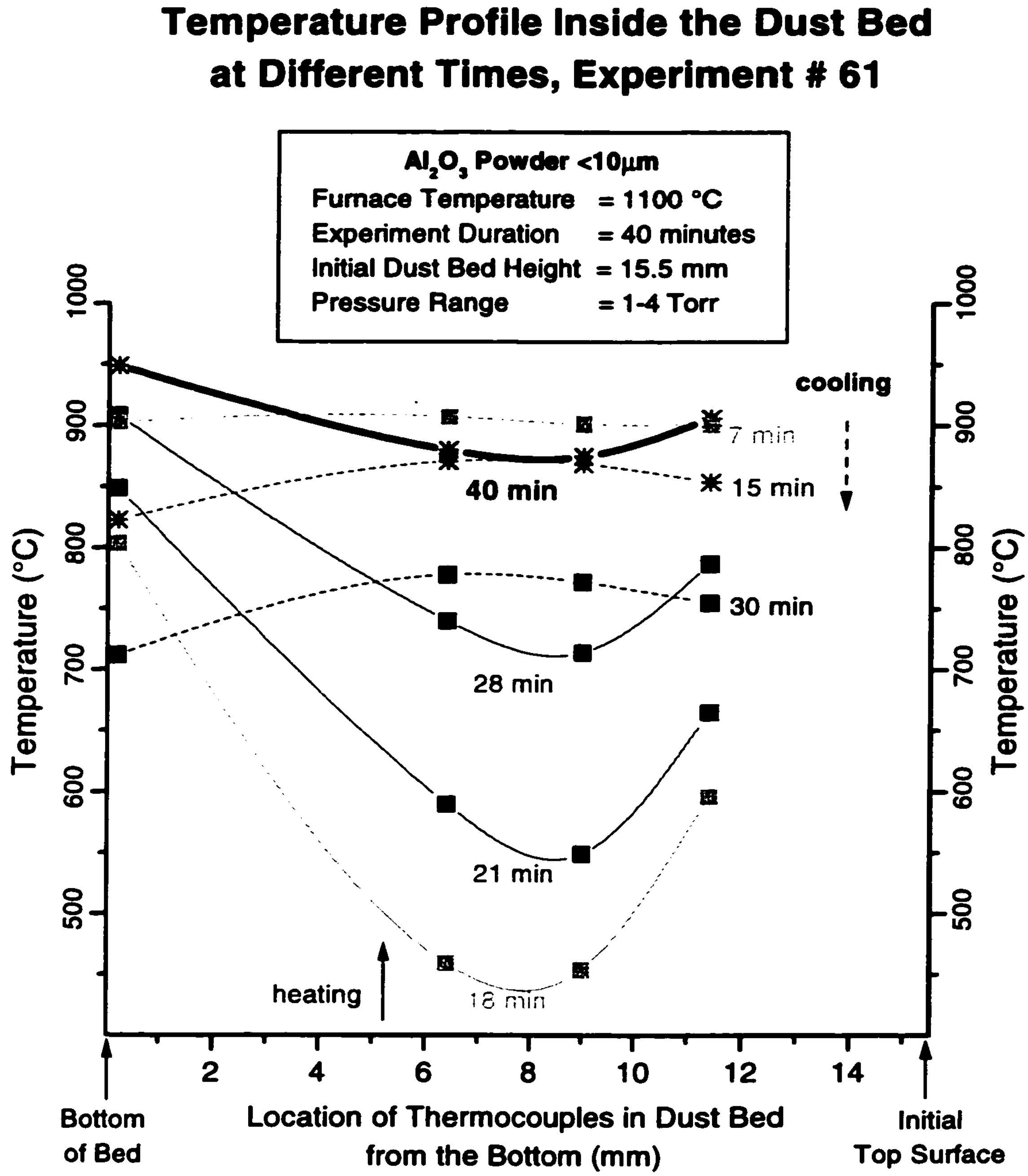

Figure 5.13: Temperature profile inside dust bed at different time during heating of alumina powder.

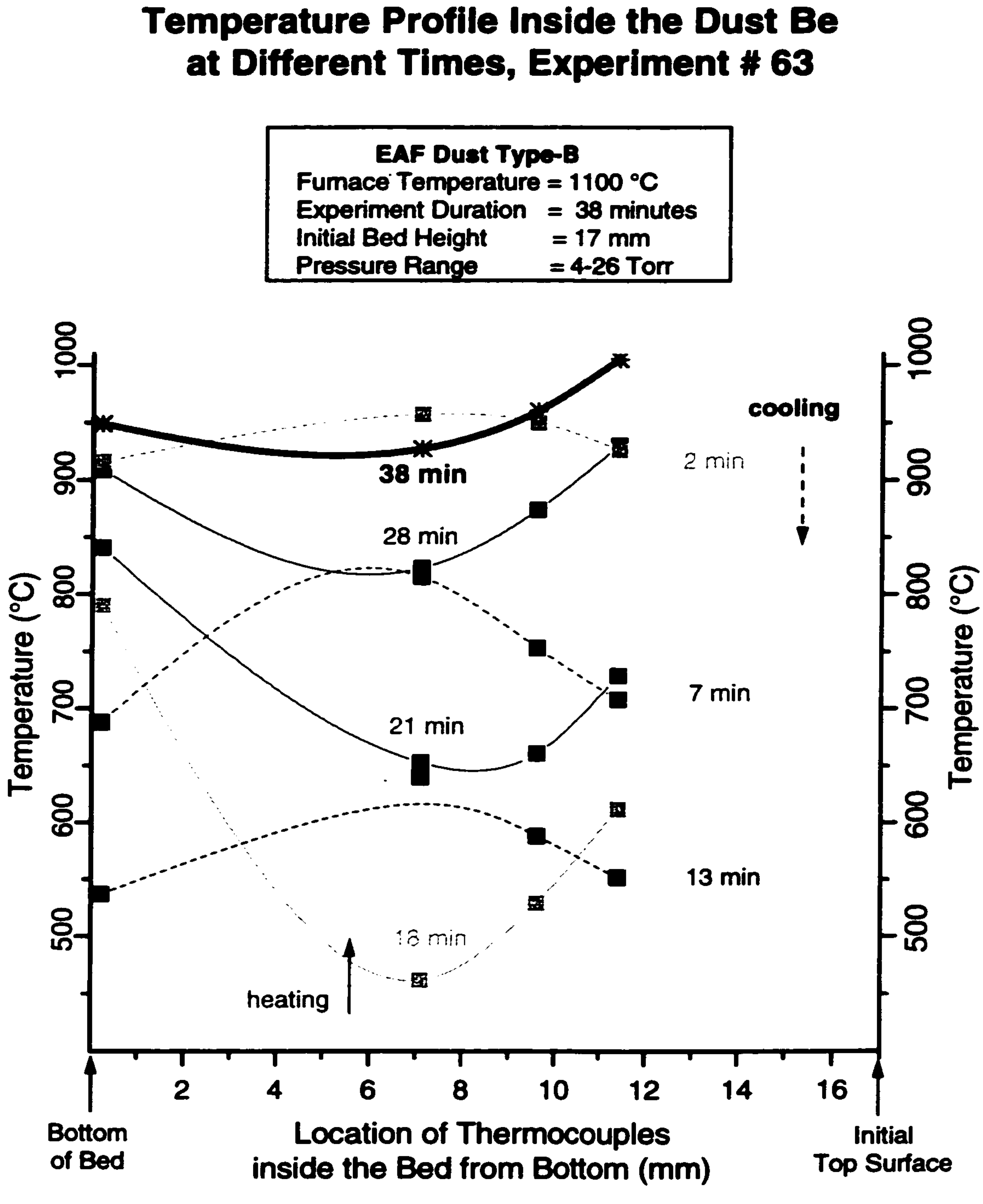

Figure 5.14: Temperature profile inside dust bed at different time during treatment of EAF dust type-B.

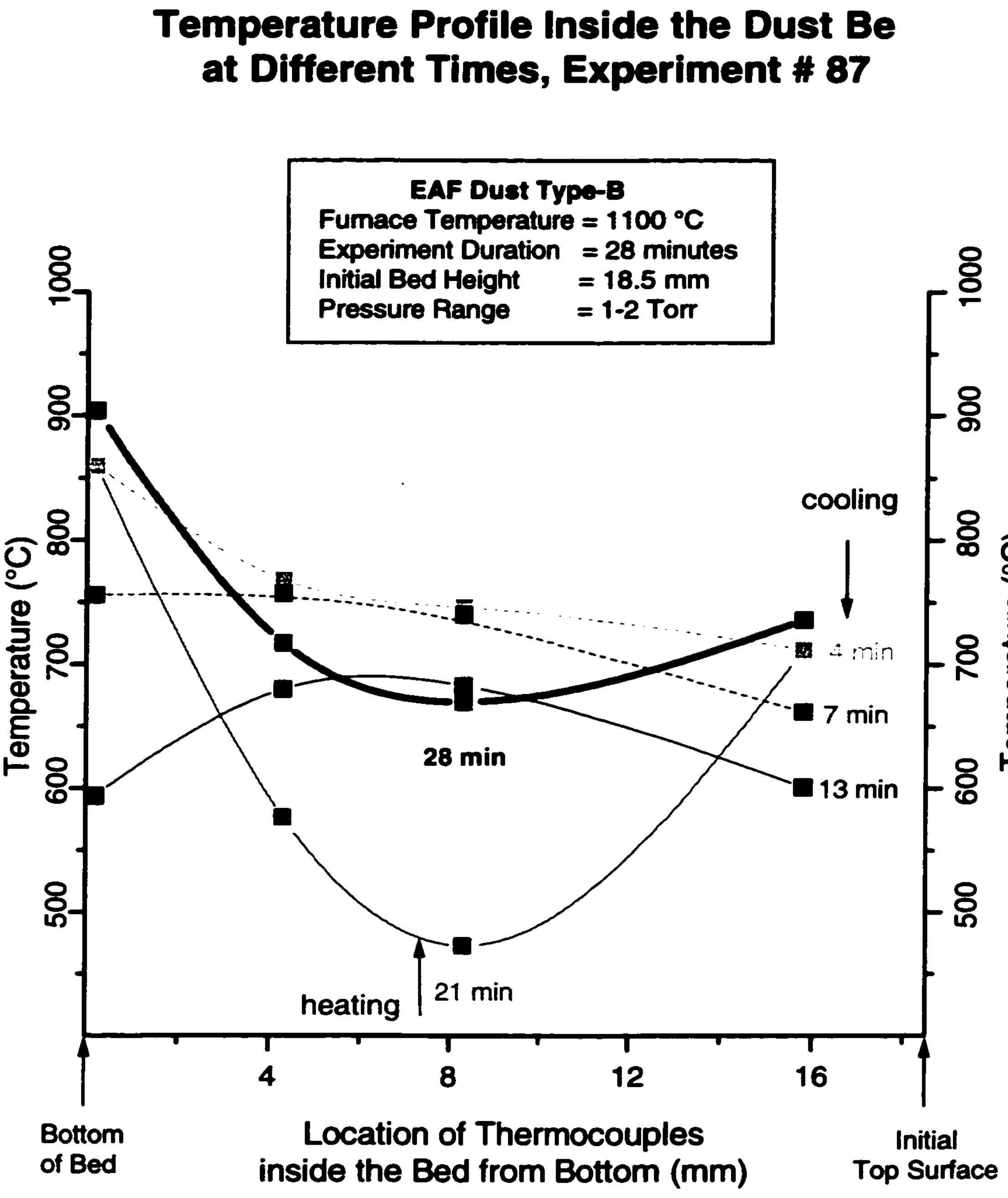

Figure 5.15: Temperature profile inside dust bed at different time during treatment of EAF dust type-B.

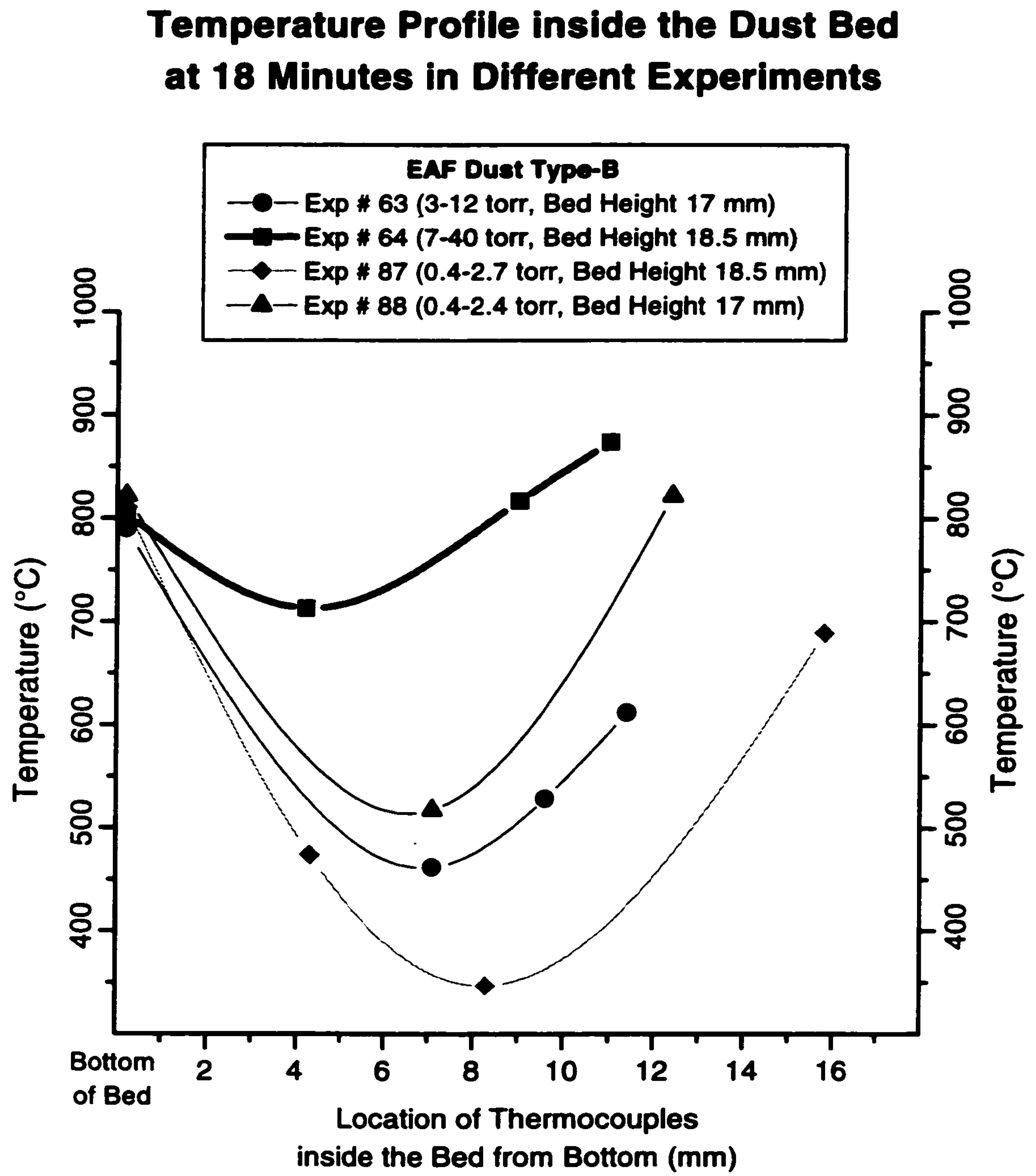

Figure 5.16: A comparison of temperature profile inside dust bed after 18 minutes heating in different experiments.

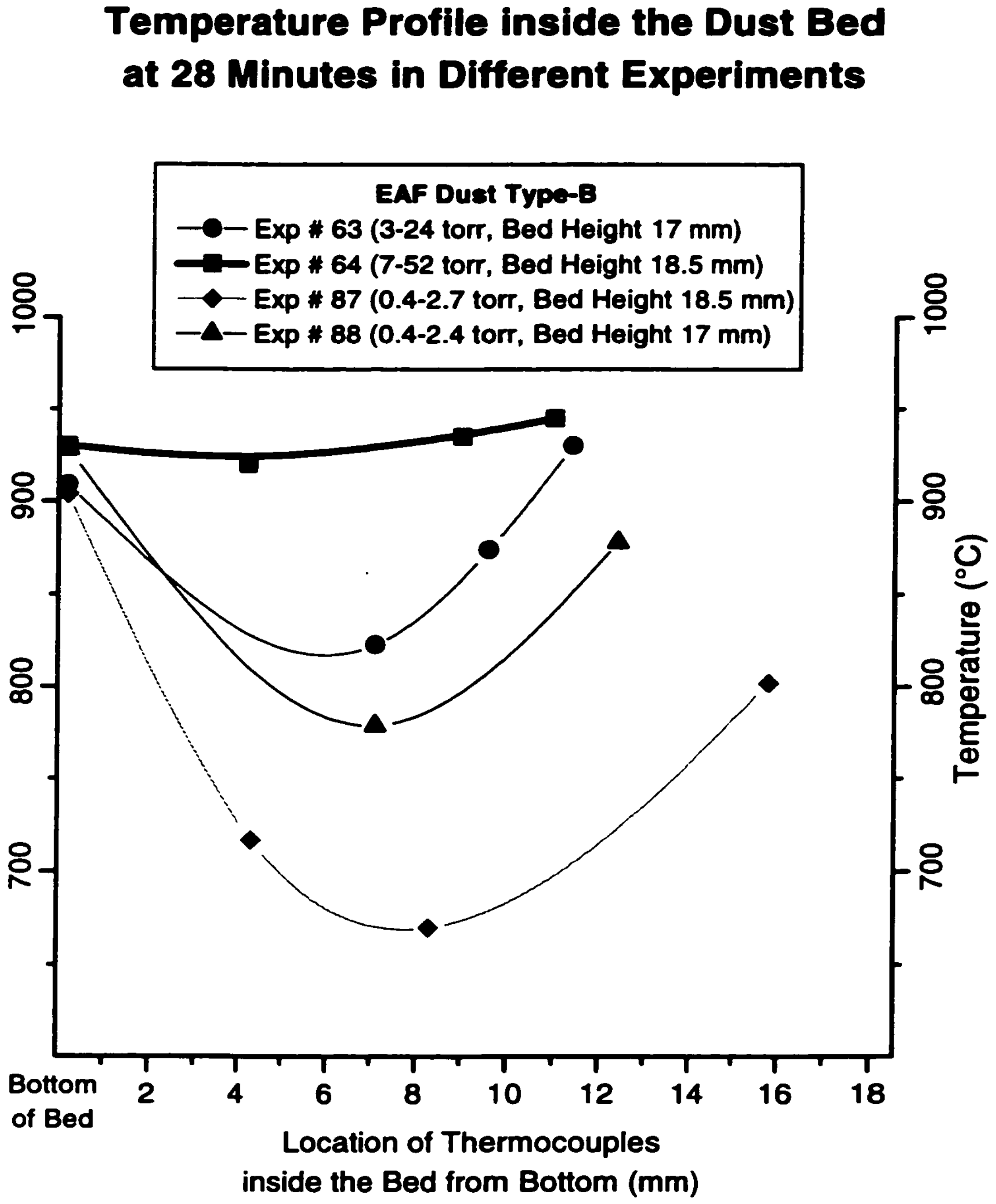

Figure 5.17: A comparison of temperature profile inside dust bed after 28 minutes heating in different experiments.

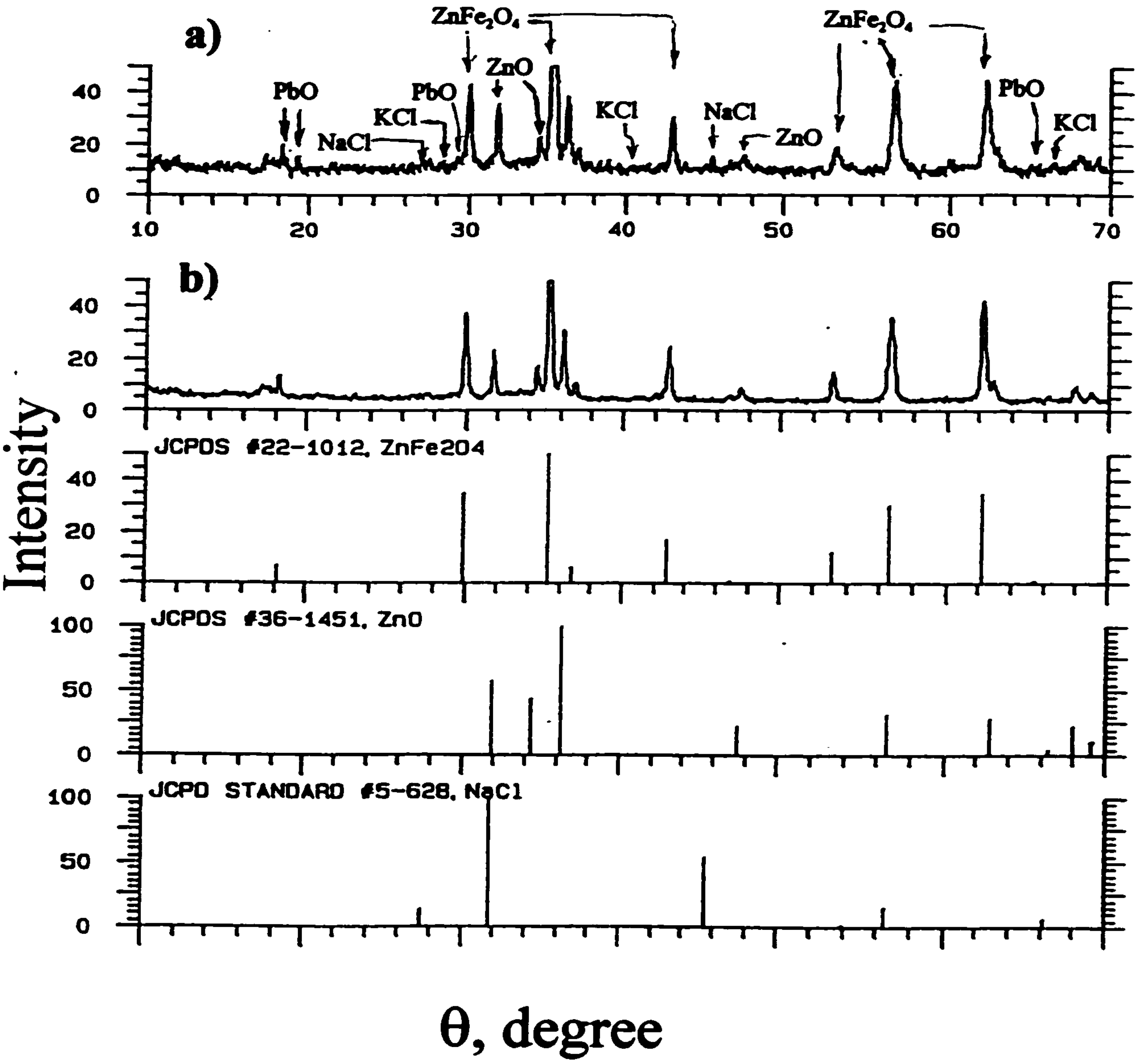

Figure 5.18: X-ray diffraction patterns of EAF dust type-A a) before and b) after 7 minutes treatment at 1100°C in rotary reaction chamber.

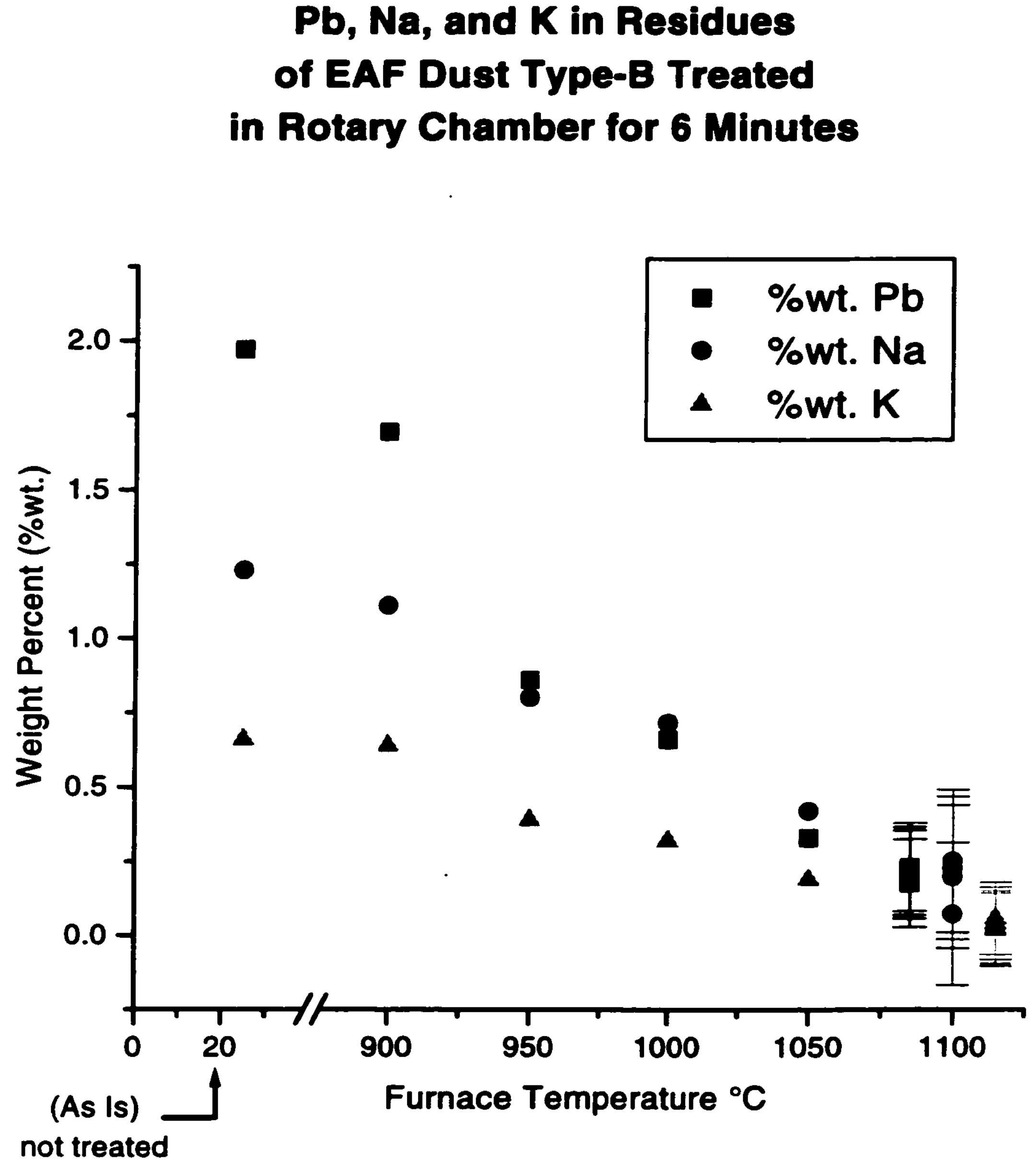

Figure 5.19: Effect of temperature on removal of volatile species. (Note: Pb and K data at 1100°C are shown at slightly different temperature for clarity)

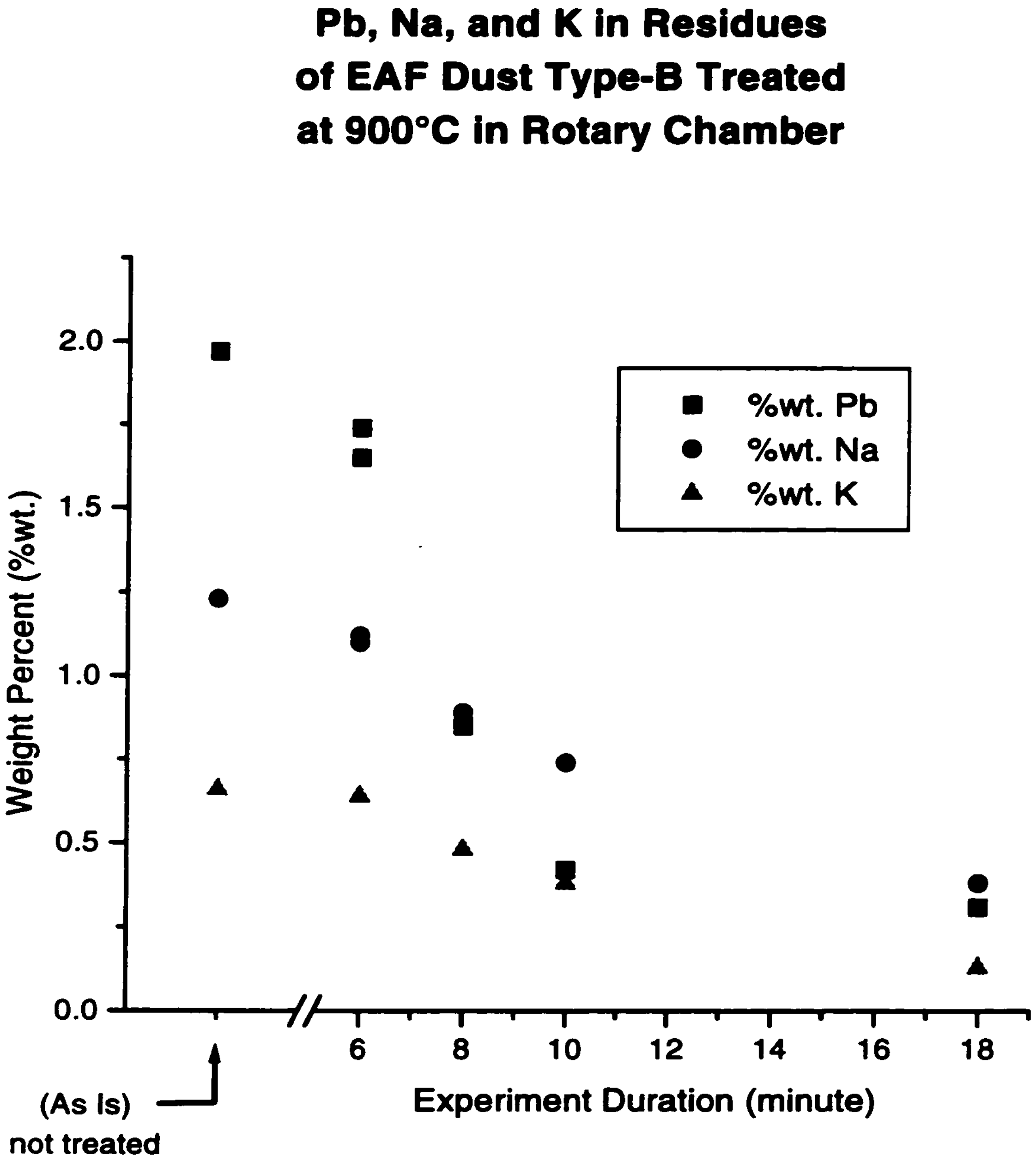

Figure 5.20: Effect of time on removal of volatile species at 900°C.

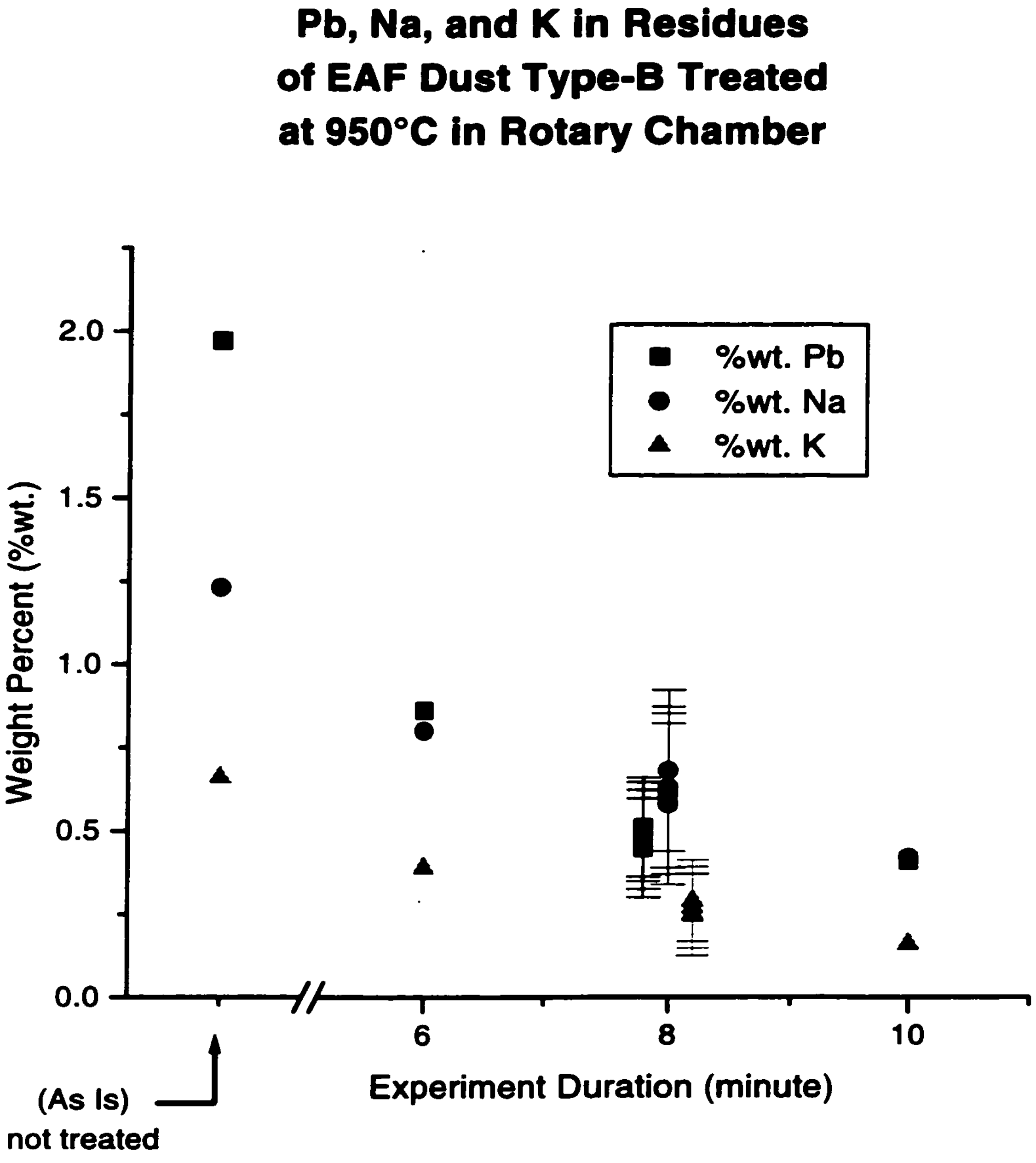

Figure 5.21: Effect of time on removal of volatile species at 950°C. (Note: Pb and K data at 8 minute are shown at slightly different time for clarity)

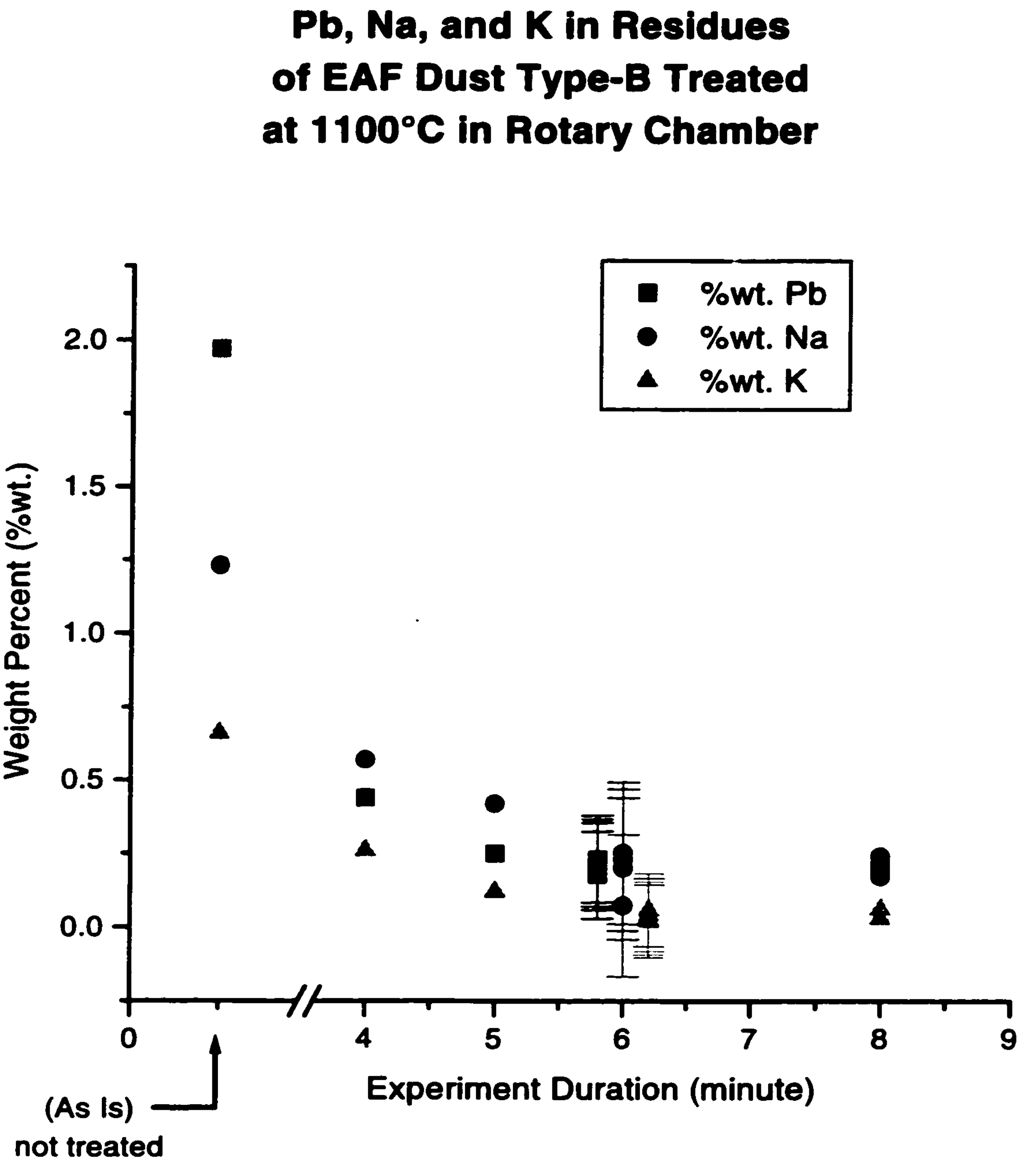

Figure 5.22: Effect of time on removal of volatile species at 1100°C. (Note: Pb and K data at 6 minute are shown at slightly different time for clarity)

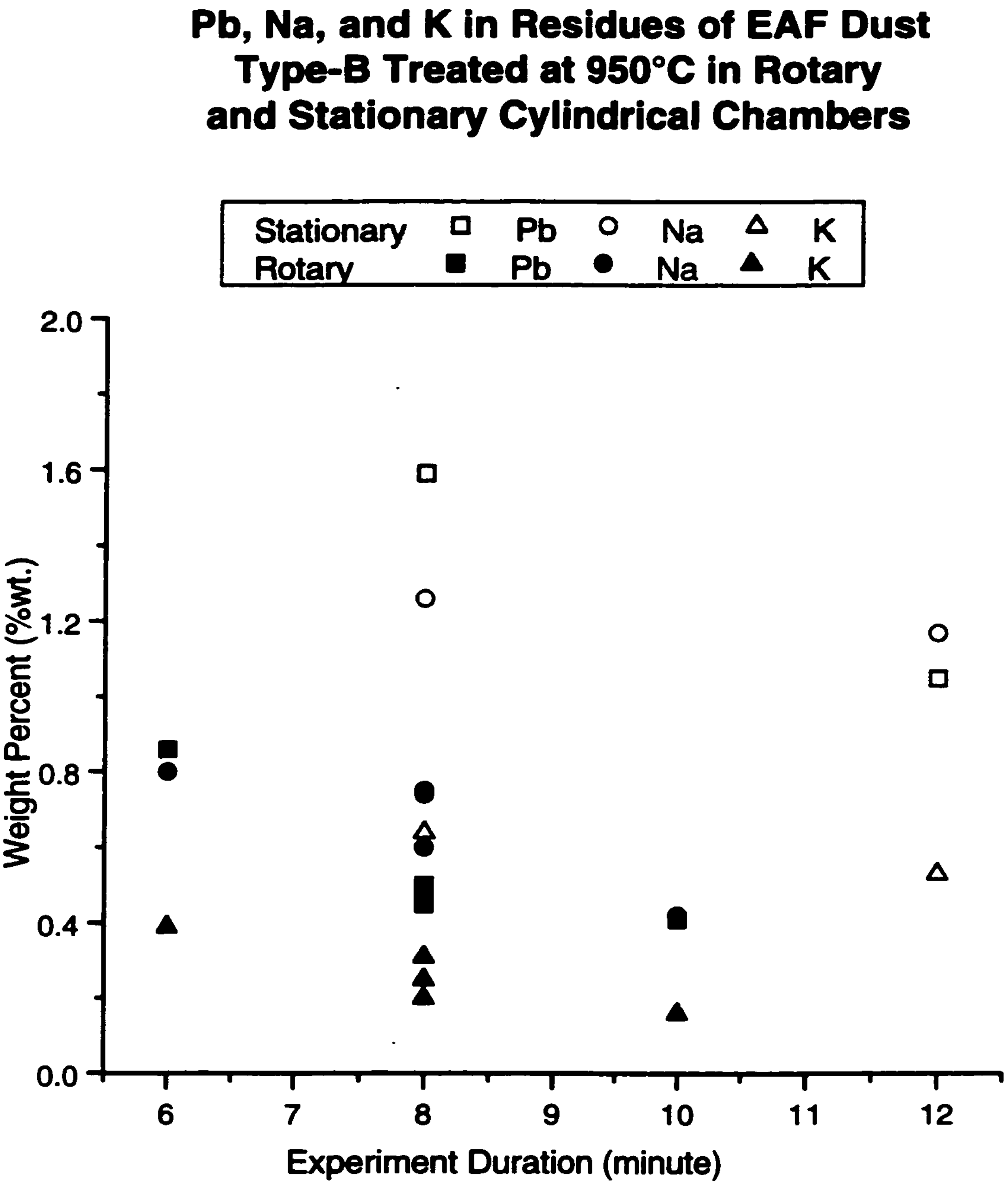

Figure 5.23: Comparison of the results of treatment at 950°*C* in stationary reaction chamber with those of rotary reaction chamber.

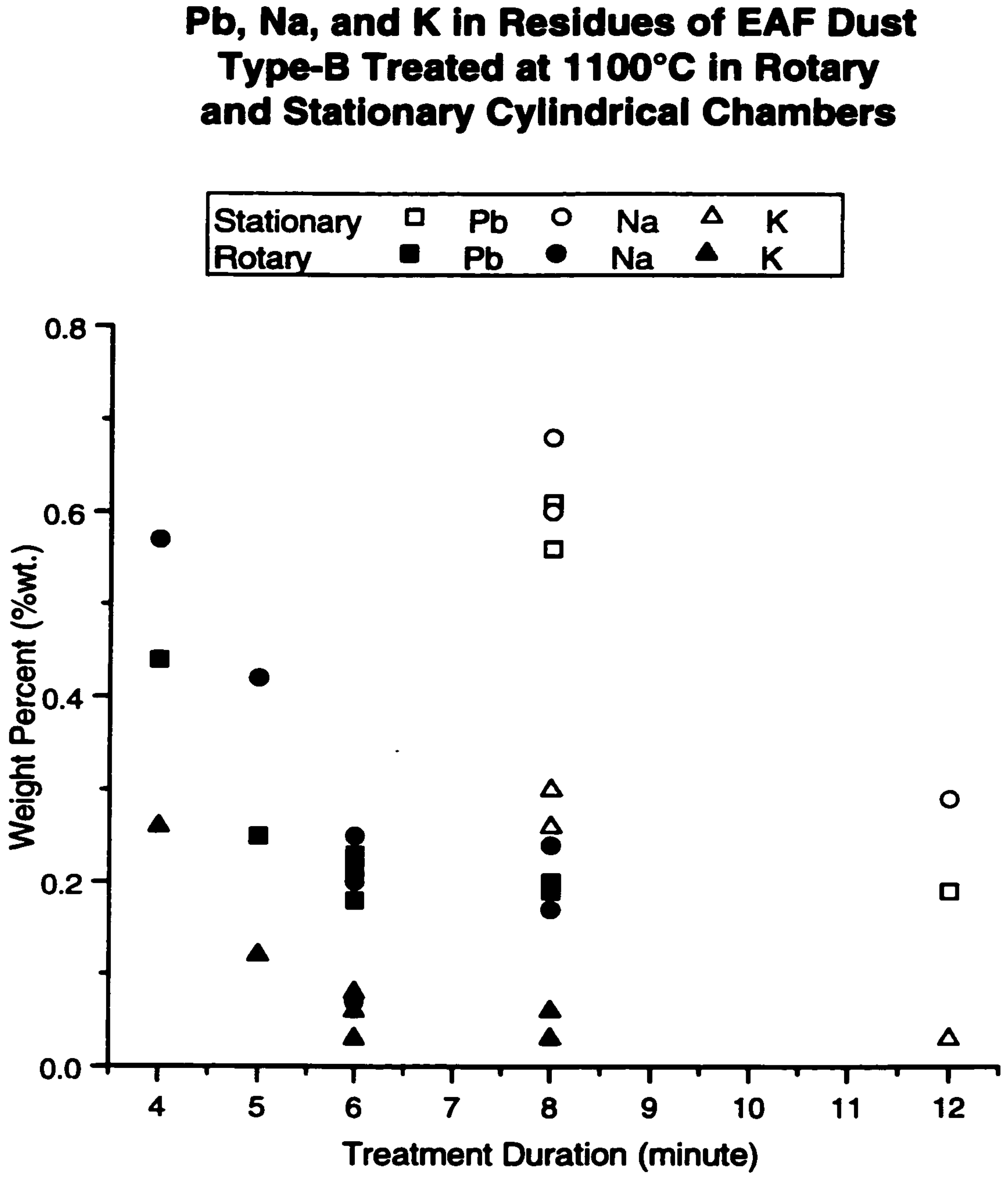

Figure 5.24: Comparison of the results of treatment at 1100°C in stationary reaction chamber with those of rotary reaction chamber.

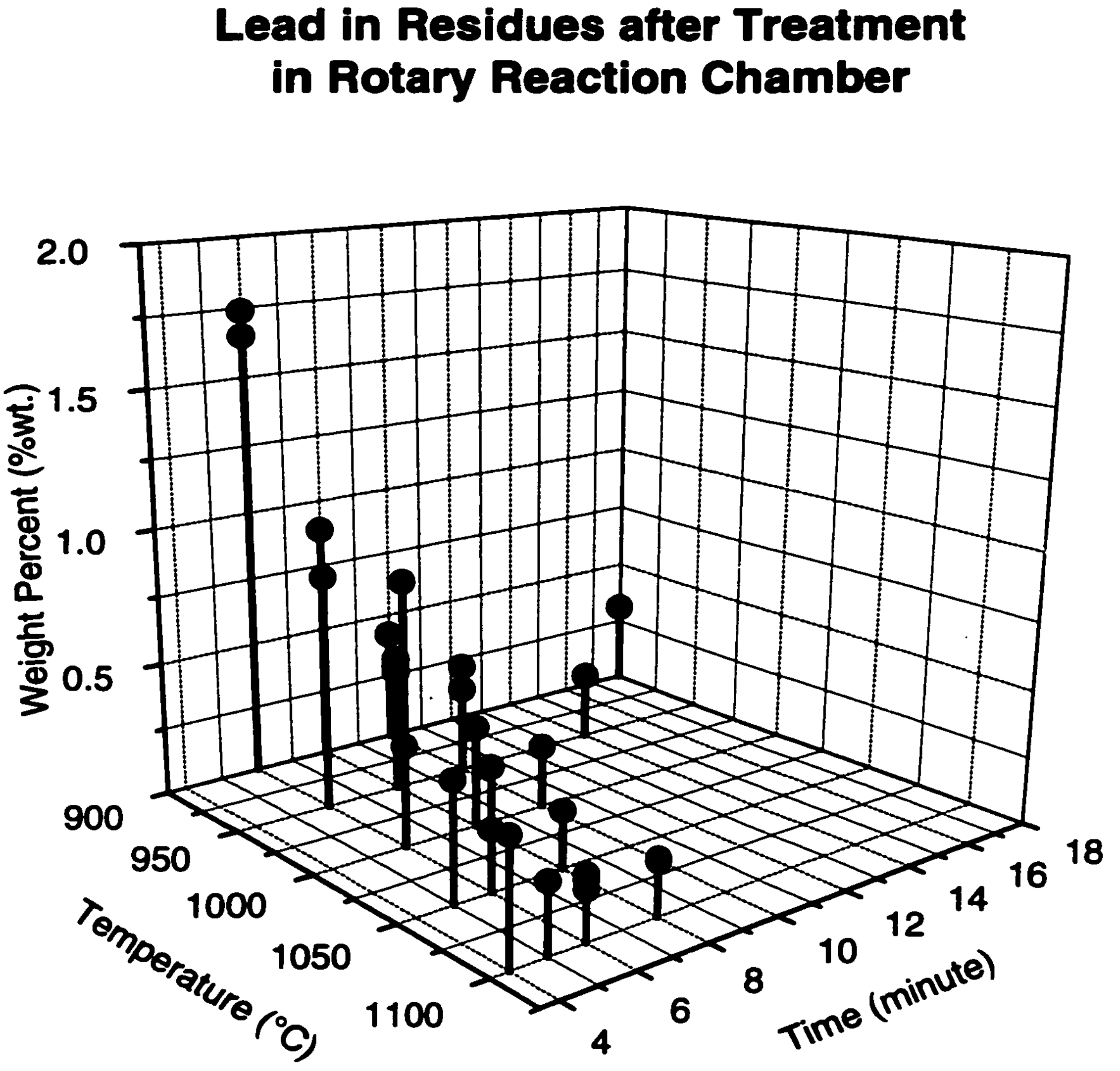

Figure 5.25: Lead content in residues after treatment of EAF dust type-B in rotary reaction chamber.

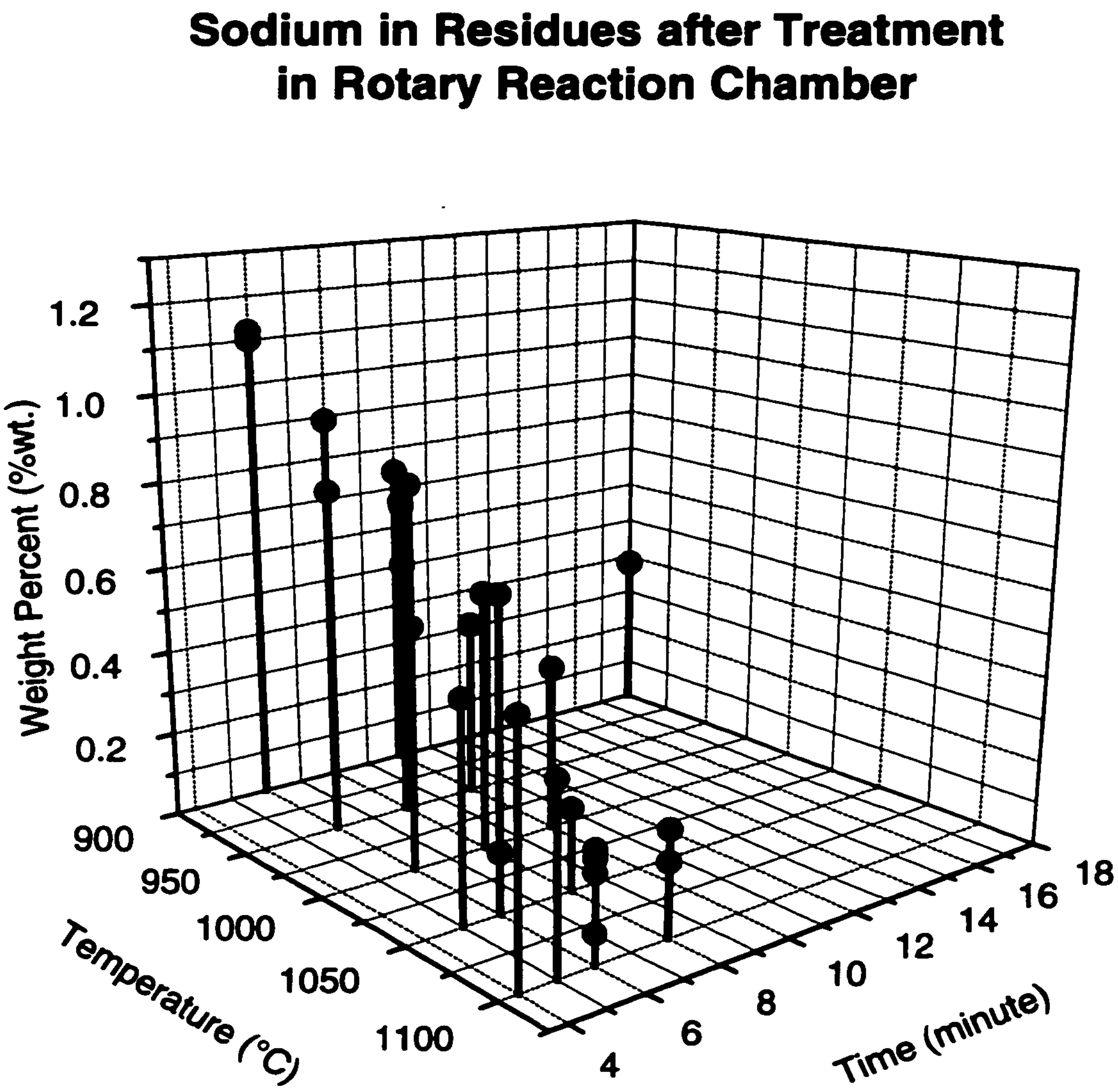

Figure 5.26: Sodium content in residues after treatment of EAF dust type-B in rotary reaction chamber.

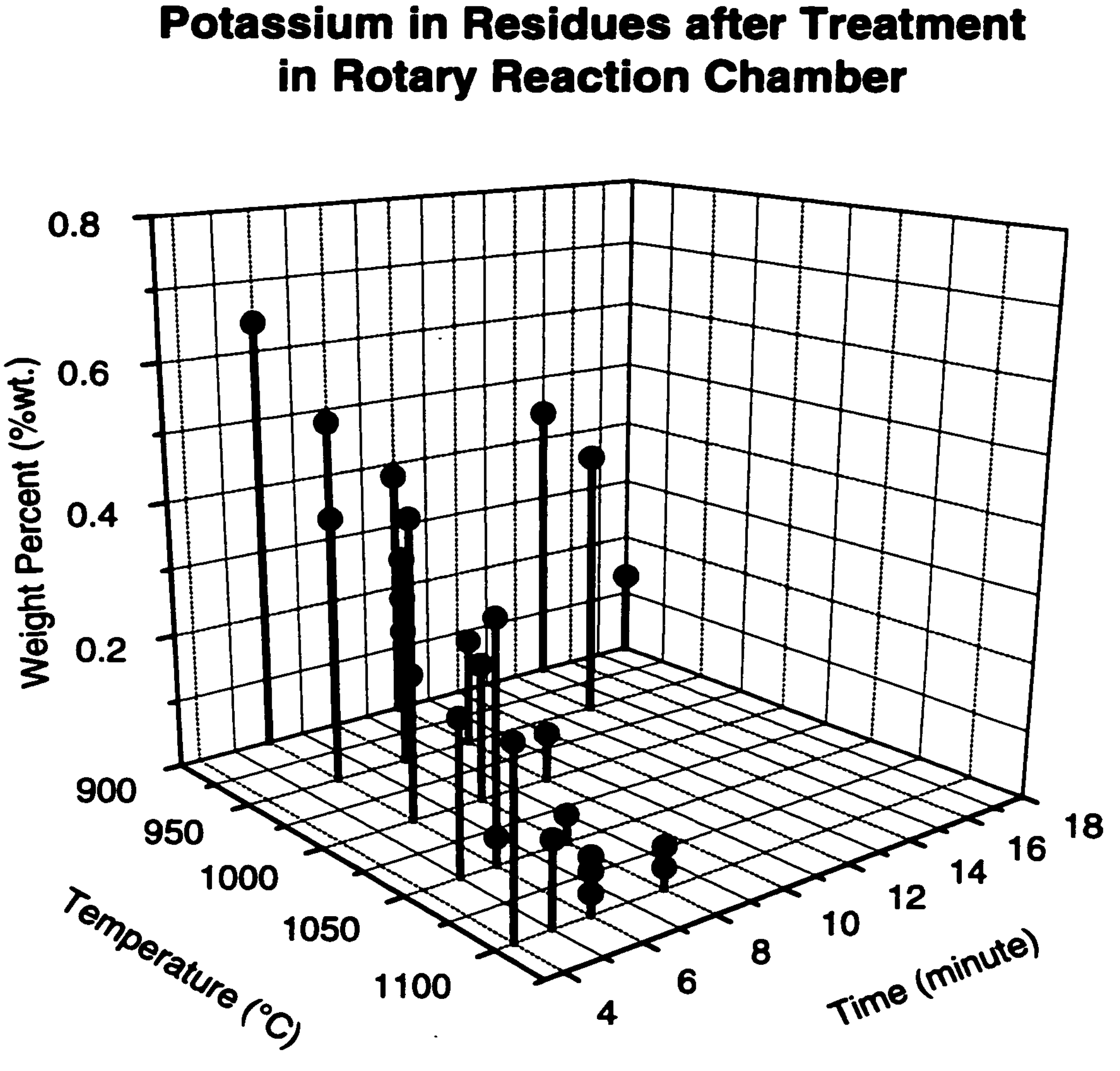

Figure 5.27: Potassium content in residues after treatment of EAF dust type-B in rotary reaction chamber.

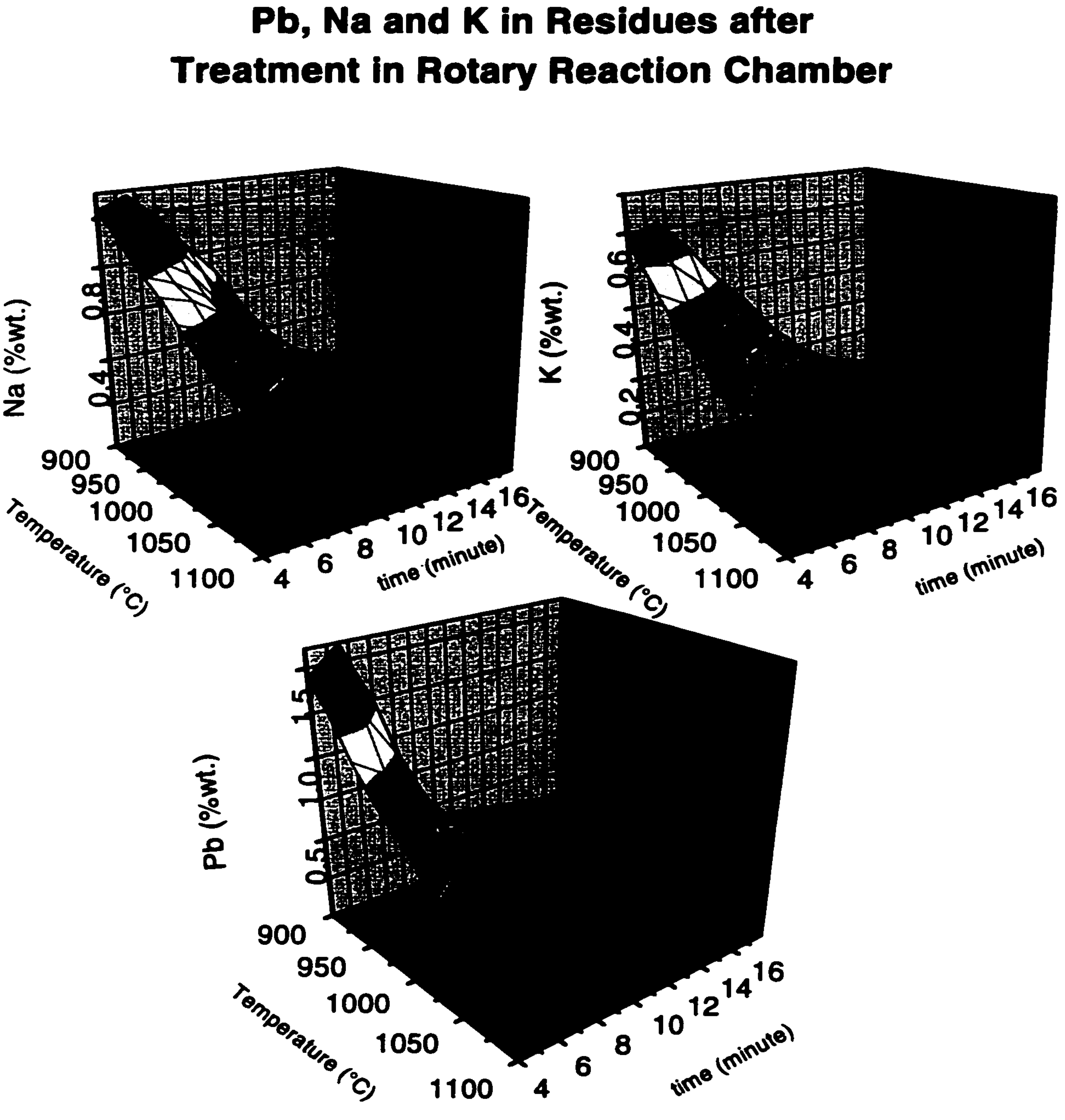

Figure 5.28: Surface diagrams representing the effect of time and temperature on composition of residues after treatment of EAF dust type-B in rotary reaction chamber.

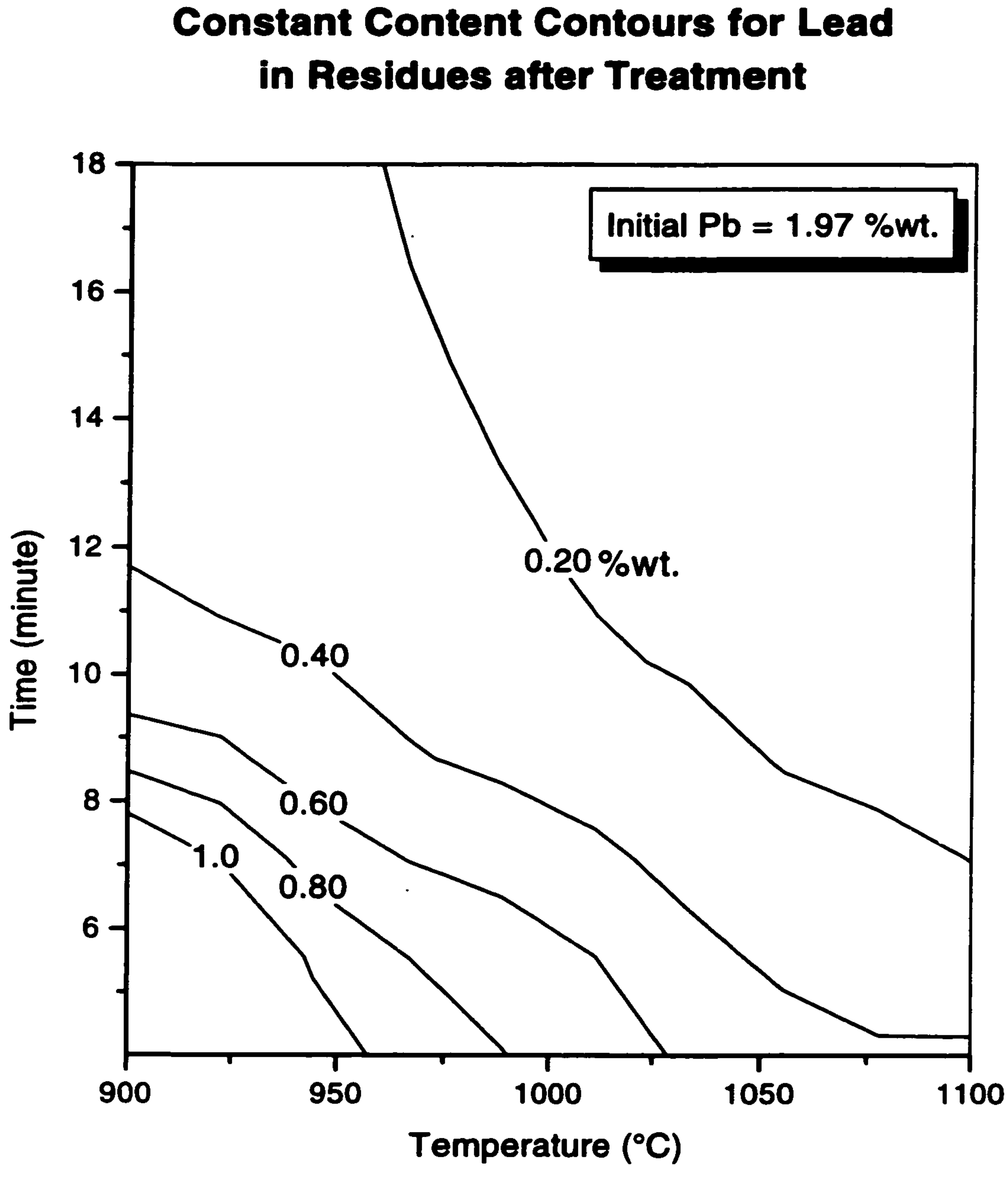

Figure 5.29: Constant content contour diagram representing the lead content in residues after treatment of EAF dust type-B in rotary reaction chamber.

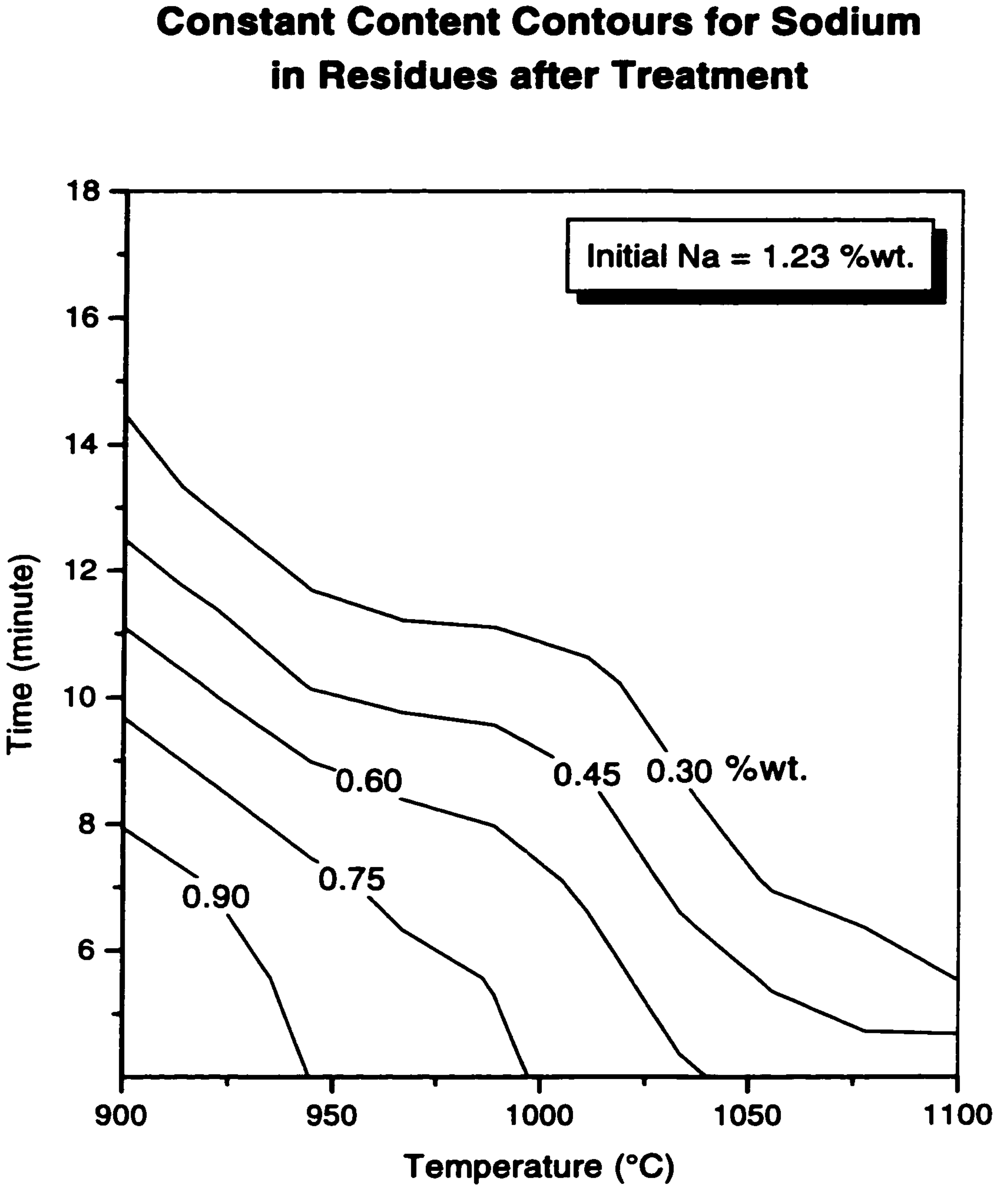

Figure 5.30: Constant content contour diagram representing the sodium content in residues after treatment of EAF dust type-B in rotary reaction chamber.

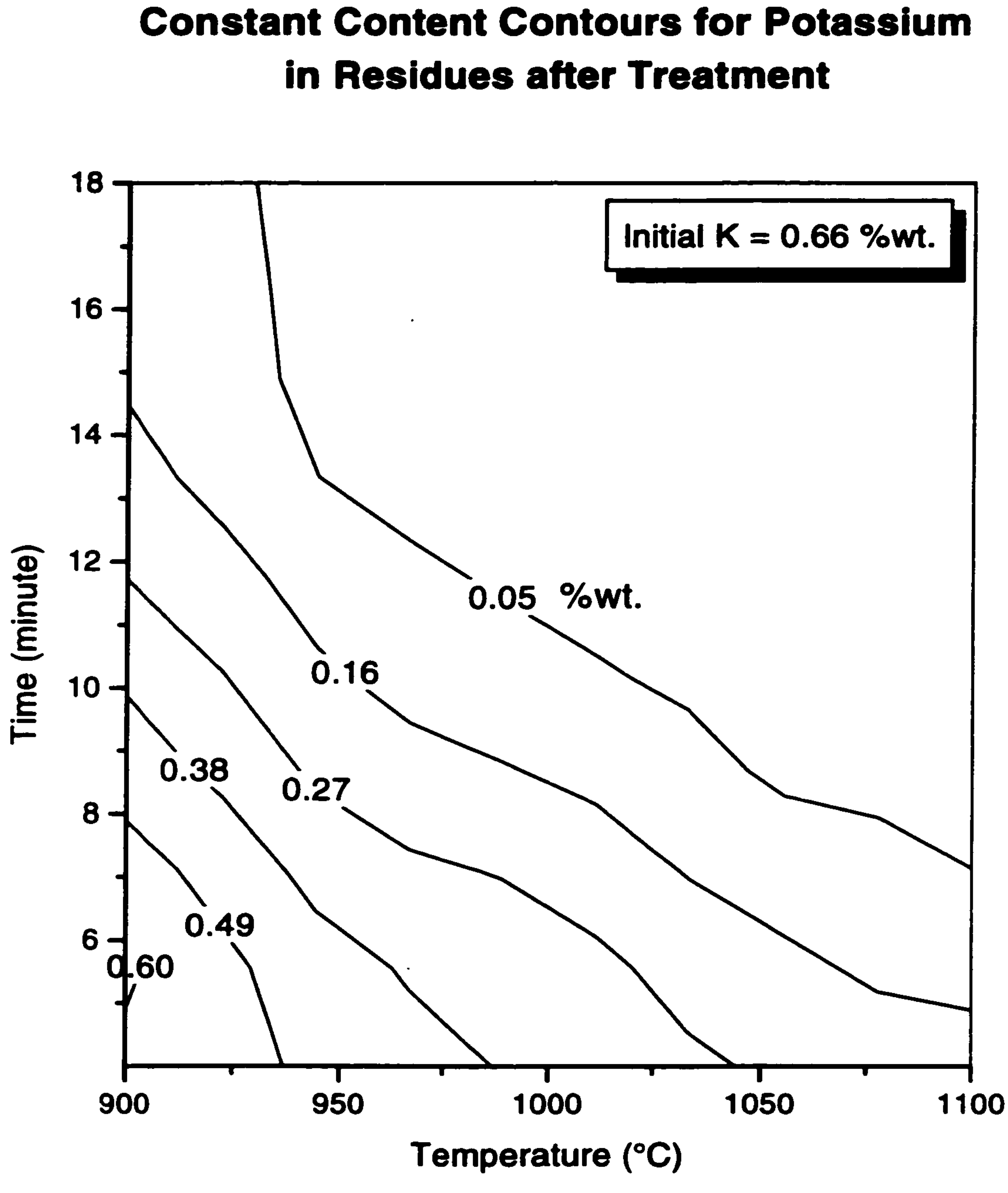

Figure 5.31: Constant content contour diagram representing the potassium content in residues after treatment of EAF dust type-B in rotary reaction chamber.

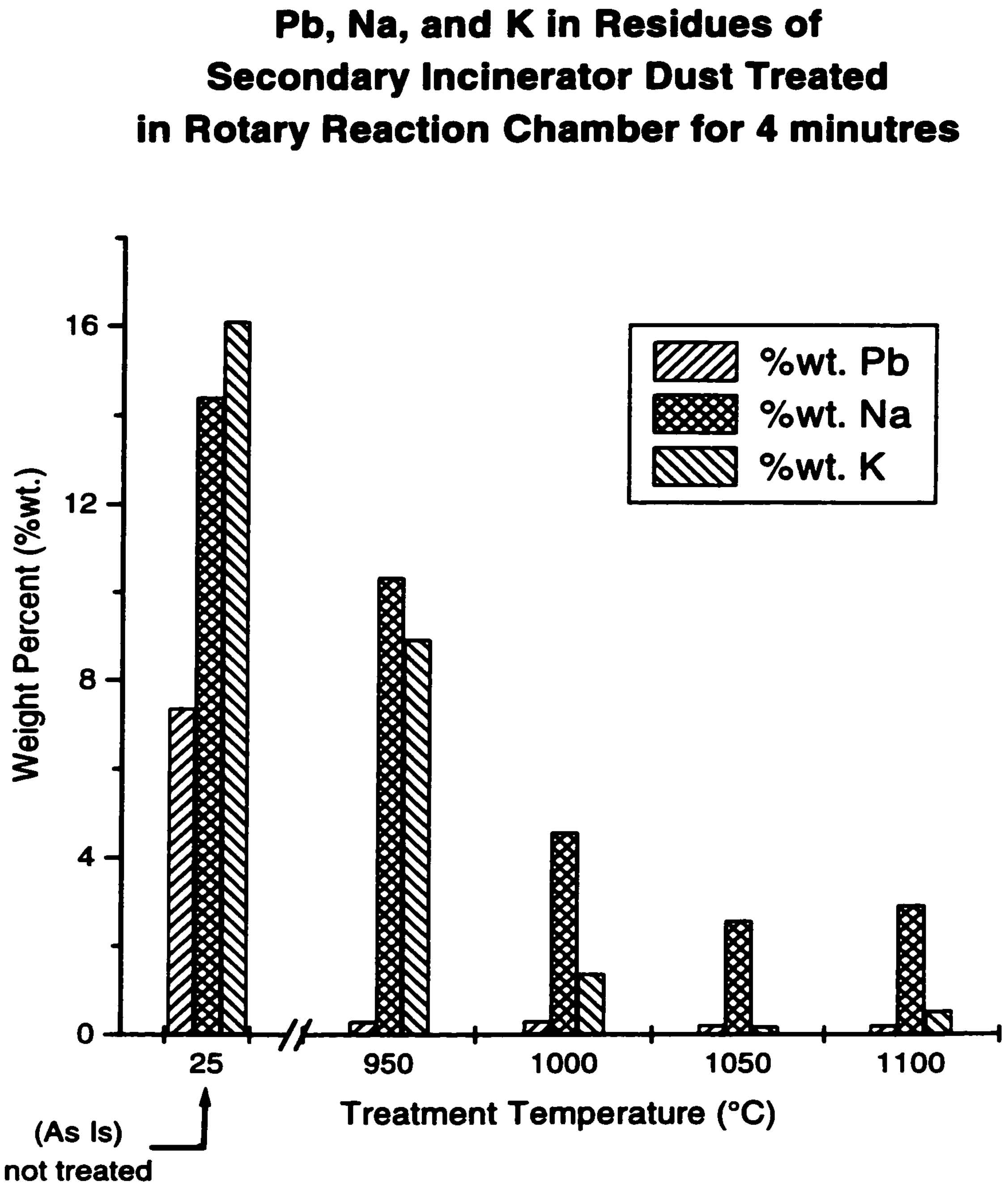

Figure 5.32: Effect of temperature on removal of volatile species from secondary incinerator dust.

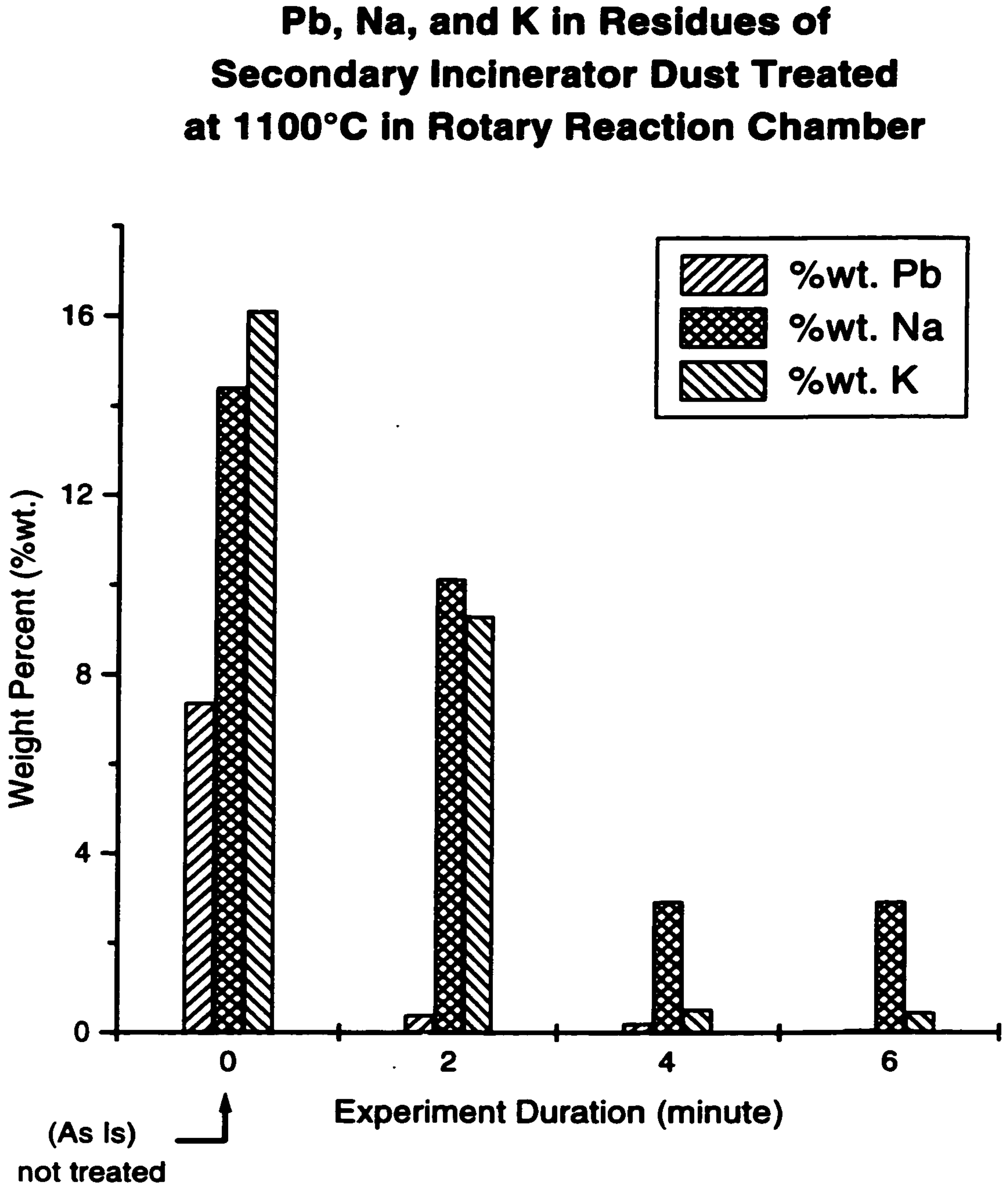

Figure 5.33: Effect of time on removal of volatile species from secondary incinerator dust.

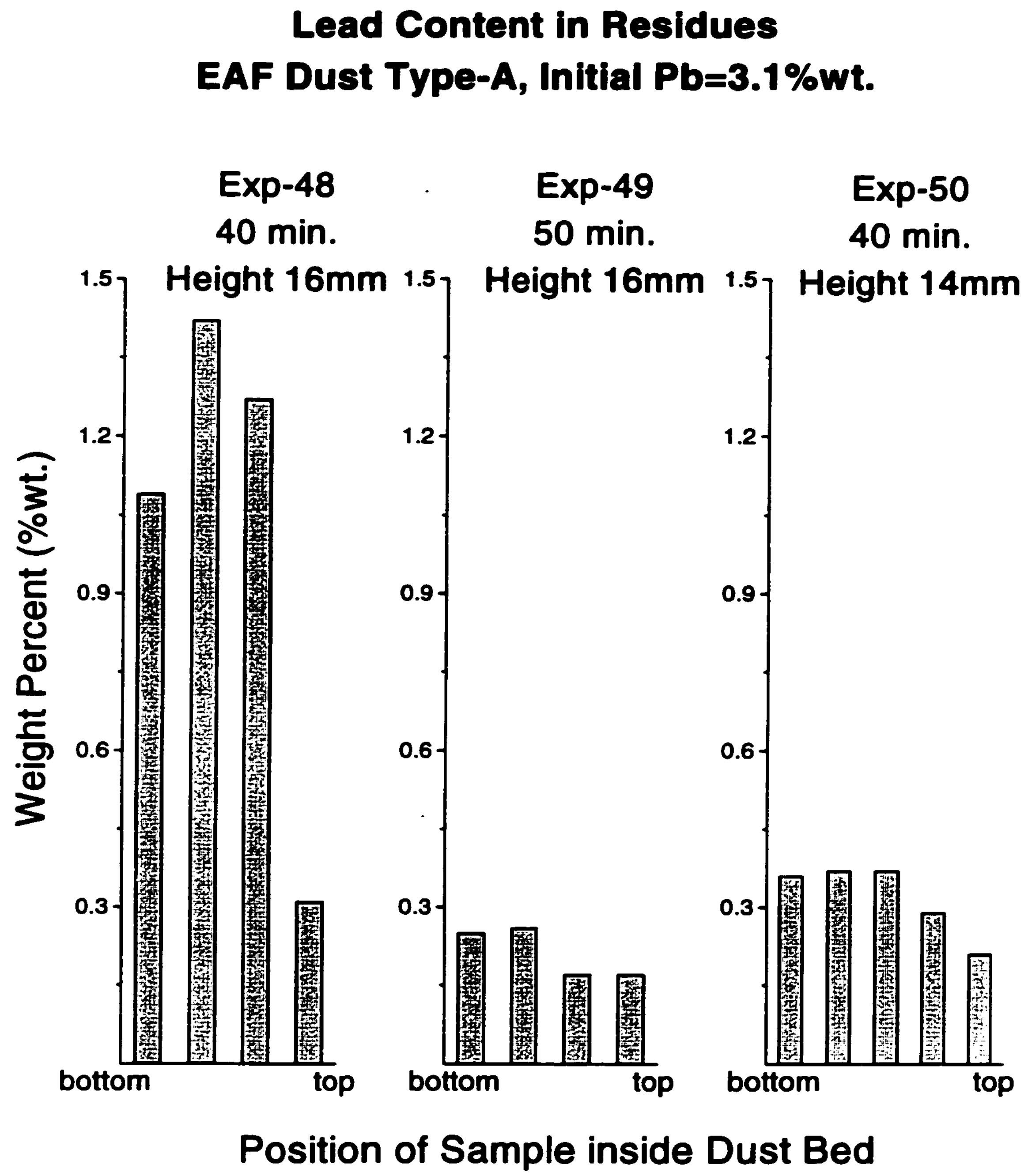

Figure 5.34: Lead content in residues taken from different heights of the dust bed, EAF dust type-A.

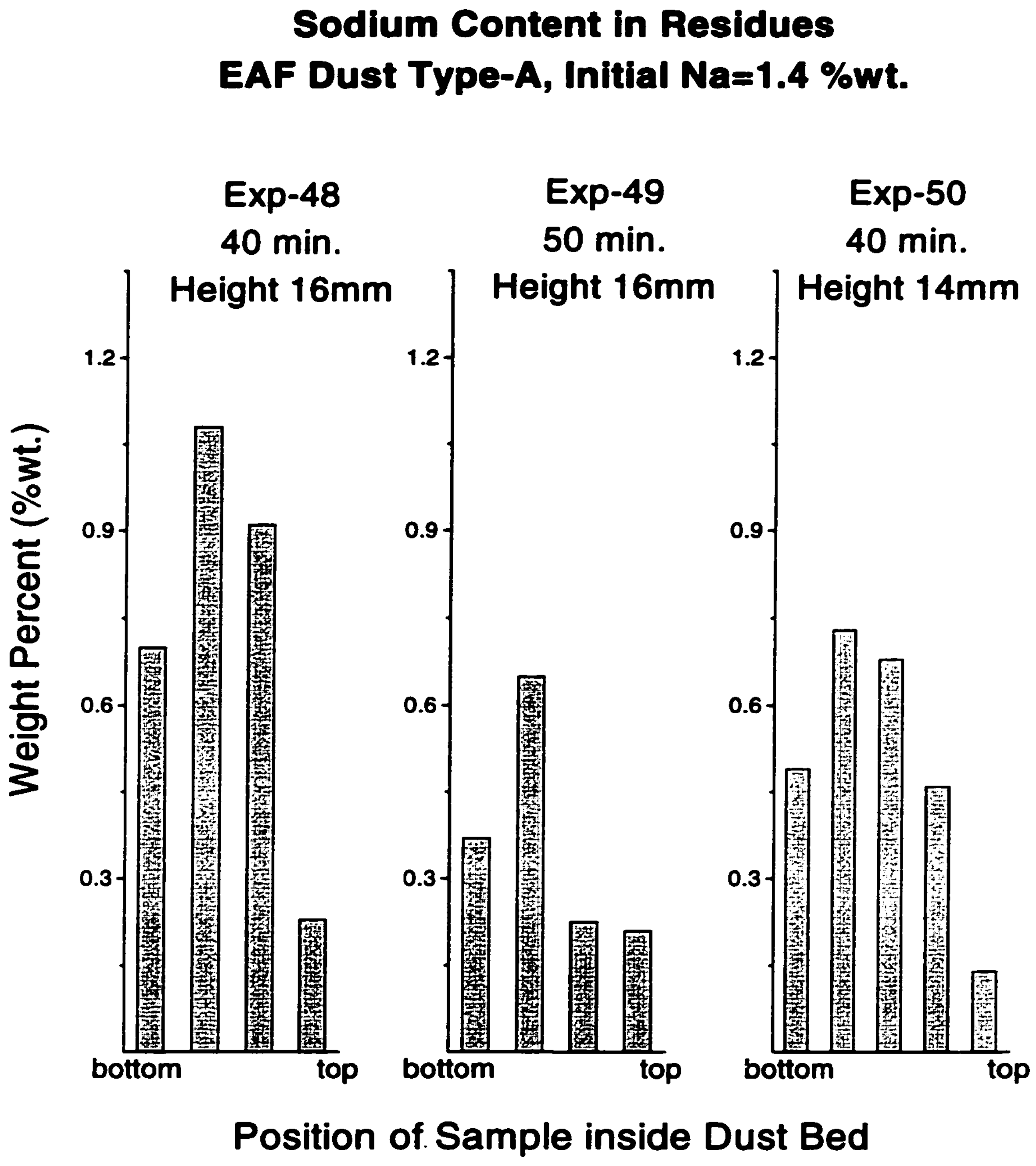

Figure 5.35: Sodium content in residues taken from different heights of the dust bed, EAF dust type-A.

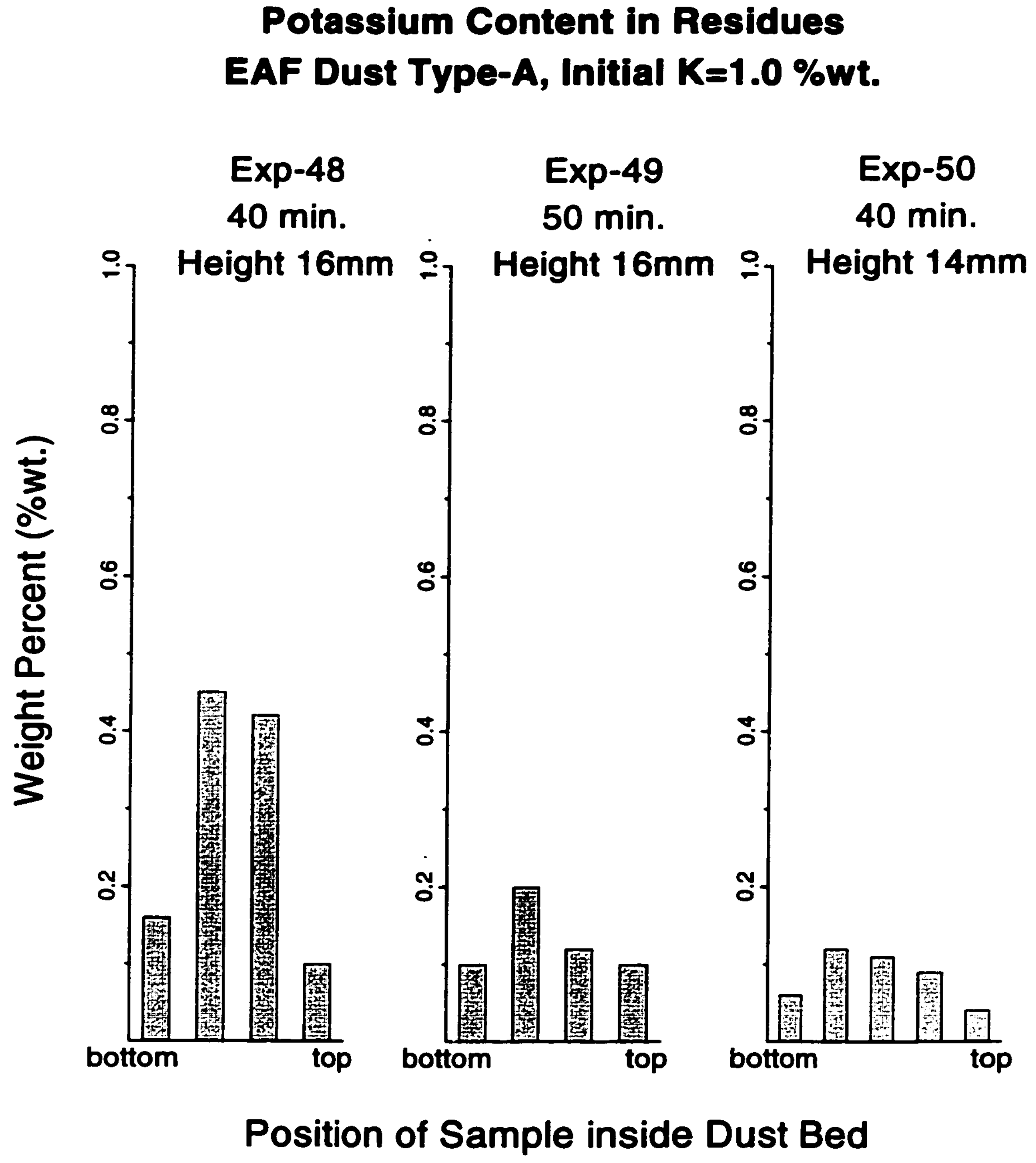

Figure 5.36: Potassium content in residues taken from different heights of the dust bed, EAF dust type-A.

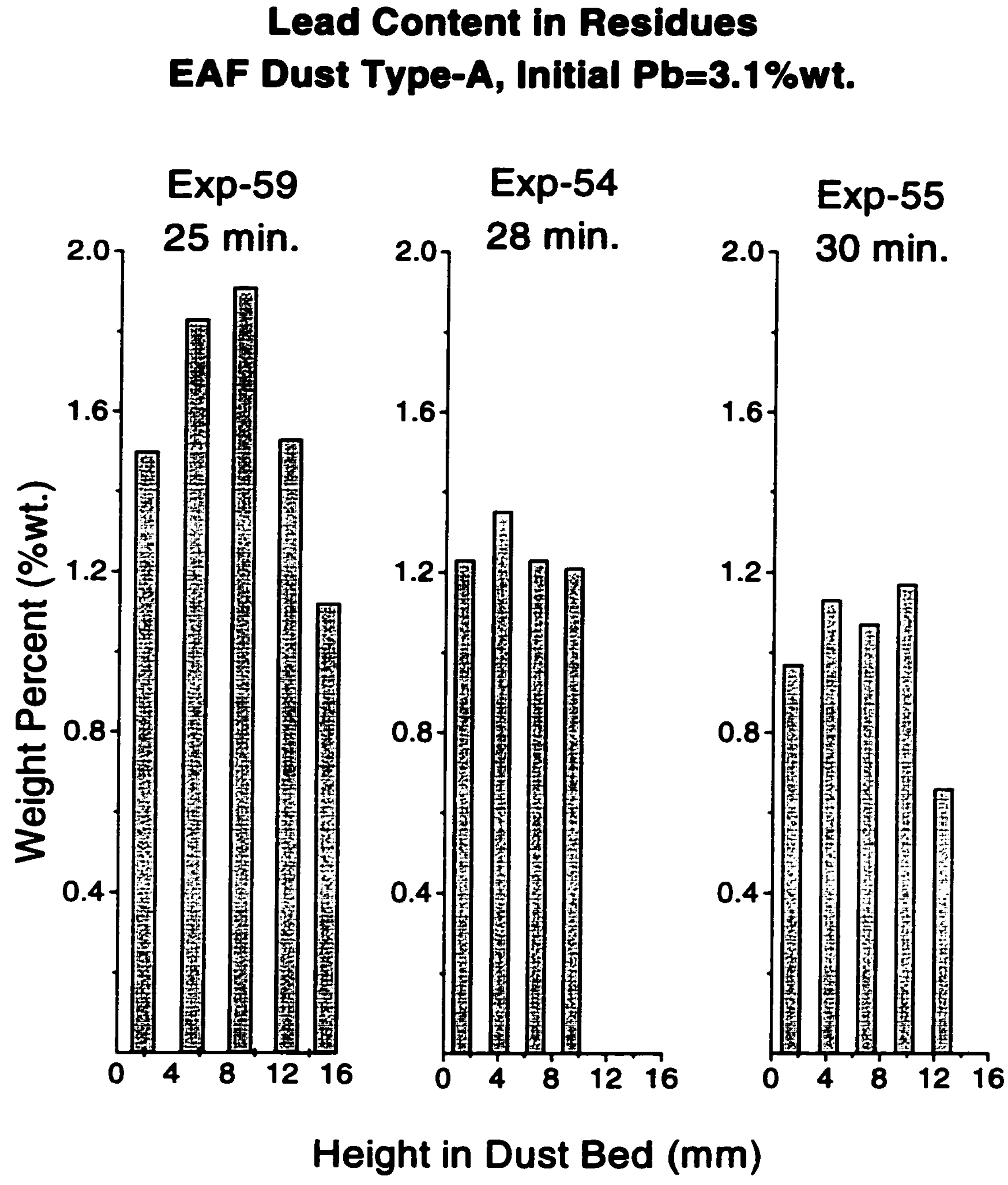

Figure 5.37: Lead content in residues taken from different heights of the dust bed, EAF dust type-A.

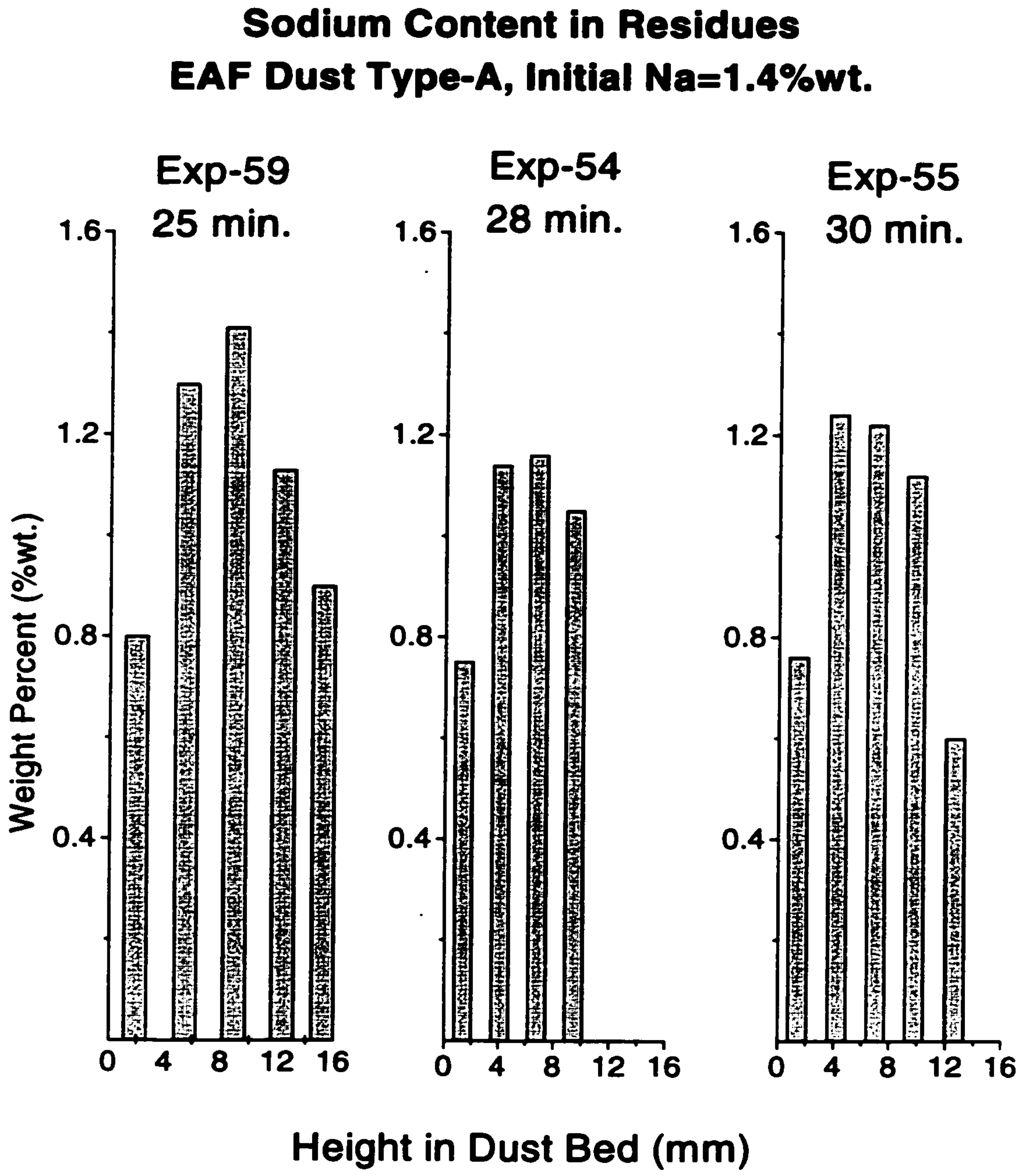

Figure 5.38: Sodium content in residues taken from different heights of the dust bed, EAF dust type-A.

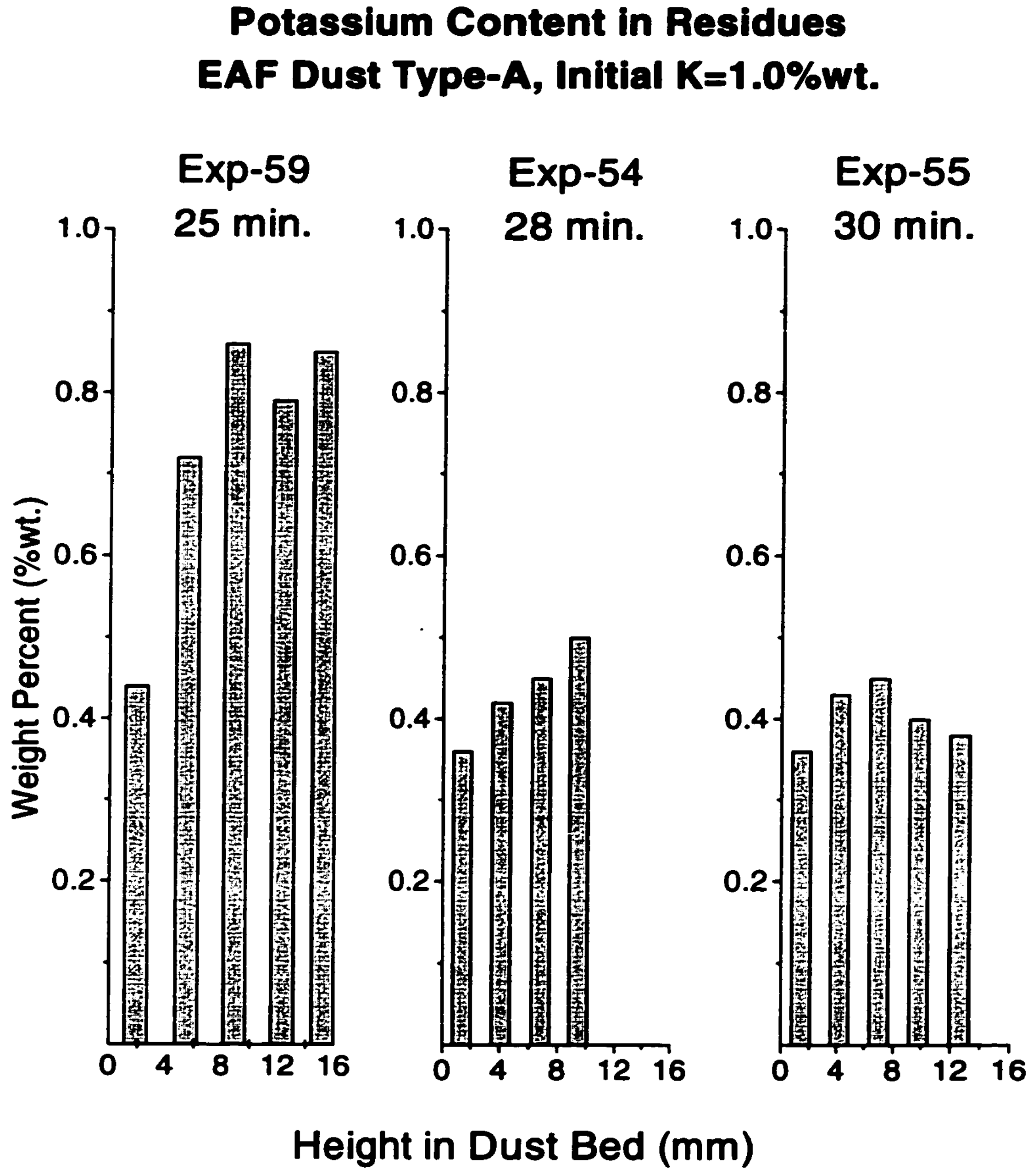

Figure 5.39: Potassium content in residues taken from different heights of the dust bed, EAF dust type-A.

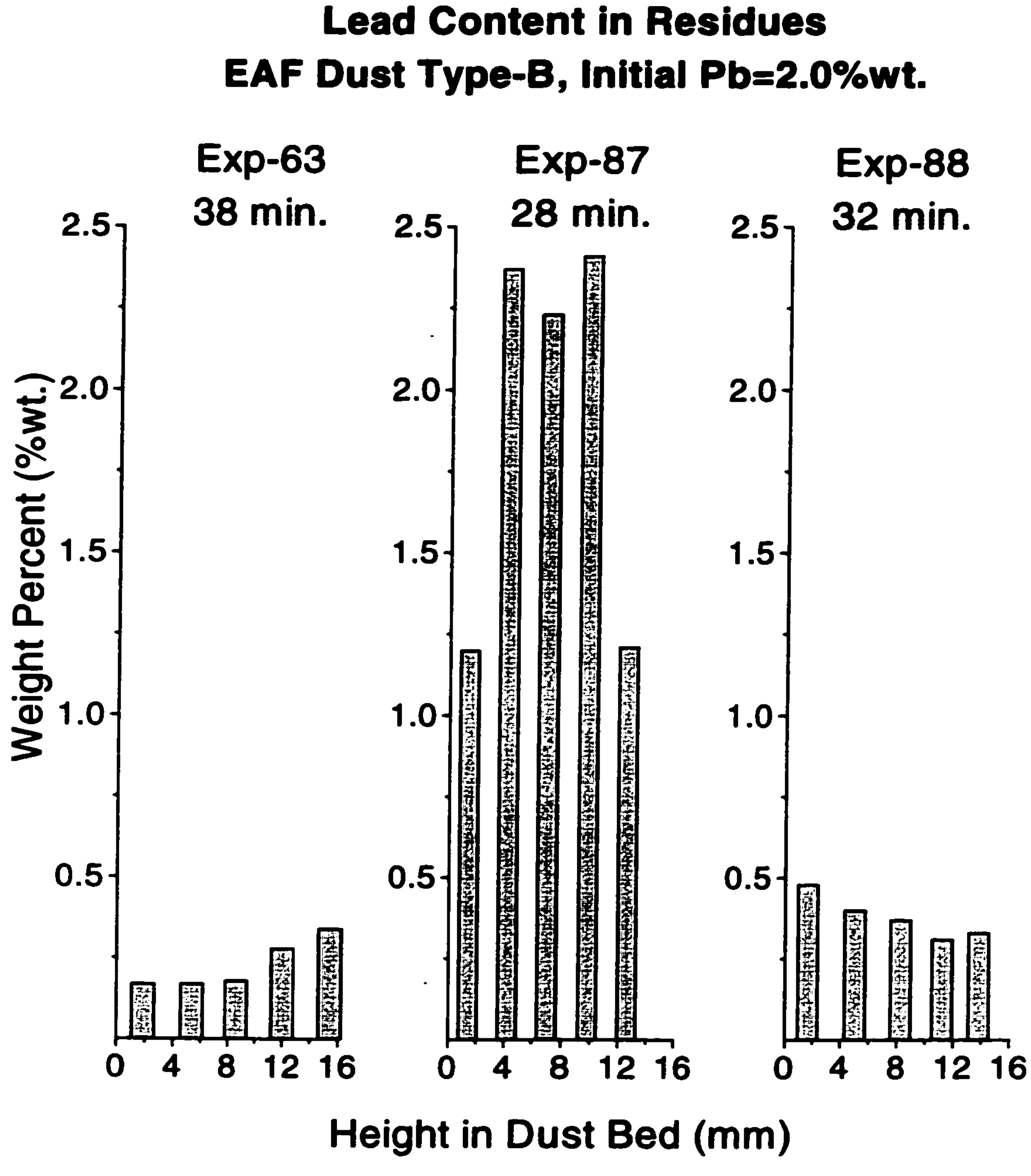

Figure 5.40: Lead content in residues taken from different heights of the dust bed, EAF dust type-B.

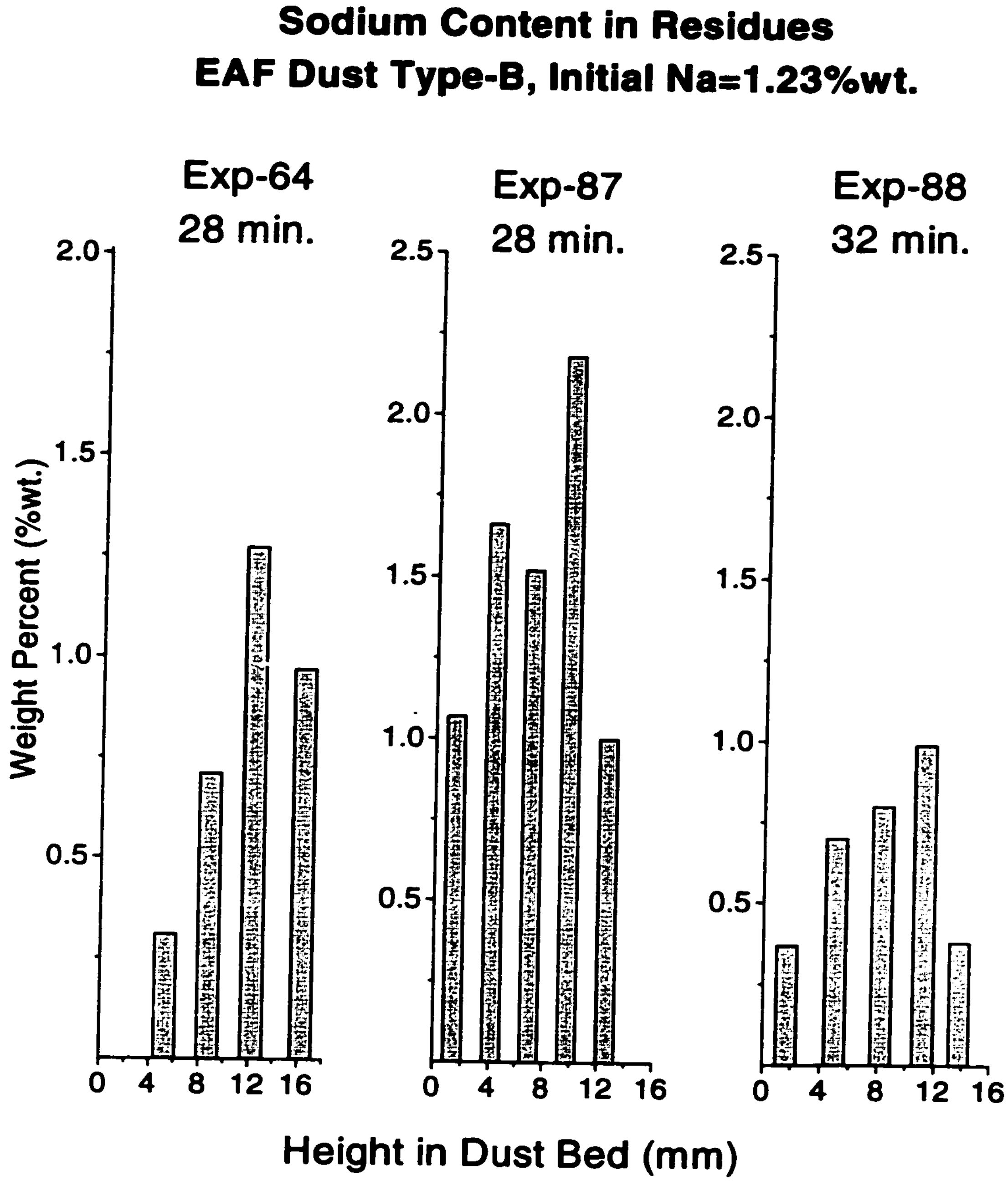

Figure 5.41: Sodium content in residues taken from different heights of the dust bed, EAF dust type-B.

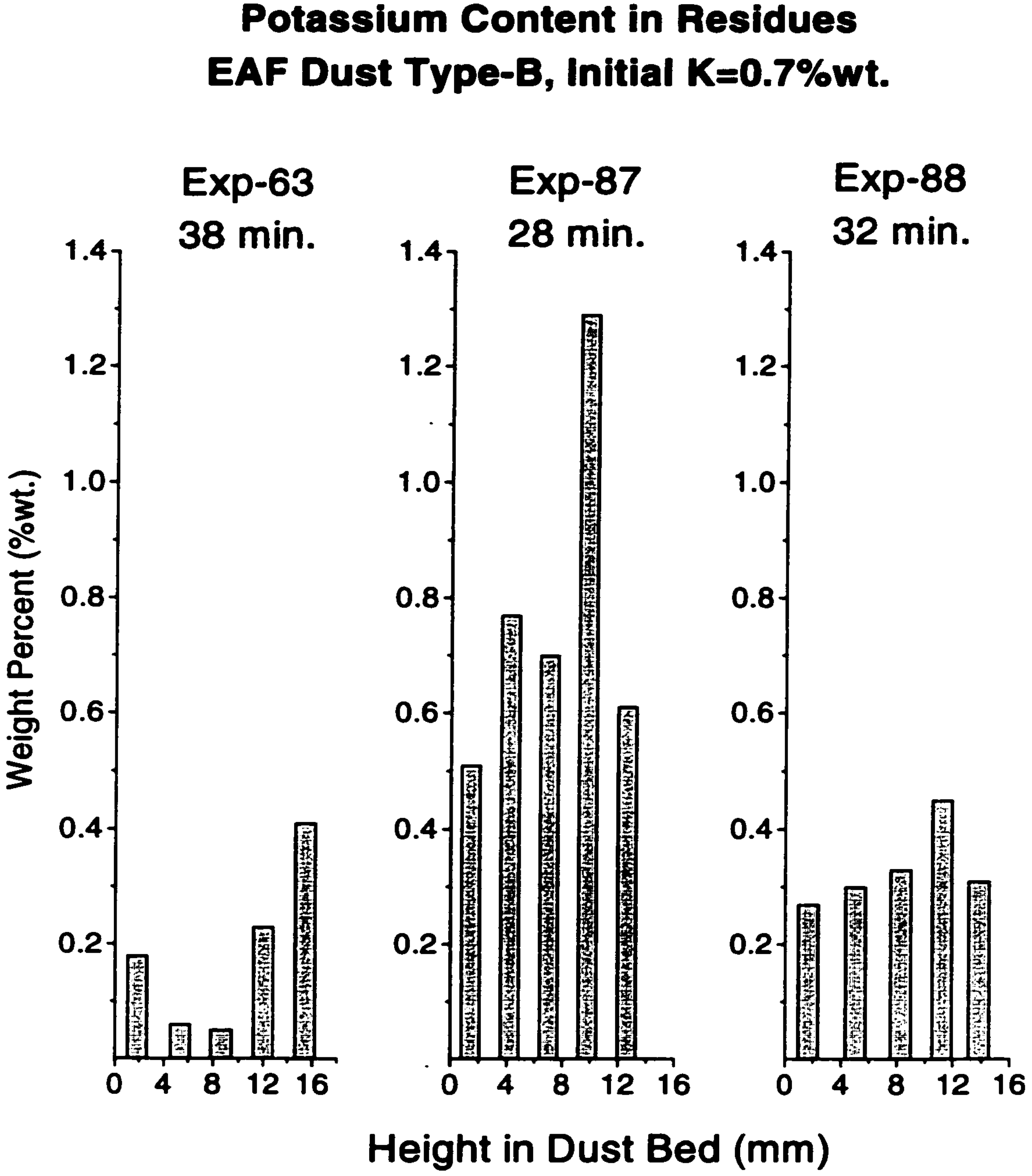

Figure 5.42: Potassium content in residues taken from different heights of the dust bed, EAF dust type-B.

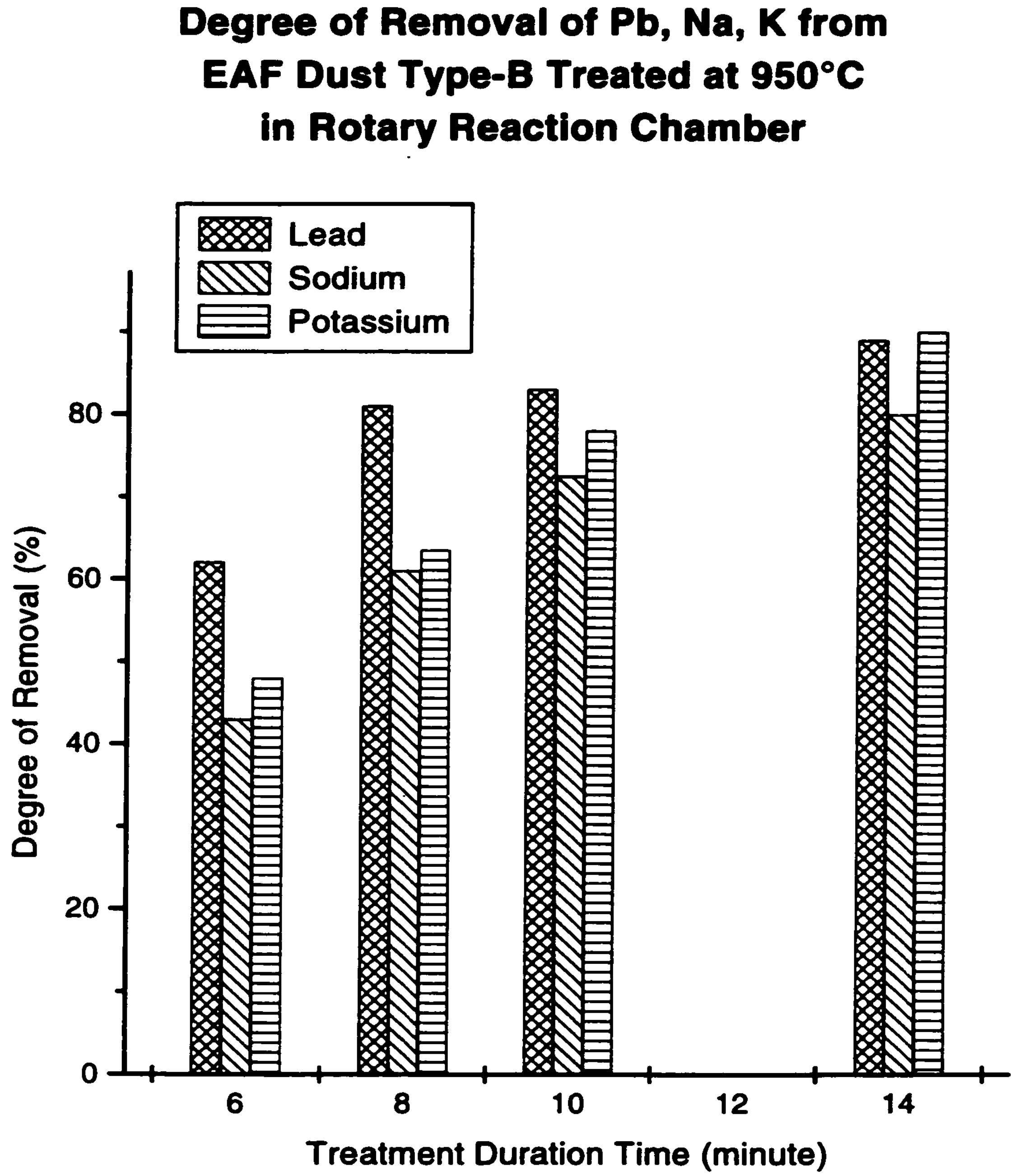

Figure 5.43: Degree of removal of volatile species from EAF dust type-B treated in rotary reaction chamber at 950°C.

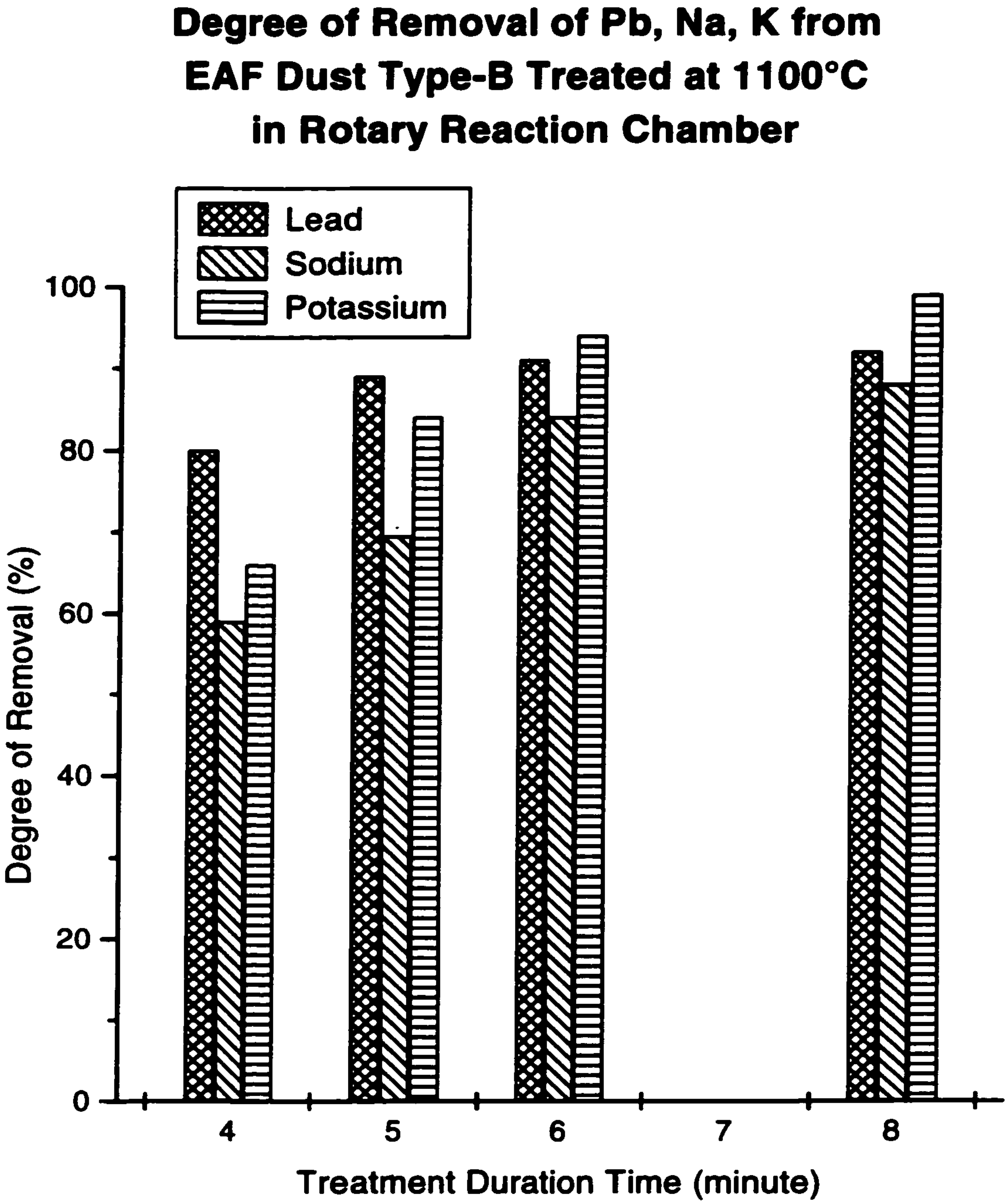

Figure 5.44: Degree of removal of volatile species from EAF dust type-B treated in rotary reaction chamber at 1100°C.

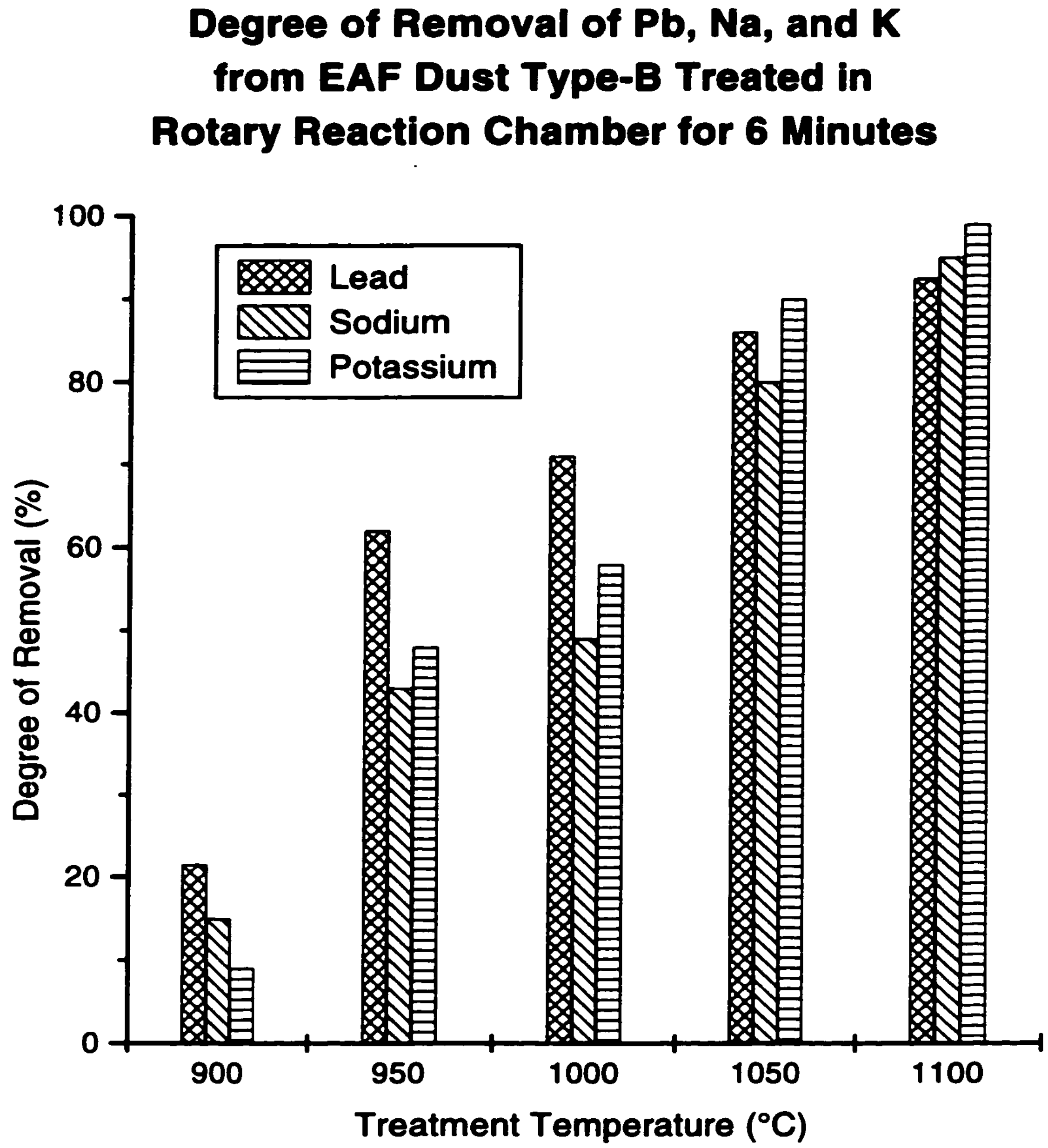

Figure 5.45: Degree of removal of volatile species from EAF dust type-B after 6 minutes of treatment in rotary reaction chamber at different temperatures.

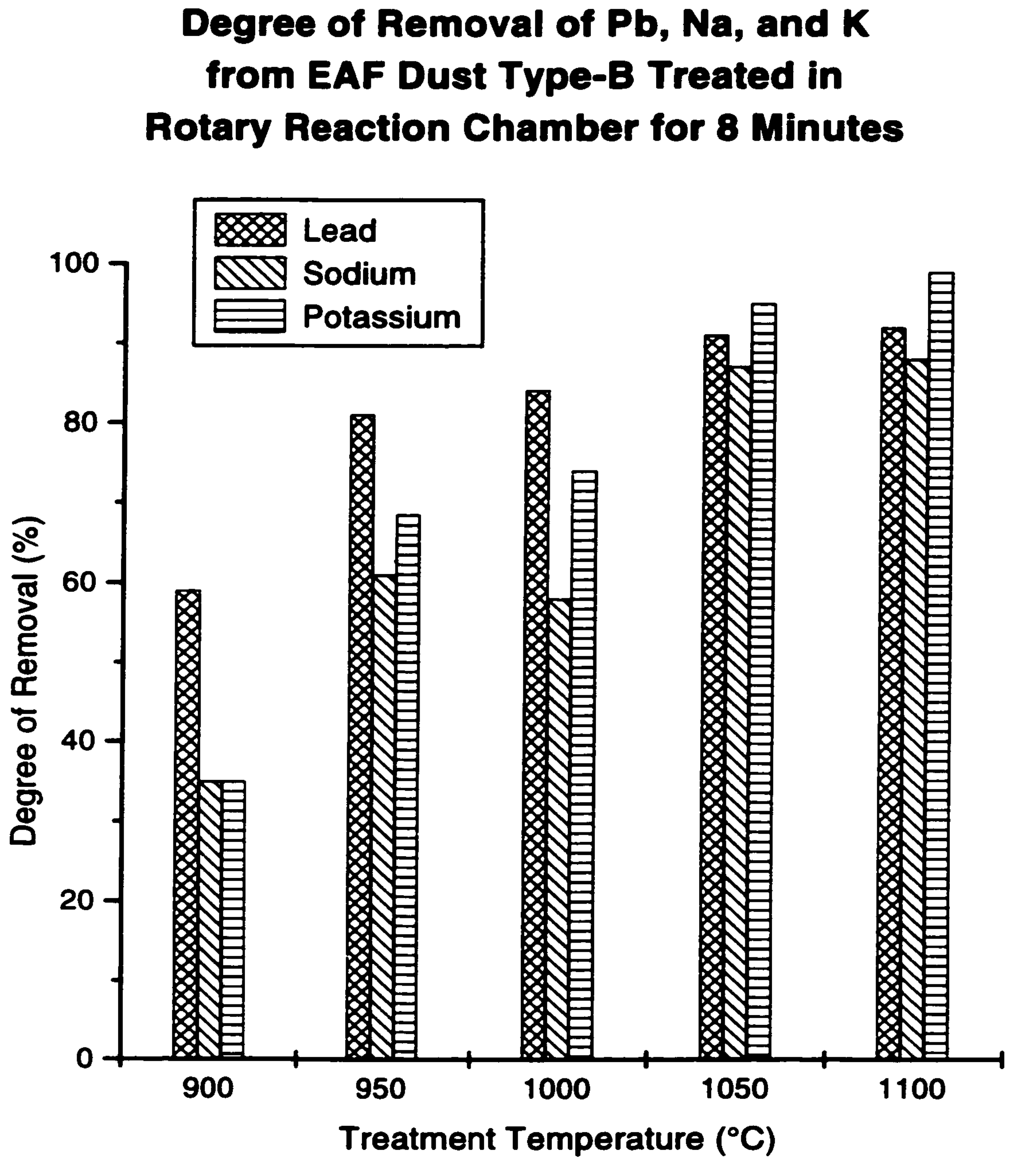

Figure 5.46: Degree of removal of volatile species from EAF dust type-B after 8 minutes of treatment in rotary reaction chamber at different temperatures.

Chapter 6

Mass and Heat Transfer

In this chapter the kinetics of mass and heat transfer in the system will be considered and possible rate controlling steps of the overall reaction will be discussed. Mass transfer in the system will be considered first and it will be shown that under the conditions investigated in the present work, mass transfer is relatively fast and unlikely to be the limiting step. The study of heat transfer and its significance on the kinetics of the system will follow and it will be shown that under the experimental conditions heat transfer across the packed bed of high porosity ($\omega \simeq 85\%$) is most likely the rate controlling step of the overall reaction.

6.1 Mass Transfer

Mass transfer in the system can be divided into the following stages

1. Mass transfer of the volatile species from condense phase to the vapor phase by evaporation within the dust bed.

2. Mass transfer in the vapor phase within the dust bed.
3. Mass transfer in the vapor phase between the two compartments.
4. Mass transfer from the vapor phase to the condensed phase by condensation.

In this section each step will be considered individually and the rate of mass transfer will be calculated based on the available information and appropriate assumptions. Due to the complexity of the system, the objective is to find an order of magnitude of the rate of mass transfer for the purpose of comparison. Most calculations are done based on the physical and chemical properties of EAF dust type-A.

6.1.1 Vapor phase properties

For the different EAF dusts used in this study, the vapor phase mainly consists of $NaCl$, KCl and PbO. If it is assumed that these compounds evaporate at the same rate during the treatment to result in a vapor phase of constant composition, the mole fraction of each species can be calculated from the chemical composition of the dust. For EAF dust type-A, $Na = 1.4\,\%wt$, $K = 1.0\,\%wt$ and $Pb = 3.1\,\%wt$, the amount of volatile species can be calculated based on their mole fraction. Based on the experimental results, after removing about 90% of volatile species, approximately 25$\%wt$ sodium, which is most likely in the form of oxide, is left in the residue. Therefore, in calculation of the mixture of vapor phase, the amount of sodium is assumed to be 1$\%wt$ and for 100 grams dust the mole fractions can be calculated as follows.

$Na = 1.0\ g \Rightarrow \frac{1}{23}$ mole $= 0.0435$ mole $\Rightarrow$ 0.52 mole fraction in vapor phase

$K = 1.0\ g \Rightarrow \frac{1}{39}$ mole $= 0.0255$ mole $\Rightarrow$ 0.30 mole fraction in vapor phase

$Pb = 3.1\ g \Rightarrow \frac{3.1}{207}$ mole $= 0.0145$ mole $\Rightarrow$ 0.18 mole fraction in vapor phase

Table 6.1: Diameters of species in the gas phase

Ion	Diameter (nm)	Molecule	Diameter (nm)
Na^{+1}	0.194	$NaCl$	0.556
K^{+1}	0.266	KCl	0.628
Pb^{+2}	0.240	PbO	0.520
Cl^{-1}	0.362		
O^{-2}	0.280		

Hence, the vapor phase is composed of 52 % $Vol.$ $NaCl$, 30 % $Vol.$ KCl and 18 % $Vol.$ PbO with an average molecular weight of,

$$\overline{M} = \sum_{i=1}^{n} x_i M_i = 0.52 \times 58 + 0.30 \times 74 + 0.18 \times 223 = 92.5\ g/mole$$

The mean free path can be calculated based on the following[38].

$$\lambda = \left(\frac{1}{\sqrt{2}}\right)\left(\frac{1}{\pi d^2 n}\right) \tag{6.1}$$

where d is the collision diameter and n is the number of molecules per unit volume. The ionic diameters of Na, K, Pb, Cl and O are tabulated in Table 6.1[39]. With the assumption that collision diameter is equal to molecular diameter, d can be calculated for each species. The calculated values of d are included in Table 6.1.

For an ideal gas n can be calculated from the following relation,

$n = \frac{\rho \times N}{M} = \frac{m \times N}{V \times M} = \frac{P \times N}{R \times T}$

At 900°C the equilibrium vapor pressure over the EAF dust type-A can be taken from Table 3.3, therefore,

$T = 900°C = 1173°K,$ $\qquad \bar{d} = 0.568\ nm = 5.68 \times 10^{-10}\ m$

$P = 206\ Pa,$

$n = \frac{206 \times 6.023 \times 10^{23}}{8.314 \times 1173} = 1.27 \times 10^{22}\ molecules\,/\,m^3$

$\lambda = \left(\frac{1}{\sqrt{2}}\right)\left(\frac{1}{\pi \times (5.68 \times 10^{-10})^2 \times 1.27 \times 10^{22}}\right) = 5.49 \times 10^{-5}\ m \simeq 0.055\ mm$

for $T = 850°C \quad \Longrightarrow \quad \lambda \simeq 0.115\ mm$

Compared with the smallest dimension of the experimental apparatus which is the diameter of the duct between the two compartments, 22 mm, λ is small and therefore viscous flow inside the duct can be assumed. The mass transfer inside the dust bed with an average void size of the order of 10 μm would be in the form of molecular flow[40].

The viscosity of a mixture of vapors can be estimated based on the viscosity of its components, using the semiempirical formula of Wilke[41, 42].

$$\eta_{mix} = \sum_{i}^{n} \frac{x_i \eta_i}{\sum_j^n x_j \Phi_{ij}} \tag{6.2}$$

in which

$$\Phi_{ij} = \frac{1}{\sqrt{8}} \left(1 + \frac{M_i}{M_j}\right)^{-\frac{1}{2}} \left[1 + \left(\frac{\eta_i}{\eta_j}\right)^{\frac{1}{2}} \left(\frac{Mj}{M_i}\right)^{\frac{1}{4}}\right]^2 \tag{6.3}$$

here n is the number of chemical species in the mixture; x_i and x_j are the mole fractions of species i and j; η_i and η_j are the viscosities at a given temperature and pressure; and M_i and M_j are the corresponding molecular weights. The coefficient of viscosity for each species at absolute temperature T may be written in terms of Lennard-Jones parameters σ and ϵ,

$$\eta_i = 2.6693 \times 10^{-5} \frac{\sqrt{M_i T}}{\sigma^2 \Omega_\eta} \tag{6.4}$$

in which η is in $g.cm^{-1}sec^{-1}$, T is in K, σ is in Ångström and Ω_η is a slowly varying function of the dimensionless temperature $\kappa T/\epsilon$. ϵ/κ and σ can be estimated through the following empirical relations [41, 42]

$$\epsilon/\kappa = 0.77 T_c \qquad \sigma = 0.841 \widetilde{V}_c^{1/3} \quad or \quad 2.44 \left(\frac{T_c}{P_c}\right)^{1/3} \tag{6.5}$$

Table 6.2: Critical properties of vapor species

Species	T_c (K)	P_c (atm)	$\tilde{V}_c$(cm^3/mole)
NaCl	3400	350.4	266
KCl	3470	177.7	625

Table 6.3: Viscosity of the vapor species at 900°C.

Species	$\epsilon\kappa$ (K)	$\kappa T/\epsilon$	Ω_η	σ(Å)	η ($g.cm^{-1}.sec^{-1}$)	η ($kg.m^{-1}.sec^{-1}$)
NaCl	2618	0.429	2.420	5.3	1.00×10^{-4}	1.00×10^{-5}
KCl	2672	0.420	2.442	6.9	6.62×10^{-5}	6.62×10^{-6}
PbO	N/A	N/A	N/A	N/A	1.06×10^{-4}	1.06×10^{-5}

ϵ/κ and T are in K, σ is in Ångström, $\tilde{V}$ is in $cm^3 mole^{-1}$, and P_c is in atmosphere. The critical properties of $NaCl$ and KCl are tabulated in Table 6.2[43].

Using Equation 6.5 the dimensionless temperature $\kappa T/\epsilon$ and the characteristic diameter of each molecule, σ, can be calculated. After substitution of σ and Ω_η in Equation 6.4 the viscosities of $NaCl$ and KCl can be determined. Due to the lack of data for the critical properties of PbO, its viscosity was estimated based on the following relation[41],

$$\eta_i = \frac{2}{2\pi^{2/3}} \frac{\sqrt{M_i \kappa T}}{d^2} \tag{6.6}$$

The results of the calculations of viscosities are summarized in Table 6.3.

The viscosity of the gas mixture is calculated based on a composition of 52% $NaCl$, 30% KCl and 18% PbO at $T = 900°C$ and $P = 206\ Pa$ to be,

$$\eta_{mix} = 9.32 \times 10^{-5}\ g.cm^{-1}.sec^{-1} = 9.32 \times 10^{-6}\ kg.m^{-1}.sec^{-1}$$

It should be noted that because of little difference in the values of the viscosities for these three species, variations of the vapor composition do not change the viscosity of the gas mixture significantly.

6.1.2 Evaporation and condensation

The rate of the physical processes of vaporization (endothermic) and condensation (exothermic) are influenced by the surface temperature which depends on the heat transfer to and from the system. If the heat transfer is assumed to be relatively fast, the evaporation or condensation can take place at a constant temperature. For such condition the maximum rate of condensation can be calculated based on the kinetic theory of gases according to the following equation[44].

$$\dot{n}_{\max} = \alpha(P_2 - P_1)\sqrt{\frac{M}{2\pi RT}} \tag{6.7}$$

where $\dot{n}_{\max}$ is the equilibrium and the maximum rate of condensation, α is a weighting factor[1], P_2 is the vapor pressure of the gas phase and P_1 is the equilibrium vapor pressure at the surface of the condensed phase. Under equilibrium conditions, the rates of evaporation and condensation are equal, therefore, for the maximum rate of evaporation the same formula, Equation 6.7, can be used.

When mass transfer between the two compartments is not a rate controlling step, pressure difference between the two compartments is small.

$$P_{hot\,compartment} \simeq P_{cold\,compartment} = P_{measured} \simeq 67\ Pa = 0.5\ torr$$

The total equilibrium vapor pressure and the partial pressure of the volatile species were calculated and reported in chapter 3. In these calculations the liquid phase was assumed to be an ideal solution so that, $X_i^{(l)} = X_i^{(g)}$. Using the equilibrium vapor pressures at 900°C from Table 3.4 the rate of evaporation for $NaCl$ can be calculated as follows.

$$T = 900°C = 1173°K$$

---

[1] α is considered to be close to one at high temperature vaporization[38].

$M_{NaCl} = 58 \times 10^{-3}\ kg/mole$

$P_1 = PP_{NaCl} = X_{NaCl} \times P_{measured} = \frac{PP_{NaCl}}{P_{eq}^{1173}} \times P_{measured} = \frac{95.4}{206} \times 67 = 31\ Pa$

$P_2 = PP_{NaCl}^{eq} = 95\ Pa$

$\dot{n}_{\max} = 1 \times (95 - 31)\sqrt{\frac{58\times10^{-3}}{2\times3.14\times8.314\times1173}} = 0.0613\ kg.m^{-2}.sec^{-1}$

For an average particle size of 5 μm, total particle surface area per unit particle volume can be estimated [38]

$S_o = \frac{6}{D} = \frac{6}{5\times10^{-6}} = 1.2 \times 10^6\ m^2/m^3$

For 25 grams EAF dust with an apparent density of 650 kg/m^3 , (porosity $\omega = 0.85$) the total free surface of particles can be calculated as

$S = V \times S_o \times (1 - \omega) = \frac{25\times10^{-3}}{650} \times 1.2 \times 10^6 \times (1 - 0.85) = 6.9\ m^2$

This is the total solid surface of the dust particles. The wetted portion of the surface where the liquid is formed could be a fraction of this area. Assigning W_w as the fraction of the surface being covered by the liquid, the rate of evaporation for 25 grams EAF dust would be

$S \times \dot{n}_{\max} \times W_w = 6.9 \times 0.0613 W_w = 0.423 W_w\ kg/sec$

In chapter 2, it was explained that during the formation of EAF dust, "more volatile species" which condense in later stages, form the finest particles and also cover the surface of the larger particles. In some cases volatile species act as a bond to agglomerate other particles. For the fine particles the specific surface is large and the condensed species covering the surface of other particles also form a large surface area. Experimental observations support this fact. The remaining residue after treatment is usually in the form of one or few pieces of loosely agglomerated particles. This agglomeration of the whole dust bed takes place due the partial melting. Nevertheless, even with a small fraction of the solid particles being covered by the liquid phase, the rate of evaporation would be several orders of magnitude faster than the overall rate of reaction observed in the present work, see Table 6.4.

For the calculation of the rate of condensation, the temperature of the cold compartment is assumed to be 650°C. This is the highest temperature of the location where most condensation takes place. The vapor pressure of $NaCl$ in equilibrium with the condensate at this temperature may be taken from Table 3.5, which is 0.78 Pa. The partial pressure of $NaCl$ in the condensation compartment can be calculated based on the measured pressure and its mole fraction.

$$\begin{array}{llll} P_1 & = PP_{NaCl} = & 31 & Pa \\ P_2 & = PP_{NaCl}^{eq} = & 0.78 & Pa \\ \dot{n}_{\max} & = & -0.030 & kg.m^{-2}.sec^{-1} \end{array}$$

Similar calculations can be performed for KCl and PbO.

For evaporation of KCl at 900°C;

$$\begin{array}{llll} P_1 & = PP_{KCl} = & 27 & Pa \\ P_2 & = PP_{KCl}^{eq} = & 79 & Pa \\ \dot{n}_{\max,ev} & = & 0.057 & kg.m^{-2}.sec^{-1} \end{array}$$

For condensation of KCl at 650°C;

$$\begin{array}{llll} P_1 & = PP_{KCl} = & 27 & Pa \\ P_2 & = PP_{KCl}^{eq} = & 1 & Pa \\ \dot{n}_{\max} & = & -0.029 & kg.m^{-2}.sec^{-1} \end{array}$$

For evaporation of PbO at 900°C;

$$\begin{array}{llll} P_1 & = PP_{PbO} = & 2.5 & Pa \\ P_2 & = PP_{PbO}^{eq} = & 7.5 & Pa \\ \dot{n}_{\max} & = & 9.5 \times 10^{-3} & kg.m^{-2}.sec^{-1} \end{array}$$

Table 6.4: Rate and time required for evaporation and condensation of each species from 25 grams EAF dust type-A under experimental conditions.

Species	Mass in sample g	Evaporation $\dot{n}$ kg.m^{-2}.sec^{-1}	S m^2	time sec	Condensation $\dot{n}$ kg.m^{-2}.sec^{-1}	S m^2	time sec
$NaCl$	0.9	0.061	0.069	0.21	0.030	0.005	6.0
KCl	0.5	0.057	0.069	0.13	0.029	0.005	3.5
PbO	0.8	0.0095	0.069	1.22	0.0038	0.005	42.

For condensation of PbO at 650°C;

$$P_1 = PP_{PbO} = 2.5 \quad Pa$$

$$P_2 = PP^{eq}_{PbO} = 0.5 \quad Pa$$

$$\dot{n}_{max} = -3.81 \times 10^{-3} \quad kg.m^{-2}.sec^{-1}$$

In Table 6.4 the calculated rates of evaporation and condensation for each species are given along with the required time of evaporation or condensation. For the calculations of the required time, the content of each species in 25 grams EAF dust type-A is considered. The wetted portion of the dust available for evaporation of each species is assumed to be 1% of the total solid surface (6.9 m^2) and the surface available for condensation of each species is assumed to be one third of the surface area (1.5×10^{-2} m^2) in condensation compartment.

From Table 6.4 it can be concluded that because of the large surface area of EAF dust, even when a small portion of it is covered by the liquid, the rate of evaporation for any of the volatile species is high enough that this step is very unlikely to be among the rate controlling steps under the experimental conditions of the present work. The rate of condensation is lower and the surface area available for condensation is also smaller. Among the volatile species lead oxide has the lowest rate of evaporation and condensation. The initial content of 0.8 gram lead oxide in 25 grams EAF dust type-A could evaporate near completion in less than 2 seconds and condense in about 42 seconds. This is much shorter than the overall treatment time of 10 – 12 minutes for the EAF dust type-A in the stationary cylindrical reaction chamber at a furnace temperature of $1100°C$. In most experiments about 10 grams steel wool was placed inside the condensation compartment. This steel wool with a wire diameter of 0.15 mm increases the condensation surface area by approximately 3×10^{-2} m^2 and therefore can reduce the condensation time to a third of above mentioned values.

6.1.3 Mass transfer within the dust bed

The density of EAF dust particles is about 4500 kg/m^3[4] while the apparent density[2] of EAF dust without compacting under the experimental conditions of the present work is between 650 to 750 kg/m^3, resulting in a porosity of approximately 82 – 85%. Considering the dust bed with 85% void space, flow of the vapor phase inside the bed may not encounter a great resistance. Due to the low pressure of the system and the small pore size of the dust packing, the major mechanism of mass transfer within the bed would be that of molecular flow. If the average dust particle size is assumed to be 5 μm for a bed of 85% porosity, the pore size would be of the order of 10 μm while the mean free path for the mixture of $NaCl$, KCl and PbO in the hot chamber at $900°C$ is of the order of 55 μm.

Here two cases of the molecular effusion and molecular flow can be considered. The flow of vapors from the top of the bed to the vacuum chamber may be a case of molecular effusion, while the mass transfer within the bed would be in the form of molecular flow.

---

[2] The apparent density of the dust packing is determined by the weight and volume of the bed.

For the first case a thin plate with many holes dividing two compartments of different pressures may be assumed. The rate of effusion of the gas molecules through a small hole can be estimated by the following equation [38]

$$\dot{n} = \frac{W_e(P_1 - P_2)}{\sqrt{2\pi MRT}} \tag{6.8}$$

where $\dot{n}$ is the rate of effusion in $mole.m^{-2}.sec^{-1}$, W_e (Clausing factor) gives the probability of passing through the hole and depends on the ratio of the orifice thickness to its radius, l/r. For a ratio of $l/r = 0.4$, the Clausing factor is reported to be $W_e = 0.834$[38].

For the mixture of the volatile species with an average molecular weight of 92.5 $g/mole$ the rate of effusion can be calculated as follows

$$\dot{n} = \frac{W_e \times (206 - 67)}{\sqrt{2 \times 3.14 \times 92.5 \times 10^{-3} \times 8.314 \times 1173}} = 1.85 W_e \; mole.m^{-2}.sec^{-1}$$

the average surface area of the voids on the top surface of the dust bed could be estimated as follows

$$A_{void} \simeq \omega_A \times A_{bed} = 0.74 \times 0.05 \times 0.09 = 3.33 \times 10^{-3} \; m^2$$

ω_A is the fraction of voids on the surface and is estimated based on the void fraction of $\omega = 0.85$.

$$\dot{n}.A_{void}.\overline{M} = 1.85 W_e \times 3.33 \times 10^{-3} \times 92.5 = 0.570 W_e \; g/sec$$

Even for a small value of W_e the rate of effusion of the volatile species from the dust bed would be orders of magnitude faster than the overall rate of reaction.

The passage of molecules through the porous media may be assumed to be equivalent to a bundle of narrow pipes between two separate compartments. In that case, the molecular flow of volatile species within the dust bed can be approximated using the empirical formulas of conductance in high vacuum system. The rate of molecular flow through such pipes can be written as [38]

$$\dot{n} = \frac{C\,(P_1 - P_2)}{ART} \tag{6.9}$$

For a cylindrical pipe with a radius of r and a length of l, the conductance can be calculated by the following empirical formula [38]

$$C = 19.4\frac{A^2}{Bl}\left(\frac{T}{M}\right)^{1/2} \tag{6.10}$$

where C is the conductance in *litre/sec*, A is the cross section area in cm^2, B is the perimeter in cm and l is the length in cm. For the cylindrical reaction chamber the maximum length of such pipes varies inside the dust bed, therefore, an average value of C over the cross section of the bed is calculated as follows,

$$C = 19.4 \times \frac{(\pi r^2)^2}{2\pi r l} \times \left(\frac{1173}{85}\right)^{1/2} = \frac{113.2r^3}{l}\ litre/sec$$

The height of the dust bed l can be written as a function of θ, for details refer to Figure 6.1.

$$l \doteq r_{ch}(\sin\theta - \sin\theta_1)$$

where, $r_{ch} = 28\,mm$ is the radius of the cylindrical reaction chamber, $\theta_1 = 0.608\,Ra$ for a maximum bed height of $h = 12\,mm$(corresponding to a bed of 25 grams dust of 650 kg/m^3 density).

$$\overline{C} = \frac{\int_{\theta_1}^{\pi/2} C(\theta)d\theta}{\int_{\theta_1}^{\pi/2} d\theta} = \frac{\int_{\theta_1}^{\pi/2} \frac{113.2r^3}{2.8(\sin\theta - \sin\theta_1)}d\theta}{\frac{\pi}{2} - \theta_1} = 444.4r^3\ litre/sec$$

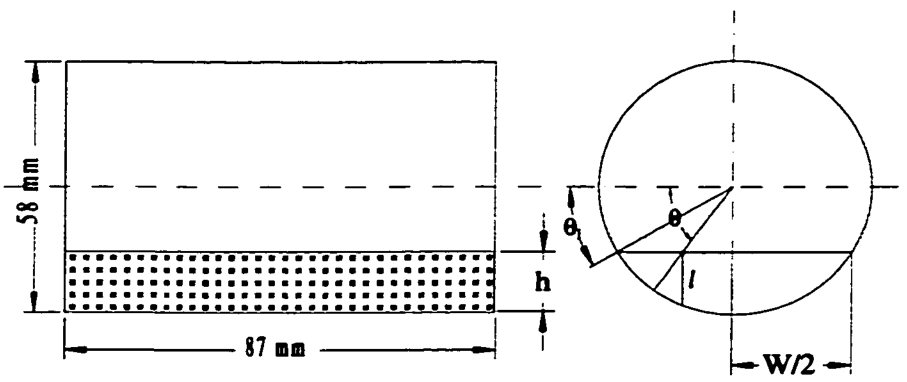

Figure 6.1: View of two cross sections for dust bed inside cylindrical reaction chamber.

converting $\overline{C}$ to SI units;

$$\overline{C} = 4.444 \times 10^5 r^3 \; m^3/sec$$

the rate of molecular flow can be calculated as

$$\dot{n} = \frac{\overline{C}(P_1 - P_2)}{\pi r^2 RT} = \frac{4.444 \times 10^5 r(203-67)}{\pi RT} = 1973r \; mole.m^{-2}.sec^{-1}$$

$$\dot{n}.A_{void}.\overline{M} = 1973r \times 3.33 \times 10^{-3} \times 85 = 558r \; g/sec$$

Figure 6.2 shows the calculated time required to remove 2 grams of volatile species from the dust bed for different average pore sizes. For a pore size of 10 μm time required for the mass transfer is approximately about 12 minutes which is about the duration of an experiment with removal of the volatile species near completion. For a pore size of 100 μm, the time required for the mass transfer within the dust bed is about one minute. It is important to note that partial melting which leads to agglomeration, greatly increases the average pore size. Some samples of the residue after treatment have been examined under a stereomicroscope. The average pore size on the surface of the dust bed is in the order of 100 μm in a bed of loosely placed dust and of the order of 10 μm in a bed with compacted dust.

In experiments with different extents of compacting of the dust bed, i.e. different porosity and pore size, Experiments # 48, # 49 and # 50, the variation of the observed overall rate shows a trend which is opposite to the case of molecular flow within the bed being the rate controlling step.

Mass transfer between the two compartments

Mass flux can be stated as the product of density and velocity, i.e.

$$\vec{J} = \rho . \vec{v} \tag{6.11}$$

Inside the connecting duct between the evaporation and condensation compartments, the density and gas velocity change but the mass flux is constant because there is neither a source nor a sink of the vapor. In order to estimate the mass flux inside the duct, the condition of a compressible fluid is considered due to the large changes in density over the length of the duct. The general form of Bernoulli's equation may be written as[45],

$$\rho \frac{D}{Dt}\left(h + \frac{v^2}{2} + \Psi\right) = \frac{\partial P}{\partial t} + (\Sigma_{ik} v_k)_{,i} - q_{k,k} \tag{6.12}$$

where h ($\equiv e + Pv$) is the enthalpy, Ψ is the force potential or potential energy per unit mass, and $q_{k,k}$ is the heat conduction term.

For the gas flow inside the connecting duct under the experimental conditions certain assumptions may be made.

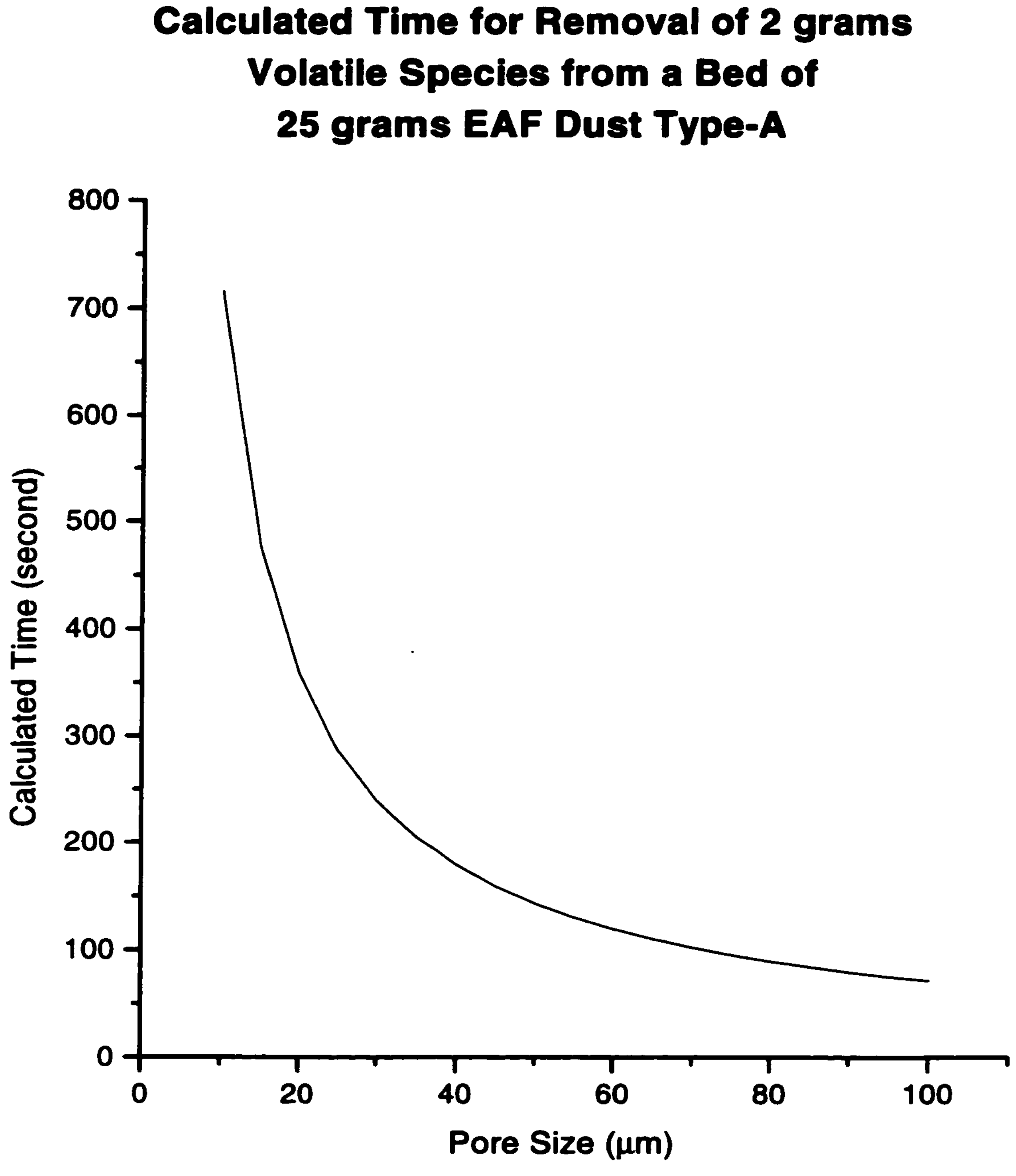

Figure 6.2: Calculated time required for removal of volatile species from dust bed based on molecular flow.

- P and T do not vary over the cross section area. The changes are only in the direction of the duct axis and therefore uni-directional flow is assumed.

- The calculations are based on the assumption of a stable condition where the temperature of the vapor phase in the evaporation compartment is $900°C$ and the temperature of the cold compartment is $650°C$.

- Under the conditions of the reduced pressure and high temperature in the system, all vapors are assumed to be ideal gases.

- Evaporation and condensation take place rapidly and the pressure of the compartments is the equilibrium vapor pressure over the condense phase. This is calculated based on a dust temperature of $900°C$ and condensate temperature of $650°C$.

- The large pressure difference between the evaporation and condensation compartments creates a high speed gas flow in the duct and it is reasonable to neglect the effect of viscosity, which is $\backsim 10^{-4}$ poises ($\backsim \frac{1}{100}$ viscosity of air), $(\Sigma_{ik}v_k)_{,i} = 0$.

- Since the length of the duct is short compared to its diameter, the effect of friction on the wall is neglected and the flow is assumed to be isentropic.

- Heat conduction by gas phase inside the duct is negligible, $q_{k,k} = 0$.

Based on the above mentioned assumptions Bernoulli's equation can be simplified and stated in the following form

$$d\left(h + \frac{v^2}{2}\right) = 0 \tag{6.13}$$

and therefore,

$$h + \frac{v^2}{2} = const. \quad or \quad h + \frac{v^2}{2} = h_o$$

substituting $h = c_p T + const.$ for a perfect gas,

$$c_p T + \frac{v^2}{2} = c_p T_o \tag{6.14}$$

also,

$$C^2 = \frac{\gamma R T}{M} \tag{6.15}$$

and

$$c_p = \frac{\gamma R}{(\gamma - 1) M} \Rightarrow c_p T = C^2/(\gamma - 1)$$

where C is the speed of sound, c_p is the specific heat and γ is the ratio of specific heats. Equation 6.14 can be written in the following form,

$$C^2 + \frac{\gamma - 1}{2} v^2 = C_o^2 \tag{6.16}$$

dividing both sides by C^2 and substituting Mach number, $Ma = v/C$,

$$\frac{T_o}{T} = 1 + \frac{\gamma - 1}{2} (Ma)^2 \tag{6.17}$$

For isentropic flow, simple relations connect the temperature and other thermodynamical properties,

$$\frac{T_o}{T} = \left(\frac{P_o}{P}\right)^{(\gamma-1)/\gamma} = \left(\frac{\rho_o}{\rho}\right)^{\gamma-1} = \left(\frac{C_o}{C}\right)^2 \tag{6.18}$$

For a constant cross section area pipe discharging to a larger space, sonic velocity occurs at the end of any significant length when the ratio of the static pressures between the outlet and inlet is below 0.5[46]. For EAF dust type-A from Table 3.3, $P^{eq}_{900°C} = 206\ Pa$ and for the condensate from Table 3.5, $P^{eq}_{650°C} = 1.65\ Pa$, therefore, the sonic velocity should be reached at the end of the duct connecting the evaporation and condensation compartments. For a diatomic ideal gas ($\gamma = 1.4$) at sonic condition, $Ma = 1$, using Equations 6.17 and 6.18,

$$\frac{T_s}{T_e} = 0.8333 \quad \frac{P_s}{P_e} = 0.5483 \quad \frac{\rho_s}{\rho_e} = 0.6339 \tag{6.19}$$

where s stands for sonic line at the end of duct and e stands for stagnant condition at the evaporation compartment. For vapor phase at $900°C$ in evaporation compartment,

$$T_e = T_{hot} = 1173°K, \text{ and } P_e = P_{hot}^{eq} = 206\ Pa$$

thus,

$$\rho_e = \frac{P\overline{M}}{RT} = 1.95 \times 10^{-3} kg/m^3$$

The conditions at the sonic line are set by Equation 6.19 such that,

$$T_s = 977°K = 704°C, \quad P_s = 112.9\ Pa \quad \text{and} \quad \rho_s = 1.23 \times 10^{-3} kg/m^3$$

Speed of sound The speed of sound in a perfect gas can be estimated from the following

$$C = \frac{\sqrt{dP}}{\sqrt{d\rho}} = \sqrt{\frac{\gamma P}{\rho}} = \sqrt{\frac{\gamma RT}{M}} \tag{6.20}$$

hence at the sonic line with the above mentioned conditions the speed of sound will be,

$$C = \sqrt{\frac{1.4 \times 112.9}{1.23 \times 10^{-3}}} = 358\ m/s$$

and therefore, mass flux between the two compartments will be,

$Ma = 1$

$v = C = 358\,m/s$

$J = \rho v = 1.23 \times 10^{-3} \times 358 = 0.44\ kg.m^{-2}.sec^{-1}$

The total weight of the volatile species in 25 grams EAF dust type-A is about 2 grams ($8\%wt$). Time to transfer 2 grams mass from the evaporation compartment to the condensation compartment with the above mentioned conditions will be,

$$t = \frac{m}{J.A} = \frac{2 \times 10^{-3}}{0.44 \times \pi \times 0.011^2} = 12\ sec$$

The required time of 12 seconds is quite small compared with the duration of a treatment near completion, which is about 10 − 12 minutes in the stationary cylindrical reaction chamber at a furnace temperature of 1100°C. Therefore, mass transfer between the two compartments is unlikely to be the rate controlling step in the system.

6.2 Heat Transfer

Heat transfer in the evaporation compartment may be considered in two steps,

Step #1 heat transfer from the reaction chamber walls to the dust bed, and

Step #2 heat transfer inside the dust bed.

In the cylindrical reaction chamber, step #1 is through radiation from the chamber walls to the top surface of the dust bed and through conduction and radiation from the chamber walls to dust particles.

In the rectangular reaction chamber, step #1 is through radiation from the chamber walls to the top surface of the dust bed and through conduction and radiation from the chamber walls to the nickel boat and from the nickel boat to dust particles.

Heat transfer in step #2 is more complicated. Heat conduction takes place through solid particles and across their contact areas. Heat radiation occurs between the surfaces of the particles and it plays a significant role as the temperature of the particles increases. Heat is consumed when partial melting and evaporation of the volatile species take place inside the dust bed. The vapor phase carries the heat and increases the overall heat transfer by convection and by releasing the latent heat of vaporization upon condensing at the colder parts of the dust bed.

Between the two steps, heat transfer inside the dust bed is much slower due to the insulating character of the porous bed of fine particles under reduced pressure. Temperature measurements inside the dust bed indicate a very slow heat transfer across the bed. For example, in an experiment with the cylindrical reaction chamber with the furnace temperature of $1100°C$, it takes about two minutes for the temperature of the inner wall to reach about $1000°C$, see Figures 5.2 and 5.3, while it takes about $10 - 12$ minutes for the centre of the dust bed of 13 mm height to reach a temperature of $900°C$, see Figure 6.10. It is obvious that in considering the rate controlling step, heat transfer inside the dust bed must be given due attention. Here a calculation of heat radiation inside the cylindrical reaction chamber is presented and then the heat transfer within the dust bed will be examined.

6.2.1 Heat radiation inside the hot zone

In order to show that heat transfer in step #1 is much faster than the observed overall rate of reaction, only the heat radiation from the chamber walls to the top surface of the dust bed will be considered. Figure 6.3 shows the schematic representation of the hot zone for the cylindrical reaction chamber. Surfaces A_1 and A_2 are the chamber walls radiating at $1100°C$. Surface A_3 is the shield surface whose temperature is

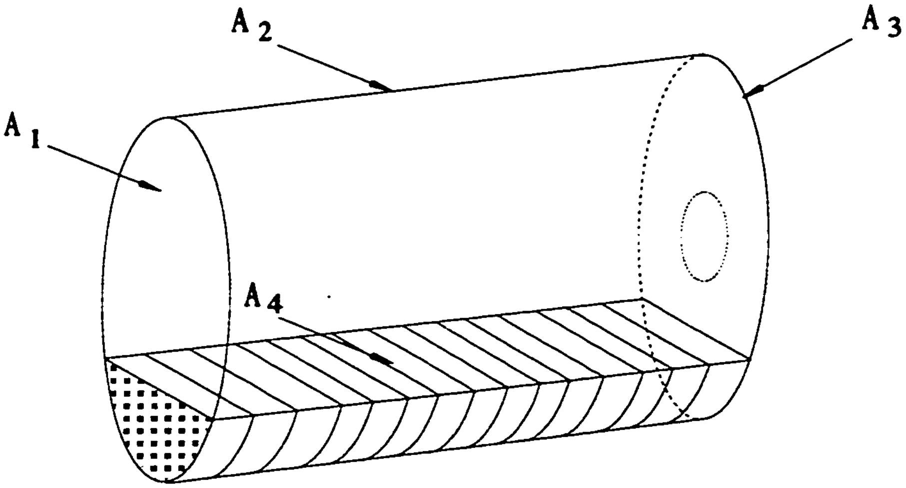

Figure 6.3: A schematic representation of the hot zone for cylindrical reaction chamber.

measured and recorded to be between 850°C and 900°C during the experiments. A_4 is the top surface of the dust bed.

Based on the Stefan-Boltzmann equation and considering the emissivity of a real surface, ε, the total emissive power e of a real surface is

$$e = \varepsilon\sigma T^4$$

In order to find the total power delivered at the surface of the dust bed, the electric analog circuit of the hot zone shown in Figure 6.4 can be used. The resistance between the nodes are defined by the following formulas.

$$R_i = \frac{1 - \varepsilon_i}{A_i \varepsilon_i} \tag{6.21}$$

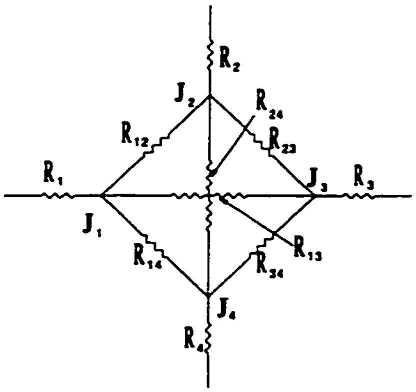

Figure 6.4: Analog electric circuit of the hot zone for the cylindrical reaction chamber.

$$R_{ij} = \frac{1}{A_i F_{ij}} = \frac{1}{A_j F_{ji}} \tag{6.22}$$

where ε_i is the emissivity of the surface i, and F_{ij} is the view factor between surfaces i and j.

The maximum height of the dust bed of apparent density 650 kg/m^3 is about 13.5 mm. The surface areas and view factors for this system are calculated as follows. Figure 6.1 shows the detail of the hot zone for these calculations.

Dust bed cross section area = 450 mm^2

h = maximum height = 13.5 mm

r_{ch} = radius of reaction chamber = 28 mm

L = length of dust bed = 90 mm

W = width of dust bed = 47.9 mm

$A_1 = A_3 = \pi r_{ch}^2 - 450 = 2010\ mm^2$

$\theta_1 = \arcsin(r_{ch} - h) = 0.544\ Radian$

$A_2 = (\pi + 2\theta_1)r_{ch}L = 4.23 \times 28 \times 90 = 10660\ mm^2$

$A_4 = WL = 47.9 \times 90 = 4310\ mm^2$

For the view factors the following relations can be written,

$$\begin{gathered} F_{12} = F_{32} \\ F_{13} = F_{31} \\ F_{14} = F_{34} \\ F_{21} = F_{23} \\ F_{41} = F_{43} \end{gathered} \tag{6.23}$$

for the flat surfaces of A_1, A_3 and A_4,

$$\begin{gathered} F_{12} + F_{13} + F_{14} = 1 \\ F_{31} + F_{32} + F_{34} = 1 \\ F_{41} + F_{42} + F_{43} = 1 \end{gathered} \tag{6.24}$$

also for any two surfaces the following relation can be used,

$$A_i F_{ij} = A_j F_{ji} \tag{6.25}$$

Note the first two relations in Equation 6.24 are not independent due to the symmetry, Equation 6.23. F_{13}, F_{14} and F_{41} can be estimated using the view factor charts for parallel disks and surfaces with common edge[47].

$F_{13} = F_{31} = 0.10$

$$F_{14} = F_{34} = 0.26$$

$$F_{41} = F_{43} = 0.12$$

from Equation 6.24

$$F_{12} = F_{32} = 0.64$$

and $F_{42} = 0.76$

for the other view factors Equation 6.25 can be used.

$$F_{24} = \frac{A_4}{A_2} F_{42} = 0.31$$

$$F_{21} = F_{23} = \frac{A_1}{A_2} F_{12} = 0.12$$

Surfaces A_1 and A_2 are oxidized nickel with an assumed emissivity of $\varepsilon_1 = \varepsilon_2 \simeq 0.8$, surface A_3 is oxidized steel with an assumed emissivity of $\varepsilon_3 \simeq 0.95$. For the dust which is mostly iron and zinc oxides the emissivity of Fe_2O_3 is assumed, $\varepsilon_4 \simeq 0.85$[38]. Therefore,

$$R_1 = \frac{1-0.8}{2.01 \times 10^{-3} \times 0.8} = 124.38\ m^{-2}$$

$$R_2 = \frac{1-0.8}{1.066 \times 10^{-2} \times 0.8} = 23.45\ m^{-2}$$

$$R_3 = \frac{1-0.95}{2.01 \times 10^{-3} \times 0.95} = 26.18\ m^{-2}$$

$$R_4 = \frac{1-0.85}{4.31 \times 10^{-3} \times 0.85} = 40.94\ m^{-2}$$

$$R_{12} = R_{32} = \frac{1}{2.01 \times 10^{-3} \times 0.64} = 777.4\ m^{-2}$$

$$R_{13} = \frac{1}{2.01 \times 10^{-3} \times 0.10} = 4975.1\ m^{-2}$$

$$R_{14} = R_{34} = \frac{1}{2.01 \times 10^{-3} \times 0.26} = 1913.5\ m^{-2}$$

$$R_{24} = \frac{1}{1.066 \times 10^{-2} \times 0.31} = 302.6\ m^{-2}$$

applying the Kirchoff's law at each node,

$$\frac{e_{b1}-J_1}{R_1} + \frac{J_2-J_1}{R_{12}} + \frac{J_3-J_1}{R_{13}} + \frac{J_4-J_1}{R_{14}} = 0$$

$$\frac{e_{b2}-J_2}{R_2} + \frac{J_1-J_2}{R_{12}} + \frac{J_3-J_2}{R_{23}} + \frac{J_4-J_2}{R_{24}} = 0$$

$$\frac{e_{b3}-J_3}{R_3} + \frac{J_1-J_3}{R_{13}} + \frac{J_2-J_3}{R_{23}} + \frac{J_4-J_3}{R_{34}} = 0$$

$$\frac{e_{b4}-J_4}{R_4} + \frac{J_1-J_4}{R_{14}} + \frac{J_2-J_4}{R_{24}} + \frac{J_3-J_4}{R_{34}} = 0$$

where,

$$T_1 = T_2 = 1100°C$$

$$e_{b1} = e_{b2} = \sigma T_1^4 = 5.669 \times 10^{-8} \times 1373^4 = 2.015 \times 10^5 \ W/m^2$$

$$T_3 = 850°C$$

$$e_{b3} = \sigma T_3^4 = 5.669 \times 10^{-8} \times 1123^4 = 9.016 \times 10^4 \ W/m^2$$

$$e_{b4} = \sigma T_4^4 = 5.669 \times 10^{-8} \times T_4^4 \ W/m^2$$

and solving the set of equations for J_1 to J_4;

$$J_1 = 1.883 \times 10^5 + 2.976 \times 10^{-9} \times T_4^4 \ W/m^2$$

$$J_2 = 1.864 \times 10^5 + 3.406 \times 10^{-9} \times T_4^4 \ W/m^2$$

$$J_3 = 9.290 \times 10^4 + 7.550 \times 10^{-10} \times T_4^4 \ W/m^2$$

$$J_4 = 2.650 \times 10^5 + 4.856 \times 10^{-8} \times T_4^4 \ W/m^2$$

The net power delivered at the surface of dust bed, A_4, can be calculated;

$$E_{4,net} = \frac{e_{b4} - J_4}{R_4} = \frac{8.13 \times 10^{-7} \times T_4^4 - 2.65 \times 10^5}{40.94} = 1.985 \times 10^{-8} T_4^4 - 6.473 \times 10^3 \ W$$

Depending on the temperature of the dust bed surface, $E_{4,net}$ would have a different value. If it is assumed that heat transfer inside the dust bed is faster than the heat transfer from the chamber walls to the dust bed, then the temperature across the dust bed must not have a large variation and it may be assumed to be almost uniform. In such a case the temperature of top surface of the bed would not go higher than the temperature of evaporation ($800 - 900°C$) before removal of the volatile species is completed. The net power exchange $E_{4,net}$ is calculated for some values of T_4 between 800 and 950°C and summarized in Table 6.5.

The total enthalpy changes (heat requirement) of EAF dust type-A from 25°C to 950°C, including those of melting and evaporation of the volatile species

Table 6.5: Calculated net power delivered at the surface of dust bed in cylindrical reaction chamber.

$\mathbf{T_4}$	°C	800	850	900	950
$\mathbf{E_{4,net}}$	W	−384	−331	−271	−203

is 960 kJ/kg. Hence, treatment of 25 grams EAF dust requires 24 kJ energy. This heat can be supplied in less than two minutes with the net power of 203 W delivered at the surface of the dust bed. It is obvious that the net power delivered to the surface is larger at lower surface temperature. Furthermore the heat transfer through the bottom and the sides of the bed is not accounted for in these calculations. Thus, it can be concluded that total heat flux to the dust bed is faster than the overall rate of reaction and therefore this step of heat transfer is unlikely to be a major rate controlling step.

6.2.2 Numerical analysis of heat transfer inside the bed

A description of the problem

It has been established from the thermodynamic computations that when EAF dust is heated, it goes through a partial melting which starts at about 450°C. Evaporation of the volatile species occurs between 800°C and 900°C. Partial melting causes a shrinkage inside the dust bed and at the same time evaporation creates extra voids. A portion of volatile species condense within the dust bed at colder spots and this affects boat heat and mass transfer inside the bed. The numerical modeling of the heat transfer inside the dust bed has been simplified with the evidences provided by the experimental observations. In the following sections the difficulties are explained and the assumptions are specified.

Simplifying assumptions

Changes in the density of the packing Partial melting leads to agglomeration and an increase of the apparent density of the dust packing. On the other hand the evaporation of the volatile species decreases the apparent density of the packing by creating extra voids inside the bed. Direct observation in the present work shows that the two opposite phenomena leave the apparent density of the dust bed roughly unchanged. Experimental results show that there is about 10% weight reduction which is almost same as the change in the bed height. The shrinkage is mostly in the bed height direction. Except for a few small cracks, there is little shrinkage in the other two directions. Therefore, in the numerical model the apparent density of the dust bed is assumed to be constant during the experiment. However, the apparent density may change from one experiment to another because of different packing conditions.

One dimensional analysis The dust bed is packed in a nickel boat. Heat transfer from the sides of the nickel boat is neglected in the finite difference code and one dimensional heat transfer in the direction of the bed height is assumed. The measurement of the temperature inside the dust bed and sampling for the chemical analysis are made in the region away from the side wall. The dimensions of the bed are $100\,mm$ in length, $80\,mm$ in width, and $15-18\,mm$ in height. A two dimensional finite difference code was developed for the analysis of the heat transfer in the smaller nickel boat ($80 \times 18 \times 12\,mm$) used in the cylindrical reaction chamber during the preliminary experiments. Use of this code for the larger nickel boat had little effect on the results of the analysis compared with those obtained from the one dimensional program.

Enthalpy calculations In chapter 3 a theoretical study of the thermodynamic aspects of treating EAF dust was presented. EAF dust is composed of many compounds with more than 16 elements. Considering all compounds and phase transformations during the heating process it is difficult to represent an overall $\bar{c}_p$ with an adequate mathematical expression. Therefore, the values of enthalpy for EAF dust calculated by "FACT" program at different temperatures are directly used in the finite difference code.

No condensation within the domain of the finite difference code Condensation of some volatile species within the dust bed has been detected. The amount and location of the condensation depend on several parameters such as the amount and the composition of volatile species in EAF dust and the temperature profile inside the dust bed. It is clear from the experimental results that condensation takes place mostly at the upper parts of the dust bed and its thermal effect has only been detected by the thermocouple at the highest location inside the bed, refer to Figures 5.9 to 5.11. For the heat transfer model, the temperature of this position is used as one of the boundary conditions; thus, the influence of the condensation on temperature is taken into account. Therefore, it is assumed that no condensation takes place at lower sections of the dust bed.

Effective thermal conductivity As was mentioned, heat transfer inside the dust bed is through all three different mechanisms, namely, radiation, conduction and convection. In a porous medium, usually, heat transfer is dealt with by the use of an overall thermal conductivity. This overall or "effective" thermal conductivity of the packed bed takes into account the effect of heat conduction by solid and gas phases and the effect of radiation between the particles. The effective thermal conductivity of powders of very fine particle size at low pressure ($< 1000\ Pa$) is reported to be in the order of 0.01 $W.m^{-1}.K^{-1}$ [48, 49], refer to Figure 7.1.

It has also been reported that the radiation contribution to the thermal conductivity of packed beds is related to the third power of the absolute temperature[49, 50]. For the purpose of the numerical analysis, a general form of the effective thermal conductivity is assumed to include the effect of both conduction and radiation.

$$k_{eff} = A + B \times T + C \times T^3 \tag{6.26}$$

In this general expression A is a positive number in the order of 0.01 $W.m^{-1}.K^{-1}$ which represents the initial thermal conductivity of the solid portion of the dust, B is a negative number in the order of 10^{-5} $W.m^{-1}.K^{-2}$ which takes into account the changes in thermal conductivity of the solid particles, and C is a positive number in the order of 10^{-10} $W.m^{-1}.K^{-4}$ which assumes the contribution of heat radiation to the overall thermal conductivity.

Enthalpy method[51]

The enthalpy method is the most general and versatile approach for the numerical simulation of phase change processes. The idea is very simple, direct and physical. The volume occupied by the phase-change material is partitioned into a finite number of control volumes and then the energy conservation (Equation 6.27) is applied to each control volume to obtain a discrete heat balance.

$$\int_{t}^{t+\Delta t} \frac{\partial}{\partial t}\left(\int_{V} E dV\right) dt = \int_{t}^{t+\Delta t} \int_{\partial V} -\vec{q}.\vec{n} dS dt \qquad (6.27)$$

where E is the energy density per unit volume (product of density ρ, and enthalpy H), $-\vec{q}.\vec{n}$ is the heat flux into the volume V across its boundary ∂V, and $\vec{n}$ is the outgoing unit normal to ∂V.

In melting and freezing, usually the reference enthalpy is assigned to be zero for solid phase at the melting point, and therefore, the liquid fraction can be easily calculated as;

$$\lambda_j = \frac{E_j}{\rho L} = \frac{H_j}{L}$$

L = latent heat , H_j = enthalpy of discrete volume j.

In order to avoid the discontinuity at the melting point, enthalpy is formulated as the sum of sensible and latent heat in the liquid, so that we have

$$E(x,t) = \begin{cases} \int_{T_m}^{T(x,t)} \rho c_x(T) dT, & T(x,t) < T_m \ \text{(solid)} \\ \\ \int_{T_m}^{T(x,t)} \rho c_L(T) dT + \rho L & T(x,t) > T_m \ \text{(liquid)} \end{cases}$$

In applying the enthalpy method to the problem in hand, there are some concerns to be addressed. In the multicomponent multiphase system of dust, there exist different species with different temperature dependent specific heats. It is difficult to assign a single expression to define an average specific heat. Partial melting of EAF dust takes place over a range of 450°C to 800°C, and cannot be assumed to be at a constant temperature. Furthermore, volatile species evaporate simultaneously during the partial melting and the enthalpy of evaporation has to be taken into account at the same time.

The enthalpy values calculated by "FACT" program are used directly in the finite difference code. This direct use of enthalpy data removes the need for any expression of the specific heat. The data include enthalpy changes due to the temperature rise and the latent heat of melting and evaporation; therefore, there is no need to formulate the enthalpy as a summation of the sensible and the latent heat. Since the melting and evaporation take place over a range of temperature, the discontinuity encountered in usual melting problems does not exist here and no special treatment for the melting point is needed in the program. The enthalpy values of EAF dust at different temperatures are stored in a data file which can be called by the main program and the enthalpy of dust at any temperature will be interpolated based on the available data.

Mathematical formulation

It is desired to find $T(x,t)$ when the heat transfer equation and the boundary conditions are as follows

$$\rho\frac{\partial H}{\partial t}=\frac{\partial}{\partial x}\left(k_{eff}\frac{\partial T}{\partial x}\right) \tag{6.28}$$

$$\begin{aligned} &T(x,0)=T_i(x), && 0\le x\le l \\ &T(0,t)=T_o(t),\ T(l,t)=T_l(t) && t>0 \end{aligned} \tag{6.29}$$

where x is the direction of heat transfer across the dust bed height. The effective thermal conductivity, k_{eff}, and enthalpy, H, are temperature dependent, while the density is assumed to be constant and known.

Discretization

The dust bed is partitioned into m sub-regions, control volumes. With each sub-region, V_j, a point is associated, node x_j. We let ΔV_j = volume of V_j, and $A_{ij} = A_{ji}$ = surface area of the face common to V_i and V_j. For the dust bed of height h and cross sectional area of A, we have

$$\Delta V_j = A \times \Delta x_j \qquad \text{and} \qquad A_{ij} = A, \qquad i, j = 1, ..., m,$$

where Δx_j = length of the jth subinterval, containing node x_j. The nodes are put at the midpoint of intervals and therefore we have

$$x_{j-\frac{1}{2}} = x_j - \Delta x_j/2 \qquad \text{and} \qquad x_{j+\frac{1}{2}} = x_j + \Delta x_j/2, \qquad j = 1, ..., m,$$

with $x_{\frac{1}{2}} = 0$, $x_{m+\frac{1}{2}} = h$.

Here a uniform partition is used, therefore, $\Delta x_j = \Delta x = h/m$, the nodes are equidistant and

$$x_{\frac{1}{2}} = 0, \qquad x_{j-\frac{1}{2}} = (j-1)\Delta x, \qquad j = 1, ..., m, \qquad x_{m+\frac{1}{2}} = m\Delta x = h.$$

Let $\Delta t_n > 0$ be time increments and define the discrete time-steps

$$t_o = 0, \qquad t_1 = \Delta t_o, \qquad t_{n+1} = t_n + \Delta t_n, ..., \qquad n = 0, 1, 2, ...$$

if $\Delta t_n = \Delta t$ for all n, then $t_n = n\Delta t, \qquad n = 0, 1, 2, ...$

With $T(x,t)$ denoting the exact solution of Equation 6.28, $T(x_j, t_n)$ represents its value at node x_j at time t_n, and its numerical approximation will be denoted by $T_j^n \approx T(x_j, t_n)$.

Equation 6.28 can be written in its primitive form of

$$E_t + q_x = 0$$

with $E = \rho H$ = enthalpy per unit volume = $E_T - E_{ref}$, and E_{ref} being enthalpy at some convenient reference temperature T_{ref} , which is 298° K in this study.

$$q = heat\ flux = -k\frac{\partial T}{\partial x}$$

(Fourier's Law)

After integrating Equation 6.28 and simplifying the results, using a fully implicit scheme,

$$E_j^{n+1} = E_j^n + \frac{\Delta t_n}{\Delta x_j}\left[q_{j-\frac{1}{2}}^{n+1} - q_{j+\frac{1}{2}}^{n+1}\right] \qquad j = 1, ..., m, \tag{6.30}$$

and for discrete fluxes

$$q = -k\frac{\partial T}{\partial x} \approx -k\frac{\Delta T}{\Delta x} \tag{6.31}$$

defining $R = \Delta x/k$ as effective thermal resistance, then $q \approx -\Delta T/R$, where for a two adjacent layers it can be shown

$$R_{j-\frac{1}{2}} = \frac{\frac{1}{2}\Delta x_{j-\frac{1}{2}}}{k_{j-1}} + \frac{\frac{1}{2}\Delta x_j}{k_j} \tag{6.32}$$

or for constant Δx;

$$R_{j-\frac{1}{2}} = \frac{\Delta x}{2}\left(\frac{1}{k_{j-1}} + \frac{1}{k_j}\right) \tag{6.33}$$

and

$$q_{j-\frac{1}{2}} = -\frac{T_j - T_{j-1}}{R_{j-\frac{1}{2}}} \tag{6.34}$$

hence, for uniform grid size $\Delta x_j = \Delta x$ and uniform time step $\Delta t_n = \Delta t$, from Equations 6.30 and 6.33

$$E_j^{n+1} = E_j^n + \frac{\Delta t}{\Delta x}\left[\frac{1}{R_{j-\frac{1}{2}}}T_{j-1}^{n+1} - \left(\frac{1}{R_{j-\frac{1}{2}}} + \frac{1}{R_{j+\frac{1}{2}}}\right)T_j^{n+1} + \frac{1}{R_{j+\frac{1}{2}}}T_{j+1}^{n+1}\right] \tag{6.35}$$

Newton Iteration

Since Equation 6.35 is a nonlinear system, it may be solved by Newton-Raphson method which has the promise of up to quadratic convergence.

The system to be solved, Equation 6.35, can be set as follows

$$\vec{F}_j(\vec{T}_j^{n+1}) = E_j^{n+1} - E_j^n - \frac{\Delta t}{\Delta x}\left[\frac{1}{R_{j-\frac{1}{2}}}T_{j-1}^{n+1} - \left(\frac{1}{R_{j-\frac{1}{2}}} + \frac{1}{R_{j+\frac{1}{2}}}\right)T_j^{n+1} + \frac{1}{R_{j+\frac{1}{2}}}T_{j+1}^{n+1}\right] \tag{6.36}$$

The Newton Algorithm applied to the system $\vec{F}(\vec{T}) = \vec{0}$ consists of the iteration ($p = 0, 1, 2,$), find ΔT by solving the linear system

$$\frac{\partial \vec{F}}{\partial \vec{T}}(\vec{T}^p)\overline{\Delta \vec{T}} = -\vec{F}(\vec{T}^p) \tag{6.37}$$

then correct $\vec{T}$ via

$$\vec{T}^{p+1} = \vec{T}^p + \overline{\Delta \vec{T}}$$

and repeat until convergence is attained.

Here $\frac{\partial \vec{F}}{\partial \vec{T}}(\vec{T}^p)$ denotes the Jacobian matrix of $\vec{F}(\vec{T})$ with repeat to $\vec{T}$. This is a tridiagonal matrix, with the following components

$$\frac{\partial F_j}{\partial T_{j-1}} = -\frac{\Delta t}{\Delta x}\cdot\frac{1}{R^p_{j-\frac{1}{2}}}$$

$$\frac{\partial F_j}{\partial T_j} = \frac{\partial E_j^{n+1}}{\partial T_j^p} + \frac{\Delta t}{\Delta x}\left(\frac{1}{R^p_{j-\frac{1}{2}}} + \frac{1}{R^p_{j+\frac{1}{2}}}\right) \tag{6.38}$$

$$\frac{\partial F_j}{\partial T_{j+1}} = -\frac{\Delta t}{\Delta x}\cdot\frac{1}{R^p_{j+\frac{1}{2}}}$$

Since this matrix is diagonally dominant, the system in Equation 6.36 may be solved very efficiently by the direct tridiagonal algorithm. The results of these computations and the comparison with the experimental results will be presented in the following section.

Finite Difference Code

The finite difference code is written in MATLAB language and takes advantage of the internal functions and tool boxes of this mathematical software. A transcript of the main program and its MATLAB handle graphics code are given in Appendix B.

6.2.3 Results of computations

The results of the computations for some experiments are given in Figures 6.5 to 6.9. These figures show the temperature variations vs. time at different positions inside the dust bed. The readings of the thermocouples at the lowest and the highest positions were taken as boundary conditions. In these figures, measured temperatures for the positions of the other two thermocouples are represented with circles and stars (green). Calculated temperatures are shown with dash lines (red).

The effective thermal conductivity of the dust bed was estimated for each experiment based on the best fitted curves. These values for different EAF dusts were estimated to be in the range of 0.009 to 0.04 $W.m^{-1}.K^{-1}$ at room temperature and in the range of 0.05 to 0.14 $W.m^{-1}.K^{-1}$ at 900°C. The change in effective thermal conductivity is primarily because of different packing conditions of the dust bed. Figures 6.5, 6.6 and 6.7 represent the temperature variations in experiments with EAF dust type-A with three different packing conditions. As can be seen in Figure 6.5, experiment #49 with the apparent density of 750 kg/m^3 (bed height $\simeq 16.5\,mm$), shows the lowest effective thermal conductivity and experiment #50, Figure 6.6, with the apparent density of 920 kg/m^3 (bed height $\simeq 13.5mm$), has the highest effective thermal conductivity.

At elevated temperatures, EAF dusts with higher content of volatile species showed higher effective thermal conductivities. This can be attributed to the contribution of heat conduction and convection by the gas phase as well as improved heat conduction through the solid phase due to agglomeration. Figures 6.8 and 6.9 show the plots of temperature vs. time for the experiments with alumina and EAF dust type-C, respectively. EAF dust type-C had an apparent density of 730 kg/m^3 and contained the lowest amount of volatile species ($\backsim 2\%wt$). It had the lowest effective thermal conductivity at $900°C$ among the EAF dusts, while at low temperature its effective thermal conductivity was comparable to those of other EAF dust packings. Alumina powder possessed an even lower effective thermal conductivity at $900°C$ in spite of the fact that its low temperature conductivity was higher than those of most EAF dust packings. This can be explained as there exists no volatile species in alumina powder so that there is no contribution of heat convection and conduction by a gas phase and little agglomeration to increase the effective thermal conductivity of the packing at high temperature. The mixture of alumina with $5\%wt\ KCl$ showed much higher conductivity at $900°C$.

6.2.4 Temperature profile inside the dust bed in cylindrical reaction chamber

Due to the limitations of the apparatus with the cylindrical reaction chamber, the temperature of the dust bed could not be measured. With the use of the heat transfer model and based on the estimated effective thermal conductivity the temperature profile inside the dust bed for the conditions of the cylindrical chamber may be calculated. Since the dust bed in cylindrical chamber is not compacted, the density and effective thermal conductivity of the dust with a similar condition is used, e.g. conditions of experiment #49 in which the dust bed is not compacted, $\rho = 750\,kg/m^3$ for EAF dust type-A. The temperature of the inner wall of the reaction chamber (bottom of the dust bed), which is measured in a number of experiments, is used as the boundary condition.

Figure 6.10 shows the result of this computer simulation for EAF dust type-A. In this simulation the apparent density is 750 kg/m^3 and the maximum height of the dust bed is $13\,mm$. The variations of temperature with time at two different positions, are plotted. The temperature at the centre of the bed, $6.5\,mm$, shows the typical plateau seen in the other temperature profiles. The quick rise after the plateau which indicates approximately the end of evaporation of volatile species for that position is at about 10 minutes. Experiments with stationary cylindrical reaction chamber have similar treatment duration for a separation of about 90 to 95% of volatile species from the dust, see Table 7.4.

Figure 6.11 shows the results of a similar simulation for the EAF dust type-B. This figure indicates a longer time needed for heating the centre of the bed to about $900°C$. This is due to the lower apparent density (650 kg/m^3) and hence lower effective thermal conductivity of the EAF dust type-B. In order to remove 90 to 95% of the volatile species from this type of EAF dust, it takes about 12 minutes in stationary cylindrical reaction chamber at a furnace temperature of 1100°C, see Table 7.4.

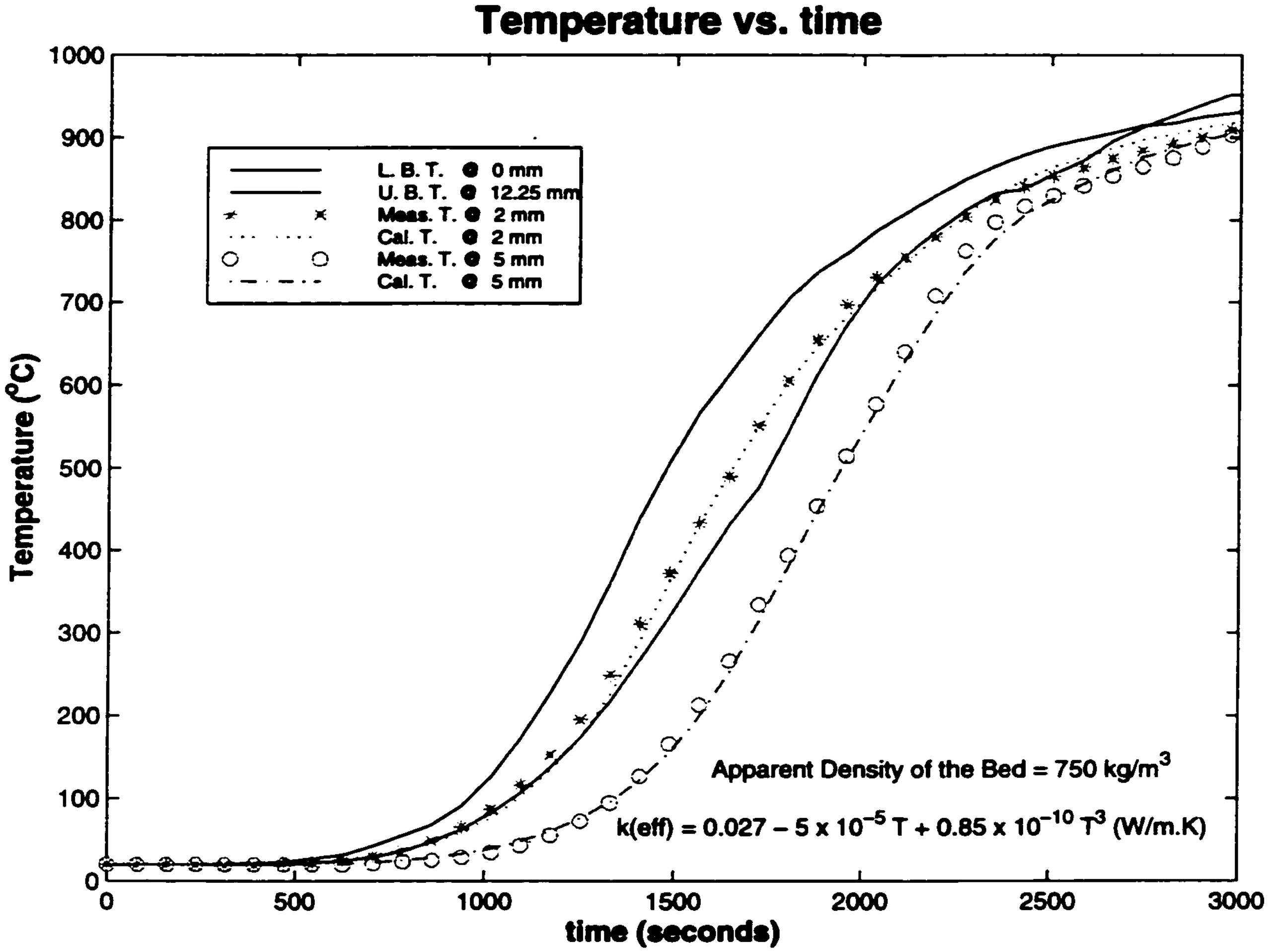

Figure 6.5: Temperature variation of EAF dust type-A at different heights inside the bed, Experiment #49, furnace temperature 1100°C.

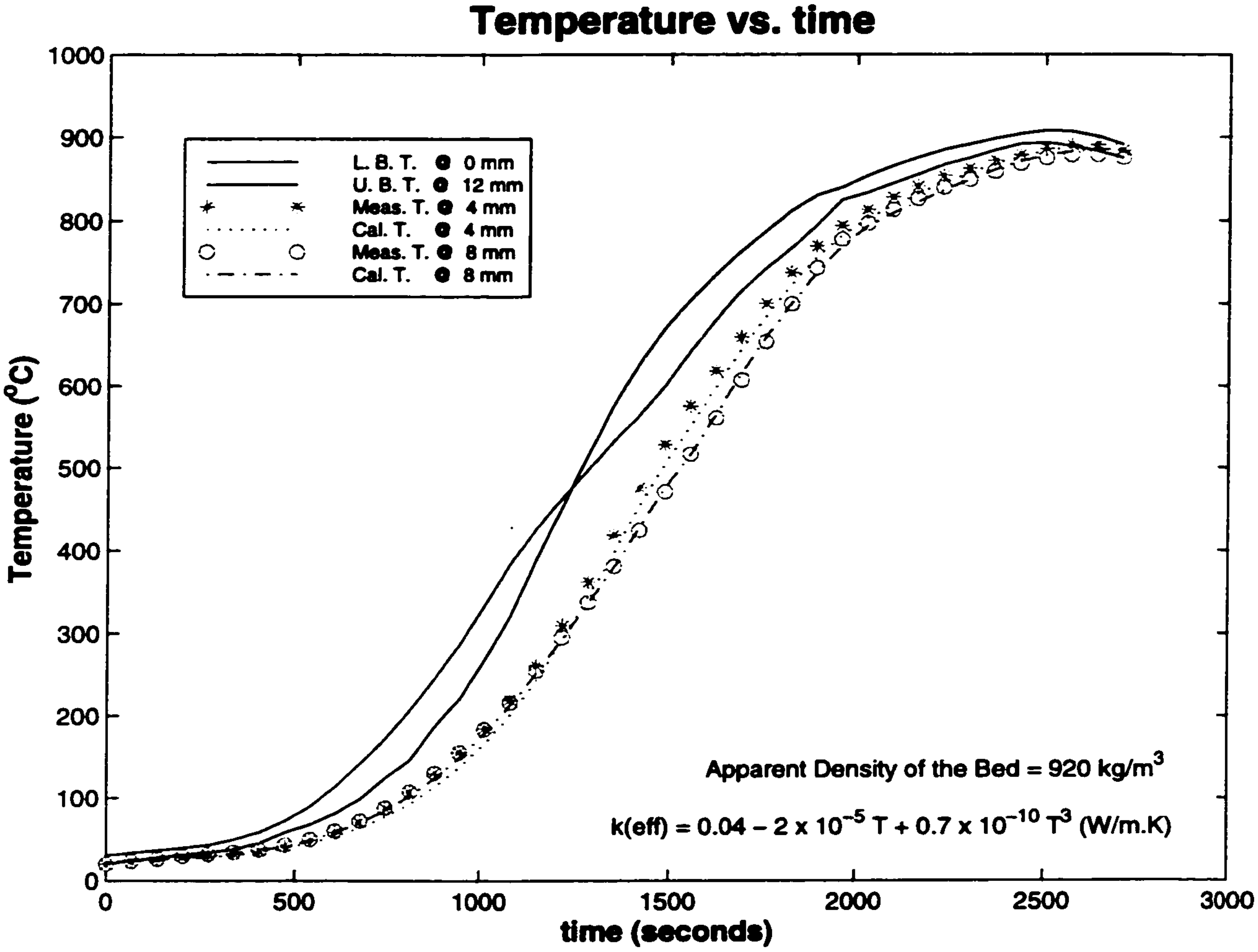

Figure 6.6: Temperature variation of EAF dust type-A at different heights inside the bed, Experiment #50, furnace temperature 1100°C.

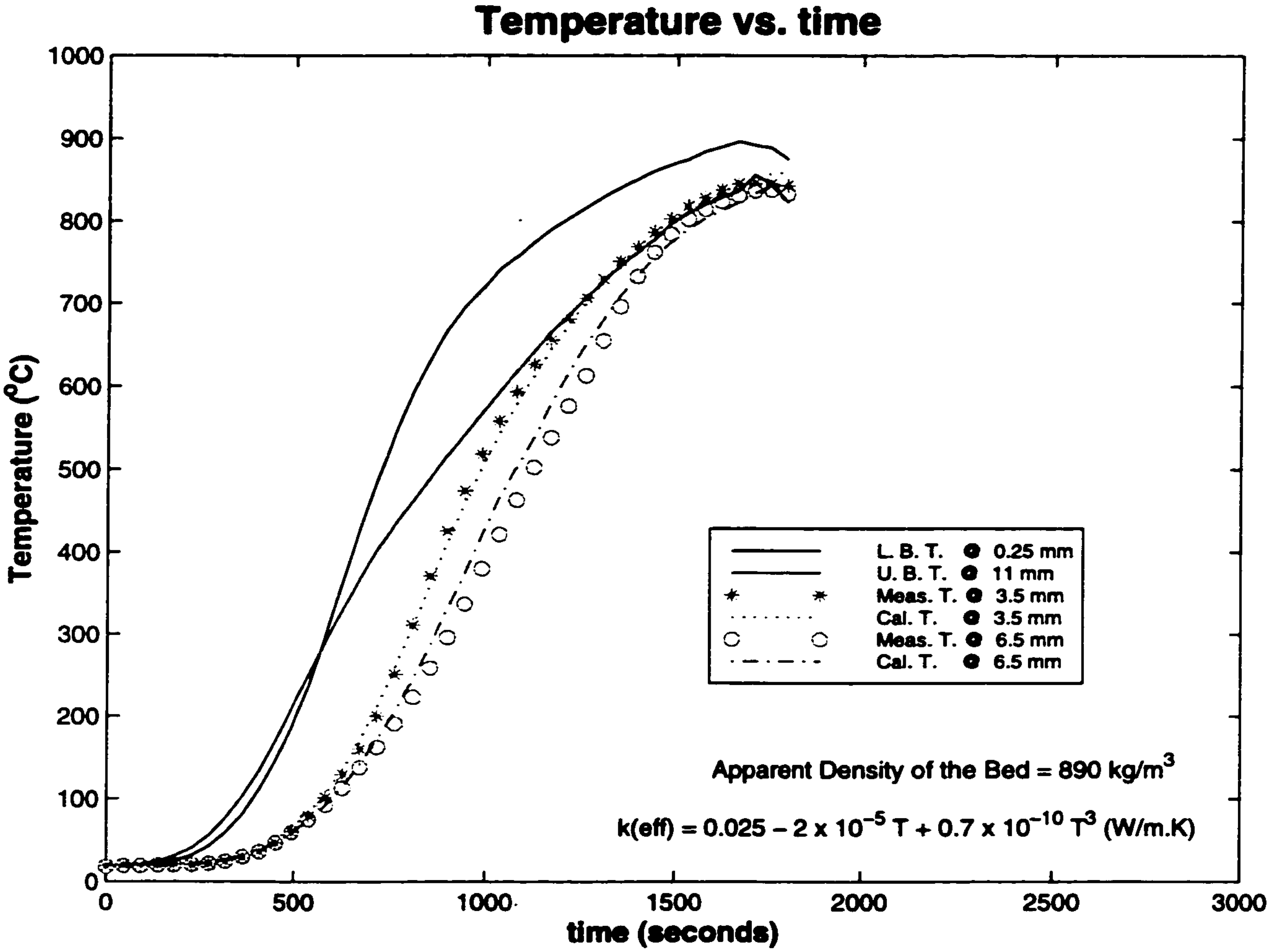

Figure 6.7: Temperature variation of EAF dust type-A at different heights inside the bed, Experiment #54, furnace temperature 1100°C.

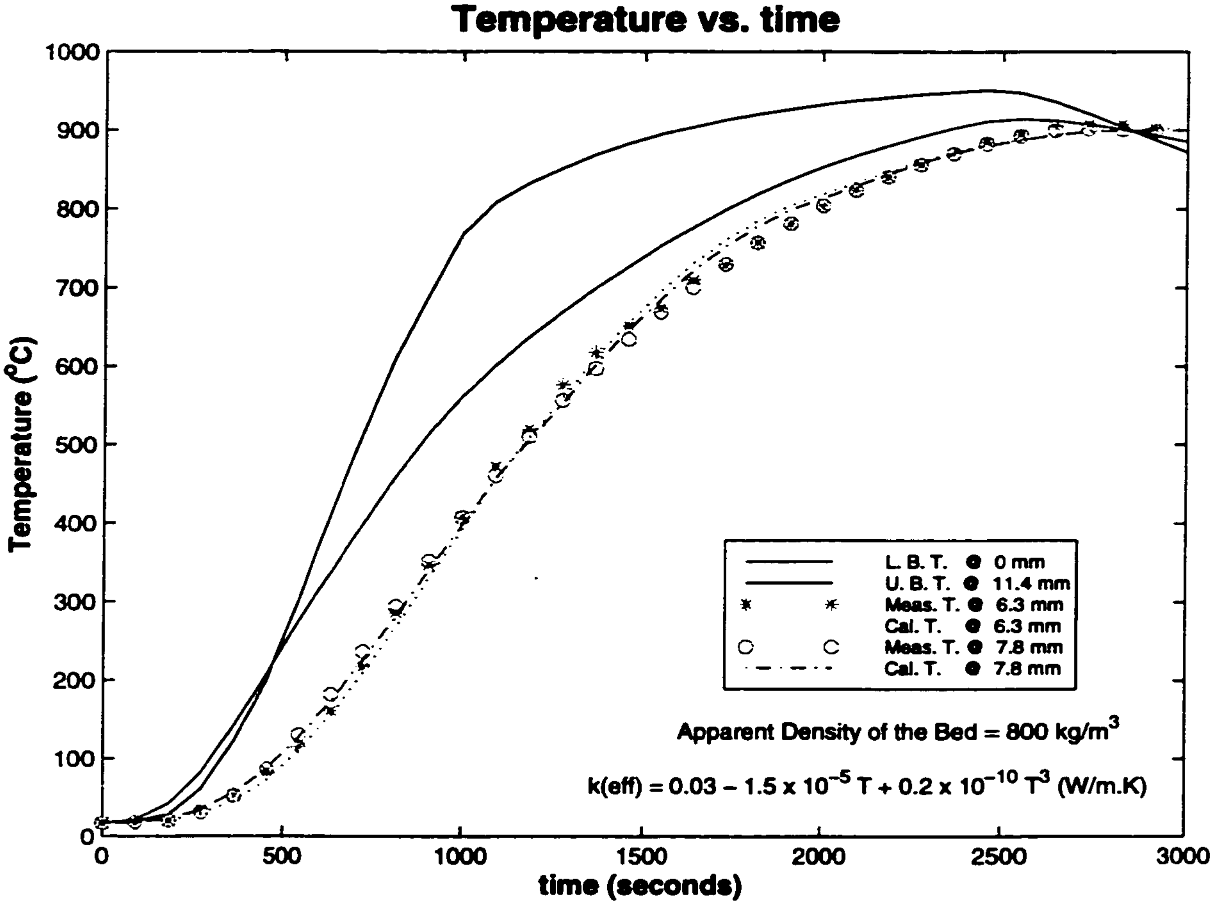

Figure 6.8: Temperature variation of alumina at different heights inside the bed, Experiment #61, furnace temperature 1100°C.

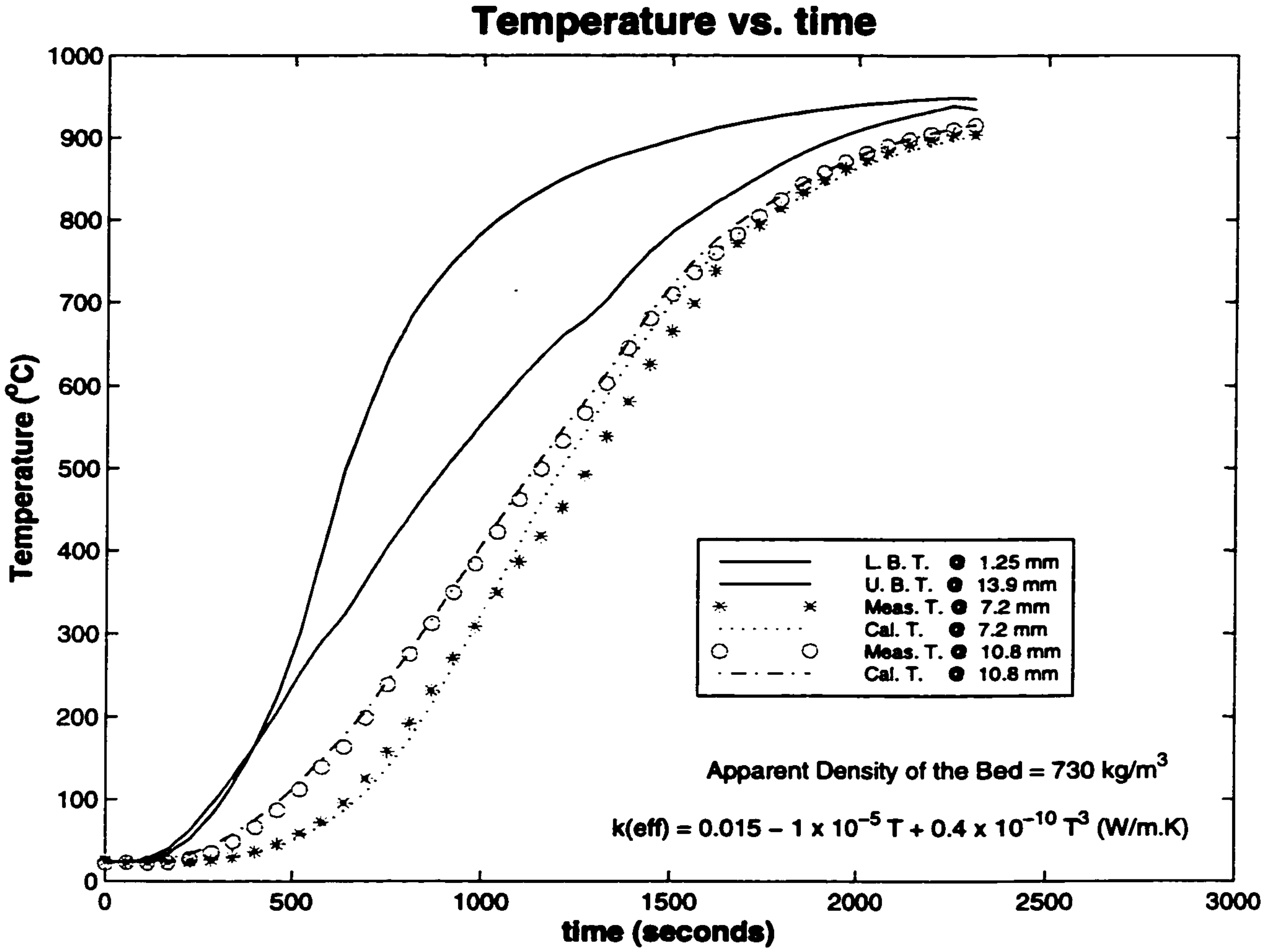

Figure 6.9: Temperature variation of EAF dust type-C at different heights inside the bed, Experiment #62, furnace temperature 1100°C.

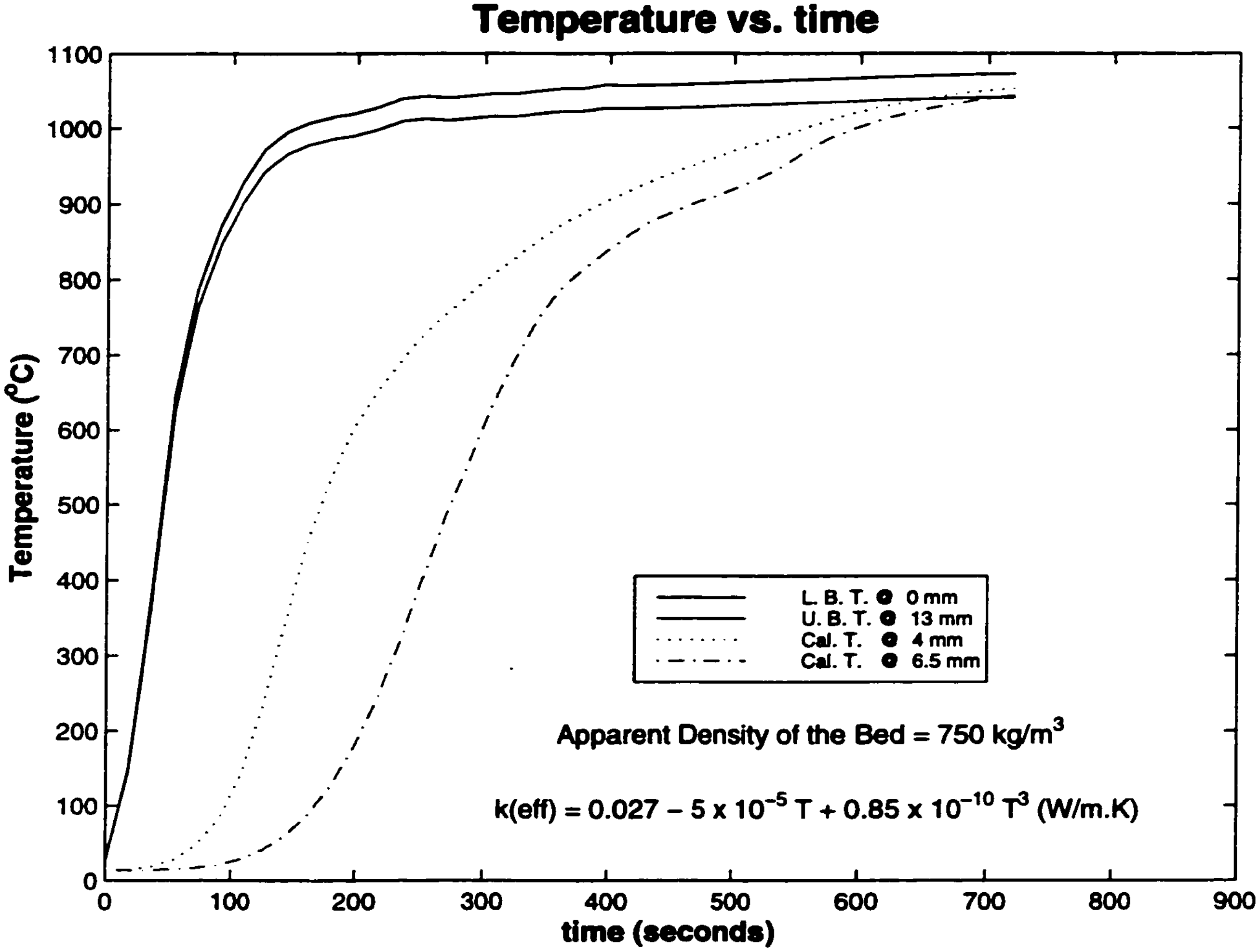

Figure 6.10: Calculated temperature of EAF dust type-A at different heights inside the bed for cylindrical reaction chamber, furnace temperature 1100°C.

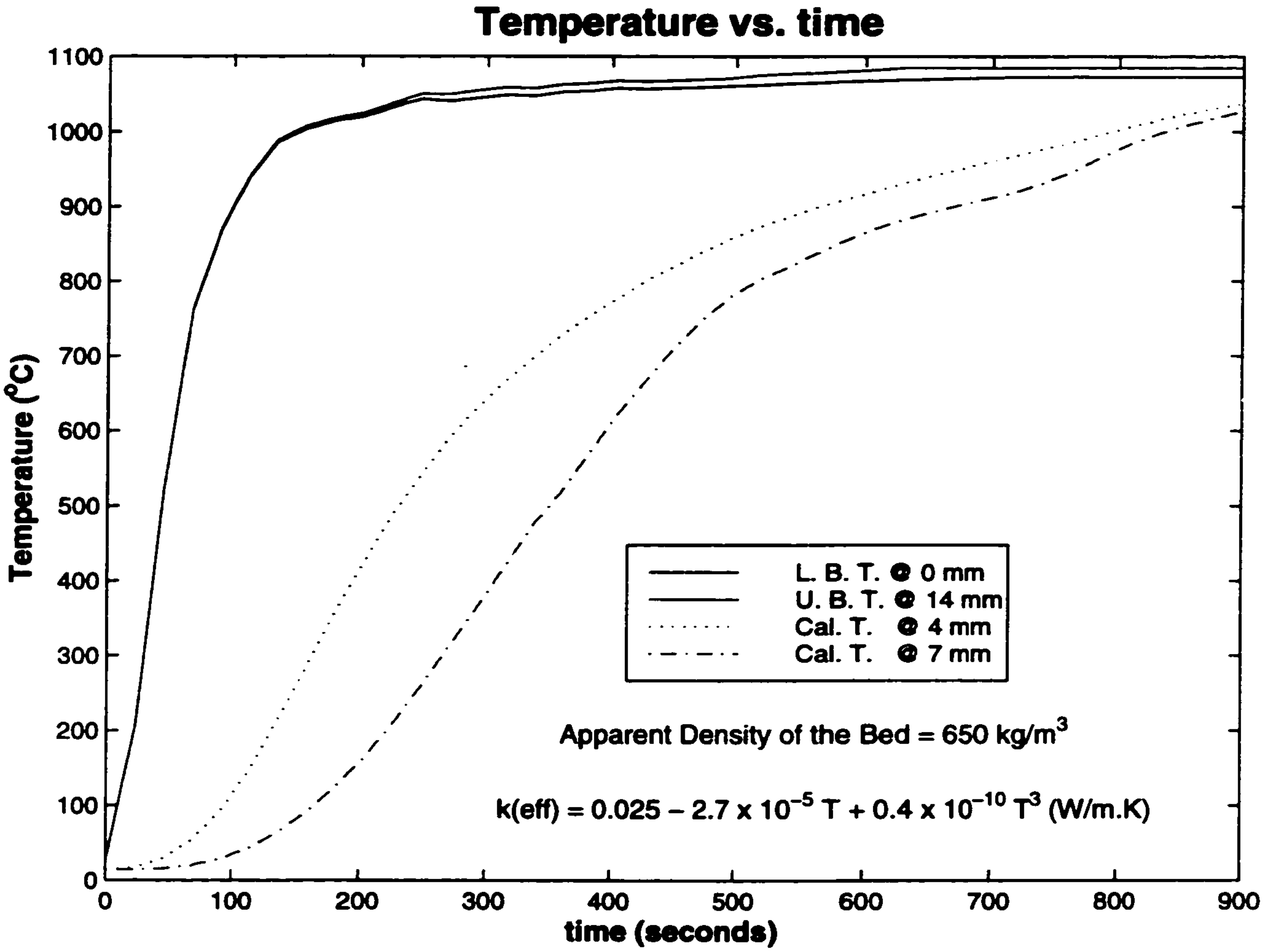

Figure 6.11: Calculated temperature of EAF dust type-B at different heights inside the bed for cylindrical reaction chamber, furnace temperature 1100°C.

Chapter 7

DISCUSSION

This chapter will be presented in two parts with respect to the scientific understanding and the potential industrial applications. The first part will briefly review the significance of the thermodynamic computations and the heat and mass transfer in the system. It also includes the comparison of experimental results and theoretical analysis which leads to a better understanding of the mechanisms of the separation process. In the second part of this chapter the potential industrial applications of the separation process will be described.

7.1 Significance of Thermodynamic Computations

7.1.1 Chemical equilibrium

In chapter 3 the procedure for thermodynamic computations of the equilibrium states was explained and the results of these computations for EAF dust type-A and type-B under different conditions were reported. The main objective was to examine the possibility of separating "more volatile species" from "less volatile species" in the dust. It was concluded that the separation was feasible from a thermodynamic point of view.

Different carrier gases and additives were considered in order to find the most favorable condition for the separation process. A reducing atmosphere and additives did not improve the conditions for removing alkali halides and lead compounds and could result in reduction of zinc oxide and consequently promote gasification of zinc. Higher oxygen potential could slightly improve the separation process. The addition of $CaCl_2$ enhanced the gasification of volatile species by providing more chlorine to the system, but resulted in more zinc gasification in the form of $ZnCl_2$.

The changes in atmosphere and the use of additives except $CaCl_2$ had little beneficial effect on the results of thermodynamic computations; therefore, these factors may be considered to be minor. Although the addition of $CaCl_2$ could improve the separation process, higher zinc loss is inevitable which is not desired for the pre-treatment of EAF dust.

Since the use of additives or carrier gases could not be of much benefit to the treatment, the separation process was designed to take advantage of reduced pressure so that evaporation and mass transfer in the gaseous phase were promoted. This also had the advantage of a closed system for environmental protection.

7.1.2 Vapor pressure and enthalpy changes

Gaseous pressure in the evaporation compartment was not measured during the experiments but it was needed in the calculations of the mass transfer in the system.

In chapter 3 the equilibrium total vapor pressure over the EAF dust as well as the partial pressure of each volatile species were calculated. The calculated equilibrium vapor pressure is the theoretical maximum pressure for a given composition of the dust. Due to the high temperature, the equilibrium state is most likely maintained in the evaporation compartment.

The enthalpy changes of the system were calculated at different temperatures. The patterns in the plots of enthalpy changes vs. temperature may illustrate the major phase transformations during heating of the dust. The values of enthalpy changes were used in the study of the heat transfer. In Chapter 6 the advantages of using these data to simplify the numerical program for the calculations of the heat conduction inside the dust bed was explained.

7.2 Discussion of the Experimental Results

The experiments were designed based on the theoretical understandings of the system. The discussion of the experimental results are presented in two parts. The first part deals with some observations and their consistency with the theoretical understanding of the system. In the second part the results of the experiments related to the rate controlling step are discussed. The mechanism of the separation process is therefore proposed based on the theoretical understanding and the experimental results.

7.2.1 Consistency of experimental observations

The effects of oxidizing and reducing atmosphere as well as the effects of adding Fe_2O_3 and $CaCl_2$ to EAF dust were examined during some preliminary experiments.

The temperature variations and the chemical composition across the dust bed were investigated using the stationary rectangular reaction chamber. In some experiments the total pressure of the system was higher ($660 - 6600\,Pa$ or $5 - 50\,torr$) than the target pressure ($66 - 133\,Pa$ or $0.5 - 1\ torr$). The significance of the results from these experiments will be discussed in the following sections.

Effects of atmosphere and additives

In chapter 3 the effects of oxidizing and reducing atmospheres on separation of the volatile species from EAF dust were considered from a thermodynamic point of view. In a preliminary set of experiments EAF dust type-A was treated under three different atmospheres of flowing air, nitrogen and $CO/CO_2(1:9)$. The experiments were run at different temperatures and times. The results are given in Table 5.10. Since duration of these experiments was long (40 to 80 minutes for 5 grams of dust), all experiments at $1100°C$, $1200°C$ and $1300°C$ resulted in about 99% removal of chlorides. All experiments under CO/CO_2 mixture resulted in more gasification of zinc, e.g. over 50% at $1300°C$. Due to the long duration of the experiments, a distinct difference can not be made between the air and nitrogen being used as a carrier gas. In these experiments at any given temperature longer treatment resulted in a higher degree of removal, regardless of the carrier gas.

On the effect of additives, from chapter 3 it was concluded that addition of Fe_2O_3 to EAF dust would slightly increase the oxygen potential of the system and improve the separation process while it retards the reduction of ZnO.

Table 7.1: Degree of removal of volatile species from EAF dust type-A treated for 10 minutes in stationary cylindrical reaction chamber.

Additive	**Dust wt. gr.**	**Total wt. gr.**	**Pb%**	**Na%**	**K%**
N/A	25	25	94.3	73.4	89.2
$\mathbf{Fe_2O_3}$	25	30	89.7	71.0	87.7

Table 7.2: Degree of removal of volatile species from EAF dust type-A treated for 8 minutes in stationary cylindrical reaction chamber at 1100°C.

Additive	**Dust wt.**	**Total wt.**	**Zn loss%**	**Pb%**	**Na%**	**K%**
$\mathbf{Fe_2O_3}$	25 gr	30 gr	5.0	82.8	66.3	84.8
$\mathbf{Fe_2O_3 + CaCl_2}$	25 gr	30 gr	9.2	92.7	84.5	88.7

The results of experiments with and without adding Fe_2O_3 to EAF dust type-A are listed in table 7.1 . These results are contrary to what is suggested by thermodynamic computations. The addition of Fe_2O_3 resulted in lower degree of removal of the volatile species when compared to the results of experiments without any additives. It should be noted that the main effect of Fe_2O_3 addition was a thicker bed which means longer distance for heat transfer and larger total heat capacity. For a 10 minute treatment at 1100°C, the degree of removal of the volatile species was lower as a result of Fe_2O_3 addition. Therefore, the effect of larger size of dust bed appeared to be greater than that due to higher equilibrium oxygen potential under the conditions investigated.

Based on the thermodynamic study, the addition of $CaCl_2$ promotes the gasification of volatile chlorides by increasing the amount of chlorine available in the system. The addition of $CaCl_2$ resulted in more zinc gasification as $ZnCl_2$. Table 7.2 shows the results of adding $CaCl_2$ to EAF dust type-A. Obviously this addition promoted evaporation and resulted in higher degrees of removal of lead, sodium and potassium, however, at the same time zinc gasification was increased.

Temperature changes inside the dust bed

Partial melting and evaporation of the volatile species that take place during heating of EAF dust can be shown by thermodynamic computations, chapter 3. In Figures 3.2 and 3.3 the calculated amounts of solid, liquid and gas phases are plotted vs. temperature for EAF dust type-A and type-B. Partial melting starts at about $450°C$ and the amount of liquid reaches a maximum at about $800°C$. During the course of evaporation $(800 - 900°C)$, the composition of the liquid phase changes due to the loss of the volatile components and the melting temperature of the remaining liquid rises, eventually the liquid phase solidifies.

This phenomenon can be explained by examining the experimental results on the graphs of dust temperature vs. time. In Figure 5.6, the temperature variation of alumina powder with time is plotted at different bed heights. Theses curves do not show any particular feature pertinent to a phase transformation. In contrast, in experiment with the mixture of same alumina and 5% KCl, Figure 5.7, a clear sign of a phase transformation can be seen at a temperature just below the melting point of KCl $(771°C)$. The lower melting temperature is most likely related to the melting of a solution of KCl with the impurities present in the mixture. This plateau of almost constant temperature is the result of a balance of the rates of heat in, heat out and heat consumption at the location of the thermocouple.

As can be seen in Figure 5.7 and also plots of EAF dust temperature vs. time in Figures 5.9 to 5.11, such a plateau of constant temperature appears only at some locations in the dust bed. The appearance and the extent of this plateau depend on the rate of heat transfer to and from the position of the thermocouple, the amount of liquid that forms and the amount of volatile species being evaporated. This can be inferred in Figure 5.5 where the temperatures of a dust rich in alkalis and chlorine are plotted vs. time. Obviously, the large amount of volatile species present in this secondary incinerator dust (approximately 70% of the total dust weight) extends the plateau of constant temperature. As the furnace temperature is raised, the rate of heat transfer to dust is increased and it takes a shorter time for melting and evaporating of the volatile species; therefore, a shorter plateau appears on the curve of the temperature profile. Similar temperature measurements for EAF dust type-B in the rotary reaction chamber do not show such a plateau, see Figure 5.4. This is due to less volatile species in EAF dust compared with the secondary incinerator dust. In comparing the temperature changes of the EAF dust in the rectangular reaction chamber with those in the rotary reaction chamber one should also take into account the rate of heat supply to dust which is slower in the case of the rectangular reaction chamber, so that the plateau of constant temperature could be detected for the EAF dust.

Examining the temperature profiles of the EAF dust, a distinct behavior can be observed in the pattern of curve #4 (blue color) in Figures 5.9 to 5.11. This is the recorded temperature at the position of the thermocouple closest to the dust surface. A negative change of slope exists at temperatures between $400°C - 600°C$. The slower rate of temperature rise is the result of partial melting of EAF dust at a slow rate. This effect of latent heat of melting can be seen as a positive change of slope on the plots of enthalpy changes vs. temperature, Figures 3.2 and 3.3. The constant temperature plateau related to the evaporation of volatile species can be observed at about $800°C - 850°C$. This is the only or the largest plateau amongst the four curves.

There also exists a temperature rise just before the plateau. The quick rise in temperature before the plateau, may be attributed to re-condensation of some vapors originated from locations of higher temperature. Re-condensation of vapors inside the dust bed is confirmed by chemical analysis. It can be seen from the results of Experiment #87 in Figures 5.40 to 5.42 that the contents of Pb, Na, and K in the residue at a height of about $8 - 12\,mm$ from the bottom of the dust bed is higher than their original values in the dust before treatment. It may be concluded that the longer plateau in curve #4 (blue color) which is related to evaporation of volatile species is a result of a higher amount of volatile species due to earlier re-condensation at this position.

Chemical composition across the dust bed

The overall degree of removal of volatile species from dust depends on the experimental conditions, such as the temperature of the evaporation compartment, the total pressure at the cold end and the duration of the experiment. However, due to a different thermal state of each location inside the bed, for the same experimental conditions in a stationary dust bed different degrees of removal across the dust bed would be expected.

In experiments with shorter duration, a clear difference can be observed in the chemical composition of the residues taken from different heights of the dust bed. The lower and the upper sections show higher degrees of removal of the volatile species while the residue from the centre part of the dust bed has a higher content of volatile species, see Figures 5.34 to 5.36.

Obviously, this is related to the difference in thermal history of the dust at different positions inside the bed. Upper and lower sections of the dust bed reach higher temperatures during the experiment, but the centre portion of the bed experiences lower peak temperatures. When the duration of treatment is extended, the variation in chemical composition across the dust bed is minimized, see Figures 5.34 - 5.36. This is because of a more uniform temperature distribution towards the end of the experiments and little changes in the chemical composition of the residue at temperatures above $900°C$.

Effect of higher total pressure in the cold compartment

Some experiments were carried out at a pressure ($660-6600\,Pa$ or $5 - 50\,torr$) which was higher than the target pressure ($66 - 133\,Pa$ or $0.5 - 1\,torr$) intended for the treatment of EAF dust in this study. The effects of this higher pressure in the cold compartment are discussed in the following sections.

Effective thermal conductivity and heat transfer As the pressure of the system increases the effective thermal conductivity of a powder packing of high porosity would rise, therefore, heat transfer inside the packing would be enhanced. From Figure 7.1[48] it may be deduced that a change of pressure from $133\,Pa$ ($1\,torr$) to $6600\,Pa$ ($50\,torr$) can cause several fold increase in the effective thermal conductivity of a packing of one micron size powder. From chapter 6, the estimated effective thermal conductivity of the dust bed for experiment #87 was $0.024\ W.m^{-1}.K^{-1}$ at $550°C$ and $0.057\ W.m^{-1}.K^{-1}$ at $900°C$ where the pressure varied in the range of $50-360\ Pa$ ($0.4 - 2.7\ torr$). In Experiment #64 with the same type of dust and the same bed height, total pressure of the cold compartment varied between $93\ Pa$ and $6930\ Pa$

(7 to 52 *torr*). For this experiment the effective thermal conductivity of the dust packing was estimated to be 0.039 $W.m^{-1}.K^{-1}$ at 550°C and 0.117 $W.m^{-1}.K^{-1}$ at 900°C.

Figures 5.16 and 5.17 compare the temperature profile across the bed of EAF dust type-B after 18 and 28 minutes in four different experiments. In experiments #63 and #64 the pressure varied and increased during the experiment due to a leak. Note the pressure of the reaction chamber in experiment #63 is 1600 Pa (12 *torr*) at 18 minutes and 3200 Pa (24 *torr*) at 28 minutes. In experiment #64 the reaction chamber has a pressure of 5330 Pa (40 *torr*) at 18 minutes and 6930 Pa (52 *torr*) at 28 minutes. Experiments #87 and #88 were carried out at the normal reduced pressure. The height of the dust bed is equal to 17 mm in experiments #63 and #88 and 18.5 mm in experiments #64 and #87.

The difference in temperature profiles of experiment #87 and #88 is due to their different bed heights. Larger bed height in experiment #87 results in lower effective thermal conductivity and longer distance for heat transfer to the centre of the dust bed. Therefore, in experiment #87 the interior temperature of the dust is lower than that of the corresponding position in experiment #88.

Experiment #63 has a similar bed height to experiment #88. At 18 minutes the temperature of the dust in experiment #63 is lower than that of experiment #88. This can be explained by the fact that the boundary temperatures in experiment #88 are higher. The bottom temperature in experiment #88 is about 40°C higher than that of experiment #63. Also on the upper part of the dust bed, experiment #88 has a steep temperature profile which indicates a higher surface temperature for the same bed height. Regardless of this, at 28 minutes the temperature profile in experiment

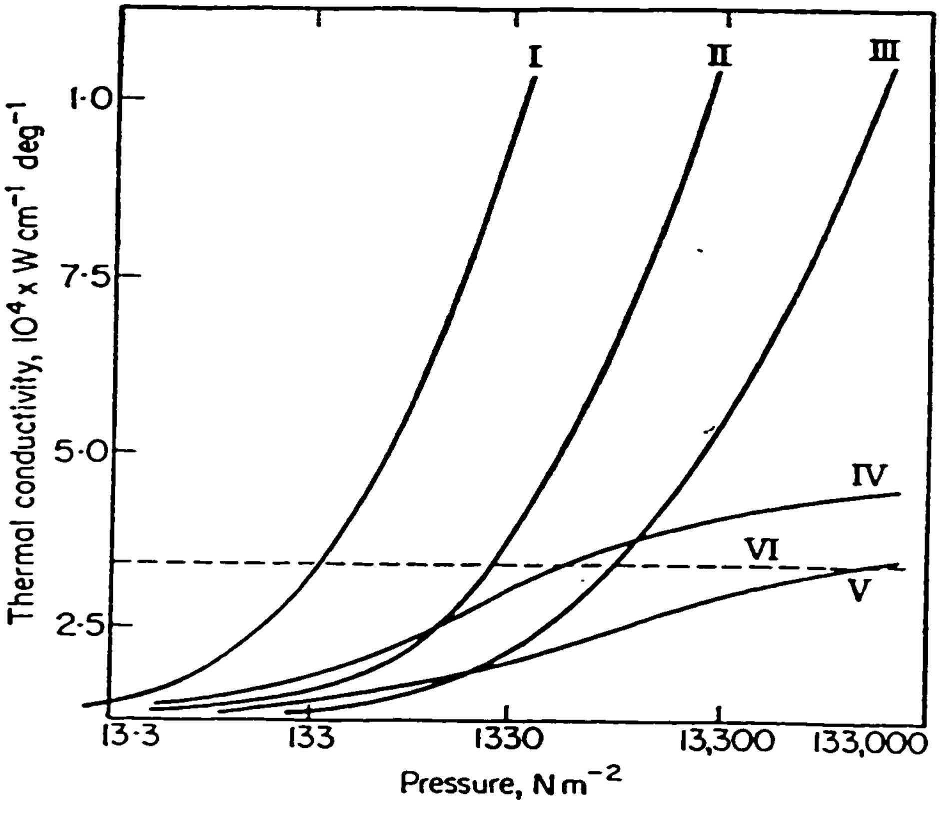

Figure 7.1: Apparent thermal conductivity of powders. I. quartz sand, grains 0.26 *mm*; II. zinc dust, grains 0.028 *mm*; III. zinc dust, grains 0.0062 *mm*; IV. spongy diatomaceous earth; V. spongy lamp soot; VI. air [48].

#63 shows higher values compared to those of experiment #88. This is because of increasing pressure in the reaction chamber.

Among these four temperature profiles, experiment #64 regardless of its larger bed height has the highest interior temperature of the dust bed. This is obviously as a result of the increased effective thermal conductivity caused by higher pressure of the reaction chamber.

Degree of removal of volatile species When the pressure at the cold end of the reaction chamber is low enough ($66 - 133\,Pa$ or $0.5 - 1\,torr$), mass transfer in the gaseous phase between the two compartments is not the limiting step as discussed in chapter 6. However, if the pressure at the cold end were higher than the total equilibrium vapor pressure over the dust at the hot zone, a pressure difference between the two compartments could not be maintained. Therefore, the mass transfer in the gaseous phase under this condition is in the form of molecular diffusion driven by the difference in partial pressure of each volatile species. In such a case the rate of overall reaction is adversely affected and a lower degree of removal will result.

The degrees of removal of volatile species for an experiment with the rotary reaction chamber run at higher total pressure, $133 - 600\,Pa$ ($1 - 4.5\ torr$), are given in table 7.3 along with those of experiments carried out under a normal reduced pressure, $66 - 200\,Pa$ ($0.5 - 1.5\,torr$). Higher total pressure in Experiment #103 is caused by an air leak in the system. The results of Experiment #103 (duration = 15 minutes) show lower degrees of removal compared to those of Experiment #101 with even shorter experiment duration (duration = 10 minutes). Both experiments are carried out at the same temperature, $900°C$, and under similar conditions other than

Table 7.3: Degree of removal of volatile species for EAF dust type-B treated in rotary reaction chamber at $900°C$.

Exp. No.	Duration minute	Pressure Pa	torr	Pb	Na	K
101	10	67 – 200	0.5 – 1.5	81.7%	47.9%	49.4%
103	15	133 – 600	1.0 – 4.5	70.7%	35.4%	40.5%
92	18	67 – 200	0.5 – 1.5	86.5%	73.5%	61.7%

the pressure.

Chemical composition of the residues across the dust bed In experiments with the rectangular reaction chamber under a higher total pressure, more volatile species in the residue are detected at the surface and in the bottom section of the dust bed after the treatment. This can be explained by considering the possibility of re-condensation of volatile species on the sides of the dust bed during the cooling of the reaction chamber at the end of the experiment. Two factors should be taken into account in this regard. One is the faster temperature drop of the surface and the bottom sections of the bed during the cooling of the reaction chamber in comparison with the centre parts. The second factor is the higher total pressure of the cold compartment which causes a much slower mass transfer from the evaporation compartment to the condensation compartment.

Figure 5.14 illustrates the temperature profile in an experiment with a total pressure of $2660 - 3330\,Pa$ ($20 - 25$ *torr*). The temperature at the centre part of the dust bed was rising even after the reaction chamber was removed from the furnace. However, the temperatures of the top and the bottom surfaces drop quickly. It should be noted that while the colder parts of the dust bed provide suitable sites for re-condensation, higher total pressure inside the reaction chamber hinders the transfer of the vapors to the condensation compartment. In other words, a system at higher total pressure leaves more volatile species in the evaporation compartment for re-condensation.

7.3 Review of Mass and Heat Transfer

In chapter 6 mass and heat transfer in the system were considered. The rate of mass transfer for each kinetic step was calculated and shown to be much faster than the observed overall rate of reaction under the conditions of the present work.

The driving force for the evaporation and condensation is the difference between the residual pressure and the equilibrium vapor pressure at the surface of the condensed phase. For evaporation the equilibrium vapor pressure is dictated by the dust temperature, but the residual pressure in the hot compartment depends on the mass transfer between the two compartments.

Mass transfer between the two compartments of different temperatures depends on the pressure gradient and it was shown that in the extreme case the flow could reach the speed of sound. With the high rate of evaporation the pressure of the hot compartment mainly depends on temperature of the dust. When there is no permanent gas in the system, the residual pressure in the cold compartment is controlled by the rate of condensation. Providing appropriate conditions for fast condensation, e.g. increasing the surface area available for condensation, the required pressure gradient between the two compartments can be achieved so that volatile species could be transferred to the condensation compartment at a relatively high speed.

Mass transfer within the dust bed was considered based on molecular flow. The major parameter affecting the molecular flow inside the dust bed is the pore size.

Therefore, agglomeration of the dust particles in a stationary bed is of particular importance. Obviously, in a rotary reaction chamber this step does not exercise any significant resistance to the overall kinetics.

Considering the heat transfer in the system it was concluded that the main kinetic step was the heat transfer across the dust bed. In chapter 6 a numerical analysis of the heat transfer inside the dust bed was presented and it was shown that the rate of heat transfer across the packed bed was comparable to the observed rate of overall reaction. In the following sections experimental evidence of this claim will be discussed.

7.4 Rate Controlling Step

7.4.1 Effect of apparent density of the dust bed

One of the most important factors leading to the low thermal conductivity of the dust bed is the high porosity of the packing. In another words, the apparent density of the packing plays an important role in the heat transfer of the dust bed at reduced pressure. In the following sections the effect of this physical property is discussed based on different types of EAF dust and different packings of the same dust.

EAF dust type-A vs. type-B

With respect to the kinetics of separation, the most important difference in physical and chemical properties of these two types of EAF dusts is the apparent density. The bulk density of EAF dust type-A without any compacting is $\backsim$ 750 kg/m^3 while EAF dust type-B has a lower value of $\backsim$ 650 kg/m^3. This difference in apparent density

Table 7.4: Degree of removal of volatile species for two different types of EAF dust treated in stationary reaction chamber at 1100°C.

Treatment Duration	Pb		Na		K	
	Type-A	Type-B	Type-A	Type-B	Type-A	Type-B
7 minutes	76%	N/A	54%	N/A	79%	N/A
8 minutes	86%	75%	72%	54%	87%	87%
10 minutes	94%	N/A	78%	N/A	95%	N/A
12 minutes	96%	91.5%	83%	79%	98.5%	96%

affects the heat transfer inside the dust bed and increases the treatment time required for the dust of lower density to reach the same degree of removal of volatile species. In fact longer duration of treatment for a dust bed of lower apparent density is because of not only a lower effective thermal conductivity but also a larger bed height for the specimen of the same mass.

Table 7.4 summarizes the results of the experiments carried out with stationary cylindrical reaction chamber for EAF dust type-A and -B at 1100°C. For 7 and 10 minute treatments, dust type-A yielded similar results to those of dust type-B treated for 8 and 12 minutes, respectively. After 12 minutes of heating, dust type-A resulted in higher degree of removal of volatile species compared with dust type-B. It should be noted that dust type-A contains more volatile species, therefore, a larger amount of material must be transferred for the same degree of removal.

Packing of the dust bed

Experiments #48, #49 and #50 were carried out in the rectangular reaction chamber with EAF dust type-A. In Experiments #48 and #49 dust was loosely placed inside the nickel boat (bed height $\simeq$ 16 and 16.5 mm, respectively). In Experiment #50 a vibrator was used to settle the dust inside the nickel boat and therefore the

Table 7.5: Estimated effective thermal conductivity of the dust bed for EAF dust type-A.

Experiment Number	**Bed Height mm**	**Packing Density kg/m^3**	**k_{eff}(W.m^{-1}.K^{-1})**			
			@25°C	**@200°C**	**@550°C**	**@900°C**
48	16.1	780	0.014	0.017	0.040	0.100
49	16.5	750	0.009	0.012	0.035	0.095
50	13.5	890	0.037	0.040	0.067	0.135

Table 7.6: Degree of removal of volatile species for two different types of EAF dust treated in rotary reaction chamber at 1100°C.

Treatment Duration	**Pb**		**Na**		**K**	
	Type-A	**Type-B**	**Type-A**	**Type-B**	**Type-A**	**Type-B**
4 minutes	N/A	80%	N/A	59%	N/A	66%
5 minutes	91.3%	89%	66.5%	69.5%	88%	84%
6 minutes	N/A	91%	N/A	84%	N/A	94%
7 minutes	95.4%	N/A	78.4%	N/A	97%	N/A
8 minutes	N/A	92%	N/A	88%	N/A	99%

dust bed was somewhat compacted (bed height $\simeq$ 13.5 mm). The effective thermal conductivities of the dust beds in these experiments were estimated as described in section 6.2.2 and are summarized in Table 7.5 for three different temperatures.

The effective thermal conductivity of the compacted dust bed (Experiment #50) was higher than those of the lower density beds. Faster heat transfer inside the dust bed for Experiment #50 resulted in a shorter treatment time (40 minutes) compared to Experiment #49 (50 minutes) yielding a similar degree of removal of volatile species. With the same duration of treatment, Experiment #50 had a higher degree of removal in comparison with Experiment #48. The results of these experiments are plotted in Figures 5.34 to 5.36.

Table 7.7: Degree of removal of volatile species for EAF dust type-B treated in stationary and rotary reaction chambers at 950°C.

Treatment Duration	Pb		Na		K	
	Stat.	Rotary	Stat.	Rotary	Stat.	Rotary
6 minutes	N/A	62%	N/A	43%	N/A	48%
8 minutes	24%	81%	4%	61%	13%	68.5%
10 minutes	N/A	83%	N/A	72.5%	N/A	78%
12 minutes	51%	N/A	13%	N/A	27%	N/A

Table 7.8: Degree of removal of volatile species for EAF dust type-B treated in stationary and rotary reaction chambers at 1100°C.

Treatment Duration	Pb		Na		K	
	Stat.	Rotary	Stat.	Rotary	Stat.	Rotary
5 minutes	N/A	89%	N/A	70%	N/A	83.5%
6 minutes	N/A	91%	N/A	84%	N/A	96%
8 minutes	74%	92%	54%	86%	62.5%	98%
12 minutes	91.5%	N/A	79%	N/A	96%	N/A

7.4.2 Effect of rotating the reaction chamber

The rotary reaction chamber was designed to eliminate the limitation of the heat transfer within the dust bed and to enhance the heat transfer to dust particles. This was accomplished by rotating the reaction chamber ($\sim$ 1 rpm), causing dust to tumble and exposing colder dust particles to the radiating surfaces, hence, benefiting from direct radiative heat transfer. Renewal of the dust particles in contact with the hot chamber walls also contributes to heat transfer to dust particles.

The effect of different apparent densities of EAF dusts type-A and type-B on their treatment time was explained for the stationary reaction chamber. In Table 7.6 the degrees of removal of lead, sodium and potassium are tabulated for the two types of EAF dust treated in the rotary reaction chamber at 1100°C. Contrary to the results of the stationary reaction chamber these results do not show any significant difference between the two types of dust with regard to the treatment time. It is obvious that the rotation of the reaction chamber has changed the kinetics and mechanism of the overall reaction under investigation.

In Figures 5.23 and 5.24 the results of treating EAF dust type-B in rotary reaction chamber are compared with those of the experiments run in the stationary reaction chamber. In these experiments the experimental conditions are the same except for the rotational motion. It can be seen that the treatment time may be substantially decreased for the same degree of removal with the rotary reaction chamber. Tables 7.7 and 7.8 summarize the degrees of removal of lead, sodium and potassium for some of these experiments. It should be noted that the total treatment time includes a heating period for the reaction chamber itself which is about 2 minutes, refer to Figure 5.2. Using the rotary reaction chamber, at 1100°C a similar degree of removal is achieved in 6 minutes compared with 12 minutes of treatment in stationary reaction chamber, Table 7.8.

At a lower furnace temperature of 950°C, Table 7.7, the effect of rotation is even more significant. While the degrees of removal in stationary reaction chamber after 8 minutes treatment, are about 24%, 4% and 13% for Pb, Na and K, respectively, under similar experimental conditions the use of rotary reaction chamber resulted in removal of 81% Pb, 61% Na and 68% K. The rotary reaction chamber provides a better heat transfer mechanism so that the treatment can be done at a lower furnace temperature within a reasonable time, whereas the stationary reaction chamber would take a much longer time to obtain similar results because there exists a very small driving force for heat transfer across the dust bed at a furnace temperature close to that of evaporation of volatile species.

7.5 Potential Industrial Applications

It was mentioned in Chapter 2 that in all high temperature processes volatile components are enriched in the collected dusts. These volatile species are mainly two types of compounds, alkali halides and oxides of heavy metals. Examples of the high temperature processes are melting of steel scrap, smelting of non-ferrous metals, municipal waste incineration and cement manufacturing.

In all these processes, the dust has to be collected for environmental protection and treated for toxicity and for more efficient recovery of the valuable components. Recycling of the dust is a part of some processes like nickel smelting and cement manufacturing. In these processes dust is further enriched in volatile compounds. For energy considerations, productivity and quality of the product, a portion of the dust has to be removed from the system. The separation process studied in this work, i.e. a closed system with two compartments of different temperatures under reduced pressure, may be used to substantially remove the volatile species from the dust generated in these processes. For the dust which is treated for metal recovery, this pre-treatment under reduced pressure will produce a residue with higher concentration of zinc and iron and low content of halides and compounds of heavy metals. For the recycling dust, this treatment can be used as an intermediate stage to reduce the level of volatile species in the dust cycle. This reduces the total amount of material to be recycled. It is also very important in cases such as cement manufacturing where a lower content of alkali halides in the kiln will result in a higher quality product.

As another example beside the EAF dust, a secondary incinerator dust was also treated in this work. This dust is generated by a resistant electric furnace which is used to melt the remaining residue and the flue dust of the incinerator furnaces of municipal wastes. The results of these experiments are presented in chapter 5. The oxide residue after treatment is rich in zinc ($\backsim$ 78%$wt.$) with a low content of lead and iron ($< 0.1\%wt.$ Pb and $3\%wt.$ Fe). This residue can be directly used as a raw material by zinc producers. The condensed phase consists of almost $90\%wt.$ $NaCl$ and KCl. In these experiments over $95\%wt.$ of the lead is separated from the residue. The condensed phase can be washed to recover the lead compounds.

The importance of the pressure difference between the evaporation compartment and condensation compartment was explained in chapter 6. When the total pressure at the cold compartment is less than half of the equilibrium vapor pressure above the dust in the evaporation compartment, the velocity of the gaseous phase reaches the speed of sound. This provides an effective mechanism of mass transportation, however, it may not be necessary in an industrial reactor where the vapor passage can be of much larger cross section area. On the other hand, temperature dependence of pressure in the evaporation compartment is an advantage for practical purposes. In the design of an industrial reactor the vacuum capability and the working temperature of the evaporation compartment have to be considered as mutual compensating parameters. A lower working temperature demands a system with more powerful vacuum capability, while a higher temperature furnace does not require a very low pressure at the condensation compartment.

For an industrial process the productivity of the reactor is very important. Considering the mass transfer in the gaseous phase being fast, it may not be a concern in a large scale operation. On the other hand, heat transfer to dust should be the centre of attention. As it is shown in this investigation, in a stationary dust packing, heat transfer inside the bed is the slowest kinetic step. Therefore, if a stationary bed is to be used, the bed height must be kept at a minimum size and the ratio of the surface to the height of the bed should be large enough. However, in a rotary reaction chamber the kinetic barrier of heat transfer across a bed of very low thermal conductivity is eliminated to result in much higher productivity.

7.6 Summary

Thermodynamic calculations and the study of mass and heat transfer in the system suggest that a closed system under reduced pressure should be superior kinetically and environmentally. The experimental observations have confirmed these anticipated differences. Experimental results show that the use of different additives or carrier gases may not significantly improve the separation process.

The most likely rate controlling step of the overall process is established in experiments with the stationary reaction chamber to be the heat transfer across the dust bed. This is further substantiated with the use of a rotary reaction chamber.

Differences in the results of different types of EAF dusts and different conditions of packing are discussed. The effect of rotating the reaction chamber on the treatment time is also explained. In all these cases, the results indicate that heat transfer inside the dust bed is most likely the rate controlling step in the overall process.

Potential industrial applications of the separation process are described. These include treatment of dusts generated in most high temperature processes. Melting of steel scrap, smelting of non-ferrous metals, municipal waste incineration and cement manufacturing are examples of these high temperature processes.

Chapter 8

CONCLUSIONS

8.1 Thermodynamic and Kinetic Considerations

Based on the thermodynamic computations, separation of "more volatile species", such as sodium and potassium chlorides and lead compounds from "less volatile species", such as zinc, iron and calcium oxides in EAF dust is feasible in a closed system consisting of two compartments, which are kept at sufficiently different temperatures.

The temperature gradient is the main parameter in the determination of the driving force, i.e. the vapor pressure gradient of the volatile species between the two compartments.

The absence of permanent gases in the system by operating the apparatus under reduced pressure enhances the mass flux in the vapor phase.

8.2 Experimental Observations

In a stationary cylindrical reaction chamber, substantial separation of components in EAF dust has been achieved. At a furnace temperature of 1100°C under a reduced pressure of the order of 133 Pa (one torr) over 95% of alkali halides and lead compounds were removed from EAF dust.

With the use of a second experimental apparatus, a stationary rectangular reaction chamber, the dominant rate-controlling step was found to be the heat transfer across the dust bed.

A rotary reaction chamber was built to investigate the effect of lowering the kinetic barrier of heat transfer to the reaction site. With the use of this apparatus a significant decrease in overall treatment time was observed. At 1100°C, total treatment time of 25 grams EAF dust, including time of heating the reaction chamber, was reduced from 12 minutes to 6 minutes for the same degree of removal. With the rotary reaction chamber under the same conditions and for the same treatment time, a similar degree of removal was achieved at a lower temperature of 950°C compared with 1100°C for the stationary reaction chamber.

EAF and secondary incinerator dusts have been successfully treated by the rotary reaction chamber at furnace temperatures as low as 950°C. Experiments run for 10 minutes at 950°C resulted in about 80% removal of volatile species from EAF dust. The combined effect of time and temperature on treatment of EAF dust has been investigated.

8.3 Mass and Heat Transfer Studies

In the absence of permanent gases, the mass flux between the evaporation and condensation compartments occurs as a flow of vapor phases following the pressure gradient induced by the temperature gradient. When the pressure of the condensation compartment is less than one half of the pressure in the evaporation compartment the velocity of gas between the two compartments would reach the speed of sound. At such conditions, the highest rate of mass flux is reached at the sonic limit of the vapor phase in the duct that connects evaporation and condensation compartments.

A finite difference code was developed for calculation of the temperature inside the dust bed. This numerical model uses the enthalpy data calculated by FACT program. The program was used to estimate the effective thermal conductivity of the dust packing through curve fitting.

Considerations of the mass transfer between the evaporation and the condensation compartments and the heat transfer inside the dust bed under experimental conditions substantiate that heat transfer across the dust bed is the most likely rate-controlling step.

Bibliography

[1] R. J. Schmitt, ed., *Proceedings of the CMP Electric Arc Furnace Dust Treatment Symposium V*, March 1996.

[2] "Waste minimization." RCRA Amendments, sec. 224, October 3 1984.

[3] Lehigh University, "Characterizatin, recovery and recycling of electric arc furnace dust," tech. rep., Bethlehem, Pa, February 1982.

[4] A. M. Hagni, *Reflected light microscopy, electron microscopy, electron spectroscopy, and x-ray diffraction mineralogical characterization of electric arc furnace dusts.* PhD thesis, University of Missouri-Rolla, 1995.

[5] R. Kaltenhauser, ed., *Disposal, Recycling and Recovery of Electric Furnace Exhaust Dust*, Iron and Steel Society, 410 Commonwealth Drive, Warrendale, PA, U.S.A. 15086, 1987.

[6] D. R. Mac Rae, "Electric arc furnace dust; disposal, recycle and recovery," tech. rep., The Center for Materials Production (CMP), May 1985.

[7] D. R. Mac Rae and P. M. Cowx, "Plasma furnace treatment of EAF dust as demonstrated by Bethlehem-Tetronics," tech. rep., The Center for Materials Production (CMP), November 1988.

[8] J. J. Bosley, ed., *Proceedings of the 1992 CMP Electric Arc Furnace Dust Treatment Symposium*, June 1992.

[9] A. D. Little, "Electric arc furnace dust - 1993 overview," tech. rep., The Center for Materials Production (CMP), July 1993.

[10] J. J. Bosley, ed., *Proceedings of the CMP Electric Arc Furnace Dust Treatment Symposium IV*, February 1994.

[11] P. M. Cowx, "Minimizing electric arc furnace dust," tech. rep., The Center for Materials Production (CMP), February 1995.

[12] S. R. Badger and W. A. Kneller, "The characterization and formation of electric arc furnace dusts," *Electric Furnace Conference Proceedings* **55**, pp. 95–98, 1997.

[13] A. F. Ellis and J. Glover, "Mechanism of fume formation in oxygen steelmaking," *Journal of The Iron and Steel Institute* **209**, pp. 593–599, 1971.

[14] A. G. Szekely, "The formation of oxide fume during oxygen refining of steel," *96th AIME annual meeting* , 1967.

[15] E. T. Turkdogan and L. E. Leake, "Prelimianry studies on the evolution of fumes from iron at high temperatures," *Journal of the Iron and Steel Institute* **192**, pp. 162–170, 1959.

[16] S. Law, "Characterization of steelmaking dust from EAF's," Tech. Rep. 8750, U.S. Bureau of Mines.

[17] C-L. Li and M-S. Tsai, "A crystal phase study of zinc hydroxide chloride in electric arc furnace dust," *Journal of Materials Science* **28**, pp. 4562–4570, 1993.

[18] A. M. Hagni, R. D. Hagni, and C. Demars, "Mineralogical characteristics of electric arc furnace dusts," *JOM* **43**, pp. 28–30, 1991.

[19] C-L. Li and M-S. Tsai, "Mechanism of spinel ferrite dust formation in electric arc furnace steelmaking," *ISIJ International* **33**(2), pp. 284–290, 1993.

[20] G. Stromeier and J. E. Bonestell, "Steelworks residues and the waelz kiln treatment of electric arc furnace dust," *Iron and Steel Engineer* **73**, pp. 87–90, 1996.

[21] T. W. Unger, "Waelz kiln recovery process for electric arc furnace dust," *Disposal, Recycling and Recovery of Electric Furnace Exhaust Dust* , pp. 103–105, 1987.

[22] ElkemTechnology, "Slag resistance furnace for treatment of EAF dust," *Steel Times* **219**, pp. 306–309, 1991.

[23] J. F. Pusateri, R. Chew, and A. E. Stanze, "On-site treatment of eaf dust via the st. joe flame reactor," *Disposal, Recycling and Recovery of Electric Furnace Exhaust Dust* , pp. 97–101, 1987.

[24] R. Lightfoot and J. B. Stockham, "The treatment of EAF dust using the Davy Hi-Plas process," *Pretreatment and reclamation of dusts, sludges and scales in steel plants, McMaster Symposium No. 21* , pp. 225–234, May 1993.

[25] S. O. Santen, "Recovery of metals from steelmaking dusts," *Pretreatment and reclamation of dusts, sludges and scales in steel plants, McMaster Symposium No. 21* , pp. 177–193, May 1993.

[26] H. J. Lehmkuhler and H. Staubner, "Reclamation of iron and steelmaking dusts, sludges and scales using the INMETCO technology," *Pretreatment and reclamation of dusts, sludges and scales in steel plants, McMaster Symposium No. 21* , pp. 237–251, May 1993.

[27] E. Matovich, "On-site disposal of electrical arc furnace dust through flash direct reduction," *Disposal, Recycling and Recovery of Electric Furnace Exhaust Dust* , pp. 107–111, 1987.

[28] N. Sakamoto, K. Takemoto, N. Yamamoto, and I. Ohkochi, "Zinc recovery from zinc-bearing dusts by use of sensible heat of hot metal," *ISIJ* **35**(11), pp. 1323–1330, 1995.

[29] S. Eriksson, H. G. Herlitz, and S. O. Santen, "Operating experience with the plasmadust process," *Disposal, Recycling and Recovery of Electric Furnace Exhaust Dust* , pp. 145–149, 1987.

[30] T. Matsuoka, S. Kurozu, and Y. Koyabu, "New technology for treating electric arc furnace dust," *Iron and Steel Engineer* **68**, pp. 37–40, 1991.

[31] C. D. Chapman and P. M. Cowx, "Treatment of EAF dust by tetronics plasma process," *Steel Times* **219**, pp. 301–304, 1991.

[32] R. Lightfoot, "Hi-plas treating steelwork dust," *Steel Times* **219**, pp. 559–562, 1991.

[33] M. Osada, H. Ono, S. Osada, and H. Osana, "Applicaion expansion of incineration ash melting technology and development of incineration ash recycling technology," Tech. Rep. 70, Nippon Steel Technical, July 1996.

[34] T. Nakao, K. Nakahara, and T. Akashi, "Electric-resistance furnace for melting ash from municipal solid waste incinerator," June 1997.

[35] C. W. Bale, A. D. Pelton, and W. T. Thompson, *Facility for the Analysis of Chemical Thermodynamics.* McGill University/Ecole Polytechnique, 1996.

[36] W. T. Thompson, A. D. Pelton, and C. W. Bale, "Extension to SOLGASMIX for interactive calculations with FACT thermodynamic database," *CALPHAD* **7**(2), pp. 113–123, 1983.

[37] G. Eriksson and W. T. Thompson, "A procedure to estimate equilibrium concentrations in multicomponent systems and related applications," *CALPHAD* **13**(4), pp. 389–400, 1989.

[38] D. R. Poirier and G. H. Geiger, *Transport Phenomena in Materials Processing*, The Minerals, Metals and Materials Society, 1994.

[39] L. H. Van Vlack, *Elements of Materials Science and Engineering*, Addison-Wesley Publishing Company, fifth ed., 1985.

[40] N. T. M. Dennis and T. A. Heppell, *Vacuum System Design*, Chapman and Hall LTD., 1968.

[41] R. B. Bird, W. E. Stewart, and E. N. Lightfoot, *Transport Phenomena*, John Wiley and Sons, 1960.

[42] B. Bird, J. O. Hirschfelder, and C. F. Curtiss, "Theoretical calculation of the equation of state and transport properties of gases and liquids," *Transactions of the ASME* **77**, pp. 1011–1038, October 1954.

[43] T. E. Daubert, *Physical and Thermodynamic Properties of Pure Chemicals*, vol. 5, Hemisphere Publication Corporation, 1989-.

[44] M. Knudsen, *Kinetic Theory of Gases*, Methuen and Co., 1934.

[45] P. A. Thompson, *Compressible-Fluid Dynamics*, McGraw-Hill, 1972.

[46] D. S. Miller, *Compressible Internal Flow*, BHRA Fluid Engineering, Cranfield, 1984.

[47] J. P. Holman, *Heat Transfer*, McGraw-Hill, 1972.

[48] R. P. Tye, *Thermal Conductivity*, vol. 1, Academic Press, 1969.

[49] F. A. Londry and A. J. Slavin, "Effective thermal conductivity of a packed bed of hollow zirconia microspheres, under vacuum and under 100 kPa of argon," *Journal of American Ceramic Society* **74**(12), pp. 3118–3125, 1991.

[50] W. Schott, "Thermal conductivity of packed beds," *A.I.Ch.E. Journal* **6**, pp. 63–67, March 1960.

[51] V. Alexiades and A. D. Solomon, *Mathematical Modeling of Melting and Freezing Processes*, Hemisphere Publication Corporation, 1993.

APPENDIX A

A sample of EQUILIB output file

```
                                                 McMaster University - LAN
 (gram) 1.4Na + 1.0K + 23.45Zn + 3.10000Pb +
 (25C,1ATM,S1) (25C,1ATM,S1) (25C,1ATM,S1) (25C,1ATM,S1)
 (gram) 0.10000Cd + 2.100Mg + 2.600Mn + 4.500Ca +
 (25C,1ATM,S1) (25C,1ATM,S1) (25C,1ATM,S1) (25C,1ATM,S1)
 (gram) 33.950Fe + 2.80000Cl2 + 0.05000F2 + 0.4Si +
 (25C,1ATM,S1) (25C,1ATM,G) (25C,1ATM,G) (25C,1ATM,S1)
 (gram) 0.3Al + <24.25+6.720A>O2 + <22.12A>N2 =
 (25C,1ATM,S1)  (25C,1ATM,G)      (25C,1ATM,G)

  2093.0     litre (   78.809      vol% N2
                   +   20.752      vol% O2
                   +  0.20965      vol% NaCl
                   +  0.11088      vol% KCl
                   +  0.51359E-01  vol% PbO
                   +  0.36152E-01  vol% NO
                   +  0.17365E-01  vol% (NaCl)2
                   +  0.35254E-02  vol% (KCl)2
                   +  0.31389E-02  vol% NaF
                   +  0.25332E-02  vol% Cd                        T
                   +  0.19072E-02  vol% CdO
                   +  0.15379E-02  vol% KF
                   +  0.42223E-03  vol% NO2
                   +  0.24901E-03  vol% PbCl2
                   +  0.14762E-03  vol% PbCl
                   +  0.13181E-03  vol% (NaF)2
                   +  0.12206E-03  vol% OAlF2
                   +  0.15978E-04  vol% Cl
                   +  0.11022E-04  vol% Pb
                   +  0.63532E-05  vol% ZnCl2
                   +  0.48839E-05  vol% O
                   +  0.31893E-05  vol% PbCl4
                   +  0.22384E-05  vol% (KF)2
                   +  0.21107E-05  vol% N2O
                   +  0.17965E-05  vol% PbF2
                   +  0.14690E-05  vol% Na
                   +  0.62157E-06  vol% PbF
                   +  0.53716E-06  vol% Zn
                   +  0.25215E-06  vol% ClO
                   +  0.24477E-06  vol% NaO
                   +  0.13468E-06  vol% K
                   +  0.48941E-07  vol% MnCl2
                   +  0.46113E-07  vol% PbF4
                   +  0.27347E-07  vol% Cl2
                   +  0.17712E-07  vol% KO
                   +  0.16102E-07  vol% ONCl
                   +  0.47896E-08  vol% MgF2
                   +  0.37878E-08  vol% CaF2
```

```
                      +  0.33806E-08 vol% O3
                      +  0.20610E-08 vol% CaCl2
                      +  0.15533E-08 vol% MgClF
                      +  0.10108E-08 vol% FeF3
                      +  0.70840E-09 vol% FeCl2
                      +  0.66743E-09 vol%* F
                      +  0.60228E-09 vol% MgCl2
                      +  0.36233E-09 vol% NaAlF4
                      +  0.30648E-09 vol% ONF
                      +  0.13264E-09 vol% NO3)
                         ( 1000.00 C, 1.0000     atm, gas_ideal)

+   2.3637      gram  (   42.511      wt.% PbO
                      +   11.688      wt.% NaCl
                      +   11.224      wt.% (Na2O)(SiO2)
                      +   8.8401      wt.% Ca2SiO4
                      +   7.4388      wt.% ZnO
                      +   4.8121      wt.% KCl
                      +   2.5277      wt.% NaF
                      +   1.7081      wt.% CaSiO3
                      +   1.5327      wt.% NaAlO2
                      +   1.2598      wt.% CaAl2O4
                      +   1.0966      wt.% MnC
                      +  0.63618      wt.% Ca2ZnSi2O7
                      +  0.61288      wt.% MgO
                      +  0.60766      wt.% Mg2SiO4
                      +  0.54328      wt.% Pb2SiO4                         T
                      +  0.51101      wt.% MnAl2O4
                      +  0.42063      wt.% PbSiO3                          T
                      +  0.32393      wt.% Na6Si2O7
                      +  0.29479      wt.% Ca2Al2SiO7
                      +  0.26132      wt.% (Na2O)2(SiO2)
                      +  0.16753      wt.% CaF2
                      +  0.15716      wt.% KF
                      +  0.15664      wt.% Fe3O4
                      +  0.11855      wt.% (Na2O)(SiO2)2                   T
                      +  0.11487      wt.% KAlO2
                      +  0.91560E-01 wt.% FeO
                      +  0.74451E-01 wt.% Zn2SiO4
                      +  0.74118E-01 wt.% K2SiO3
                      +  0.39701E-01 wt.% MgAl2O4
                      +  0.38036E-01 wt.% MgOCaOSi2O4
                      +  0.31909E-01 wt.% CaO
                      +  0.22133E-01 wt.% Mn2SiO4
                      +  0.19866E-01 wt.% SiO2
                      +  0.13177E-01 wt.% Al2O3
                      +  0.10547E-01 wt.% Pb
                      +  0.89696E-02 wt.% CaAl4O7
                      +  0.38588E-02 wt.% MgF2
                      +  0.35512E-02 wt.% K2Si2O5
                      +  0.36569E-03 wt.% PbCl2
                      +  0.31344E-03 wt.% Cd                              T
                      +  0.28703E-03 wt.% PbF2
                      +  0.22265E-03 wt.% NaNO2                           T
                      +  0.16748E-03 wt.% NaNO3                           T
                      +  0.14525E-03 wt.% CaAl2Si2O8
                      +  0.98237E-04 wt.% CdCl2                           T
                      +  0.57754E-04 wt.% CaCl2
                      +  0.26299E-04 wt.% KNO3                            T
                      +  0.79502E-05 wt.% Na2O
                      +  0.16334E-05 wt.% (FeO)2(SiO2)
                      +  0.54908E-06 wt.% ZnF2
                      +  0.47820E-06 wt.% MnCl2
                      +  0.41158E-06 wt.% ZnCl2                           T
                      +  0.13039E-06 wt.% MnF2
                      +  0.13019E-06 wt.% Na
                      +  0.12844E-06 wt.% Zn
                      +  0.23173E-07 wt.% Na3AlF6
```

```
                    +  0.20005E-07 wt.% MgCl2
                    +  0.14838E-07 wt.% K2Si4O9                             T
                    +  0.85962E-08 wt.% K
                    +  0.69847E-08 wt.% Fe
                    +  0.52124E-08 wt.% FeF2
                    +  0.11314E-08 wt.% FeCl2
                    +  0.24695E-09 wt.% K2O)
                       ( 1000.00 C, 1.0000     atm, liquid)

                    +   50.607     gram (ZnO)(Fe2O3)                        T
                       ( 1000.00 C, 1.0000     atm, S1, a= 1.0000     )

                    +   20.281     gram CaFe2O4
                       ( 1000.00 C, 1.0000     atm, S1, a= 1.0000     )

                    +   11.924     gram ZnO
                       ( 1000.00 C, 1.0000     atm, S1, a= 1.0000     )

                    +   3.2562     gram MgO
                       ( 1000.00 C, 1.0000     atm, S1, a= 1.0000     )

                    +   3.1933     gram Mn3O4
                       ( 1000.00 C, 1.0000     atm, S1, a= 1.0000     )

                    +   1.6552     gram MgOCa3O3Si2O4
                       ( 1000.00 C, 1.0000     atm, S1, a= 1.0000     )

                    +  0.86749     gram MnAl2O4
                       ( 1000.00 C, 1.0000     atm, S1, a= 1.0000     )

                    +  0.00000     gram Fe2O3
                       ( 1000.00 C, 1.0000     atm, S2, a=0.85774     )

                    +  0.00000     gram Mn3O4                               X
                       ( 1000.00 C, 1.0000     atm, S2, a=0.79279     )

                    +  0.00000     gram Mn2O3
                       ( 1000.00 C, 1.0000     atm, S1, a=0.73817     )

                    +  0.00000     gram ZnAl2O4
                       ( 1000.00 C, 1.0000     atm, S1, a=0.62037     )

                    +  0.00000     gram (MgO)(Fe2O3)
                       ( 1000.00 C, 1.0000     atm, S1, a=0.61225     )

                    +  0.00000     gram CaOMgOSiO2
                       ( 1000.00 C, 1.0000     atm, S1, a=0.59968     )

                    +  0.00000     gram Ca2Fe2O5
                       ( 1000.00 C, 1.0000     atm, S1, a=0.58122     )

where "A" on the reactant side is  20.00

The cutoff concentration has been specified to 1.000E-10

Data on  2 product species identified with "X" have not been extrapolated in
computing the phase assemblage

Data on 59 product species identified with "T" have been extrapolated

*********************************************************************
  DELTA H     DELTA G     DELTA V     DELTA S     DELTA U    DELTA Cp    PROD V
    (J)         (J)         (l)        (J/C)        (J)        (J/C)       (l)
*********************************************************************
-S1---S1---S1---S1---S1---S1---S1---S1---S1---G1---G1---S1---S1---G1---G1---
 1.257E+05 -5.085E+06  1.584E+03  9.556E+02 -3.481E+04  1.286E+02  2.093E+03
=============================== last line ===============================
```

List of compounds from FACT database used in EQUILIB program.

```
                                                  McMaster University - LAN
□

#     SPECIES                   LAST CALCULATION    PHASE        CP RANGE (C)
                                --gram-----activity-  -----      ------------
+      1 N                   0.1625E-13 0.5791E-16 G1 Gas-1        25 - 5727
+      2 N2                v  442.3     0.7881     G1 Gas-1        25 - 5727
+      3 N3                  0.5021E-17 0.5964E-20 G1 Gas-1        25 - 5727
+      4 O                   0.1565E-04 0.4884E-07 G1 Gas-1        25 - 5727
+      5 O2                v  133.0     0.2075     G1 Gas          25 - 5727
+      6 O3                v 0.3251E-07 0.3381E-10 G1 Gas-1        25 - 5727
+      7 NO                v 0.2173     0.3615E-03 G1 Gas-1        25 - 5727
+      8 N2O               v 0.1861E-04 0.2111E-07 G1 Gas-1        25 - 5727
+      9 NO2               v 0.3892E-02 0.4222E-05 G1 Gas-1        25 - 5727
+     10 NO3                 0.1648E-08 0.1326E-11 G1 Gas-1        25 - 5727
+     11 N2O3                0.5622E-11 0.3692E-14 G1 Gas-1        25 - 5727
+     12 N2O4                0.1123E-13 0.6090E-17 G1 Gas-1        25 - 5727
+     13 N2O5                0.6053E-17 0.2797E-20 G1 Gas-1        25 - 5727
+     14 F                   0.2540E-08 0.6674E-11 G1 Gas-1        25 - 5727
+     15 F2                v 0.5012E-19 0.6583E-22 G1 Gas-1        25 - 5727
+     16 NF                  0.2786E-17 0.4213E-20 G1 Gas-1        25 - 5727
+     17 NF2                 0.3019E-23 0.2897E-26 G1 Gas-1        25 - 5727
+     18 FNNF                0.9381E-29 0.7094E-32 G1 Gas-1 Cis    25 - 5727
+     19 FNNF                0.4542E-29 0.3435E-32 G2 Gas-2 Tran   25 - 5727
+     20 NF3                 0.9952E-32 0.6996E-35 G1 Gas-1        25 - 5727
+     21 N2F4                0.8335E-56 0.4000E-59 G1 Gas-1        25 - 5727
+     22 OF                  0.4363E-12 0.6223E-15 G1 Gas-1        25 - 5727
+     23 O2F                 0.1915E-11 0.1875E-14 G1 Gas-1        25 - 5727
+     24 OF2                 0.3079E-23 0.2846E-26 G1 Gas-1        25 - 5727
+     25 ONF                 0.3009E-08 0.3065E-11 G1 Gas-1        25 - 5727
+     26 NO2F                0.1944E-11 0.1492E-14 G1 Gas-1        25 - 5727
+     27 FONO2               0.4435E-20 0.2733E-23 G1 Gas-1        25 - 5727
+     28 NF3O                0.4822E-35 0.2767E-38 G1 Gas-1        25 - 5727
+     29 Na                  0.6766E-05 0.1469E-07 G1 Gas-1        25 - 5727
+     30 Na2                 0.1378E-13 0.1496E-16 G1 Gas-1        25 - 5727
+     31 NaO                 0.1912E-05 0.2448E-08 G1 Gas-1        25 - 5727
+     32 NaF                 0.2640E-01 0.3139E-04 G1 Gas          25 - 2227
+     33 (NaF)2              0.2218E-02 0.1318E-05 G1 Gas-1        25 - 5727
+     34 Mg                  0.5273E-16 0.1083E-18 G1 Gas-1        25 - 5727
+     35 Mg2                 0.4563E-38 0.4685E-41 G1 Gas-1        25 - 5727
+     36 MgN                 0.1034E-22 0.1347E-25 G1 Gas-1        25 - 5727
+     37 MgO                 0.2589E-14 0.3206E-17 G1 gas          25 - 5727
+     38 MgF                 0.1053E-12 0.1214E-15 G1 Gas-1        25 - 5727
+     39 MgF2                0.5978E-07 0.4790E-10 G1 Gas-1        25 - 5727
+     40 (MgF2)2             0.9308E-15 0.3729E-18 G1 Gas-1        25 - 5727
+     41 Al                  0.3290E-30 0.6087E-33 G1 Gas-1        25 - 5727
+     42 Al2                 0.4658E-61 0.4308E-64 G1 Gas-1        25 - 5727
+     43 AlN                 0.1041E-39 0.1268E-42 G1 Gas-1        25 - 5727
+     44 AlO                 0.3213E-22 0.3732E-25 G1 Gas-1        25 - 5727
+     45 AlO2                0.1577E-19 0.1334E-22 G1 Gas-1        25 - 5727
+     46 Al2O                0.9632E-40 0.6872E-43 G1 Gas-1        25 - 5727
+     47 (AlO)2              0.1632E-33 0.9474E-37 G1 Gas-1        25 - 5727
+     48 AlF                 0.2029E-19 0.2203E-22 G1 Gas-1        25 - 5727
+     49 AlF2                0.1685E-15 0.1294E-18 G1 Gas-1        25 - 5727
+     50 AlF3                0.6879E-10 0.4089E-13 G1 Gas-1        25 - 5727
+     51 (AlF3)2             0.2333E-22 0.6934E-26 G1 Gas-1        25 - 5727
+     52 OAlF                0.9768E-11 0.7867E-14 G1 Gas-1        25 - 5727
+     53 OAlF2               0.1980E-02 0.1221E-05 G1 Gas-1        25 - 5727
+     54 NaAlF4              0.9144E-08 0.3623E-11 G1 Gas-1        25 - 5727
+     55 Si                  0.2511E-38 0.4463E-41 G1 Gas-1        25 - 5727
+     56 Si2                            0.2092E-75 G1 Gas-1        25 - 5727
+     57 Si3                            0.5387-107 G1 Gas-1        25 - 5727
+     58 SiN                 0.1349E-37 0.1600E-40 G1 Gas-1        25 - 5727
```

```
+    59 Si2N              0.6068E-68 0.4316E-71 G1 Gas-1       25 - 5727
+    60 SiO               0.3901E-19 0.4416E-22 G1 Gas-1       25 - 5727
+    61 SiF               0.2579E-32 0.2734E-35 G1 Gas-1       25 - 5727
+    62 SiF2              0.1085E-23 0.8194E-27 G1 Gas-1       25 - 5727
+    63 SiF3              0.4018E-18 0.2357E-21 G1 Gas-1       25 - 5727
+    64 SiF4              0.1286E-12 0.6169E-16 G1 Gas-1       25 - 5727
+    65 OSiF2             0.5264E-13 0.3201E-16 G1 Gas-1       25 - 5727
+    66 Cl                0.1135E-03 0.1598E-06 G1 Gas-1       25 - 5727
+    67 Cl2             v 0.3885E-06 0.2735E-09 G1 Gas         25 - 5727
+    68 ClO               0.2599E-05 0.2521E-08 G1 Gas-1       25 - 5727
+    69 ClO2              0.1797E-09 0.1330E-12 G1 Gas-1       25 - 5727
+    70 Cl2O              0.5883E-13 0.3379E-16 G1 Gas-1       25 - 5727
+    71 ONCl              0.2112E-06 0.1610E-09 G1 Gas-1       25 - 5727
+    72 NO2Cl             0.7483E-10 0.4585E-13 G1 Gas-1       25 - 5727
+    73 ClF               0.3008E-10 0.2757E-13 G1 Gas-1       25 - 5727
+    74 ClF3              0.7706E-35 0.4160E-38 G1 Gas-1       25 - 5727
+    75 ClF5              0.2150E-62 0.8227E-66 G1 Gas-1       25 - 5727
+    76 (ClF3)2                      0.2220E-79 G1 Gas         25 -  727 T
+    77 ClO3F           v 0.5082E-25 0.2476E-28 G1 Gas-1       25 - 5727
+    78 NaCl               2.455     0.2096E-02 G1 Gas         25 - 1727
+    79 (NaCl)2           0.4066     0.1737E-03 G1 Gas-1       25 - 5727
+    80 MgCl              0.4700E-14 0.3926E-17 G1 Gas-1       25 - 5727
+    81 MgCl2             0.1149E-07 0.6023E-11 G1 Gas         25 - 5727
+    82 (MgCl2)2          0.2325E-18 0.6093E-22 G1 Gas-1       25 - 5727
+    83 MgClF             0.2451E-07 0.1553E-10 G1 Gas-1       25 - 5727
+    84 AlCl              0.1349E-21 0.1079E-24 G1 Gas-1       25 - 5727
+    85 AlCl2             0.2238E-19 0.1141E-22 G1 Gas-1       25 - 5727
+    86 AlCl3             0.6903E-16 0.2584E-19 G1 Gas-1       25 - 5727
+    87 (AlCl3)2          0.1949E-37 0.3647E-41 G1 Gas-1       25 - 5727
+    88 OAlCl             0.8753E-14 0.5570E-17 G1 Gas-1       25 - 5727
+    89 AlClF             0.5067E-17 0.3106E-20 G1 Gas-1       25 - 5727
+    90 AlClF2            0.1651E-11 0.8206E-15 G1 Gas-1       25 - 5727
+    91 AlCl2F            0.1839E-13 0.7852E-17 G1 Gas         25 - 5727
+    92 SiCl              0.1073E-34 0.8427E-38 G1 Gas-1       25 - 5727
+    93 SiCl2             0.8941E-28 0.4508E-31 G1 Gas-1       25 - 5727
+    94 SiCl3             0.4549E-27 0.1689E-30 G1 Gas-1       25 - 5727
+    95 SiCl4           v 0.1411E-25 0.4146E-29 G1 Gas-1       25 - 5727
+    96 SiClF3            0.1724E-17 0.7141E-21 G1 Gas-1       25 - 5727
+    97 SiCl3F            0.8364E-24 0.2721E-27 G1 Gas-1       25 - 5727
+    98 K                 0.1055E-05 0.1347E-08 G1 Gas-1       25 - 5727
+    99 K2                0.7265E-16 0.4637E-19 G1 Gas-1       25 - 5727
+   100 KO                0.1955E-06 0.1771E-09 G1 Gas-1       25 - 5727
+   101 KF                0.1790E-01 0.1538E-04 G1 Gas         25 - 1727
+   102 (KF)2             0.5211E-04 0.2238E-07 G1 Gas-1       25 - 5727
+   103 KCl                1.656     0.1109E-02 G1 Gas         25 - 2227
+   104 (KCl)2            0.1053     0.3525E-04 G1 Gas-1       25 - 5727
+   105 Ca                0.3652E-20 0.4548E-23 G1 Gas-1       25 - 5727
+   106 Ca2               0.8116E-46 0.5053E-49 G1 Gas-1       25 - 5727
+   107 CaO               0.1834E-16 0.1632E-19 G1 gas         25 - 5727
+   108 CaF               0.4236E-14 0.3579E-17 G1 Gas-1       25 - 5727
+   109 CaF2              0.5925E-07 0.3788E-10 G1 Gas-1       25 - 5727
+   110 CaCl              0.1892E-14 0.1251E-17 G1 Gas-1       25 - 5727
+   111 CaCl2             0.4583E-07 0.2061E-10 G1 Gas-1       25 - 5727
+   112 Mn                0.9184E-14 0.8345E-17 G1 Gas-1       25 - 5727
+   113 MnCl2             0.1234E-05 0.4894E-09 G1 Gas         25 - 1727
+   114 Fe                0.1446E-15 0.1293E-18 G1 gas         25 - 5727
+   115 FeO               0.1699E-11 0.1180E-14 G1 gas         25 - 5727
+   116 FeF               0.6583E-14 0.4391E-17 G1 Gas-1       25 - 5727
+   117 FeF2              0.1369E-10 0.7284E-14 G1 Gas-1       25 - 5727
+   118 FeF3              0.2285E-07 0.1011E-10 G1 Gas-1       25 - 5727
+   119 FeCl              0.2247E-15 0.1229E-18 G1 Gas-1       25 - 5727
+   120 FeCl2             0.1799E-07 0.7084E-11 G1 Gas-1       25 - 5727
+   121 FeCl3             0.6253E-11 0.1924E-14 G1 Gas-1       25 - 5727
+   122 (FeCl2)2          0.7537E-19 0.1484E-22 G1 Gas-1       25 - 5727
+   123 (FeCl3)2          0.1495E-26 0.2300E-30 G1 Gas-1       25 - 5727
+   124 AlCl6Fe           0.7986E-32 0.1349E-35 G1 Solid       25 - 1227
+   125 Zn                0.7036E-05 0.5372E-08 G1 Gas-1       25 - 5727
+   126 ZnCl2             0.1735E-03 0.6353E-07 G1 Gas        732 - 1727
```

```
+   127 Cd                     0.5704E-01 0.2533E-04 G1 Gas         767 -  927 T
+   128 CdO                    0.4906E-01 0.1907E-04 G1 gas          25 - 2727
+   129 Pb                     0.4575E-03 0.1102E-06 G1 Gas-1        25 - 5727
+   130 Pb2                    0.4179E-11 0.5034E-15 G1 Gas-1        25 - 5727
+   131 PbO                     2.297     0.5136E-03 G1 Gas          25 - 2227
+   132 PbF                    0.2817E-04 0.6216E-08 G1 Gas-1        25 - 5727
+   133 PbF2                   0.8825E-04 0.1797E-07 G1 Gas-1        25 - 5727
+   134 PbF4                   0.2616E-05 0.4611E-09 G1 Gas-1        25 - 5727
+   135 PbCl                   0.7176E-02 0.1476E-05 G1 Gas-1        25 - 5727
+   136 PbCl2                  0.1387E-01 0.2490E-05 G1 Gas-1        25 - 5727
+   137 PbCl4                  0.2230E-03 0.3189E-07 G1 Gas-1        25 - 5727
+   138 N2O4                   0.6248E-19 0.3386E-19 L1 Liquid-1     25 -  228 T
+   139 Na                     0.3077E-08 0.6674E-08 L1 Liquid-1     25 - 1328
+   140 Na2O                   0.1879E-06 0.1512E-06 L1 Liquid       25 - 1227
+   141 NaNO2                  0.5263E-05 0.3803E-05 L1 Liquid      284 -  527 T
+   142 NaNO3                  0.3959E-05 0.2322E-05 L1 Liquid       25 -  427 T
+   143 NaF                    0.5975E-01 0.7094E-01 L1 Liquid       25 - 2227
+   144 Mg                     0.1222E-18 0.2506E-18 L1 Liquid-1     25 - 1727
+   145 MgO                    0.1449E-01 0.1792E-01 L1 Liquid       25 - 3227
+   146 MgF2                   0.9121E-04 0.7299E-04 L1 Liquid-1     25 - 2727
+   147 Al                     0.2069E-26 0.3824E-26 L1 Liquid-1     25 - 2727
+   148 Al2O3                  0.3115E-03 0.1523E-03 L1 Liquid       25 - 2727
+   149 AlF3                   0.1195E-12 0.7097E-13 L1 Liquid-1     25 - 3727
+   150 NaAlO2                 0.3623E-01 0.2203E-01 L1 Liquid       25 - 1867
+   151 Na3AlF6                0.5477E-09 0.1301E-09 L1 Liquid-1     25 - 2727
+   152 Na5Al3F14              0.7941E-27 0.8572E-28 L1 Liquid-1     25 - 2727
+   153 MgAl2O4                0.9384E-03 0.3289E-03 L1 Liquid       25 - 2108
+   154 Si                     0.4312E-31 0.7655E-31 L1 Liquia-1     25 - 4227
+   155 SiO2                   0.4696E-03 0.3896E-03 L1 Liquid       25 - 2727
+   156 (Na2O)(SiO2)           0.2653     0.1084     L1 Liquid       25 - 1177
+   157 (Na2O)2(SiO2)          0.6177E-02 0.1673E-02 L1 Liquid       25 - 1177
+   158 (Na2O)(SiO2)2          0.2802E-02 0.7670E-03 L1 Liquid       25 -  977 T
+   159 Na6Si2O7               0.7657E-02 0.1247E-02 L1 Liquid       25 - 1124
+   160 Mg2Si                  0.7168E-65 0.4660E-65 L1 Liquid-1     25 - 3727
+   161 Mg2SiO4                0.1436E-01 0.5090E-02 L1 Liquid       25 - 2727
+   162 NaCl                   0.2763     0.2357     L1 Liquid       25 - 1727
+   163 MgCl2                  0.4729E-09 0.2476E-09 L1 Liquid       25 - 2227
+   164 AlCl3                  0.7320E-21 0.2737E-21 L1 Liquid-1     25 - 1228
+   165 SiCl4                  0.4622E-31 0.1356E-31 L1 Liquid       25 -  228 T
+   166 K                      0.2032E-09 0.2591E-09 L1 Liquid-1     25 - 1228
+   167 K2O                    0.5837E-11 0.3090E-11 L1 Liquid       25 - 1027
+   168 KNO3                   0.6216E-06 0.3065E-06 L1 Liquid       25 -  427 T
+   169 KF                     0.3715E-02 0.3188E-02 L1 Liquid       25 - 1727
+   170 KAlO2                  0.2715E-02 0.1380E-02 L1 Liquid       25 - 2327
+   171 K2SiO3                 0.1752E-02 0.5661E-03 L1 Liquid       25 - 1027
+   172 K2Si2O5                0.8394E-04 0.1952E-04 L1 Liquid       25 - 1046
+   173 K2Si4O9                0.3507E-09 0.5227E-10 L1 Liquid       25 -  827 T
+   174 KCl                    0.1137     0.7607E-01 L1 Liquid       25 - 2227
+   175 Ca                     0.2185E-21 0.2718E-21 L1 Liquid-1     25 - 2227
+   176 CaO                    0.7542E-03 0.6706E-03 L1 Liquid       25 - 3227
+   177 CaF2                   0.3960E-02 0.2529E-02 L1 Liquid-1     25 - 3727
+   178 CaAl2                  0.2885E-66 0.1529E-66 L1 Liquid     1080 - 1527 T
+   179 CaAl4                             0.5480-119 L1 Liquid      777 - 1427
+   180 CaAl2O4                0.2978E-01 0.9394E-02 L1 Liquid       25 - 1604
+   181 CaAl4O7                0.2120E-03 0.4066E-04 L1 Liquid       25 - 1765
+   182 CaSiO3                 0.4037E-01 0.1733E-01 L1 Liquid       25 - 2227
+   183 Ca2SiO4                0.2090     0.6048E-01 L1 Liquid       25 - 2227
+   184 MgOCaOSi2O4            0.8991E-03 0.2070E-03 L1 Liquid       25 - 1727
+   185 CaAl2Si2O8             0.3433E-05 0.6153E-06 L1 Liquid       25 - 2227
+   186 Ca2Al2SiO7             0.6968E-02 0.1267E-02 L1 Liquid       25 - 2227
+   187 CaCl2                  0.1365E-05 0.6132E-06 L1 Liquid-1     25 - 2727
+   188 Mn                     0.3031E-12 0.2750E-12 L1 Liquid-1     25 - 2727
+   189 MnO                    0.2592E-01 0.1822E-01 L1 Liquid       25 - 2227
+   190 MnF2                   0.3082E-08 0.1653E-08 L1 Liquid      930 - 1820
+   191 MnAl2O4                0.1208E-01 0.3483E-02 L1 Liquid       25 - 1835
+   192 MnSi                   0.8375E-41 0.5029E-41 L1 Liquid     1275 - 1727 T
+   193 Mn5Si3                            0.5405-146 L1 Liquid     1300 - 1727 T
+   194 Mn2SiO4                0.5232E-03 0.1292E-03 L1 Liquid       25 - 2727
```

```
+   195 MnCl2                 0.1130E-07 0.4478E-08 L1 Liquid        650 - 1231
+   196 Fe                    0.1651E-09 0.1474E-09 L1 Liquid         25 - 5727
+   197 FeO                   0.2164E-02 0.1502E-02 L1 Liquid         25 - 1727
+   198 Fe3O4                 0.3702E-02 0.7972E-03 L1 Liquid         25 - 2227
+   199 FeF2                  0.1232E-09 0.6546E-10 L1 Liquid-1       25 - 2727
+   200 (FeO)2(SiO2)          0.3861E-07 0.9446E-08 L1 Liquid         25 - 1277
+   201 FeCl2                 0.2674E-10 0.1052E-10 L1 Liquid-1       25 - 1728
+   202 FeCl3                 0.5080E-15 0.1561E-15 L1 Liquid-1       25 - 1228
+   203 Zn                    0.3036E-08 0.2315E-08 L1 Liquid-1       25 - 1727
+   204 ZnO                   0.1758     0.1077     L1 Liquid         25 - 2227
+   205 ZnF2                  0.1298E-07 0.6259E-08 L1 Liquid        875 - 1505
+   206 Zn2SiO4               0.1760E-02 0.3937E-03 L1 liquid         25 - 1527
+   207 ZnCl2                 0.9728E-08 0.3559E-08 L1 Liquid        318 -  732 T
+   208 CaZn                  0.3105E-27 0.1468E-27 L1 Liquid        477 -  727 T
+   209 CaZn2                 0.1559E-35 0.4550E-36 L1 Liquid        690 -  727 T
+   210 Ca2ZnSi2O7            0.1504E-01 0.2390E-02 L1 liquid         25 - 1425
+   211 Cd                    0.7409E-05 0.3286E-05 L1 Liquid        321 -  767 T
+   212 NaCd2                 0.1635E-17 0.3289E-18 L1 Liquid        382 -  627 T
+   213 CdCl2                 0.2322E-05 0.6316E-06 L1 Liquid        568 -  961 T
+   214 Pb                    0.2493E-03 0.5999E-04 L1 Liquid-1       25 - 2727
+   215 PbO                    1.005     0.2245     L1 Liquid         25 - 1727
+   216 PbF2                  0.6785E-05 0.1380E-05 L1 Liquid-1       25 - 1728
+   217 Mg2Pb                 0.1554E-38 0.3028E-39 L1 Liquid        549 -  827 T
+   218 PbSiO3                0.9942E-02 0.1750E-02 L1 liquid         25 -  927 T
+   219 Pb2SiO4               0.1284E-01 0.1264E-02 L1 liquid         25 -  927 T
+   220 PbCl2                 0.8644E-05 0.1550E-05 L1 Liquid-1       25 - 1728
+   221 N2O4                             0.7782E-22 S1 Solid-1        25 -  228 T
+   222 N2O5                             0.5329E-26 S1 Solid          22 -   27 T
+   223 Na                               0.4282E-08 S1 Solid-1        25 -  728 T
+   224 NaO2                             0.9507E-05 S1 Solid-1        25 - 1727
+   225 Na2O                             0.2156E-06 S1 Solid-A        25 - 1227
+   226 Na2O                             0.2245E-06 S2 Solid-B        25 - 1227
+   227 Na2O                             0.2307E-06 S3 Solid-C        25 - 1227
+   228 Na2O2                            0.6292E-07 S1 Solid-1        25 -  512 T
+   229 Na2O2                            0.8638E-07 S2 Solid-2        25 - 2227
+   230 NaNO2                            0.4678E-06 S1 Alpha          25 -  161 T
+   231 NaNO2                            0.1805E-05 S2 Beta          161 -  284 T
+   232 NaNO3                            0.2458E-06 S1 Solid          25 -  427 T
+   233 NaNO3                            0.4255E-06 S2 Solid          25 -  427 T
+   234 NaF                              0.7022E-01 S1 Villiau.te     25 - 2227
+   235 Mg                               0.1846E-18 S1 Solid-1        25 -  928 T
+   236 Mg3N2                            0.1079E-47 S1 Solid-1        25 - 2227
+   237 Mg3N2                            0.1132E-47 S2 Solid-2        25 - 2227
+   238 Mg3N2                            0.1155E-47 S3 Solid-3        25 - 2227
+   239 MgO                 v  3.256      1.000     S1 periclase      25 - 3227
+   240 MgF2                             0.1836E-03 S1 Solid-1        25 - 1727
+   241 Al                               0.2692E-26 S1 Solid-1        25 -  928 T
+   242 AlN                              0.8146E-19 S1 Solid-1        25 - 2727
+   243 Al2O3                            0.5917E-02 S1 gamma          25 - 2727
+   244 Al2O3                            0.1038E-01 S2 delta          25 - 2727
+   245 Al2O3                            0.9268E-02 S3 kappa          25 - 2727
!   246 Al2O3               v            0.1952E-01 S4 corundum(a     25 - 2727
+   247 AlF3                             0.4835E-11 S1 Solid          25 - 2727
+   248 AlF3                             0.5031E-11 S2 Solid          25 - 2727
+   249 NaAlO2                           0.5523E-01 S1 Solid-A        25 - 1867
+   250 NaAlO2                           0.6032E-01 S2 Solid-B        25 - 1867
+   251 NaAl9O14                         0.2201E-06 S1 Beta-alumi     25 - 1976
+   252 Na2Al12O19                       0.9096E-09 S1 Beta"-alum     25 - 1443
+   253 Na3AlF6                          0.1205E-09 S1 Solid Alph     25 -  927 T
+   254 Na3AlF6                          0.1431E-09 S2 Solid Beta     25 - 1227
+   255 Na5Al3F14                        0.1001E-30 S1 Solid-1        25 - 1227
+   256 MgAl2O4             v            0.3822     S1 spinel         25 - 2108
+   257 Si                               0.2458E-30 S1 Solid-1        25 - 2227
+   258 Si3N4                            0.1688E-78 S1 Solid Alph     25 - 2727
!   259 SiO2                v            0.2837E-03 S1 Quartz(l)      25 -  577 T
+   260 SiO2                v            0.5300E-03 S2 Quartz(h)      25 - 2727
+   261 SiO2                v            0.1257E-04 S3 Tridymite(     25 -  119 T
+   262 SiO2                v            0.5426E-03 S4 Tridymite(     25 - 2727
```

```
+  263 SiO2               v     0.4925E-04 S5 Cristobali   25 -  264 T
+  264 SiO2               v     0.5408E-03 S6 Cristobali   25 - 2727
+  265 SiO2               v     0.2474E-03 S7 coesite      25 - 2727
+  266 SiO2               v     0.1367E-05 S8 stishovite   25 - 2727
+  267 (Na2O)(SiO2)             0.1549     S1 Solid        25 - 1177
+  268 (Na2O)2(SiO2)            0.2908E-02 S1 Solid        25 - 1177
!  269 (Na2O)(SiO2)2            0.4229E-03 S1 Solid-A      25 -  977 T
+  270 (Na2O)(SiO2)2            0.5348E-03 S2 Solid-B      25 -  977 T
!  271 (Na2O)(SiO2)2            0.5444E-03 S3 Solid-C      25 -  977 T
+  272 Na6Si2O7                 0.2078E-02 S1 Solid        25 - 1124
+  273 Na6Si8O19                0.6949E-16 S1 Solid        25 -  809 T
+  274 Mg2Si                    0.8489E-65 S1 Solid-1      25 - 2227
+  275 MgSiO3             v     0.8324E-02 S1 Low-clinoe   25 - 2227
+  276 MgSiO3             v     0.9407E-02 S2 High-T-cli   25 - 2227
+  277 MgSiO3             v     0.9425E-02 S3 orthoensta   25 - 2227
+  278 MgSiO3             v     0.7636E-02 S4 protoensta   25 - 2727
+  279 MgSiO3             v     0.7570E-02 S5 High-P-cli   25 - 2727
+  280 MgSiO3             v     0.1631E-04 S6 Mg-ilmenit   25 - 2727
+  281 MgSiO3             v     0.1516E-03 S7 Mg-garnet    25 - 2727
+  282 MgSiO3             v     0.6111E-06 S8 Mg-perovsk   25 - 2727
+  283 Mg2SiO4            v     0.1588     S1 Forsterite   25 - 2727
+  284 Mg2SiO4            v     0.3451E-02 S2 beta-forst   25 - 2727
+  285 Mg2SiO4            v     0.7446E-03 S3 gamma-fors   25 - 2727
+  286 Na2MgSi4O10              0.3412E-07 S1 Solid        25 -  927 T
+  287 Na2Mg2Si6O15             0.1177E-11 S1 Solid        25 -  927 T
+  288 Al2SiO5            v     0.1233E-04 S1 andalusite   25 - 2727
+  289 Al2SiO5            v     0.1339E-04 S2 sillimanit   25 - 2727
+  290 Al2SiO5            v     0.6561E-05 S3 kyanite      25 - 2727
+  291 (Al2O3)(SiO2)2           0.6836E-19 S1 Solid        25 - 1527
+  292 Al6Si2O13                0.9382E-11 S1 Mullite      25 - 1890
+  293 NaAlSiO4                 0.1472E-03 S1 Nepheline-   25 -  196 T
+  294 NaAlSiO4                 0.1676     S2 Nepheline-   25 - 1727
+  295 NaAlSiO4                 0.1706     S3 Nepheline-   25 - 1727
+  296 NaAlSiO4                 0.1705     S4 Carnegicit   25 - 1727
+  297 NaAlSi2O6          v     0.5499E-05 S1 Jadeite      25 - 1027
+  298 NaAlSi3O8          v     0.8514E-07 S1 Low          25 - 1118
+  299 NaAlSi3O8          v     0.1834E-06 S2 High         25 - 1118
+  300 Mg3Al2Si3O12       v     0.8057E-08 S1 Pyrope       25 - 1427
+  301 Mg2Al4Si5O18             0.2351E-15 S1 cordierite   25 - 1477
+  302 NaCl                     0.1427     S1 Halite       25 - 1727
+  303 NaClO4                   0.6520E-20 S1 Solid I      25 -  308 T
+  304 NaClO4                   0.4810E-19 S2 Solid II     25 - 1227
+  305 MgCl2                    0.7447E-10 S1 Solid        25 - 1727
+  306 AlCl3                    0.8202E-24 S1 Solid-1      25 -  928 T
+  307 OAlCl                    0.2018E-08 S1 Solid-1      25 - 2727
+  308 NaAlCl4                  0.5543E-23 S1 Solid-1      25 -  727 T
+  309 Na3AlCl6                 0.5901E-24 S1 Solid-1      25 - 1727
+  310 K                        0.1664E-09 S1 Solid-1      25 - 1228
+  311 KO2                      0.2169E-05 S1 Solid-1      25 - 1227
+  312 K2O                      0.1597E-11 S1 Solid        25 - 1027
+  313 K2O2                     0.1581E-10 S1 Solid        25 -  490 T
+  314 KNO3                     0.3821E-07 S1 Solid-A      25 -  427 T
+  315 KNO3                     0.1083E-06 S2 Solid-B      25 -  427 T
+  316 KF                       0.2266E-02 S1 Solid        25 - 1727
+  317 KAlO2                    0.6901E-01 S1 Solid-A      25 - 2327
+  318 KAlO2                    0.7401E-01 S2 Solid-B      25 - 2327
+  319 KAl9O14                  0.2369E-06 S1 K-Beta-alu   25 - 1920
+  320 K2Al12O19                0.1053E-08 S1 K-Beta"-al   25 - 1146
+  321 K3AlF6                   0.3616E-13 S1 Solid-1      25 - 1727
+  322 K2SiO3                   0.5516E-03 S1 Solid        25 - 1027
+  323 K2Si2O5                  0.1771E-04 S1 Solid-A      25 - 1046
+  324 K2Si2O5                  0.2021E-04 S2 Solid-B      25 - 1046
+  325 K2Si2O5                  0.2282E-04 S3 Solid-C      25 - 1046
+  326 K2Si4O9                  0.2218E-10 S1 Solid-A      25 -  827 T
+  327 K2Si4O9                  0.2561E-10 S2 Solid-B      25 -  827 T
+  328 KAlSiO4                  0.5696E-02 S1 Kaliophyll   25 -  538 T
+  329 KAlSiO4                  0.3846E-01 S2 Kaliophyll   25 - 1727
!  330 KAlSi2O6                 0.2320E-03 S1 Leucite(RH   25 -  683 T
```

```
+   331 KAlSi2O6                        0.6801E-03 S2 Leucite(RH   25 - 1693
+   332 KAlSi3O8         v              0.4305E-07 S1 Microcline   25 - 1200
+   333 KAlSi3O8         v              0.9227E-07 S2 K-Feldspar   25 - 1200
+   334 KAlSi3O8         v              0.9194E-07 S3 Sanidine     25 - 1200
+   335 KMg3AlSi3O10F2                  0.6276E-13 S1 Solid        25 -  300 T
+   336 KCl                             0.4364E-01 S1 Sylvite      25 - 2227
+   337 KClO4                           0.1551E-19 S1 Solid I      25 -  299 T
+   338 KClO4                           0.1252E-18 S2 Solid II     25 - 1227
+   339 K2ClNO3                         0.2486E-09 S1 Solid        25 -  356 T
+   340 KAlCl4                          0.2108E-22 S1 Solid-1      25 -  727 T
+   341 K3AlCl6                         0.5420E-24 S1 Solid-1      25 - 1727
+   342 K3Al2Cl9                        0.6070E-47 S1 Solid-1      25 - 1227
+   343 Ca                              0.2298E-21 S1 Solid Alph   25 - 1228
+   344 Ca                              0.2449E-21 S2 Solid Beta   25 - 1228
+   345 Ca3N2                           0.4674E-57 S1 Solid        25 - 1195
+   346 CaO              v              0.4251E-01 S1 lime         25 - 3227
+   347 CaO2                            0.9534E-03 S1 Solid        25 -  154 T
+   348 Ca(NO3)2                        0.8563E-18 S1 Solid        25 -  561 T
+   349 CaF2                            0.5947E-02 S1 Solid        25 - 1152
+   350 CaF2                            0.5670E-02 S2 Solid        25 - 1728
+   351 CaMg2                           0.1462E-57 S1 Solid        25 -  730 T
+   352 CaAl2                           0.2174E-66 S1 Solid        25 - 1080
+   353 CaAl4                           0.1141-119 S1 Solid        25 -  777 T
+   354 CaAl2O4                         0.4957E-01 S1 Solid        25 - 1604
+   355 CaAl4O7                         0.3858E-02 S1 Solid        25 - 1765
+   356 CaAl12O19                       0.9782E-09 S1 Solid        25 - 1833
+   357 Ca3Al2O6                        0.2370E-03 S1 Solid        25 - 1541
+   358 CaSi                            0.1151E-46 S1 Solid        25 - 1240
+   359 CaSi2                           0.6342E-78 S1 Solid        25 - 1027
+   360 Ca2Si                           0.2561E-66 S1 Solid        25 -  927 T
+   361 CaSiO3           v              0.9554E-01 S1 Wollastoni   25 - 1542
+   362 CaSiO3           v              0.9296E-01 S2 Pseudowoll   25 - 1542
+   363 Ca2SiO4                         0.4197     S1 Solid-beta   25 - 2227
+   364 Ca2SiO4                         0.4432     S2 Solid-alph   25 - 2227
+   365 Ca2SiO4                         0.2809     S3 Solid alph   25 - 2227
+   366 Ca3SiO5                         0.1540E-01 S1 Hatrurite    25 - 2227
+   367 Ca3Si2O7                        0.6726E-01 S1 Solid        25 - 4727
+   368 Na4CaSi3O9                      0.2671     S1 Solid        25 - 1027
+   369 Na2CaSi5O12                     0.2101E-09 S1 solid        25 - 1027
+   370 Na2Ca2Si3O9                     0.9069E-01 S1 Solid        25 - 1027
+   371 Na2Ca3Si6O16                    0.2029E-07 S1 Solid        25 - 1027
+   372 CaOMgOSiO2       v              0.5997     S1 Monticelli   25 - 1727
+   373 MgOCaOSi2O4      v              0.3599E-02 S1 Diopside(c   25 - 1727
+   374 MgOCa2O2Si2O4                   0.8004E-01 S1 Akermanite   25 - 1727
+   375 MgOCa2O2Si2O4                   0.8927E-01 S2 Akermanite   25 - 1727
+   376 MgOCa3O3Si2O4    v  1.655        1.000     S1 Merwinite    25 - 1575
+   377 CaAl2SiO6        v              0.2758E-02 S1 Ca-Tscherm   25 - 2727
+   378 CaAl2Si2O8                      0.9979E-08 S1 Hexagonal    25 -   77 T
+   379 CaAl2Si2O8       v              0.6147E-04 S2 Anorthite    25 - 2227
+   380 Ca2Al2SiO7       v              0.1009     S1 Gehlenite    25 - 2227
+   381 Ca3Al2Si3O12     v              0.3683E-04 S1 grossular    25 - 2727
+   382 CaCl2                           0.3306E-06 S1 Solid-1      25 - 1727
+   383 CaOCl2                          0.5873E-13 S1 Solid        25 -  227 T
+   384 Mn                              0.3191E-12 S1 Solid Alph   25 - 1149
+   385 Mn                              0.3398E-12 S2 Solid Beta   25 - 1089
+   386 Mn                              0.3354E-12 S3 Solid Gamm   25 - 1140
+   387 Mn                              0.3251E-12 S4 Solid Delt   25 - 1628
+   388 Mn4N                            0.1353E-47 S1 Solid        25 -  527 T
+   389 Mn5N2                           0.1721E-61 S1 Solid        25 -  527 T
+   390 MnO                             0.1409     S1 Solid        25 - 2227
+   391 MnO2                            0.4556E-01 S1 Pyrolusite   25 -  250 T
+   392 Mn2O3                           0.7382     S1 Braunite     25 - 1077
+   393 Mn3O4                3.193       1.000     S1 Solid-A      25 - 1172
+   394 Mn3O4                           0.7928     S2 Solid-B    1172 - 1560 T
+   395 MnF2                            0.1456E-08 S1 Solid        25 -  930 T
+   396 MnF3                            0.8733E-16 S1 Solid        25 -  727 T
+   397 MnAl2O4             0.8675       1.000     S1 Solid        25 - 1835
+   398 MnSi                            0.1325E-40 S1 Solid        25 - 1275
```

```
+   399 Mn3Si                               0.6519E-65 S1 Solid       25 -  727 T
+   400 Mn5Si3                              0.1067-144 S1 Solid       25 - 1300
+   401 Mn10Si17                                       S1 Solid       25 - 1152
+   402 MnSiO3                              0.8689E-03 S1 Rhodonite   25 - 2227
+   403 Mn2SiO4               v             0.6375E-03 S1 Tephroite   25 - 2728
+   404 MnCl2                               0.1103E-08 S1 Scacchite   25 -  650 T
+   405 Fe                                  0.2144E-09 S1 bcc         25 - 1539
+   406 Fe                                  0.2154E-09 S2 fcc         25 - 1539
+   407 Fe2N                                0.1367E-21 S1 Solid        0 -  727 T
+   408 Fe4N                                0.5745E-41 S1 Solid-A     25 -  480 T
+   409 Fe4N                                0.1042E-40 S2 Solid-B    480 -  627 T
+   410 FeO                   v             0.2920E-02 S1 Wustite     25 - 1727
+   411 Fe2O3                 v             0.4339     S1 Hematite    25 -  684 T
+   412 Fe2O3                 v             0.8577     S2 Hematite   682 - 1600
+   413 Fe2O3                 v             0.3439E-03 S3 High-Press  25 -  684 T
+   414 Fe2O3                 v             0.6799E-03 S4 High-Press 682 - 1600
+   415 Fe3O4                 v             0.8276E-02 S1 Magnetite   25 -  577 T
+   416 Fe3O4                 v             0.5124E-01 S2 Magnetite  575 - 2227
+   417 Fe3O4                 v             0.3129E-07 S3 High-Press  25 -  577 T
+   418 Fe3O4                 v             0.1937E-06 S4 High-Press 575 - 2227
+   419 FeF2                                0.9300E-10 S1 Solid-1     25 - 1727
+   420 FeF3                                0.1527E-11 S1 Solid-1     25 - 1727
+   421 (Na2O)(Fe2O3)                       0.4013E-02 S1 Solid       25 - 1345
+   422 (MgO)(Fe2O3)                        0.6122     S1 Solid       25 - 2200
+   423 FeAl2O4               v             0.2649E-03 S1 Hercynite   25 - 1753
+   424 FeSi                                0.6142E-36 S1 Solid       25 -  627 T
+   425 FeSi2                               0.3407E-68 S1 Solid       22 -   27 T
+   426 Fe3Si                               0.4958E-56 S1 Solid       22 -   27 T
+   427 Fe3Si7                              0.2391-237 S1 Solid       22 -   27 T
+   428 FeSiO3                v             0.3049E-05 S1 Orhtoferro  25 - 1727
+   429 FeSiO3                v             0.4033E-09 S2 Fe-perovsk  25 - 2727
+   430 (FeO)2(SiO2)          v             0.3424E-07 S1 Fayalite    25 - 1277
+   431 (FeO)2(SiO2)          v             0.3132E-08 S2 beta-fayal  25 - 2727
+   432 (FeO)2(SiO2)          v             0.3090E-08 S3 gamma-faya  25 - 2727
+   433 Fe2Al4Si5O18                        0.2717E-23 S1 ferrocordi  25 - 1227
+   434 Fe3Al2Si3O12          v             0.1905E-17 S1 almandine   25 - 2727
+   435 FeCl2                               0.2467E-11 S1 Solid-1     25 - 1728
+   436 FeCl3                               0.1010E-17 S1 Solid-1     25 - 1228
+   437 FeOCl                               0.1472E-05 S1 Solid       25 -  528 T
+   438 Al2Cl8Fe                            0.5857E-60 S1 Solid       25 -  218 T
+   439 CaFe2O4                   20.28      1.000     S1 solid       25 - 1225
+   440 Ca2Fe2O5                            0.5812     S1 solid       25 - 1448
+   441 CaFe4O7                             0.3261     S1 solid       25 - 1225
+   442 CaFeSi2O6             v             0.3196E-06 S1 Clinoheden  25 - 2727
+   443 Ca3Fe2Si3O12          v             0.2317E-02 S1 andradite   25 - 2727
+   444 (MnO)(Fe2O3)                        0.5518     S1 Solid       25 -  727 T
+   445 Zn                                  0.1300E-08 S1 Solid-1     25 -  728 T
+   446 Zn3N2                               0.2550E-34 S1 Solid       25 -  427 T
+   447 ZnO                       11.92      1.000     S1 Zincite     25 - 2227
+   448 ZnF2                                0.4021E-08 S1 Solid       25 -  875 T
+   449 Na2O2Zn                             0.1289E-05 S1 Solid       25 -  727 T
+   450 ZnAl2O4                             0.6204     S1 solid       25 - 1960
+   451 Zn2SiO4                             0.7220E-02 S1 solid       25 - 1527
+   452 ZnCl2                               0.5552E-09 S1 Solid       25 -  318 T
+   453 CaZn                                0.3335E-28 S1 Solid       25 -  477 T
+   454 CaZn2                               0.1209E-36 S1 Solid       25 -  690 T
+   455 Ca2ZnSi2O7                          0.5570E-01 S1 solid       25 - 1425
+   456 (ZnO)(Fe2O3)              50.61      1.000     S1 Ferrite     25 -  727 T
+   457 Cd                                  0.1675E-05 S1 Solid       25 -  321 T
+   458 CdO                                 0.3356     S1 Solid       25 - 1227
+   459 CdF2                                0.1678E-07 S1 Solid       25 - 1072
+   460 NaCd2                               0.2299E-19 S1 Solid       25 -  382 T
+   461 MgCd                                0.7972E-24 S1 Solid       22 -   27 T
+   462 Mg3Cd                               0.2626E-61 S1 Solid       22 -   27 T
+   463 MgCd3                               0.1162E-34 S1 Solid       22 -   27 T
+   464 (CdO)(Al2O3)                        0.2133E-01 S1 Solid       25 -  927 T
+   465 (CdO)(SiO2)                         0.1087E-02 S1 Solid       25 -  827 T
+   466 CdCl2                               0.1330E-06 S1 Solid       25 -  568 T
```

```
+   467 Pb                                  0.3724E-04 S1 Solid-1       25 -  828 T
+   468 PbO                                 0.1753     S1 Litharge (    25 - 1727
+   469 PbO                                 0.1770     S2 Massicot (    25 - 1727
+   470 PbO2                                0.1541E-03 S1 Solid-1       25 -  927 T
+   471 Pb3O4                               0.3150E-04 S1 Solid-1       25 - 1227
+   472 Pb(N3)2(PbO)                                   S1 Solid         25 - **** T
+   473 PbF2                                0.5305E-06 S1 Solid         25 - 1228
+   474 PbF2                                0.1094E-05 S2 Solid         25 - 1228
+   475 Na2O2Pb                             0.3165E-06 S1 Solid         25 -  727 T
+   476 Mg2Pb                               0.3000E-40 S1 Solid-A       25 -  437 T
+   477 Mg2Pb                               0.3695E-40 S2 Solid-B      437 -  549 T
+   478 (PbO)(Al2O3)                        0.2286E-01 S1 Solid         25 - 2027
+   479 (PbO)(Al2O3)6                       0.3721E-08 S1 Solid         25 - 2027
+   480 (PbO)2(Al2O3)                       0.5057E-02 S1 Solid         25 - 2027
+   481 PbSiO3                              0.7357E-03 S1 solid alph    25 -  927 T
+   482 PbSiO3                              0.7371E-03 S2 solid beta    25 -  927 T
+   483 Pb2SiO4                             0.3599E-03 S1 solid alph    25 -  927 T
+   484 Pb2SiO4                             0.3605E-03 S2 solid beta    25 -  927 T
+   485 (PbO)4(SiO2)                        0.1556E-04 S1 Solid         25 -  725 T
+   486 PbCl2                               0.3327E-06 S1 Solid-1       25 - 1228
+   487 PbFCl                               0.7461E-06 S1 Solid         25 -   37 T
+   488 CaPb                                0.2517E-22 S1 Solid         25 -  950 T
+   489 Ca2Pb                               0.2573E-41 S1 Solid         25 - 1110
+   490 Pb(MnO4)2(PbO)3                                S1 Solid         25 - **** T
+   491 PbZnSiO4                            0.5108E-02 S1 solid         25 - 1010

    492 Mg3O4                                             SOLN-TISP
    493 FeMg2O4                                           SOLN-TISP
    494 MnMg2O4                                           SOLN-TISP
    495 MgFe2O4                                           SOLN-TISP
    496 Fe3O4                                             SOLN-TISP
    497 MnFe2O4                                           SOLN-TISP
    498 MgMn2O4                                           SOLN-TISP
    499 FeMn2O4                                           SOLN-TISP
    500 Mn3O4                                             SOLN-TISP

    501 MgAl2O4                                           SOLN-ALSP
    502 FeAl2O4                                           SOLN-ALSP
    503 MnAl2O4                                           SOLN-ALSP
    504 Al8O12                                            SOLN-ALSP

    505 MgO                                               SOLN-MONOA
    506 FeO                                               SOLN-MONOA
    507 MnO                                               SOLN-MONOA
    508 CaO                                               SOLN-MONOA

    509 MgO                                               SOLN-MONOB
    510 CaO                                               SOLN-MONOB
    511 MgAl2O4                                           SOLN-MONOB

    512 FeO                                               SOLN-MONOC
    513 CaO                                               SOLN-MONOC
    514 FeAl2O4                                           SOLN-MONOC

    515 MnO                                               SOLN-MONOD
    516 CaO                                               SOLN-MONOD
    517 MnAl2O4                                           SOLN-MONOD

    518 MgO                                               SOLN-MONOE
    519 ZnO                                               SOLN-MONOE

    520 CaO                                               SOLN-C2SB
    521 SiO2                                              SOLN-C2SB
    522 (CaO)002(SiO2)001                                 SOLN-C2SB

    523 Al2O3                                             SOLN-MULL
    524 SiO2                                              SOLN-MULL
    525 (Al2O3)003(SiO2)002                               SOLN-MULL
```

```
526 CaO                                             SOLN-C2SA
527 SiO2                                            SOLN-C2SA
528 (CaO)002(SiO2)001                               SOLN-C2SA

529 Al2O3                                           SOLN-AL2O
530 FeO                                             SOLN-AL2O
531 MnO                                             SOLN-AL2O

532 CaMgSiO4                                        SOLN-MONT
533 Mg2SiO4                                         SOLN-MONT
534 CaFeSiO4                                        SOLN-MONT

535 Ca2MgSi2O7                                      SOLN-MELI
536 Ca2FeSi2O7                                      SOLN-MELI

537 CaMgSiO4                                        SOLN-CFSM
538 Fe2SiO4                                         SOLN-CFSM
539 Ca2SiO4                                         SOLN-CFSM

540 FeO                                             SOLN-MAGN
541 Fe2O3                                           SOLN-MAGN
542 (FeO)001(Fe2O3)001                              SOLN-MAGN

543 FeO                                             SOLN-HEMA
544 Fe2O3                                           SOLN-HEMA

545 MgSiO3                                          SOLN-WOLLA
546 FeSiO3                                          SOLN-WOLLA
547 CaSiO3                                          SOLN-WOLLA
548 MnSiO3                                          SOLN-WOLLA

549 MgSiO3                                          SOLN-WOLLB
550 ZnSiO3                                          SOLN-WOLLB

551 FeO                                             SOLN-WUST
552 Fe2O3                                           SOLN-WUST
553 CaO                                             SOLN-WUST
554 ZnO                                             SOLN-WUST

555 Mg2SiO4                                         SOLN-CASI
556 Fe2SiO4                                         SOLN-CASI
557 Ca2SiO4                                         SOLN-CASI
558 Pb2SiO4                                         SOLN-CASI
559 Zn2SiO4                                         SOLN-CASI

560 Na2Ca2Si3O9                                     SOLN-NCSO
561 Na4CaSi3O9                                      SOLN-NCSO

562 Mg2SiO4                                         SOLN-OLIVA
563 Fe2SiO4                                         SOLN-OLIVA
564 Ca2SiO4                                         SOLN-OLIVA
565 Mn2SiO4                                         SOLN-OLIVA

566 Ca2SiO4                                         SOLN-OLIVB
567 Pb2SiO4                                         SOLN-OLIVB

568 Fe2SiO4                                         SOLN-OLIVC
569 Zn2SiO4                                         SOLN-OLIVC
570 Mn2SiO4                                         SOLN-OLIVC

571 MgO                                             SOLN-SLAGA
572 FeO                                             SOLN-SLAGA
573 MnO                                             SOLN-SLAGA
574 Na2O                                            SOLN-SLAGA
575 SiO2                                            SOLN-SLAGA
576 CaO                                             SOLN-SLAGA
577 Al2O3                                           SOLN-SLAGA
```

578	K2O	SOLN-SLAGA
579	FeO	SOLN-SLAGB
580	MnO	SOLN-SLAGB
581	SiO2	SOLN-SLAGB
582	CaO	SOLN-SLAGB
583	Al2O3	SOLN-SLAGB
584	Fe2O3	SOLN-SLAGB
585	PbO	SOLN-SLAGB
586	ZnO	SOLN-SLAGB
587	MgO	SOLN-SLAGC
588	FeO	SOLN-SLAGC
589	MnO	SOLN-SLAGC
590	SiO2	SOLN-SLAGC
591	CaO	SOLN-SLAGC
592	Al2O3	SOLN-SLAGC
593	PbO	SOLN-SLAGC
594	ZnO	SOLN-SLAGC
595	MgO	SOLN-SLAGD
596	Na2O	SOLN-SLAGD
597	SiO2	SOLN-SLAGD
598	CaO	SOLN-SLAGD
599	Al2O3	SOLN-SLAGD
600	K2O	SOLN-SLAGD
601	NaF	SOLN-SLAGD
602	KF	SOLN-SLAGD
603	CaF2	SOLN-SLAGD
604	MgF2	SOLN-SLAGD
605	NaCl	SOLN-SLAGD
606	KCl	SOLN-SLAGD
607	CaCl2	SOLN-SLAGD
608	MgCl2	SOLN-SLAGD
609	MgO	SOLN-SLAGE
610	FeO	SOLN-SLAGE
611	Na2O	SOLN-SLAGE
612	SiO2	SOLN-SLAGE
613	CaO	SOLN-SLAGE
614	Al2O3	SOLN-SLAGE
615	K2O	SOLN-SLAGE
616	Fe2O3	SOLN-SLAGE
617	Al2O3	SOLN-CORU
618	Fe2O3	SOLN-CORU
619	FeAl2O4	SOLN-FESP
620	Fe3O4	SOLN-FESP
621	Zn2SiO4	SOLN-WILL
622	Mg2SiO4	SOLN-WILL
623	Mg2SiO4	SOLN-FORS
624	Zn2SiO4	SOLN-FORS
625	MgO	SOLN-ZNIT
626	FeO	SOLN-ZNIT
627	MnO	SOLN-ZNIT
628	ZnO	SOLN-ZNIT
629	NaCl	SOLN-ACLA
630	KCl	SOLN-ACLA
631	NaCl	SOLN-ACLB
632	KCl	SOLN-ACLB
633	NaF	SOLN-AFA

```
   634 KF                                                  SOLN-AFA

   635 NaF                                                 SOLN-AFB
   636 KF                                                  SOLN-AFB

   637 KNO3                                                SOLN-NKNA
   638 NaNO3                                               SOLN-NKNA

   639 KNO3                                                SOLN-NKNB
   640 NaNO3                                               SOLN-NKNB

   641 NaF                                                 SOLN-SALT
   642 NaCl                                                SOLN-SALT
   643 KF                                                  SOLN-SALT
   644 KCl                                                 SOLN-SALT
   645 NaNO3                                               SOLN-SALT
   646 KNO3                                                SOLN-SALT

   647 Pb                                                  SOLN-PBLQ
   648 Na                                                  SOLN-PBLQ
   649 Zn                                                  SOLN-PBLQ
   650 Fe                                                  SOLN-PBLQ
   651 O                                                   SOLN-PBLQ

   652 Fe                                                  SOLN-FELQ
   653 Al                                                  SOLN-FELQ
   654 Ca                                                  SOLN-FELQ
   655 Mn                                                  SOLN-FELQ
   656 N                                                   SOLN-FELQ
   657 O                                                   SOLN-FELQ
   658 Pb                                                  SOLN-FELQ
   659 Si                                                  SOLN-FELQ

   660 Pb                                                  SOLN-SPEI
   661 Fe                                                  SOLN-SPEI
   662 Zn                                                  SOLN-SPEI
"+"     denotes current species selection
"v"     denotes volume data - either for gases (see Option GREAL/NOGREAL);
        or compressibility/expansivity (solid, liquid) employed when P > 1.
"T"     denotes temperature outside Cp range at 1000.00 (C)
****    denotes limited data, species only used at 298 K
================================= last line =================================
```

APPENDIX B

MATLAB code for numerical model of the heat transfer inside the dust bed.

```
%Last updated:          April 2, 1997
%This Program simulates one dimensional heat transfer in caf-dust bed
%based on fully implicit scheme . Certain simplifying conditions apply.
%
%
%       Input data to be supplied are:
%       density rhol, (assumed to be constant)
%       coefficients of effective thermal conductivity kc0, kc1, kc2, kc3, (kc2=0)
%       initial temperature Ti;
%       time and number of time steps tf(could be set by "bc" file), nt;
%       height of dust and number of nodes l, m;
%       tolerance for temperature tolT;
%
%       H (J/m^3)is the enthalpy calculated based on enthalpy data
%       supplied by file ent.dat (from FACT computed for 100 grams);
%       Th's are temperatures of calculated H's;
%       E is also Enthalpy (or internal Energy) which would be interpolated
%       from H data at required temperature.
%
%       bc.dat          gives the boundary condition data including
%                       the positions of thermocouples in the first row.
%
%       Other parameters used are:
%
%       tbc             time in boundary condition file
%
%       dt              discrete time
%       dx              discrete length
%       Tknown          known temperatures which were measured
%       nT              number of known temperatures
%       To              first boundary temperature (bottom)
%       Tl              second boundary temperature (top)
%       Tch             other known temperatures to check the calculations
%       Ei              initial enthalpy
%       E               enthalpy calculated based on H
%       dHT             differential of H in respect to temperature
%       k               effective thermal conductivity calculated based on
%                       kc's
%       R               thermal resistance
%       DT              temperature difference to be solved with set of equations
%       A               the sparse matrix of coefficients
%       b               the result vector           (       A * DT = b      )
%       tt              temporal time
%


A=sparse(m,m);
b=zeros(m,1);

% Setting the Boundary Conditions
% Boundary Conditions are presented in a data file in the following
% format
```

```
% First row includes the position of thermocouples from the bottom of boat in mm
% After the first row,
% first column represents time
% Other columns represent temperature in degree C

load bc.dat;
for i=1:length(bc(1,:))-1
        x(i)=bc(1,i+1)/1000;          % set thermocouple locations in m
end
nT=i;
l=x(nT)-x(1);                         % set the bed height
bc(1,:)=[];                           % remove first row of bc
tbc(:,1)=bc(:,1);
for j=1:nT,
        Tknown(:,j)=bc(:,j+1);
end
tf=max(tbc);
t=zeros(nt+1,1);
Ti=sum(Tknown(1,:))/nT;
T=Ti*ones(nt+1,m);
dt=tf/nt;
dx=l/m;
for n=1:nt+1,
        t(n)=(n-1)*dt;
        To(n,1)=interp1(tbc,Tknown(:,1),t(n));
        for j=1:nT-2,
        Tch(n,j)=interp1(tbc,Tknown(:,j+1),t(n));
        end
        Tl(n,1)=interp1(tbc,Tknown(:,nT),t(n));
end

% initializing enthalpy data

load ent.dat
Th(:,1)=ent(:,1);
H(:,1)=10*rhol*ent(:,2);
for i=1:length(H)-1,
        Ta(i)=(Th(i)+Th(i+1))/2;
end
Ei=interp1(Th,H,Ti);
E=Ei*ones(nt+1,m);
dHT=diff(H)./diff(Th);

% setting the initial effective thermal conductivity

k=zeros(m,1);
for j=1:m,
        k(j)=kc0+kc1*(T(1,j)+273)+kc3*(T(1,j)+273)^3;
        R(j)=dx/k(j);
end


DT=Ti*ones(m,1);
tt=dt;
n=1;

% calculating the matrix coefficients (A) and result vector (b)

while (n<=nt)
    Ao=-2*dt*k(1)/dx^2;
        A(1,2)=-dt/(R(1)*dx);
        A(1,1)=interp1(Ta,dHT,T(n+1,1))-A(1,2)-Ao;
        b(1)=E(n,1)-E(n+1,1)-Ao*(To(n+1)-T(n+1,1))-A(1,2)*(T(n+1,2)-T(n+1,1));

        Al=-2*dt*k(m)/dx^2;
        A(m,m-1)=-dt/(R(m-2)*dx);
        A(m,m)=interp1(Ta,dHT,T(n+1,m))-A(m,m-1)-Al;
        b(m)=E(n,m)-E(n+1,m)-A(m,m-1)*(T(n+1,m-1)-T(n+1,m))-Al*(Tl(n+1)-T(n+1,m));
```

```
        for j=2:m-1,
                A(j,j-1)=-dt/(R(j-1)*dx);
                A(j,j+1)=-dt/(R(j)*dx);
                A(j,j)=interp1(Ta,dHT,T(n+1,j))-A(j,j-1)-A(j,j+1);
                b(j)=E(n,j)-E(n+1,j)-A(j,j-1)*(T(n+1,j-1)-T(n+1,j))-(j,j+1)*(T(n+1,j+1)-
                T(n+1,j));
        end

% solve for DT

        DT=A\b;

% Update Temp's and k's

        T(n+1,:)=T(n+1,:)+DT(:)';

        for j=1:m,
                k(j)=kc0+kc1*(T(n+1,j)+273)+kc3*(T(n+1,j)+273)^3;
                E(n+1,j)=interp1(Th,H,T(n+1,j));
        R(j)=dx/k(j);
        end

% If the error is acceptable update enthalpy and go to the next step

        if      max(abs(DT))<=tolT
                t(n+1)=tt;
                tt=tt+dt;
                n=n+1;
                if n <= nt,
                        E(n+1,:)=E(n,:);
                        T(n+1,:)=T(n,:);
                end
        end
end

for i=1:6,
        Teff(i)=(i-1)*175+25;
        keff(i)=kc0+kc1*(Teff(i)+273)+kc3*(Teff(i)+273)^3;
end

%-----------------------
% Begin graphics section
%-----------------------

for i=1:nT-2,
        nm(i)=fix((x(i+1)+dx/2)/dx);
end
plot(t,T1,'b',t,To,'k',t,Tch(:,[1:nT-2]),'go',t,T(:,[nm(:)]),'r:');
axis([0 3000 0 1000]);
title('Temperature vs. time');
xlabel('time (sec.)');
ylabel('Temperature (C)');
legend('Top Temp','Bottom Temp','measured','measured','calculated','calculated');
text(3200,550,'k(eff) (W/degree.m), T(C)','fontsize',10);
text(3200,450,'k(eff) @25 =','fontsize',10);
text(3200,350,'k(eff) @200=','fontsize',10);
text(3200,250,'k(eff) @375=','fontsize',10);
text(3200,150,'k(eff) @550=','fontsize',10);
text(3200,50,'k(eff) @725=','fontsize',10);
text(3200,-50,'k(eff) @900=','fontsize',10);
keff1=num2str(keff(1));
text(3900,450,keff1,'fontsize',10);
keff2=num2str(keff(2));
text(3900,350,keff2,'fontsize',10);
keff3=num2str(keff(3));
text(3900,250,keff3,'fontsize',10);
keff4=num2str(keff(4));
```

```
text(3900,150,keff4,'fontsize',10);
keff5=num2str(keff(5));
text(3900,50,keff5,'fontsize',10);
keff6=num2str(keff(6));
text(3900,-50,keff6,'fontsize',10);
```

MATLAB handle graphics for heat transfer model.

```
% Initializing Graphics

clear;
clc; figure(1); clf;
set(gcf,'pos',[100 100 650 450]);
set(gca,'pos',[0.12 0.2 0.6 0.7]);
whitebg('w');

% Setting default values (which could be edited)

nt=40;
m=20;
rho1=750;
tolT=5;
kc0=0.03;
kc1=-0.45e-4;
kc2=0;
kc3-1.e-10;

% Graphics Handles

Hm_run=uimenu('Label','&Run');
        Hm_ent=uimenu(Hm_run,'Label','ent','CallBack','eafd_ent');
Hm_view=uimenu('Label','&View');
        Hm_vzoom=uimenu(Hm_view,'Label','zoom','CallBack','zoom');
        Hm_vgrid=uimenu(Hm_view,'Label','gird','CallBack','grid');

Ht1=text(0.2,0.6, 'Click on any number and','FontUnderline','on','color','b');
Ht2=text(0.2,0.5, 'change it to approperiate value','FontSize',16);
Ht3=text(0.2,0.4, 'then click on "START" botton');
set(Ht3,'FontUnderline','on','FontWeight','bold','color','r')

Hc_reset = uicontrol(gcf,'Style','push',...
        'position',[10 12 40 23],'String','reset',...
        'CallBack','clear; ent_hg');

Hc_start = uicontrol(gcf,'Style','push',...
        'position',[60 12 40 23],'String','Start','CallBack','eafd_ent');

Hc_ntstr = uicontrol(gcf,'Style','text',...
        'position',[110 12 30 20],'String','nt =');
Hc_nt = uicontrol(gcf,'Style','edit',...
        'position',[140 12 30 20],'backgroundcolor',[1 1 1],...
        'String','40','callback','nt=eval(get(Hc_nt,''string''))');
Hc_mstr = uicontrol(gcf,'Style','text',...
        'position',[180 12 30 20],'String',' m =');
Hc_m = uicontrol(gcf,'Style','edit',...
        'position',[210 12 30 20],'backgroundcolor',[1 1 1],...
        'String','20','callback','m=eval(get(Hc_m,''string''))');
Hc_kstr = uicontrol(gcf,'Style','text',...
        'position',[250 12 40 20],'String','k(ef) =');
```

```
Hc_kc0 = uicontrol(gcf,'Style','edit',...
       'position',[290 12 35 20],'backgroundcolor',[1 1 1],...
       'String','.03','callback','kc0=eval(get(Hc_kc0,''string''))');
Hc_kstr0 = uicontrol(gcf,'Style','text',...
       'position',[325 12 20 20],'String',' + ');
Hc_kc1 = uicontrol(gcf,'Style','edit',...
       'position',[345 12 50 20],'backgroundcolor',[1 1 1],...
       'String','-0.45e-4','callback','kc1=eval(get(Hc_kc1,''string''))');
Hc_kstr1 = uicontrol(gcf,'Style','text',...
       'position',[395 12 30 20],'String','x T ');
Hc_kc3 = uicontrol(gcf,'Style','edit',...
       'position',[425 12 50 20],'backgroundcolor',[1 1 1],...
       'String','1.e-10','callback','kc3=eval(get(Hc_kc3,''string''))');
Hc_kstr3 = uicontrol(gcf,'Style','text',...
       'position',[475 12 80 20],'String','x T^3 (T in K)');
Hc_rhostr = uicontrol(gcf,'Style','text',...
       'position',[610 460 70 20],'String','Density =');
Hc_rho = uicontrol(gcf,'Style','edit',...
       'position',[680 460 40 20],'backgroundcolor',[1 1 1],...
       'String','750','callback','rho1=eval(get(Hc_rho,''string''))');
Hc_dimstr = uicontrol(gcf,'Style','text',...
       'position',[720 460 50 20],'String','kg/m^3');
Hc_bcstr = uicontrol(gcf,'Style','text',...
       'position',[610 420 50 20],'String','bc.dat =');
cpstr='copy '
bcstr=' bc.dat'
Hc_bc = uicontrol(gcf,'Style','edit',...
       'position',[660 420 120 20],'backgroundcolor',[1 1 1],...
       'String','','callback',...
       'command=[cpstr get(Hc_bc,''string'') bcstr]; dos(command)');
Hc_tolstr = uicontrol(gcf,'Style','text',...
       'position',[610 381 120 22],'String','Temp. Tollorence');
Hc_tol = uicontrol(gcf,'Style','popupmenu',...
       'position',[730 380 42 20],'backgroundcolor',[1 1 1],...
       'String','30|20|10|5|3|2|1',...
       'Value',4,...
       'UserData',[30;20;10;5;3;2;1],...
       'CallBack',[...
              'UD=get(Hc_tol,''UserData'');',...
              'tolT=UD(get(Hc_tol,''value''))']);
```